Advancing in vitro studies of cell-glycocalyx interactions : development of a mechanically and biochemically defined platform

Oksana Kirichuk

THÈSE

Pour obtenir le grade de

DOCTEUR DE L'UNIVERSITÉ GRENOBLE ALPES

École doctorale : PHYS - Physique
Spécialité : Physique pour les Sciences du Vivant
Unité de recherche : Laboratoire Interdisciplinaire de Physique

Avancées dans les études *in vitro* des interactions cellule-glycocalyx : développement d'une plateforme définie mécaniquement et biochimiquement

Advancing *in vitro* studies of cell-glycocalyx interactions: development of a mechanically and biochemically defined platform

Présentée par :

Oksana KIRICHUK

Direction de thèse :

Delphine DEBARRE CHARGEE DE RECHERCHE HDR, CNRS DELEGATION ALPES	Directrice de thèse
Lionel BUREAU DIRECTEUR DE RECHERCHE, CNRS DELEGATION ALPES	Co-directeur de thèse

Rapporteurs :

OLIVIER THEODOLY
DIRECTEUR DE RECHERCHE, CNRS DELEGATION PROVENCE ET CORSE
MARTA BALLY
ASSOCIATE PROFESSOR, UMEÅ UNIVERSITET

Thèse soutenue publiquement le **20 décembre 2023**, devant le jury composé de :

OLIVIER THEODOLY DIRECTEUR DE RECHERCHE, CNRS DELEGATION PROVENCE ET CORSE	Rapporteur
MARTA BALLY ASSOCIATE PROFESSOR, UMEÅ UNIVERSITET	Rapporteure
EMMANUELLE PLANUS PROFESSEURE DES UNIVERSITES, UNIVERSITE GRENOBLE ALPES	Présidente
LILIANE GUERENTE MAITRESSE DE CONFERENCES HDR, UNIVERSITE GRENOBLE ALPES	Examinatrice

Invités :

RALF RICHTER
ASSOCIATE PROFESSOR, UNIVERSITY OF LEEDS

Acknowledgements

As I look back on my three-year PhD journey, I can't help but feel grateful for the amazing people who've been there for me every step of the way and played important roles in both my academic and personal life. I would like to take this opportunity to say a big thank you to all of you.

First of all, I express my sincere gratitude to my thesis supervisors: Delphine Débarre, Ralf P. Richter and Lionel Bureau. From the first day of my PhD, I've felt your support and your active involvement in my research. You've given me the freedom and independency to navigate my own study, but I've always known that I could count on you for advice and guidance when I hit a roadblock in my experiments. Your enthusiasm and passion for science made my PhD journey truly interesting and exciting. You've been exemplary scientists in my eyes, and I'm thrilled to have had the chance to work with and learn from you. Beyond being great supervisors, your help and support have been invaluable in my daily life, from my first days in France and the challenges I faced during my move to the UK in the midst of the Covid pandemic, to the particularly tough times of the past year. Thank you for everything.

I would like to acknowledge two project students, Clément Lassagne and Elena Murillo Vilella, whom I had the pleasure of supervising during their M1 program. Having you both on the team was a great experience, and I am grateful for the opportunity to work with you for a year. Your contributions to the project were incredibly valuable, and I appreciate the motivation and enthusiasm you put into your experiments. Working with you also provided me with a fresh perspective on the role of a supervisor, for which I am sincerely grateful.

My PhD was a part of the tight collaboration between LIPhy at the Université Grenoble Alpes, and Richter Lab at the University of Leeds, and I feel truly lucky to have had the opportunity to work in two different countries and to have been embraced as a member of both research groups. As my experimental training commenced with a 4-months stay at the Richter Lab, I would like to first extend my appreciation to all the group members, especially those who warmly welcomed me and introduced me to the world of surface functionalization. I want to acknowledge Sumitra Srimasorn, a postdoctoral researcher at the Richter Lab, for introducing me to the QCM-D method and providing unwavering support during the initial stages of my PhD. Your guidance and your own example were crucial in shaping my development as a researcher. A big thank you to Chunyue Wang, a PhD student at the Richter Lab, for your invaluable help during my first experiments, and for being such a cheerful and supportive colleague. Your positive attitude was a constant source of motivation, making my days in the lab much more enjoyable. My gratitude goes to Xiaoli Zhang, a postdoc at the Richter Lab, for training me in the spectroscopic ellipsometry method and for numerous insightful scientific discussions that we've had. Finally, I am deeply thankful to Abigail R. E. Roberts, a PhD student in the lab, for all your help and support, especially during the challenging final months of my thesis writing.

During my time at LIPhy, I had the pleasure of working and collaborating with many wonderful people. I want to express my thanks to Maaike Sangster, a PhD student in the BIOP team of LIPhy, who introduced me to the flow cytometry method and provided a helping hand with my initial experiments. I would like to acknowledge Yeraldinne Carrasco Salas, a postdoctoral researcher at LIPhy, who helped me a lot with my microfluidic experiments. You were great company in the lab, especially during those late nights when we were finishing our experiments. I am thankful to Daria Tsvirkun, a research engineer at MC2 group, for your significant help with cell culture and for sharing your expertise about the biological aspects of my project. Your contributions were instrumental in my research journey, and I genuinely appreciate your support.

I would like to extend my gratitude to the members of the Département de Chimie Moléculaire, where I conducted a significant part of my experimental work, in particular, most of QCM-D

experiments. I am deeply thankful to Liliane Guerente, Angeline Van der Heyden and Hugues Bonnet for your invaluable help with setting up my experiments.

A big thanks goes to all the friends I made at the lab who made my three years of work so much more enjoyable: Dandara, Edouardo, Emrys, Mattieu, Georges, Laila, Yeraldinne, and many others. Thank you for all the fun moments and engaging discussions we shared, and for creating a wonderfully friendly atmosphere during our lunch breaks and outside-of-work activities.

I'm also grateful for all my friends outside of the lab. Some of you have been my friends for years, and we manage to stay connected even though we're living in different countries all over the world. Others I had the pleasure of meeting here in France, and I genuinely appreciate the warmth and support of our friendship. It's truly the best thing anyone moving abroad could ever wish for.

I'd like to express my gratitude to all the members of the volunteering association "Ukraine-Grenoble-Isère", a group I've been proud to be a part of for nearly two years. Our day-to-day efforts have given me a profound sense of belonging, and our meetings have always been a comforting piece of home.

My heartfelt gratitude goes to my family, both in Ukraine and around the world, who have always been by my side. Despite the challenges of the war in my country, we've managed to stay more connected than ever, and your constant support has been my anchor through it all. I couldn't have navigated this journey without you. Thank you!

Lastly, I express my endless appreciation to my beloved husband, Ilya. You've always been there for me, believing in me, supporting me in all my beginnings, and taking part in all the craziest ideas that ever come to my head. Your unconditional love has been the driving force behind all my achievements and without you, none of this would have been possible. Looking forward to the new adventures together!

Oksana Kirichuk
October 2023

Abstract

Cell adhesion to the blood vessel wall is a complex, highly regulated physiological process. Red blood cells must repel from the blood vessel wall to prevent blood clotting while immune cells can be recruited from the vascular system to migrate into surrounding tissues. Cell adhesion hinges on the critical role played by the glycocalyx, a soft gel-like layer coating the vascular wall. However, how glycocalyx mechanical (softness, thickness) and biochemical (the composition and the density of surface receptors) properties affect this regulation is still poorly understood. Our hypothesis is that selective cell adhesion requires an intricate interplay of mechanical and biochemical cues. Elucidating the physical and molecular mechanisms that underpin selective adhesion directly in real blood vessels is challenging owing to the complexity and lack of control in *in vivo* systems. In my research, I aimed to construct an *in vitro* molecular interaction platform to facilitate mechanistic analyses. The platform combines a molecularly-defined model of the glycocalyx with mimetics of white blood cells under flow. While developing such a platform posed challenges, it offers the advantage of precise control over the physical and biochemical parameters of both the glycocalyx mimetic and cell mimetics.

The newly developed glycocalyx model includes several key ingredients with tightly controlled properties: a brush of hyaluronan (HA, an essential component of the endothelial glycocalyx) is combined with P-selectin (an adhesion molecule on the endothelial cell surface critical for the homing of leukocytes). Building on previous experience in my research group, I employed a silica-supported lipid bilayer (SLB) bearing a monolayer of streptavidin (SAv), that can bind biotinylated molecules *via* biotin-SAv bonds. I introduce here a control of the in-plane mobility of molecules anchored to the fluid lipid bilayer using glutaraldehyde (GTA) as a cross-linking agent for SAv. Controlled grafting densities of one-end biotinylated HA chains of various lengths then create brushes of different mechanical properties. I also present a new methodology for quantitatively tuning the grafting density of smaller biotinylated molecules, which is deployed here to control the grafting density of an 'adapter protein' for anchoring P-selectin. The new *in vitro* model of the glycocalyx thus affords control over the lateral mobility, the surface density and the orientation of two distinct functional molecules.

The second key component of the newly developed platform consists of white blood cell mimetics, developed based on commercially available microbeads with the size of a cell and a SAv coating. I introduce a methodology for simultaneous grafting of two types of proteins onto the bead surface: biotinylated CD44 (a ligand expressed on leukocyte surfaces, interacting specifically with HA) and PSGL-1 (a ligand of P-selectin). Additionally, I present a method for controlling the surface density of each of these proteins.

I use a combination of methods as monitoring and quality control tools of glycocalyx model formation and bead functionalization: quartz crystal microbalance with dissipation monitoring (QCM-D); spectroscopic ellipsometry (SE), reflection interference contrast microscopy (RICM); confocal microscopy with fluorescence recovery after photobleaching (FRAP) capabilities, and flow cytometry.

This newly established platform provides a controlled environment for studying blood cell adhesion, effectively bridging the divide between cell-glycocalyx chemical interactions and the mechanical aspects of cell migration under flow, including attachment and repulsion from the vascular wall. This platform holds the potential for expansion to encompass other surface adhesion molecules or to integrate multiple adhesion molecules, to gradually advance from the bottom up our understanding of the mechanisms governing cell adhesion to blood vessels.

Résumé en français

L'adhésion des cellules à la paroi des vaisseaux sanguins est un processus complexe. Les globules rouges doivent s'éloigner de la paroi du vaisseau pour éviter la formation de caillots, tandis que les cellules immunitaires peuvent migrer dans les tissus. Ce processus repose sur le glycocalyx, une couche de macromolécules couvrant la paroi des vaisseaux. Cependant, nous ne comprenons pas complètement comment les propriétés du glycocalyx (souplesse, épaisseur, composition des récepteurs) affectent cette régulation. Notre hypothèse est que l'adhésion sélective des cellules fait intervenir des facteurs mécaniques et biochimiques. Il est difficile d'étudier ce phénomène dans de vrais vaisseaux sanguins, c'est pourquoi mon étude s'est concentrée sur le développement d'une plateforme *in vitro*. Cette plateforme combine un modèle de glycocalyx avec des modèles synthétiques de globules blancs sous flux, permettant un contrôle précis des paramètres physiques et biochimiques du modèle de glycocalyx et des modèles de cellules.

Le modèle de glycocalyx nouvellement développé comprend plusieurs ingrédients clés dont les propriétés sont étroitement contrôlées : une brosse d'acide hyaluronique (HA, un composant essentiel du glycocalyx endothélial) est combinée à la sélectine P (une molécule d'adhésion à la surface des cellules endothéliales qui joue un rôle essentiel dans l'orientation des leucocytes). En m'appuyant sur l'expérience précédente de mon groupe de recherche, j'ai utilisé une bicouche lipidique supportée sur une lamelle de verre (SLB) portant une monocouche de streptavidine (SAv), qui peut lier des molécules biotinylées par l'intermédiaire de liaisons biotine-SAv. Je présente ici un contrôle de la mobilité dans le plan des molécules ancrées à la bicouche lipidique fluide en utilisant le glutaraldéhyde (GTA) comme agent de réticulation pour la SAv. Des densités de greffage contrôlées de chaînes d'HA biotinylées à une extrémité et de différentes longueurs permettent de créer des brosses aux propriétés mécaniques différentes. Je présente également une nouvelle méthodologie permettant d'ajuster quantitativement la densité de greffage de molécules biotinylées plus petites, qui est utilisée ici pour contrôler la densité de greffage d'une "protéine adaptatrice" pour l'ancrage de la P-sélectine. Le nouveau modèle *in vitro* du glycocalyx permet ainsi de contrôler la mobilité latérale, la densité de surface et l'orientation de deux molécules fonctionnelles distinctes.

Le deuxième élément clé de la nouvelle plateforme consiste en des modèles de globules blancs, développés sur la base de microbilles disponibles dans le commerce ayant la taille d'une cellule et une fonctionalisation de surface avec de la SAv. Je présente une méthodologie pour le greffage simultané de deux types de protéines à la surface des billes : CD44 biotinylé (un ligand exprimé à la surface des leucocytes, interagissant spécifiquement avec l'HA) et PSGL-1 (un ligand de la P-sélectine). En outre, je présente une méthode permettant de contrôler la densité de surface de chacune de ces protéines.

J'utilise une combinaison de méthodes comme outils de quantification et de contrôle de la qualité de la formation du modèle de glycocalyx et de la fonctionnalisation des billes : microbalance à quartz avec mesure de dissipation (QCM-D) ; ellipsométrie spectroscopique (SE), microscopie à contraste interférentiel par réflexion (RICM) ; microscopie confocale avec redistribution de fluorescence après photoblanchiment (FRAP), et cytométrie en flux.

Cette plateforme nouvellement établie offre des conditions contrôlées pour l'étude de l'adhésion des cellules sanguines, reliant les interactions chimiques cellule-glycocalyx et les aspects mécaniques de la migration cellulaire sous flux. Elle est facilement complexifiable ou adaptable, permettant une compréhension de plus en plus fine de l'adhésion des cellules aux vaisseaux sanguins.

Un résumé détaillé de chaque chapitre en français se trouve à l'Annexe C.

List of abbreviations

Ab – antibodies
BSA – bovine serum albumin
DOPC – 1,2-dioleoyl-sn-glycero-3-phosphocholine
DOPE-cap-b – 1,2-dioleoyl-sn-glycero-3-phosphoethanolamine-N-(Cap Biotinyl)
EDTA - ethylenediaminetetraacetic acid
EG - endothelial glycocalyx
FITC – fluorescein isothiocyanate
FRAP – fluorescence recovery after photobleaching
GAGs – glycosaminoglycans
GTA – glutaraldehyde
HA – hyaluronic acid
HEPES – 4-(2-hydroxyethyl)-1-piperazineethanesulfonic acid
HS – heparan sulfate
ICAM-1 – Intercellular adhesion molecule 1
LFA-1 – Lymphocyte function-associated antigen 1
OEGs – oligo-ethylene glycols
PDMS - polydimethylsiloxane
PE – phycoerythrin
PSGL-1 – P-selectin glycoprotein ligand 1
QCM-D – quartz crystal microbalance with dissipation monitoring
RICM – reflection interference contrast microscopy
SAM – self-assembled monolayer
SAv – streptavidin
SE – spectroscopic ellipsometry
SLB – supported lipid bilayer
SuAv - superavidin
SUV – small unilamellar vesicles
TAv – traptavidin
VCAM-1 – Vascular cell adhesion molecule 1
VLA-4 – Very late antigen 4

Contents

1 Introduction

Contents

This manuscript presents experimental work aimed at establishing an *in vitro* platform for the investigation of cell-glycocalyx interactions in well-controlled conditions. In this introductory chapter, I will describe the biological and physical aspects of cell-glycocalyx interactions under flow, outline the scope of my study while highlighting the existing research gap, and provide a concise overview of the analytical methods employed in this project.

1.1 Blood cell adhesion under flow

Blood cell migration in the vascular system is a complex and highly regulated process. Within the bloodstream, red blood cells (erythrocytes) make up approximately 99.9% of all circulating cells, while white blood cells (leukocytes – circulating immune cells) constitute only about 0.01% [35]. Despite their relatively small number, leukocytes play a very important role during inflammatory response, tissue repair and immune regulation, as they can be recruited from the vascular system to migrate into surrounding tissues.

The recruitment of white blood cells relies on a meticulously controlled cascade of binding interactions between cell adhesion molecules located on the endothelium – a layer of cells lining the interior surface of the blood vessels – and their corresponding ligands expressed on the surfaces of circulating leukocytes. Prior studies [88, 112, 141]. have extensively examined the leukocyte adhesion cascades, elucidating various sequential stages: initial cell capture at the endothelium, subsequent deceleration in rolling velocity, arrest, enhancement of adhesion, spreading, intravascular crawling, and ultimately, paracellular or transcellular transmigration (Fig. 1.1).

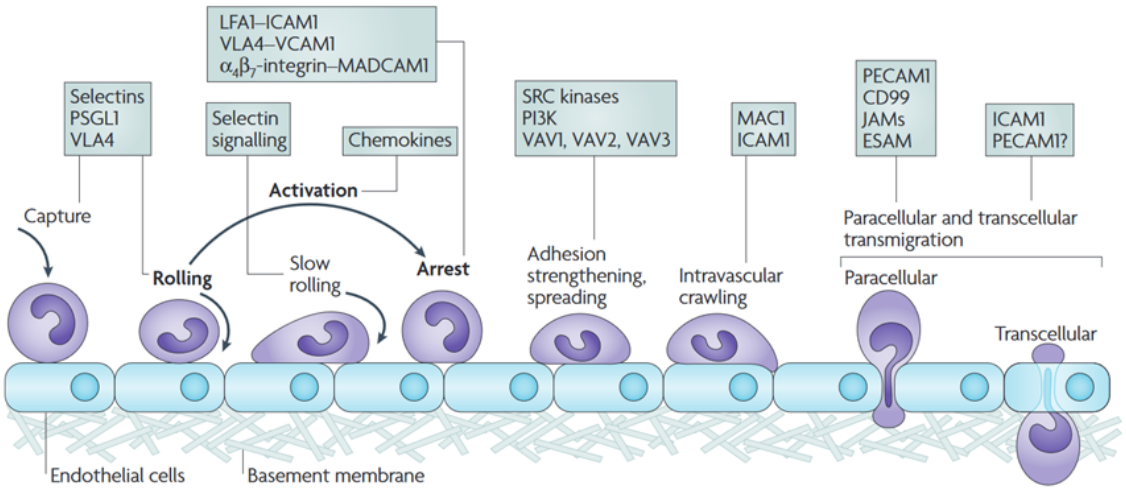

Figure 1.1: Leukocyte adhesion cascade. Key molecules involved in each of the steps of cell adhesion and transmigration to tissues: ESAM, endothelial cell-selective adhesion molecule; ICAM1, intercellular adhesion molecule 1; JAM, junctional adhesion molecule; LFA1, lymphocyte function-associated antigen 1 (also known as L2-integrin); MAC1, macrophage antigen 1; MADCAM1, mucosal vascular addressin cell-adhesion molecule 1; PSGL1, P-selectin glycoprotein ligand 1; PECAM1, platelet/endothelial-cell adhesion molecule 1; PI3K, phosphoinositide 3-kinase; VCAM1, vascular cell-adhesion molecule 1; VLA4, very late antigen 4 (also known as 41-integrin). Image taken from [88].

1.1.1 Leukocyte capture and rolling

One of the first steps in the cell adhesion cascade involves leukocytes rolling along the surface of endothelial cells, primarily facilitated by a family of molecules known as selectins. This interac-

tion aims to bring leukocytes into proximity with other endothelial signaling molecules and serves as the initiation point for the biochemical cascade involving other players [103].

The selectins comprise three subtypes: L-selectin, expressed on leukocytes; E-selectin, found on the surfaces of activated endothelial cells; and P-selectin, expressed on platelets and the surfaces of activated endothelial cells (Fig. 1.2A). Initially identified as a ligand for P-selectin, P-selectin glycoprotein ligand 1 (PSGL-1) has since been recognized as the dominant ligand for all three selectin types [88]. This interaction is calcium-dependent for all types of selectins [120]. In addition to PSGL-1, E-selectin can bind to E-selectin ligand 1 (ESL-1) and glycosylated CD44 [61].

Among these selectins, P-selectin is typically considered the first key player in cell-endothelium interactions. P-selectin is stored in Weibel-Palade bodies (storage granules located in endothelial cells), and inflammatory signals rapidly (within minutes [76]) induce the exposure of this protein on the apical surface of endothelial cells. In contrast, E-selectin is newly synthesized in response to inflammatory stimuli, and its recruitment takes hours following the initiation of an immune response [102]. P-selectin can exist on the endothelial cell surface as a monomer or dimer. Research has shown that P-selectin dimerization can enhance the stability of cell rolling due to the formation of two-by-two pairings between P-selectin and PSGL-1 homodimers (Fig. 1.2B), making this arrangement more favorable for cell capture under flow [131].

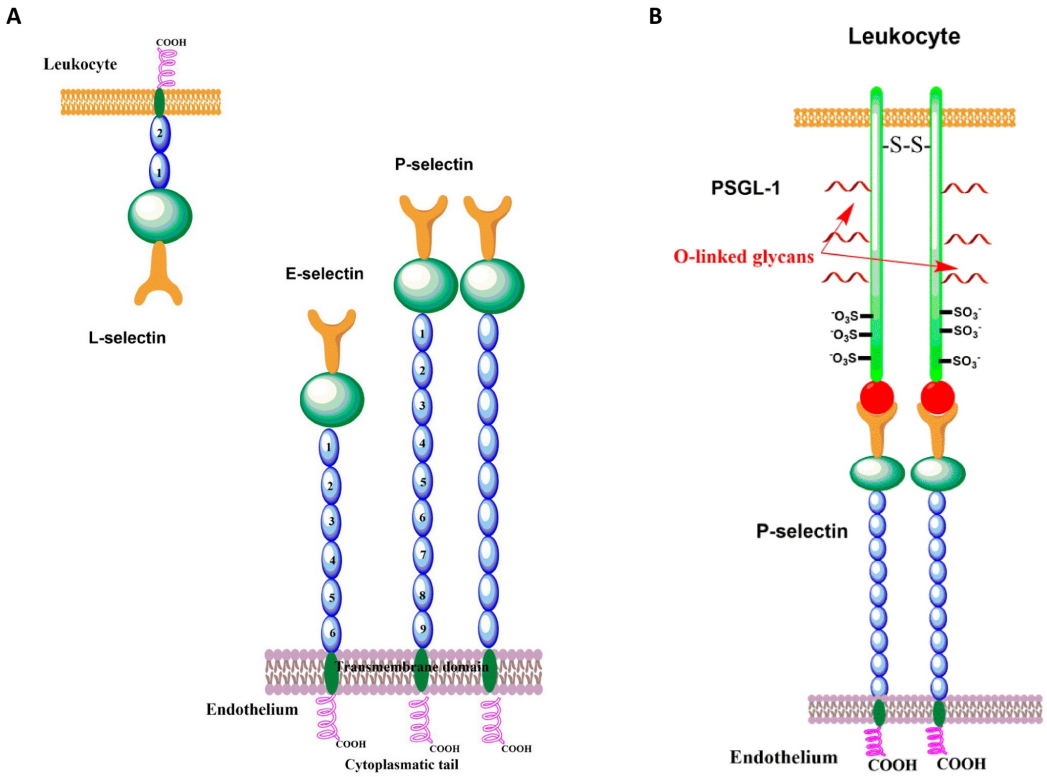

Figure 1.2: A. Family of selectins. Schematic representation of L-, E and P- selectin molecular structures. **B. P-selectin interacting with PSGL-1.**. Schematic representation of P-selectin with PSGL-1 homodimer. Pictures adapted from [157].

Remarkably, both P-selectin and L-selectin exhibit an intriguing behavior: their adhesion strength increases with shear stress, and the rolling leukocytes can detach when the flow ceases. This phenomenon is intricately tied to the catch bond properties between selectins and their ligands, which strengthen when subjected to pulling forces [148]. The catch bond phenomenon was

initially experimentally demonstrated for the P-selectin/PSGL-1 interaction [99]. Substantial evidence indicates that external mechanical forces lead to a conformational alteration at the junction of the lectin and epidermal growth factor-like domains of P-selectin. This alteration then propagates through the lectin domain, ultimately causing the PSGL-1 binding site to transition from a low-affinity to a high-affinity conformational state [84]. Furthermore, research has revealed that the rolling motion of leukocytes promotes the formation of new selectin-PSGL-1 bonds; these new bonds form before the old ones are broken [169].

1.1.2 Leucocyte activation and stabilized adhesion

Selectin-mediated rolling serves as the mechanism by which white blood cells encounter chemokines, initiating the process of activation of the circulating immune cell. For example, chemokines like CCL5 (also known as RANTES), CXCL4, and CXCL5, which are deposited onto the inflamed endothelium by platelets, induce the arrest of rolling monocytes [70, 164]. This activation results in the increase in the quantity of integrins on the leukocyte's surface [103]. In the subsequent stage of the adhesion cascade, these integrins engage with immunoglobulins expressed on the surfaces of endothelial cells, specifically, intercellular adhesion molecule 1 (ICAM-1) and vascular cell adhesion molecule 1 (VCAM-1) [19]. This interaction results in significantly stronger adhesion forces compared to those observed during selectin-mediated adhesion, leading to a decrease in rolling velocity and eventual cell arrest.

Among the most extensively studied integrins involved in stabilizing leukocyte adhesion are β_1-integrin VLA-4 (very late antigen 4) and β_2-integrin LFA-1 (Lymphocyte function-associated antigen 1). These integrins establish stable bonds with their respective ligands on endothelial cells: VCAM-1 and ICAM-1 [88].

1.1.3 Transendothelial cell migration

Transendothelial cell migration is a process that occurs after a leukocyte comes to a complete stop under flow conditions. During this process, the white blood cell traverses the layer of endothelial cells and migrates towards the interstitial tissues, where it can participate in immune responses or tissue repair. The initiation of transmigration is closely linked to endothelial cell ligands, such as ICAM-1 and VCAM-1 [88]. Additionally, this transmigration process is associated with and reliant on elevated levels of intracellular endothelial calcium (Ca^{2+}) [68].

Certain endothelial junctional molecules, including PECAM-1 (platelet and endothelial cell adhesion molecule 1), JAM-A (junctional adhesion molecule A), JAM-B, and JAM-C, can also serve as initiators for white blood cell transmigration [112].

1.2 Vascular glycocalyx: a mechanical barrier shielding the vascular wall from the blood cells

While the basic cell adhesion cascades and the involved molecular players have been intensively studied and described in the literature, the significance of the endothelial glycocalyx, a gel-like glycan-rich meshwork covering the endothelial cell surface (Fig. 1.3) has received limited attention. This soft layer which can extend up to a few micrometers in thickness, is present on all vascular endothelial cells. It was first identified and characterized in 1970 [100], and was not initially recognized as a key contributor in cell adhesion process under flow.

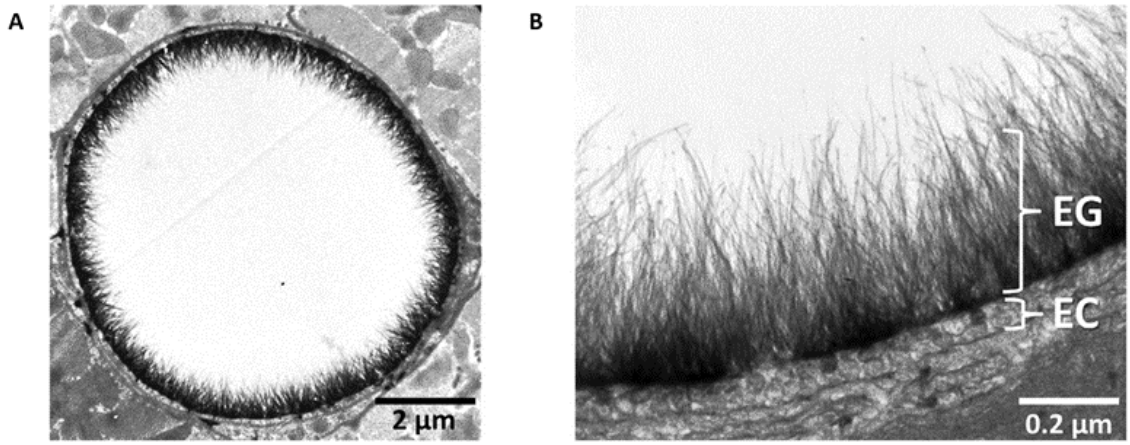

Figure 1.3: Electron microphotograph of endothelial glycocalyx. A. A luminal aspect of goat coronary capillary fully covered with endothelial glycocalyx. **B.** Endothelial glycocalyx (EG) is multiple as thick as endothelial cell (EC). Images taken from [162].

1.2.1 Structure of the endothelial glycocalyx

To date, there remains a limited understanding of the specific organization of the various structural components that constitute the endothelial glycocalyx (EG), resulting in its formation as a coat of micrometer thickness. The current comprehension of the EG describes it as a composite structure comprising proteoglycans that contribute to the mesh-like structure, and glycoproteins – cell adhesion molecules located beneath this mesh (as shown in Fig. 1.4) [130]. The glycoproteins within the EG include membrane-bound selectins, primarily P-selectin and E-selectin, as well as immunoglobulins like ICAM-1, VCAM-1, and others, along with α- and β-integrins [12].

Proteoglycans are composed of a core protein covalently linked to glycosaminoglycan (GAG) chains – linear polysaccharides comprising 20-200 repeating disaccharide units [87]. Notably, GAGs constitute up to 95% of the overall proteoglycan composition within the endothelial glycocalyx, with the remaining 5% of the mass attributed to the core protein content [87]. This distinction emphasizes the dominant role of GAGs within the glycocalyx structure.

Within the endothelial glycocalyx, five primary types of GAGs are present: hyaluronan or hyaluronic acid (HA), heparan sulfate (HS), chondroitin sulfate (CS), dermatan sulfate (DS), and keratan sulfate (KS). The most abundant GAGs, constituting up to 90% of the entire EG structure and significantly contributing to its mesh-like configuration, are heparan sulfate, chondroitin sulfate, and hyaluronan.

Among the various GAGs found within the EG, hyaluronan (HA) stands out as the largest and distinctive in that it is not covalently attached to any core protein. Instead, it directly anchors to the endothelial cell membrane through the transmembrane receptor CD44 [123]. Furthermore, HA distinguishes itself from other GAGs in endothelial glycocalyx by its lack of sulfate groups in its composition. Instead, it is characterized by the presence of carboxyl groups, which also play a role in imparting a negative charge to this polymer [123].

1.2.2 Mechanical properties of the glycocalyx

The glycocalyx exhibits varying thicknesses in different vascular structures, with reported measurements of approximately 0.2 to 0.5 µm in microvessels [163], from 0.6 to 0.8 µm in veins [23] and up to 4.5 µm in large arteries [104], all of which have been determined through microscopy techniques. It is worth noting that quantifying the thickness of this soft and heterogeneous layer is a non-trivial task, and the exact measurement largely depends on the protocol employed for tissue sample preparation and *ex vivo* fixation before visualizing it with microscopy.

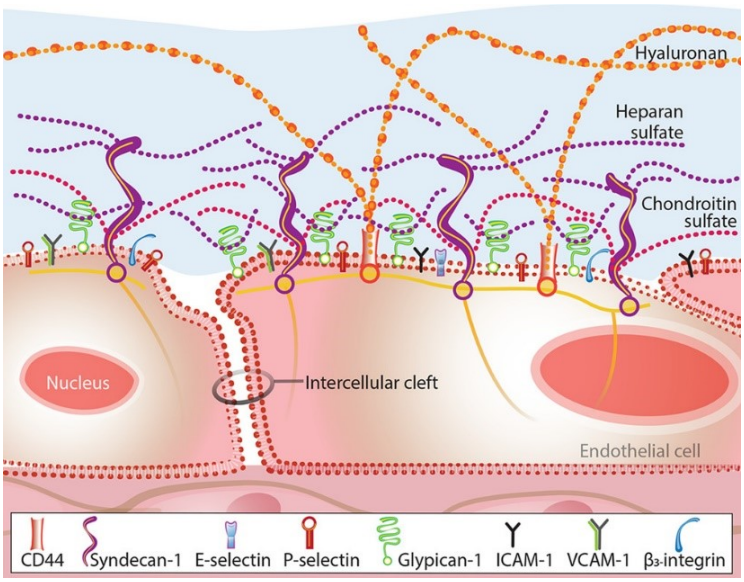

Figure 1.4: Model of the structure of the endothelial glycocalyx. It is shown as a mesh formed by GAGs (hyaluronan, heparan sulfate, chondroitin sulfate) covering the surface adhesion molecules (E-selectin, P-selectin, ICAM-1, VCAM-1 and others) located underneath. Figure taken from [50].

The highly hydrated glycocalyx layer is characterized by its remarkable softness, with values typically falling within the range of 10-1000 Pa [98,119], as measured by atomic force microscopy (AFM).

However, it is important to emphasize that the mechanical properties of the glycocalyx can undergo significant changes in response to certain pathological conditions, such as the systemic inflammatory response. Studies have shown that inflammatory reactions influenced by endotoxins can lead to a substantial decrease in the thickness of the human microvascular glycocalyx, reducing it from 0.6 µm to 0.3 µm [116]. Similarly, glycocalyx shedding has been observed following exposure to C-reactive protein, a well-known marker of inflammation and sepsis. Both *in vitro* and *in vivo* experiments have demonstrated that such exposure can lead to a more than two-fold reduction in glycocalyx thickness due to the release of hyaluronan and heparan sulfate chains [38].

The softness of the glycocalyx is also influenced by its degradation under pathological conditions. *In vitro* experiments have demonstrated that the treatment of bovine microvascular endothelial cells with 4% hydroxyethyl starch, leading to a reduction in glycocalyx thickness from 0.6 µm to 0.4 µm, resulted in a corresponding decrease in the elastic moduli of the glycocalyx, from 60 to 30 Pa [72].

1.2.3 Role of vascular wall glycocalyx in blood cell adhesion

Present on the surface of all vascular endothelial cells, endothelial glycocalyx serves as the initial point of contact for circulating cells as they reach the vascular endothelial lining. It functions as a soft, repelling cushion for most circulating cells, including red blood cells, thus contributing to the smooth flow within the microcirculation [133]. This function is particularly crucial in preventing blood clotting within the microvessels.

Conversely, research indicates that the glycocalyx can modulate the adhesion of certain types of white blood cells [31,142]. Some of the GAGs composing this soft cushion contain binding sites for leukocytes, participating in the initial phase of cell adhesion. In this phase, leukocytes interact with the binding sites presented by GAGs, which leads to a reduction in their speed under flow and indenting of the thick mesh. One notable interaction involves the long hyaluronan chains, which provide numerous binding sites for the cell receptor CD44 expressed on the surface of leukocytes. It has been demonstrated that CD44/HA interactions are essential for the capture and rolling of

activated T-lymphocytes [36], the adhesion of neutrophils that carry the CD44 receptor [80, 101] and the attachment and rolling of hematopoietic progenitor cells [30].

The current research gap revolves around comprehending the relationship between the mechanical characteristics of the glycocalyx mesh and its functional properties. While some evidence suggests that the mechanical attributes of the glycocalyx may impact leukocyte adhesion, a definitive quantification of this connection remains lacking.

For instance, one study hypothesized that an increased thickness of the endothelial glycocalyx could potentially repel circulating leukocytes, hindering their adhesion [31]. Another simulation-based research suggested that heightened rigidity in the glycocalyx layer, attributed to overproduction of hyaluronan and other glycocalyx components, might lead to reduced adhesion of circulating tumor cells [49]. However, as of now, the correlation between the mechanical properties of the glycocalyx, specifically its thickness and softness, and leukocyte adhesion has not been quantified. This gap in understanding is, in part, attributed to the absence of precise tools for conducting controlled studies in this context and the inherent complexity of investigating this phenomenon within living systems.

In the present study, our focus centers on development of the necessary tools for exploring the influence of the glycocalyx's mechanical properties on the ability of circulating cells to access the surface adhesion molecules situated beneath the thick glycocalyx mesh.

1.3 Physical principles of cell-glycocalyx interaction under flow

1.3.1 Impact of soft walls on cell adhesion: a soft matter physics perspective

While the migration of blood cells in the vascular system and the hydrodynamic concepts of the blood flow has been described in numerous studies [20, 171], the glycocalyx component of blood vessels has received relatively little attention in this context. One theoretical study conceptualized the glycocalyx as a compressible substrate lining the vascular wall and estimated the optimal elastic properties necessary for this layer to effectively repel circulating blood cells [10]. Another study elucidated the physical principles of elastohydrodynamic (EHD) forces acting on a rigid sphere near a soft wall [159] and with certain approximations, these insights can be applied to the scenario of blood cells interacting with a soft glycocalyx layer. However, the number of published works focusing on the experimental demonstration of the mechanics of regulation of circulating cells has been limited. A collaborative effort between LIPhy and the Richter Lab pioneered the investigation of this process *in vitro*, describing how the soft glycocalyx can repel cells [34] and developing the method to study cell adhesion to soft films [33].

For simplicity, the glycocalyx layer was represented as a dense HA brush, given its significance in the glycocalyx structure. The mechanical properties of this brush, including its thickness, flexibility, and spacing between chain attachment points, were precisely controlled and quantified. To mimic circulating cells, spherical particles with a 15 µm diameter, matching the typical size of blood cells [144], were employed.

Utilizing a newly developed experimental setup featuring controlled shear flow within an *in vitro* setting, the microspheres were tracked as they traversed the flow chamber and interacted with the HA brush. Detailed information regarding the components of this *in vitro* system will be provided in Section 1.7.

A precise control over the flow rate (Q) was achieved with the use of a syringe pump. The shear rate at the flow chamber wall was subsequently determined using the formula:

$$\dot{\gamma} = \frac{6Q}{WH^2} \tag{1.1}$$

where Q represents the flow rate in the system, W and H are width and height of the flow chamber.

The gravitational force exerted to the bead can be calculated as follows:

$$F_g = \frac{4}{3}\pi R^3 \Delta\rho g \tag{1.2}$$

with R – a bead radius, $\Delta\rho$ – density difference between the bead and the fluid.

The shear rate was gradually increased in the system as the beads moved along the chamber (Fig. 1.5A). It was demonstrated that in the absence of HA brush the bead velocity V increased proportionally with the shear rate, while the bead height h remained constant during all the observation time.

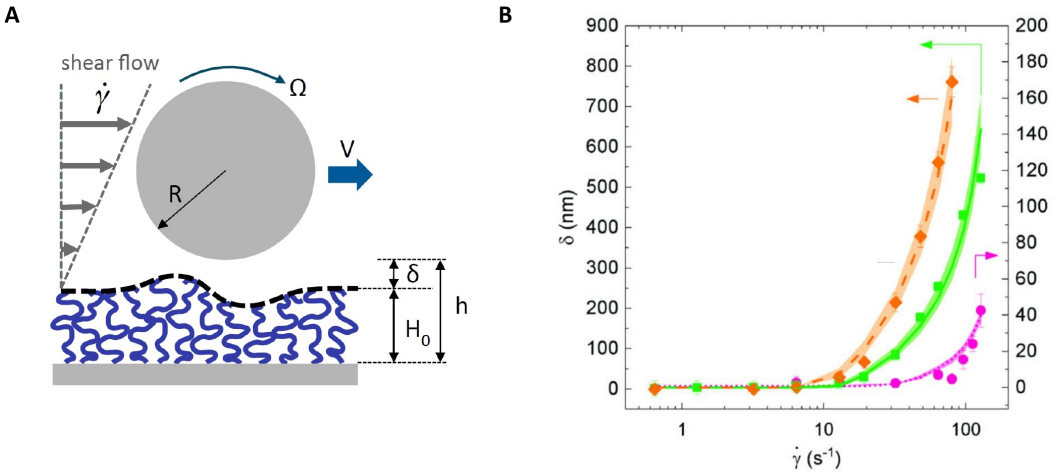

Figure 1.5: Bead repells from the soft wall. A. Bead travelling in a shear flow of velocity gradient. H_0 is the thickness of HA brush, h – measured bead height, V – bead translation velocity, Ω – bead angular velocity, δ – bead-layer distance. **B.** Theoretical predictions and experimental data for bead-layer distance δ depending on the shear rate $\dot{\gamma}$. Symbols represent experimental data obtained for different HA brushes: HA-840 (840 kDa) with high density of grafting points (green square), HA-840 with low density of grafting points (orange diamond), and HA-58 (pink circle) brushes. Lines represent theoretical predictions for $\delta(\dot{\gamma})$ with M = 5 Pa (dashed line), 57 Pa (solid line), and 15 000 Pa (dotted line). Images taken from [34].

To explain the origins of this phenomenon, Davies et al. [34] examined the contributions of two primary forces: inertial lift force F_{in} and elastohydrodynamic lift force F_{EHD}.

As demonstrated previously [27], the inertial lift force can influence the beads even under low Reynolds numbers, which is the case in the scenario being described. It can be defined as follows:

$$F_{in} \propto \rho R^2 (V - \dot{\gamma} R)^2 \tag{1.3}$$

Where ρ – fluid density, R – radius of the microbead.

However, it was estimated that the inertial lift force in the range of studied shear rates was smaller than the gravity force applied to the bead. Therefore, inertial effects alone could not lead to the bead lift.

Another force that is applied to the bead moving under flow is an elastohydrodynamic (EHD) lift force. This force originates from the elastic deformations induced in the soft surface layer by the pressure field [10]. As the bead moves, it deforms the flow near the surface, creating a counterflow that leads to deformations in the brush, ultimately causing the bead to experience repulsion. EHD force was described as:

$$F_{EHD} \propto \frac{\eta^2 R^2 H_0 (V - \Omega R)^2}{M\delta^3} \tag{1.4}$$

Where H_0 is the thickness of HA brush, Ω – bead angular velocity, M – longitudinal elastic modulus of the brush, δ – bead-layer distance.

At a given shear rate, the balance of vertical forces on the bead is defined as:

$$F_{EHD} + F_{in} = F_g \tag{1.5}$$

A bead-layer distance can then be calculated from Equations 1.2-1.5. This parameter exhibits an increase with rising flow rates in the system, and this effect is magnified with a decrease in the elastic modulus of the brush. Consequently, the softness of HA layer acts to repel cell mimetics that are not specifically interacting with glycocalyx. This theory was successfully validated by experiments (Fig. 1.5B). This investigation underscores the potential mechanical significance of the glycocalyx in regulating cell adhesion under flow conditions.

However, unlike microbeads, living cells in physiological systems exhibit deformability, which also plays a role in their repulsion from the compliant vascular wall. It was demonstrated that a red blood cell with a radius (R) of approximately 3 m, flowing in plasma ($\eta \approx 1.5$ mPa s) under a physiological shear rate $\dot{\gamma} \approx 100$ s^{-1}, at a distance $\delta \approx 0.5$ m from a glycocalyx with a thickness of one micrometer, experiences an elastohydrodynamic force F_{EHD} of approximately 0.15 pN due to glycocalyx softness [34]. At the same time, the deformation of the red blood cell gives rise to a lift force of approximately 0.25 pN [34,56]. Thus, it becomes evident that the contributions of cell and wall deformations to the lubrication forces are of comparable magnitude when considering distances on the order of sub-micrometers from the vascular wall.

1.3.2 Interplay between the soft walls and the specific of cell-glycocalyx biochemical interactions

The previous section has described the scenario of cell-glycocalyx interplay, when cells are not attracted to the glycocalyx by specific biochemical interactions, as is the case with red blood cells. Now, how would the soft wall impact cell adhesion under flow, when the attractive biochemical mechanisms between the glycocalyx and receptors expressed on the surface of circulating immune cells come into play?

This particular research question was largely overlooked in literature, primarily due to the challenges associated with studying such mechanisms *in vivo*. The study conducted by Heather Davies as part of a collaboration between LIPhy and Richter Lab has provided valuable insights into the intricate interplay between biochemical interactions and mechanical properties that govern cell adhesion under flow (unpublished data). The central hypothesis driving this study was that the mechanical properties of HA brush significantly impact the adhesion of white blood cell mimetics under flow conditions.

The main observations of this investigation were the following:

- Microbeads carrying CD44 on their surface exhibited specific interactions with the HA layer, including rolling on the soft layer and indenting the thick brush. This interaction became more pronounced with the increase of the surface density of CD44 receptor at the bead surface.
- As the softness of the brush increased, the beads indented the layer more, compressing the soft hyaluronan cushion.
- With the increase of the shear rate in the system, the beads began to detach from the layer.
- The rate of bead indentation and detachment primarily depended on the elastic modulus of the brush: the stiffer the brush, the less the bead indented it, making it easier for the beads to detach.

In the presence of specific CD44/HA interactions, the physical model describing cell movement within blood vessels becomes significantly more intricate due to the involvement of multiple contributing forces. The bead movement can be described as a combination of rolling and sliding (Fig. 1.6). Upon indenting the glycocalyx brush, the elastic HA brush generates a repulsive elastic force ($\overrightarrow{F_{el}}$). As the bead moves along the brush, CD44 receptors engage with numerous binding sites on HA chains, resulting in the emergence of a bonding force ($\overrightarrow{F_{\text{bonds}}}$). When the chains undergo elongation due to flow, this force possesses a vertical component, resulting in an increased indentation of the brush. The HA chains located at the trailing edge of the bead undergo elongation and eventual rupture under tension. Additionally, the bead experiences gravitational force $\overrightarrow{F_g}$ and hydrodynamic force $\overrightarrow{F_{\text{hydro}}}$. In total, the dynamics of bead movement are governed by the following force equilibrium equation:

$$\overrightarrow{F_{el}} + \overrightarrow{F_{\text{bonds}}} + \overrightarrow{F_g} + \overrightarrow{F_{\text{hydro}}} = 0 \tag{1.6}$$

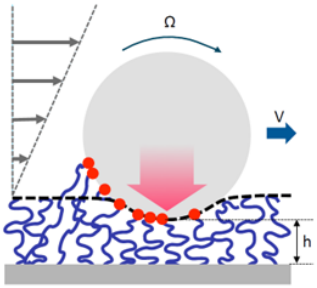

Figure 1.6: CD44-functionalized bead interacting with the hyaluronan brush under flow. Ω – bead angular velocity, V – bead translation velocity, h – compressed brush height.

Most importantly, this research has demonstrated that in presence of CD44 receptor blood cell mimetics were slowing down in the flow, rolling and substantially indenting the hyaluronan brush. This opens the potential for further investigation, as once the full glycocalyx indentation is achieved, the cell adhesion molecules located on the surface of the endothelial cells come into play and start interacting with the corresponding ligands on leukocyte surface, leading to even more enhanced cell adhesion.

1.4 Research hypothesis

Aiming to delve deeper into the understanding of the initial steps of blood cell adhesion, we would like to investigate the interplay between physical and biochemical mechanisms taking part in the next stage of cell-glycocalyx interaction: what happens after the cell indents the thick glycocalyx layer and how it gets the access to the surface adhesion molecules? We hypothesize that the **glycocalyx indentation provides access to the underlying surface adhesion molecules** (Fig. 1.7) and we are interested in how the mechanical properties of glycocalyx can affect the ability of the cells to reach these receptors. Furthermore, we anticipate that **the fluidity of the endothelial cell-mimetic surface may play a role in the recruitment of cell adhesion molecules** during their interaction with corresponding ligands on the leukocyte surface.

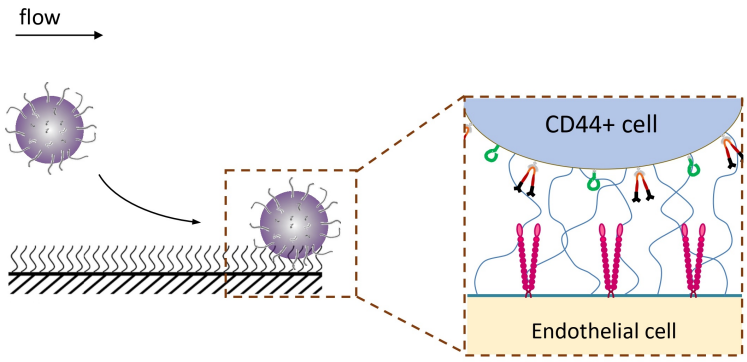

Figure 1.7: Graphical representation of the research hypothesis. Blood cell carrying CD44 receptor specifically interacts with the glycocalyx, indents it and reaches the surface adhesion molecules located underneath at the surface of endothelial cell.

1.5 *In vitro* platform for studying cell-glycocalyx interaction

Investigating the intricate interplay between the physical and biochemical aspects of cell adhesion *in vivo* poses significant challenges. This complexity arises from the difficulty in precisely characterizing the mechanical properties of the soft glycocalyx layer and in controlling physical parameters within living systems. Therefore, the most promising way to tackle this research question is to use an *in vitro* system with precisely defined characteristics, allowing for controlled manipulation of physical parameters.

The application of an *in vitro* platform offers several advantages compared to *in vivo* systems:

1. Fine-tuning the mechanical properties of the glycocalyx, such as its thickness and elasticity, enables a systematic evaluation of their impact on cell interaction with the soft wall.

2. The manipulation of the type and surface density of endothelial receptors permits the assessment of the distinct influence of each receptor type on cell adhesion under flow.

3. Substituting living leukocytes with cell mimetics allows for a reliable differentiation between the impact of specific receptors binding to the glycocalyx and those binding to endothelial cell adhesion molecules during the cell adhesion process.

4. Regulating the flow dynamics within the system facilitates the examination of cell-glycocalyx interactions under different shear conditions.

5. Employing a specialized microscopy-based system enables more robust observation and characterization of the interaction between blood cell mimetics and the glycocalyx model under flow conditions.

The *in vitro* platform previously established by Davies et al. [33] with tunable mechanical properties of glycocalyx and controlled shear rate in the microfluidic system effectively facilitated the examination of the physical aspects of cell interaction with the soft wall. However, this established platform could not be used to address the research hypothesis of my project, necessitating the development of several new tools specifically tailored for this investigation.

1.6 Overall aim and specific objectives

In summary, the overarching goal of this project is as follows:

To understand how the mechanical properties of glycocalyx control the blood cell access to the surface receptors during the initial stage of the cell adhesion.

The specific research objectives of this thesis encompass the following:

1. Develop a new molecularly defined *in vitro* model of the endothelial cell surface that combines a glycocalyx-like layer of tunable thickness and elasticity with cell adhesion receptors buried within.

2. Develop a method to quantitatively tune the density of surface-anchored cell-surface molecules.

3. Develop coated microbeads as white blood cell mimetics that co-present on their surface two distinct receptors: one binding to the glycocalyx and the other to an endothelial cell adhesion receptor.

1.7 Methodology

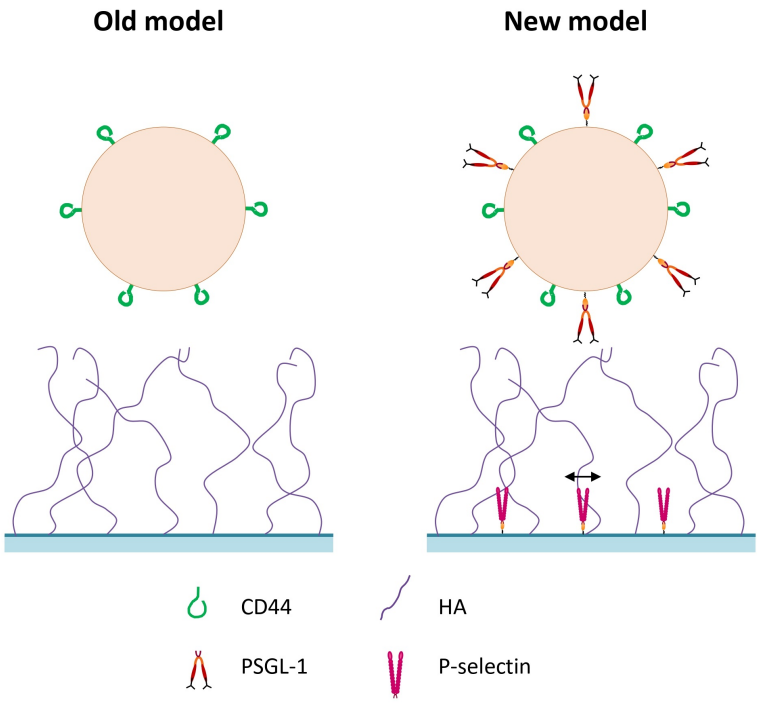

Figure 1.8: Glycocalyx and white blood cells biomimetics: old and improved models. In new model, surface receptor P-selectin is added to the glycocalyx mimetic and its ligand PSGL-1 is incorporated into the cell mimetic. The new model incorporates fluid anchoring of receptors within the glycocalyx mimic, enabling the exploration of receptor recruitment effects.

In this study, we have chosen to focus on one specific endothelial surface receptor – P-selectin, and its corresponding ligand, PSGL-1, which is expressed on the surface of leukocytes. As previously detailed in Section 1.1, this receptor-ligand pair is known to play a pivotal role in the initial phases of blood cell adhesion to the endothelium. Consequently, it represents one of the earliest interactions that occur after the cell has indented the dense glycocalyx layer.

I have used a previously developed platform [33] as a foundation for further refinement and enhancement, making it more tailored to address our specific research inquiry. Figure 1.8 illustrates a schematic comparison between the original and enhanced models.

A refined model of the vascular wall glycocalyx consists of a dense HA brush, with P-selectin endothelial receptors situated beneath it. The specifics of this model's development will be expounded upon in Chapter 2. The advanced cell mimetic features two distinct receptor types on its surface: the CD44 receptor binding to the HA brush and PSGL-1 serving as a ligand for P-selectin. Further elaboration on the development of these cell mimetics will be provided in Chapter 4.

1.8 Existing analytical methods to address the research aim

Throughout the project, a number of analytical techniques for surface characterization were employed. While these methods are well-established, I include in this section a brief description of each for the non-specialist reader. One of these analytical methods - quantitative fluorescent measurement of receptor surface densities - stands out as I have developed the methodology over the course of my project, and will be described separately in the Appendix A.

1.8.1 Quartz crystal microbalance with dissipation monitoring (QCM-D)

Quartz crystal microbalance with dissipation monitoring (QCM-D) is an acoustic real-time sensing technique developed in 1990's [140]. It allows measuring the nanoscale changes in mass per unit surface area at the surface of the sensor which results in changes in resonance frequency. QCM-D also measures energy dissipation, which is related to the viscoelastic properties of the biomolecular film attached to the sensor surface (the relative thickness of the layer, the relative softness).

In my study, I employed the QCM-D technique to monitor the formation of layers and observe specific molecular interactions while developing the glycocalyx molecular model (refer to Chapter 2 for detail). Additionally, this method was used as a means to control the quality of surface functionalization.

The sensors for the QCM-D are made of piezoelectric material (typically, quartz). The sensor gets excited and driven to mechanical resonance by an external electric field. The material on the sensor surface modifies the resonance properties (frequency and bandwidth, or energy dissipation) and by detecting these changes information about the bound material is obtained. Based on detected changes in frequency (f), variations in adsorbed mass can be inferred, and energy dissipation (D) yields information about intermolecular interactions (Fig. 1.9).

The QCM-D system enables measurements of frequency and dissipation at multiple overtones (n). The overtone order should be odd (1, 3, 5...) to ensure an antisymmetric motion pattern of the quartz. Conversely, when the overtone order is even (2, 4, 6...), the deformation becomes symmetric, and there is no electrical current between the electrodes. As the overtone number increases, the penetration depth of the transverse wave from the oscillation crystal into the coated material and bulk fluid decreases, which allows for insight into certain vertical regions of the adhered film. Therefore, measurement at multiple overtones can be beneficial for studying the viscoelastic properties of the material.

For investigations involving intermolecular interactions using QCM-D, the 5th overtone is a

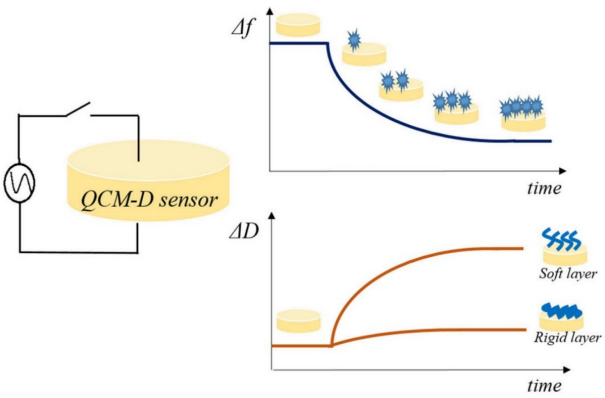

Figure 1.9: Schematic representation of frequency and dissipation monitoring in QCM-D. The data is acquired when the electric field is turned off. Increasing adsorbed mass at the sensor surface leads to a decrease in frequency Δf, and changes in dissipation ΔD reflect the surface rigidity. Picture taken from [156].

commonly favored choice. In my study, I also adopted the 5th overtone to present our experimental data, aligning with this established practice.

The principle of work of QCM-D is based on Sauerbrey relationship developed in 1959 [143] relating adsorbed mass Δm with the change in frequency Δf:

$$\Delta m = \frac{C}{n}\Delta f \tag{1.7}$$

where n – harmonic number; C – mass sensitivity constant.

In this equation, mass sensitivity constant can be defined as:

$$C = \frac{t_q \rho_q}{f_0} \tag{1.8}$$

where t_q - thickness of quartz, ρ_q - density of quartz, f_0 - resonance frequency.

C = 18 ng $\cdot \mathrm{cm}^{-2} \cdot \mathrm{Hz}^{-1}$ for commonly used QCM-D sensors $(f_0 = 4.95\mathrm{MHz})$.

Sauerbrey relationship remains valid for adsorbed masses that are small compared to the mass of the crystal), evenly distributed and that form a rigid film. The latter condition is particularly important for biological applications. The rigidity condition is fulfilled when:

$$\frac{\Delta D_n}{-\Delta f_n} \ll 0.4 \cdot 10^{-6}\ \mathrm{Hz}^{-1} \tag{1.9}$$

It is important to note that QCM-D detects the total mass mechanically coupled to the sensor, including the mass of the coupled water. Therefore, frequency change Δf cannot usually be directly translated into the bound mass of the molecule.

Energy dissipation D can be described as:

$$D = \frac{E_{\mathrm{lost}}}{2\pi E_{\mathrm{stored}}} \tag{1.10}$$

where E_{lost} - energy dissipated per oscillation, E_{stored} – total energy stored in the system.

Dissipation of the system increases with the decrease of the film rigidity [134], which is the case, for example, for HA brush formation.

In a QCM-D setup, reagents are sequentially introduced into the system using a controlled flow mode via a pump. They interact with the sensor surface, enabling direct observation of intermolecular interactions. Consequently, this method enables the examination of the binding/adsorption dynamics.

1.8.2 Spectroscopic ellipsometry (SE)

Spectroscopic ellipsometry (SE) is a highly sensitive optical technique relying on the analysis of changes in light polarization upon its reflection from a planar interface [48]. This method offers valuable insights into the structure of the interface and enables the precise measurement of parameters such as areal mass density, thickness, and optical properties of adsorbed multilayer films at the nanoscale level (< 1 ng/cm^2) with high time resolution (milliseconds). Notably, SE can be conducted without the need for labeling.

In this project, I used the SE to quantitatively determine the areal mass density of surface-bound proteins. This method was employed as part of the development process for precise control of protein surface density, as elaborated in Chapter 3.

The principle of spectroscopic ellipsometry is shown in Figure 1.10. The incident light's polarization is determined by its electric field, which comprises two components: an electric field oscillating in the plane of incidence (referred to as the p-polarized component) and another oscillating perpendicular to the plane of incidence (referred to as the s-polarized component). When these two components are in phase, they combine to produce linearly polarized light. Upon reflection from the sample, the s- and p-components exhibit disparate behavior, leading to a phase difference and different amplitudes. Consequently, this results in elliptically polarized light, and the two key parameters are detected by the instrument: the phase difference between p and s-polarized light (Δ) and the amplitude ratio (Ψ). It's important to note that SE is not a direct means

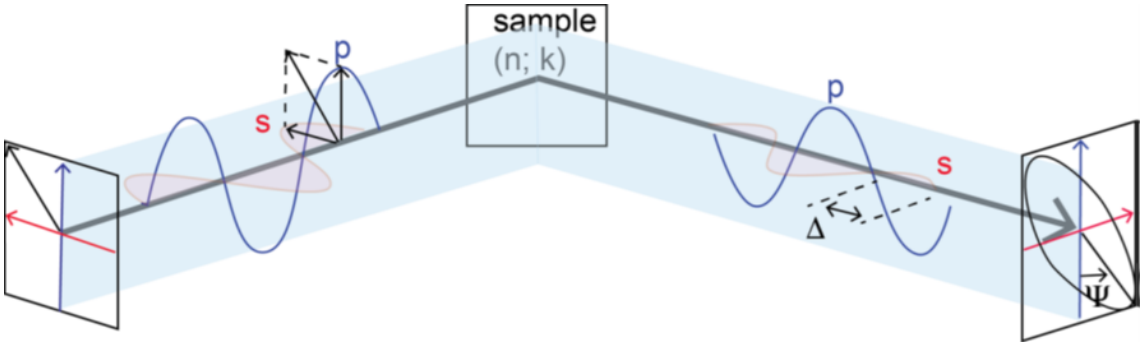

Figure 1.10: Principle of spectroscopic ellipsometry.

of obtaining optical properties of the film; instead, it necessitates the application of mathematical models to fit the measured Δ and Ψ angles.

The fitting of SE data entails the application of a complex regression-based mathematical model (Fig. 1.11) which typically relies on a multilayer model. Optical properties of a given layer are represented by the Cauchy approximation:

$$n(\lambda) = A + \frac{B}{\lambda^2} + \frac{C}{\lambda^4} \tag{1.11}$$

where n – refractive index of the layer; λ – wavelength; A, B, C – dispersion parameters. A defines the refractive index range, while B and C determine the dispersion characteristics.

Depending on the specific model employed, various film properties can be extracted, including thickness (d), refractive index (n), extinction coefficient (k), dispersion parameters (A, B, C), volume fraction of medium A in B, surface roughness, and others. The model used in this study is described in detail in Methods section.

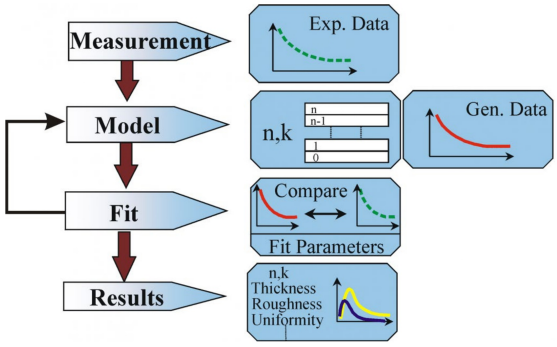

Figure 1.11: Spectroscopic ellipsometry data analysis.

The combined use of QCM-D and ellipsometry allows a detailed investigation of real-time formation and alteration of thin layers at the solid-liquid interface. These two techniques complement each other effectively, providing insights into various aspects, such as mass, thickness, mechanical properties, as well as the organization or structure of the layers [128].

In my research, a combined QCM-D/SE assay was employed to establish a calibration curve correlating frequency changes detected by QCM-D with areal mass density measurements obtained through SE. This assay was conducted by R. P. Richter, and the findings are detailed in Chapter 3.

There are different experimental setups allowing to simultaneously conduct QCM-D and SE measurements, some of which are commercially available (e.g., QSense Explorer Ellipsometry from Biolin Scientific) and others are custom-made. Experiments conducted over the course of this project were performed in an open fluid cell designed by Carton et al. [21].

1.8.3 Confocal microscopy and FRAP

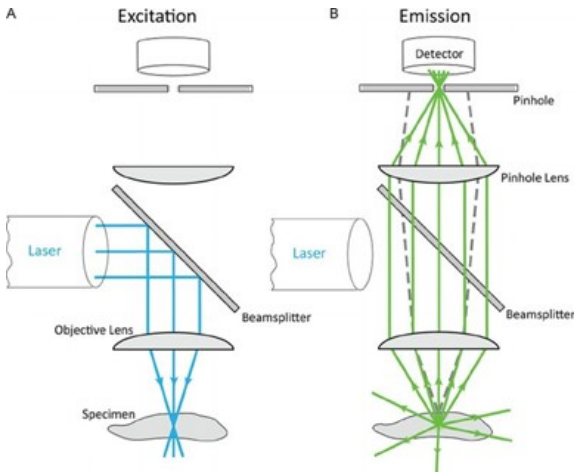

Figure 1.12: Working principle of confocal microscope. A. Excitation: a laser beam (depicted by blue lines) is focused onto the specimen, generating fluorescence within the excitation cone. **B.** Emission: fluorescence emitted from the focal point only (indicated by green lines) is collected and collimated by the objective lens, then further focused by a secondary lens onto a pinhole in front of the detector. Fluorescence originating from areas outside the focal point is not imaged though the pinhole and therefore are effectively blocked. Image taken from [74].

Confocal microscopy is an optical imaging method that employs diffraction-limited point illumination, and signal detection through an optically-conjugated pinhole to eliminate unwanted

out-of-focus signals. In the context of surface functionalization, this technique serves as a crucial tool, enabling the evaluation of the uniformity of the formed biolayers.

In confocal microscopy, laser-based excitation light is commonly used to produce intense fluorescence or reflectance specifically at the focal point [117]. A laser beam with collimated light undergoes reflection by a dichroic beam splitter and is subsequently focused by an objective lens onto a diffraction-limited spot within the sample (as depicted in Fig. 1.12A). Fluorescence is generated within the cone of illumination, encompassing the focused spot but extending beyond it.

The objective lens efficiently gathers the emitted fluorescence signal originating from excited fluorophores within the focal plane, forming a collimated beam. This collimated fluorescence beam is directed back through the dichroic beam splitter and further focused through a pinhole onto a detector, as illustrated in Fig. 1.12B (represented by green lines). Importantly, fluorescence arising from regions outside the focal point, such as the sample's surface, is not well collimated by the objective lens (grey lines in Fig. 1.12B). Consequently, it remains unfocused and is effectively blocked from reaching the pinhole.

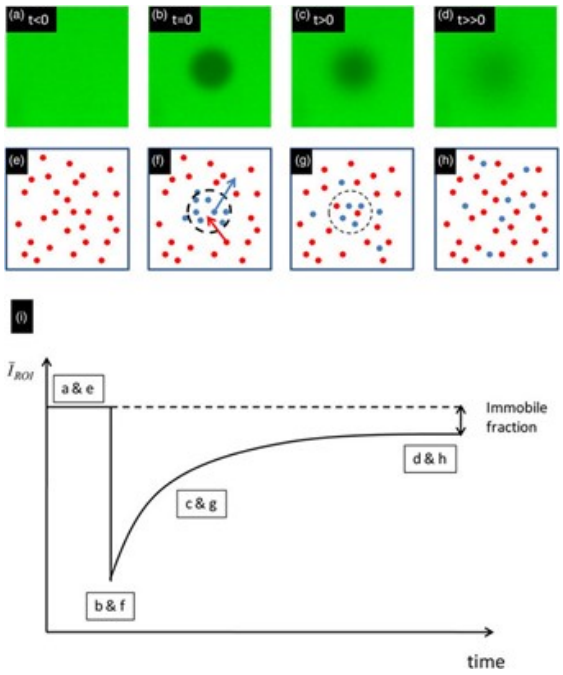

Figure 1.13: Principle of FRAP. Panels **A-D** illustrate the principle of a FRAP measurement, **E-H** – scheme of molecular diffusion, **I** – detected intensity of fluorescence measured inside the bleached region over time. Picutre taken from [94].

Fluorescence recovery after photobleaching (FRAP) is a well-established fluorescence microscopy technique employed to elucidate the dynamics of mobile fluorescent molecules. These dynamics encompass processes such as diffusion, transient binding events, and directed transport [94]. FRAP analysis can be conducted using a classical epifluorescence microscope, without the strict requirement of a confocal microscope.

To evaluate the mobility of the layer using FRAP, a defined region within the field of view is subjected to intense laser illumination, causing rapid photobleaching of fluorophores within that region. Subsequently, a series of images is acquired over time over a larger region of the sample (often until complete fluorescence recovery within the bleached region) (Fig. 1.13A-H), and the fluorescence intensity within this region is quantified. The mobile layers are characterized by returning to the initial or close to initial level of fluorescence due to the molecular diffusion (Fig.

1.13I). The resulted curve (intensity vs time) can then be fitted with an exponential function:

$$I = A - e^{-\frac{t-\tau}{B}} \tag{1.12}$$

where A, τ – fitted parameters, B – characteristic diffusion time.

Using this empirical formula and a circular bleached area, the diffusion coefficient can then be defined as follows [127, 149]:

$$D = \frac{d^2}{16\tau} \tag{1.13}$$

where d corresponds to the diameter of the bleached area.

The confocal setup accessible at LIPhy does not include a dedicated FRAP module allowing circular or point bleaching. Consequently, for the assessment of layer mobility, I performed bleaching and monitored the recovery within a square region measuring 10x10 µm. As an approximation, I chose to make use of Eq. 1.13 to calculate the diffusion coefficient of the square region which corresponds to the same surface area as the circular area of diameter d.

In my project, confocal microscopy was used to observe the fabricated glycocalyx mimetic, evaluate its uniformity, and measure its fluidity using FRAP. These aspects will be expounded upon in Chapter 2. Furthermore, confocal microscopy was used to quantitatively measure the surface density of bound receptors, specifically P-selectin. The detailed methodology for this assessment will be presented in Chapter 3 and the "Quantification of receptor surface density through fluorescence analysis" section in Appendix A.

1.8.4 Reflection interference contrast microscopy (RICM)

Reflection interference contrast microscopy (RICM) is an optical technique allowing to measure the distance between an object and the underlying surface [91]. In my project, it was used to assess the thickness of the formed hyaluronic acid (HA) brushes and to elucidate the interactions between the functionalized microbeads and the glycocalyx mimetic. Furthermore, it served as a tool for quality control to ensure the uniformity of the layer.

RICM detects the interference pattern between light waves reflected from the object of interest and the underlying surface, allowing to characterize the thickness of the layers with a precision of a few nm in the case of simple objects such as spherical microbeads (Fig. 1.14A). When the beads are introduced into the system, the reflection from the lower surface of the beads (closest to the substrate) is combined with that of the top surface of the coverslip to generate a fringe pattern (Fig. 1.14B). This pattern can be converted into an intensity profile as a function of the distance from the center and fitted using the following formula [33]:

$$I(r) = A_1 e^{-\frac{r_1}{w_1^2}} + A_2 e^{-\frac{r_2}{w_2^2}} \cos\left(\phi_0 + \frac{2\pi n_{\text{buffer}}}{\lambda}\delta h(r)\right) \tag{1.14}$$

where A_1, A_2 account for the amplitude of the offset and of the fringes respectively, w_1, w_2 account for their empirical decrease with the bead distance to the surface, r_1 and r_2 are effective reflection coefficients, n_{buffer} is the refractive index of the medium, ϕ_0 accounts for the phase difference in r_1 and r_2, and $\delta h(r)$ describes the geometrical path length difference between the ray reflecting on the bead and the one reflecting on the substrate surface.

By recording fringe patterns at two distinct wavelengths (green and red light), it is possible to accurately determine the height of the microbeads over a range of about 1 µm. This method can be applied to measure the thickness of formed biolayers by allowing microbeads to settle on them. Furthermore, it enables real-time tracking of microbead motion in 3D, facilitating the characterization of precise interactions between the layer and functionalized microbeads.

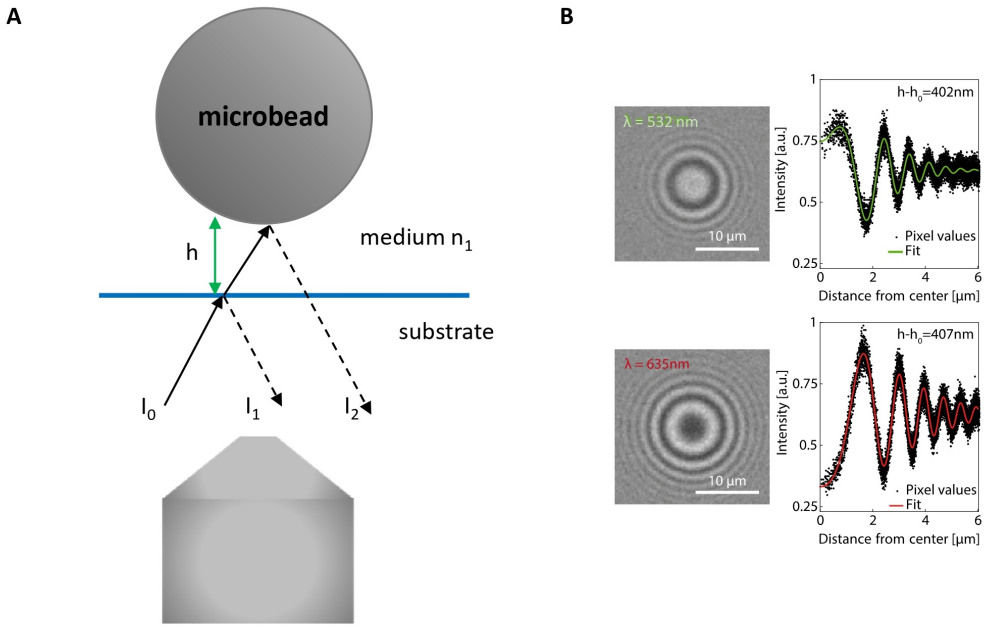

Figure 1.14: Measuring the thickness of the layer with the use of RICM. A. Principle of RICM imaging of a microbead close to a surface (colloidal probe RICM). Interferences between I_1 and I_2 are detected and provide information on height h. **B.** Example of microbead is imaged in green and red light and corresponding intensity profiles as a function of the distance from the pattern center.

1.8.5 Flow cytometry

Flow cytometry is a widely employed technique for quantifying the physical and chemical attributes of individual cells or particles in a liquid medium based on their light scattering and fluorescence emission properties [1]. In this method, a sample containing cells or particles is introduced into a fluidic system where they traverse the path of an excitation laser (Fig. 1.15). The light scattered by these entities is quantified using two optical detectors: forward scatter (FSC), which detects scattering along the laser's path, and side scatter (SSC), which measures scattering at a ninety-degree angle relative to the laser. In addition, fluorescence emission is quantified by one or more additional detectors around chosen wavelength ranges.

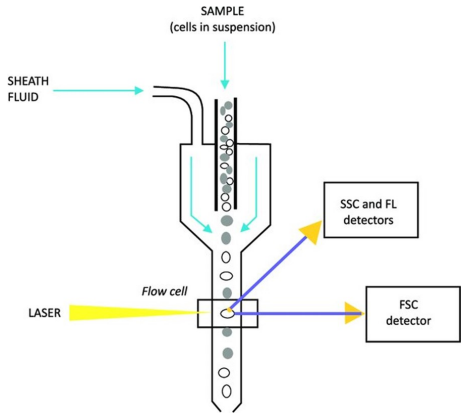

Figure 1.15: Principle of the flow cytometry. A sample stream diluted with sheath fluid passes through a laser beam. The scattered light is then detected and quantified by forward scatter, side scatter, and fluorescence detectors. Figure taken from [125]

Flow cytometry is a valuable tool for quantifying the density of specific receptors on cells or cell mimetics [110]. In this case, cells or cell mimetics are labeled with fluorescently tagged antibodies that bind to the receptor of interest, and the resulting fluorescence is quantified.

Over the course of my project, I used the flow cytometry to quantify the density of specific receptors of interest (CD44 and PSGL-1) on microbeads employed as cell mimetics. The outcome of these experiments will be elaborated upon in Chapter 4.

2

Glycocalyx model with defined mechanical and biochemical characteristics

Short summary

In order to study cell-glycocalyx interactions in well-controlled conditions *in vitro*, a novel molecular model of the vascular wall glycocalyx has been developed. Based on a supported lipid bilayer, it incorporates both a thick hyaluronan brush and the surface adhesion molecule P-selectin distributed homogeneously across the surface. Furthermore, a method allowing to tune the mobility of this system has been developed. The chosen model system allows to controllably tune the mechanical properties of the glycocalyx mimetic as well as the type and the density of surface receptors located underneath.

Acknowledgements

Most of the experiments presented in this chapter were designed, performed and analyzed by myself, except for the measurement of HA-840 brush thickness presented in Fig. 2.18. I would like to acknowledge Clément Lassagne, an M1 student under my supervision, for performing this experiment and my thesis supervisor Delphine Débarre for analyzing the experimental data. The QCM-D experiments were performed in the Richter Lab, at the University of Leeds, or in the Département de Chimie Moléculaire (DCM) at UGA.

Contents

2.1 Introduction

2.1.1 Model system of vascular wall glycocalyx

To explore the influence of the mechanical characteristics of the vascular wall glycocalyx on its regulation of access to the surface receptor P-selectin, I embarked on the development of a complex, multicomponent model system. One of the key elements within this system is the molecular representation of the vascular glycocalyx, created *in situ* on a glass substrate within the microfluidic channel.

Compared to systems based on living cells, such molecular model has several advantages:

1. *Well-controlled parameters.* In contrast to cell-based layers, the molecular model provides enhanced versatility in parameter selection for the investigation of cell-glycocalyx interactions. Using the established protocols for surface functionalization, both physical properties (e.g., softness, stiffness) and biochemical qualities (e.g., type of grafted receptors and distance between them) of the model glycocalyx can be controlled and adjusted.

2. *Focus on a specific types of interaction: HA/CD44 and PSGL-1/P-selectin.* In living systems, the cell-glycocalyx interplay involves numerous types of molecular interactions. In contrast, model system provides the capability to isolate and investigate specific interactions of interest. This enables a focused exploration of the significance of individual surface receptors in cell adhesion. Additionally, both physical and chemical characteristics of the surface can be adjusted beyond physiological ranges, making the interaction of interest more enhanced and easier to study.

3. *Ease of handling*. While cell-based systems demand specific precautions, such as temperature control, pH control, and precise medium composition for integration into microfluidic devices, molecular models are more straightforward to work with and exhibit greater stability under varying external conditions. Moreover, glycocalyx molecular mimetics remain stable over extended periods (over 24 hours or more), facilitating the experimental planning.

In the research preceding my study [33] (described in detail in sections 1.3.1-1.3.2) the model system of glycocalyx consisted of a thick brush formed of hyaluronan chains that were grafted on a glass support. In my project, I made improvements to this model by incorporating surface adhesion molecules (P-selectin) buried within the thick HA brush (Fig. 2.1). Furthermore, I increased the ability to adjust the surface mobility of the molecular model by transitioning from a self-assembled monolayer (SAM) to a supported lipid bilayer (SLB) molecular platform.

The new glycocalyx model had to meet the following requirements:

1. It had to simultaneously present two types of molecules: HA brush and P-selectin surface receptors.

2. The grafted molecules needed to be stable in time and to remain functional towards the specific interactions with their ligands (CD44 for HA brush and PSGL-1 for P-selectin).

3. The glycocalyx mimetic needed to have defined mechanical and chemical characteristics:

   - To study the specific interaction between the circulating cells and the surface receptors, located on the endothelial cell surface, the hyaluronan brush must be of physiologically relevant thickness (about 1 micron [83]) and softness (10-1000 Pa [98]), allowing the cells reach the receptors;
   - To provide a negative control for this interaction, the HA film must be stiff and thick, so it can prevent cells from reaching the receptors (see Section 2.1.4.2 for detail);

– To evaluate the significance of a specific interaction in cell adhesion, the surface receptors need to be located on a biologically relevant distance from each other. However, to validate the function of co-presented P-selectin receptors alongside a thick HA brush, higher receptor densities can be employed.

In the following sections I will provide a detailed description of the approaches employed in creating the glycocalyx molecular model: the establishment of the molecular platform and the strategies employed to achieve the stable and precisely controlled anchoring of the molecules of interest.

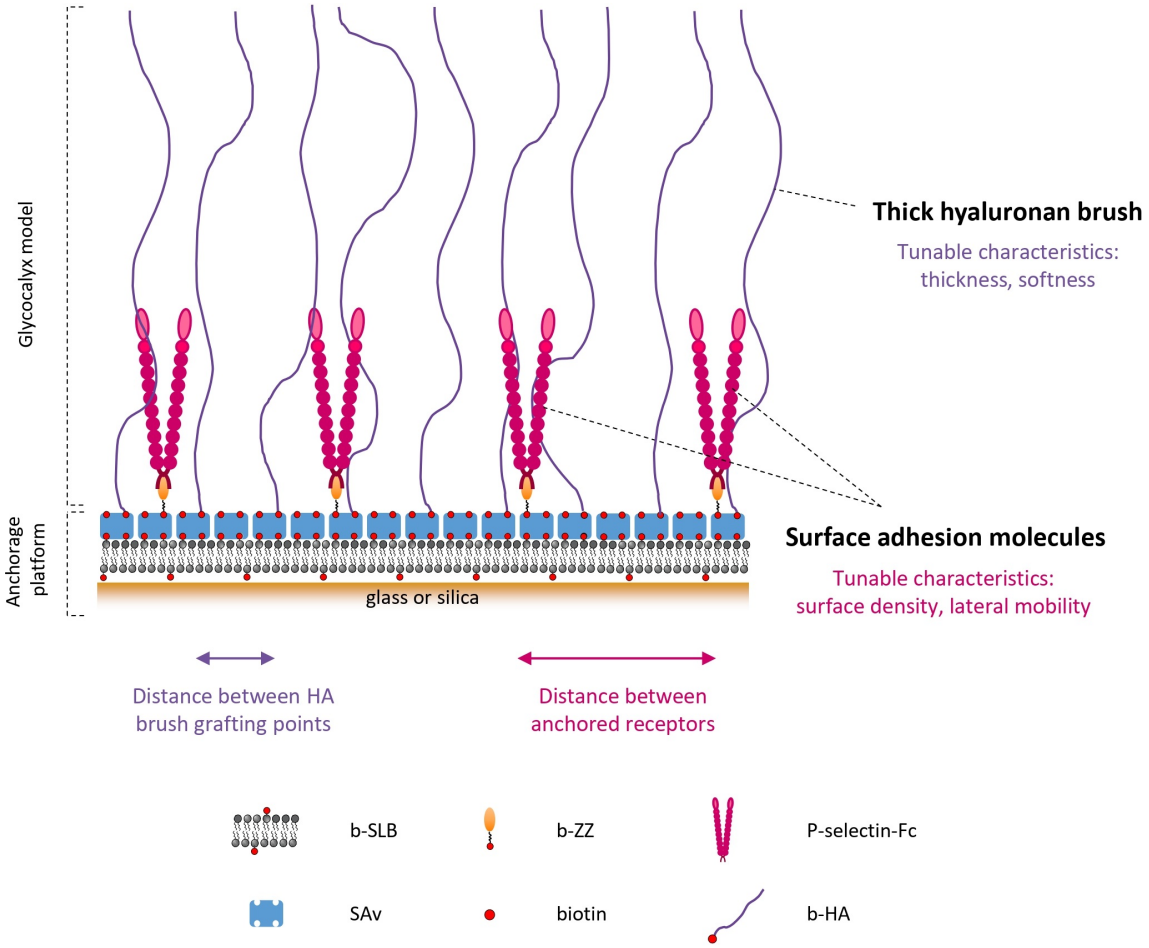

Figure 2.1: Schematic drawing of molecular model of glycocalyx. The anchorage platform is composed of a biotinylated supported lipid bilayer (b-SLB) formed on glass or silica support and streptavidin (SAv) monolayer facilitating the anchoring of biotinylated species through stable biotin-streptavidin bonds. The glycocalyx mimetic comprises long, one-end anchored biotinylated hyaluronan (HA) chains and P-selectin molecules with Fc tags, linked to the platform using the b-ZZ adapter protein via Fc-ZZ bonds. The molecular model has several tunable characteristics: mechanical properties of HA brush (thickness and softness), surface density and lateral mobility of P-selectin receptors.

2.1.2 Biotin-streptavidin interaction for receptor anchoring

An important aspect in the development of the glycocalyx molecular model was the search for an effective anchoring mechanism to immobilize the receptors on the molecular platform. Our choice centered on the utilization of biotin-streptavidin interactions.

Among many different approaches to surface anchorage of the receptors, biotin-streptavidin binding stands out due to its high affinity $K_d \approx 10^{-14}$ M [166] and specificity. Streptavidin (SAv) is a tetrameric protein known for its exceptional thermal [55] and long-time stability. The relative simplicity of protein biotinylation [24, 79] has resulted in a wide range of applications of biotin-streptavidin binding. SAv monolayer serves as a universal support for anchoring biotinylated molecules including proteins [69, 154], nucleic acids [122] and sugars, in particular glycosaminoglycans such as HA [59, 138].

In the research preceding my project [33], streptavidin within the molecular platform was substituted with its mutant counterpart known as traptavidin (TAv). Traptavidin is a variant of streptavidin characterized by reduced flexibility in the L3/4 loop (Fig. 2.2), the structural element responsible for closing over the biotin-binding pocket. The enhanced orderliness of this loop is anticipated to lower the entropic cost associated with biotin binding and hinder dissociation. This reduction in the off-rate, coupled with increased thermostability, leads to a notably stronger binding affinity between TAv and biotin or biotinylated molecules. The off-rate for the TAv-biotin interaction is approximately 10-fold lower compared to the biotin-streptavidin interaction, as previously reported [28, 29]. This property might be advantageous for our specific applications, particularly when our functionalized surface is subjected to drag forces during flow assays.

SAv and TAv were the two options considered for the design of our glycocalyx model. One of the objectives in optimizing this model was to evaluate the performance of both SAv and TAv and subsequently select the optimal protein for our specific application.

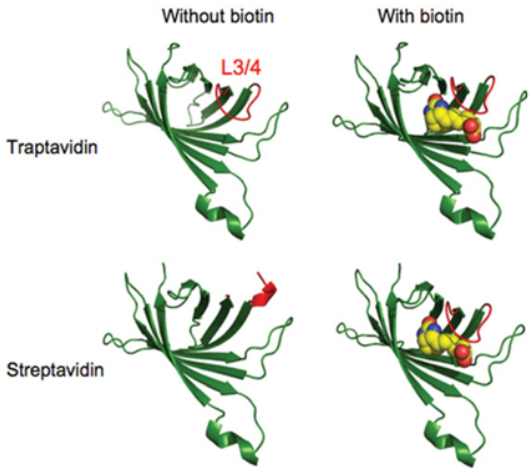

Figure 2.2: Comparison between traptavidin and streptavidin structures with and without biotin. In both the apo- and biotin-bound states of TAv, the L3/4 loop region (colored red) exhibits a well-defined closed conformation. In apo-SAv, the L3/4 loop is disordered, but it adopts an ordered conformation in biotin-bound streptavidin. Image taken from [29].

2.1.3 Choice of the anchorage platform for presenting the SAv or TAv monolayer

There are several approaches to present the biotin layer on the surface, allowing formation of SAv or TAv monolayers. Two popular methods among them are the creation of self-assembled monolayers or supported lipid bilayers.

2.1.3.1 Self-assembled monolayers

Self-assembled monolayers (SAMs) are molecular structures formed on a solid surface as a result of the adsorption of an active molecule from the solution [95, 158]. This versatile platform has been used in surface functionalization for more than 25 years. Some extensively studied types of SAMs are the ones that resulted from the adsorption of thiols (organic compounds containing a sulfur atom bonded to a hydrogen atom as part of their molecular structure) on gold, silver, platinum, and palladium [22, 165]. A common approach to form a self-assembled monolayer is to expose a gold-coated surface to thiols, for example, oligo-ethylene glycols (OEG), containing a certain fraction (usually up to 10%) of biotinylated compounds (b-OEG). The interaction between thiols and gold results in the formation of covalent gold-thiolate (Au-S) bonds. By varying the fraction of biotinylated OEG thiols, the final density of bound streptavidin or traptavidin can be tuned [146].

The schematic drawing of formation of thiol-based SAM is demonstrated in Fig. 2.3. The process of self-assembly is marked by an initial rapid adsorption phase, followed by a subsequent slower organization phase during which the surface density of thiol molecules continues to increase. Therefore, the thiol adsorption is a long process, so the functionalization is usually done overnight.

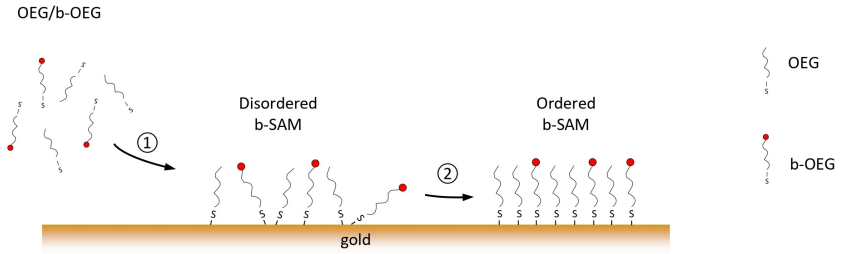

Figure 2.3: Schematic drawing of thiol-based SAM formation at the gold-coated surface. ① Rapid adsorption phase, ② slow organization phase. Biotinylated and non-biotinylated OEG molecules are attached to the gold surface via covalent gold-thiolate bonds.

2.1.3.2 Supported lipid bilayers

Supported lipid bilayers (SLBs) have been widely used for surface preparation for since their first development in 1985 [152]. They are formed as a result of rupture and spreading of the lipid vesicles on hydrophilic solid support (Fig. 2.4).

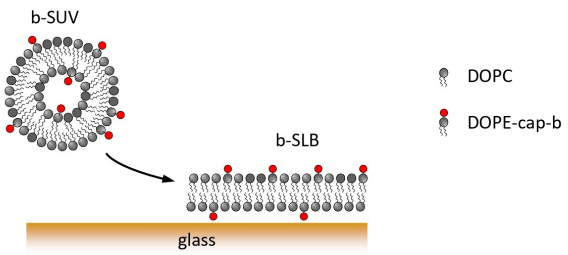

Figure 2.4: Schematic drawing of SLB formation at the glass support.

The bilayer structure arises from the unique characteristics of phospholipid molecules, which have a polar head group and two hydrophobic hydrocarbon tails. These lipid molecules spontaneously aggregate to bury their hydrophobic tails inside and expose their hydrophilic heads to water either forming spherical vesicles with tails inside or bilayers with tails sandwiched between hydrophilic head groups [3]. When facing the solid support, the phospholipids arrange in energetically most-favorable sheet bilayer.

Supported lipid bilayers can be formed *in situ* on a glass support and are widely used as a tool to stably and homogeneously present biotin [6]. For this, a defined fraction of biotinylated phospholipids is incorporated in lipid suspension. It was demonstrated that SAv coverage depends on the biotinylated fraction of lipids in solution [59]. Based on previously established protocols [44], in our study we chose to use an inert phospholipid 1,2-dioleoyl-sn-glycero-3-phosphocholine (DOPC) mixed with the biotinylated compound 1,2-dioleoyl-sn-glycero-3-phosphoethanolamine-N-(Cap Biotinyl) (DOPE-cap-b) in a (95:5) ratio. The chemical structures of these lipids are presented in Fig. 2.5.

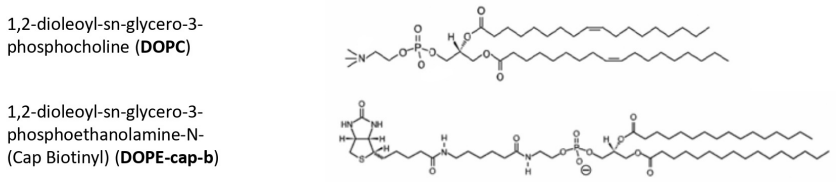

Figure 2.5: Chemical structure of DOPC and DOPE-cap-b. Image taken from [136].

The fluidity of supported lipid bilayers is a key characteristic, with lipids capable of lateral diffusion within the bilayer. This lateral mobility is influenced by temperature. Lipid bilayers can undergo different thermodynamic phases, including the gel and fluid phases, with the phase transition temperature (T_m) increasing as tail lengths lengthen and decreasing with more double bonds [113]. The lateral mobility of lipids affects the subsequent binding of proteins to the SLB-covered support [6].

It was reported that at room temperature biotinylated DOPE diffuse along the surface with a rate of a few $\mu m^2/s$ [107]. A similar diffusion constant (about 2 $\mu m^2/s$) was observed for streptavidin molecules anchored on biotinylated SLB platform [107]. Therefore, by measuring the diffusion constant of fluorescently labelled SAv one can assess the fluidity of the supported lipid bilayers.

Based on their size, lipid vesicles can be categorized into three groups: small unilamellar vesicles (SUVs), typically smaller than 100 nm (usually between 30 and 50 nm); large unilamellar vesicles (LUVs), ranging from 100 nm to 1 µm; and giant unilamellar vesicles (GUVs), above 1 µm [92]. In surface chemistry, SUVs are most commonly used to create solid-supported lipid bilayers.

A well-established protocol for SUVs preparation [135] has been used for over 20 years. The mix of lipids dissolved in chloroform is first dried under vacuum, then resuspended in working buffer and homogenized during several freeze-thawing cycles. There are several techniques allowing to create unilamellar vesicles, including sonication, extrusion [63], reverse phase evaporation [151] and others. In our study we used sonication in pulse mode to prepare vesicles of diameter typically ranging from 20 to 30 nm [136].

The homogeneity of the formed SLB is dependent on the type and physical properties of the solid support, including its roughness, type of cleaning, and surface charge [137]. These factors can also influence the organization of proteins binding to the SLB, making quality control essential for SLB formation.

2.1.4 HA brush formation

As one of the major components of extracellular matrix, hyaluronan has been the subject of extensive research [62, 93, 109]. Hyaluronan consists of repeating disaccharides composed of N-acetylglucosamine (GlcNAc) and glucuronic acid (GlcA) [147] (Fig. 2.6). In solution, hyaluronan polymer chains exhibit random coil behaviour [42] but when they are grafted onto a surface, the molecules can adopt either a mushroom-like or brush-like conformation, depending on the grafting density [138].

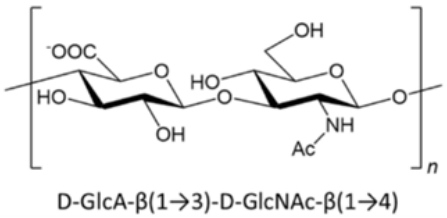

Figure 2.6: Disaccharide unit structures of hyaluronan. Image taken from [150].

There are well-established protocols for the formation of HA brushes where one-end biotinylated hyaluronan polymers are grafted onto the streptavidin monolayer via their reducing end [150]. My host labs, Richter Lab and LIPhy, have made major contributions to establishing HA brushes and their characterization [138, 150].

The formation of the HA brush can be effectively monitored utilizing the QCM-D method (Fig. 2.7). Upon introduction into the system, biotinylated HA chains exhibit rapid binding to SAv. This initial phase of rapid binding, particularly prominent for smaller molecular weights like HA-58 (Mw = 58 kDa), is succeeded by a slower binding phase. This transition reflects the crowding of molecules at the surface and the transition from bound HA molecules in a mushroom configuration to a brushlike configuration. HA binding is characterized by significant shifts in dissipation, accompanied by relatively minor changes in resonance frequency. These responses serve as indicators of the development of a highly hydrated and very soft layer [138].

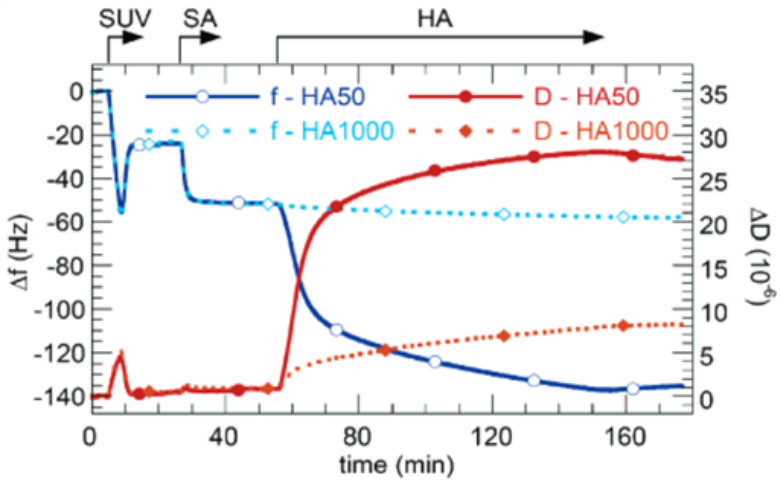

Figure 2.7: HA brushes formation monitored with QCM-D. QCM-D frequency shifts (ΔF – blue line) and dissipation shifts (ΔD – red line) for the 5th overtone measured over time. The start and the duration of incubation with each sample (SUVs, streptavidin and HA) are indicated with black arrows at the top of the graphs. QCM-D responses for binding of two types of HA molecules are presented: HA-50 (58 kDa) and HA-1000 (1083 kDa). Image taken from [138].

Additionally, there are numerous techniques allowing to estimate the thickness and stiffness of the formed HA films [7, 138]. In my project, we chose to use colloidal probe RICM to determine

the thickness and the intermolecular distance of grafted HA chains (please refer to "RICM" section in Chapter 1 for details).

From the measured brush thickness the distance between its grafting points can be estimated using the following equation, as described previously [33]:

$$\xi^2 = \frac{8}{\pi^2}\frac{\rho v}{b}\left(\frac{l_c}{H_0}\right)^3 \tag{2.1}$$

where b – the monomer unit length (b = 1 nm, considering the basic HA disaccharide unit as the monomer), l_c – the polymer contour length calculated as $b \times$ (polymer Mw) / (monomer Mw), ρ = 13.9 – intrinsic chain stiffness (a measure for the bending rigidity), v = 3.67 nm^3 – monomer effective excluded volume.

Brush elastic (longitudinal) modulus, a measure of brush stiffness, is defined as:

$$M \approx \frac{13kT}{\pi\xi^3} \tag{2.2}$$

where kT is the thermal energy.

2.1.4.1 Grafting the HA brushes of physiological mechanical properties

In prior research, a protocol for creating HA brushes with physiological mechanical properties was developed [33]. The resulting HA brush, as depicted in Figure 2.8, was generated on a self-assembled monolayer (SAM) using HA molecules with a molecular weight of 840 kDa and exhibited an elastic modulus of approximately 40 Pa. This modulus falls within the range of physiological characteristics (10-1000 Pa [98]). In my project, I followed this established protocol to generate a glycocalyx model with physiological mechanical properties.

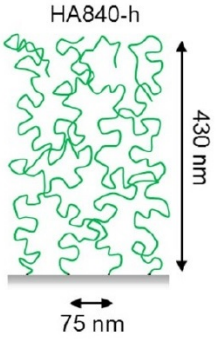

Figure 2.8: Schematic representation of HA-840 and brush formed on SAM. Image taken from [33].

2.1.4.2 Generating the HA brushes with non-physiological mechanical properties

To investigate the impact of glycocalyx softness on the regulation of blood cell access to the endothelial cell surface, thereby facilitating the specific P-selectin/PSGL-1 interaction, we aimed to establish a controlled scenario where this interaction could be effectively blocked. To achieve this, our objective was to create a control glycocalyx model with a dense and rigid HA brush. We hypothesize that such a brush would be capable of screening surface receptor interactions even in the presence of HA/CD44 interactions, thereby demonstrating that sufficient indentation of the HA layer is required for stabilized interaction of the cell with the vascular endothelium. To be

effective, this control brush needs to be of sufficient thickness and rigidity to be only marginally indented by interacting cells under flow.

Quantitatively, the total length of the P-selectin/PSGL-1 molecular pair comprises the length of the P-selectin molecule (estimated at approximately 40 nm [160]), PSGL-1 (approximately 50 nm [89]), and twice the length of the b-ZZ adapter protein (around 8.5 nm [44]), which links P-selectin to the SAv-coated surface and PSGL-1 to the microbead surface (Fig. 2.9). In total, the compressed HA brush had to possess a thickness of no less than 110 nm to effectively prevent this interaction.

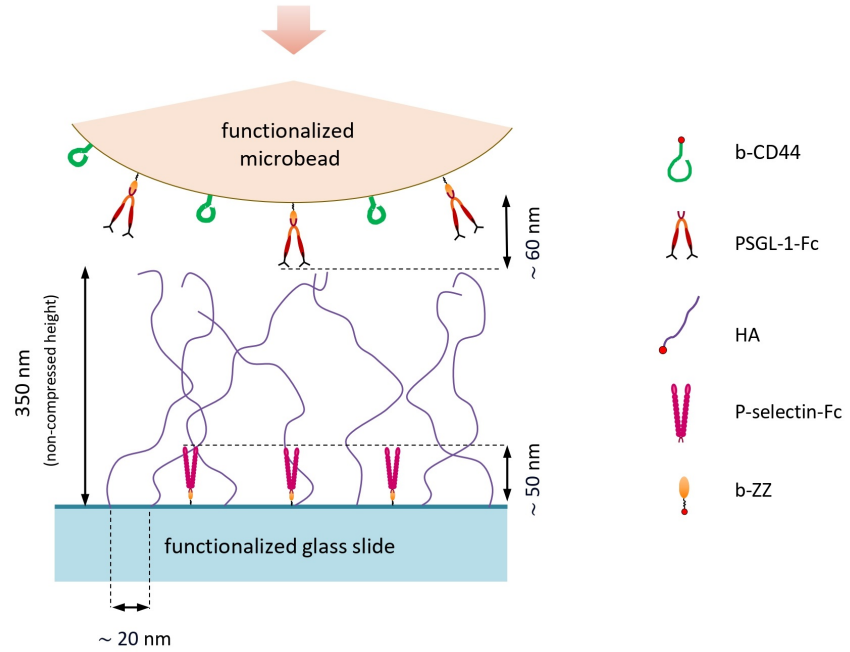

Figure 2.9: Schematic drawing of HA brush allowing to screen the interaction between the beads functionalized with PSGL-1 and P-selectin located underneath the thick HA brush.

In pursuit of this objective, we opted for HA molecules with a molecular weight of 280 kDa. Relying on previous measurements [33], we estimated that in its uncompressed state, such HA brush should have a minimum thickness of 300 nm and a distance of approximately 20 nm between grafting points to achieve a Young's modulus of around 1 kPa for the resulting brush. Based on previous results on the compressive force exerted by CD44-functionalized beads on HA brushes at physiological shear rates, such thickness and elasticity ensure that the brush is not compressed below 110 nm.

It is important to highlight that achieving such high grafting densities is a challenging task. We thus employed targeted strategies to optimize the incubation conditions for enhancing the grafting of HA molecules.

Among the various strategies available for promoting HA brush formation, two have shown particular promise. The first strategy involves manipulating the charge of HA. It carries a negative charge at pH levels above ≈3.0 and is thus highly responsive to changes in ionic strength within the solution. Previous research has demonstrated that increasing the concentration of ions of sodium [7, 64] or calcium [114] in the solution results in screened electrostatic interactions, reducing the repulsion between adjacent hyaluronan chains. Importantly, alterations in HA molecule conformation under these conditions are typically reversible. Therefore, an accelerated HA brush formation can be achieved by incubating it in a high-concentration ion solution to promote denser brush formation. Then the brush can be rinsed with a buffer with physiological ionic concentrations and the grafted chains should stay stably anchored at the surface.

The second strategy involves adjusting the pH of the solution during HA incubation. It was demonstrated that a pH lower than 6.0 leads to the reversible protonation of HA resulting in a more compact HA conformation [26, 52]. Therefore, a low-pH solution can be used to graft an HA brush with increased density.

Accordingly, we chose to implement these two strategies to create thick HA films:

1. Increasing NaCl concentration during HA incubation (1 M instead of 150 mM, as in usual working buffer);
2. Lowering the pH of the incubation solution during HA incubation (pH 3.0 instead of pH 7.4).

Additionally, as HA incubation is a kinetically limited process, we decided to increase the incubation time to 15 hours (overnight incubation) to maximize the brush density while keeping a reasonable experimental duration.

2.1.5 Surface receptor P-selectin grafted with the help of b-ZZ adapter protein

During the development of the glycocalyx model we needed to stably graft P-selectin receptors at the surface. As biotinylated P-selectin was not commercially available and its synthesis would be both challenging and time-consuming, the conventional biotin-streptavidin anchorage used for the HA chains was not applicable for fixing this protein on the surface.

However, major suppliers such as R&D systems offer a wide range of proteins, including P-selectin, linked with the Fc region of immunoglobulin molecules. This region can specifically and stably bind to the Z domain of protein A and is widely used as a tool for protein immobilization [25, 153].

In the past, the Richter Lab had synthesized an adapter protein called b-ZZ based on the concept of another protein construct developed in the Gorlich Lab (Gottingen, Germany). This adapter protein is composed of tandem repeats of the Z domain of protein A coupled with N-terminal biotin via a flexible linker of approximately 5 nm contour length (the primary structure of b-ZZ is described in [44]). This adapter protein shows specificity for binding Fc tag and had been successfully used to anchor intercellular adhesion molecule 1 (ICAM-1) on a streptavidin-coated support, exhibiting excellent binding affinity and stability [108]. Based on this experience, we decided to employ b-ZZ adapter protein to graft P-selectin with the Fc tag onto our anchorage platform.

2.2 Results

2.2.1 What anchor platform to use – SLBs vs SAMs?

As discussed before, both SLB and SAM are well-established platforms and can be readily adapted to create biomimetic layers. In the following sections, I will provide a comparative analysis of these two platforms and evaluate the advantages and limitations of using each of them in our specific application.

2.2.1.1 Preparation of interaction platforms based on SAMs vs. SLBs - Practical aspects to consider

Table 2.1 presents a comparison of various practical aspects of SAM and SLB formation. It is evident that surface preparation for SAM formation is generally more complex and time-consuming compared to SLB. The process of forming self-assembled monolayers involves gold deposition on the glass coverslip prior to functionalization (see the corresponding "Methods" section for details), making it a more expensive and lengthy procedure compared to SLB formation.

When utilized for optical analysis, the presence of phase changes at the glass/gold/buffer interface presents a greater challenge for obtaining quantitative RICM measurements compared to coverslips lacking a deposited gold layer. Additionally, the functionalization time differs between the two platforms. Achieving a SAM of good quality typically requires an overnight *ex situ* incubation, while SLB formation is generally rapid, requiring less than 10 minutes and can be done *in situ.*

Table 2.1: Comparison between SAM and SLB formation.

Parameter	SAM	SLB
Type of solid support	✗ Gold-coated surface (e.g., glass coverslip with gold deposition)	✓ Clean glass or silica surface (e.g., glass coverslip)
Surface preparation	QCM-D Au-coated sensors (one-time use per sensor): • Thorough rinsing with ultrapure water • Exposure to UV/O_3 for 30 min ✓ Total preparation time: about 40 min	QCM-D Si-coated sensors (multiple use per each sensor): • Immersing into SDS 2% for 30 min • Thorough rinsing with ultrapure water • Exposure to UV/O_3 for 30 min ✓ Total preparation time: about 1 h
	Glass coverslips: • Cleaning with piranha solution • Ti deposition followed by Au deposition under vacuum • Thorough rinsing with ultrapure water • Exposure to UV/O_3 for 30 min ✗ Total preparation time: about 4-5 h	Glass coverslips: • Cleaning with piranha solution • Rinsing with ultrapure water • Exposure to H2O plasma for 3 min ✓ Total preparation time: about 2 h
Functionalization time	✗ Overnight	✓ About 30 min
Optical analysis (for glass coverslips)	✗ Sub-optimal for optical analysis due to the phase shift in RICM images induced by the gold layer	✓ Optimal for optical analysis

To control the SAM and SLB formation and assess the SAv or TAv binding to them *in situ* we employed QCM-D. For SAM, the addition of a BSA solution was employed to test for non-specific binding and evaluate the quality of the formed layer. Given BSA's ability to adsorb to a wide range of surfaces, including gold, the BSA test evaluates the homogeneous formation of the SAM on the

glass surface. As shown in Figure 2.10A (10-20 min), the QCM-D frequency and dissipation shifts demonstrated minimal response for BSA binding (ΔF < 1 Hz, ΔD < 0.2 ppm), indicating a high-quality SAM formation. However, it is important to highlight that achieving such a good quality of self-assembled monolayer requires careful precautions. In the initial tests, insufficient cleaning of the QCM-D sensor and/or vial used for overnight functionalization resulted in significant non-specific binding of BSA, indicating poor SAM quality (see Fig. B.1 in Supplementary Information). These results emphasize the importance of thorough cleaning procedures to ensure proper SAM formation.

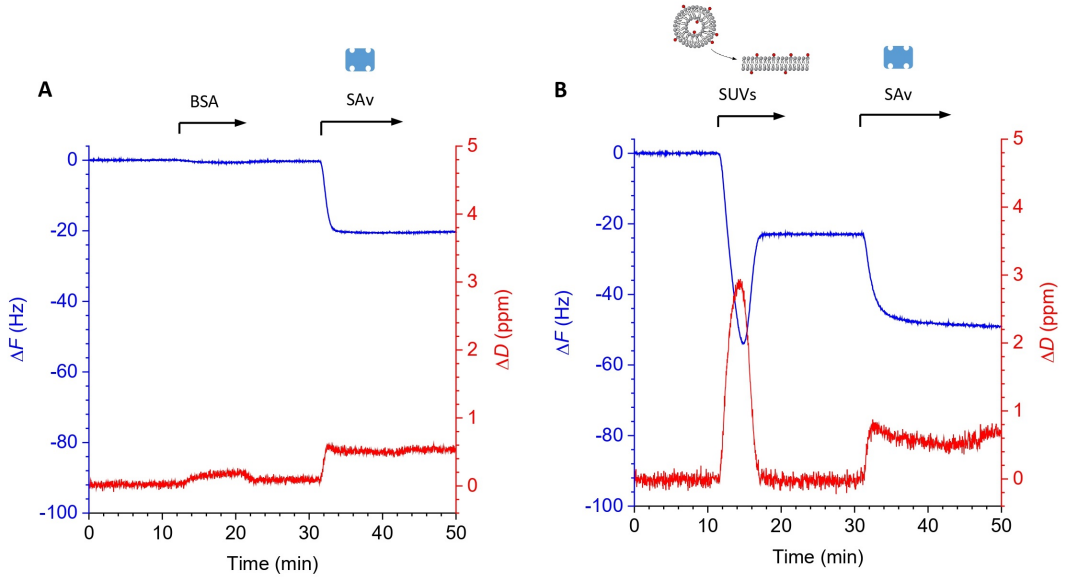

Figure 2.10: SAv monolayer formation on SLB or SAM monitored by QCM-D. QCM-D frequency shifts (ΔF – blue line) and dissipation shifts (ΔD – red line) for the 5th overtone measured over time. Flow rate at all steps is 20 µL/min. The start and the duration of incubation with each sample are indicated with black arrows at the top of the graphs. Before and after each incubation step there were rinsing steps with HEPES buffer. **A.** BSA test for the non-specific binding to the SAM, followed by SAv formation. BSA incubation resulted in very little response (ΔF = -0.3 ± 0.1 Hz and ΔD < 0.1 ppm) indicating that the formed SAM is inert to non-specific binding. Streptavidin monolayer formation resulted in the final shifts: ΔF = -20.0 ± 0.1 Hz and ΔD = 0.4 ± 0.1 ppm. Conditions: BSA – 1.5 µM (100 µg/mL), SAv – 0.33 µM. Conditions for SAM formation: QCM-D sensor was immersed in SAM solution (0.02 mM b-OEG-thiol + 0.98mM OEG-thiol in ultrapure water) for 16 hours prior to use. **B.** SLB formation followed by streptavidin monolayer creation. The two-step response for SUVs incubation represents the initial binding of the vesicles onto the layer followed by their rupture and spreading, the final shifts: ΔF = -23.0 ± 0.1 Hz and ΔD < 0.1 ppm. Final shifts after SAv formation: ΔF = -26.3 ± 0.2 Hz and ΔD = 0.7 ± 0.1 ppm. Conditions: SUVs (DOPC:DOPE-cap-b = 95:5) – 50 µg/mL, SAv – 0.33 µM.

SLB formation monitored by QCM-D is presented in Fig. 2.10B. The two-phase response upon SUVs incubation (10-20 min) reveals the characteristic pattern of initial intact binding followed by rupture and spreading as the surface coverage increases. The final shifts observed (ΔF = -23.0 ± 0.1 Hz and ΔD < 0.2 ppm) indicate the formation of a high-quality SLB with minimal residual liposomes [137]. Such consistent responses were observed in the majority of my QCM-D tests, indicating highly reproducible SLB formation that did not necessitate additional precautions.

Streptavidin exhibited stable binding to both of the anchor platforms (30-40 min in Fig.2.10A-B). The slight disparity in final frequency shifts (ΔF = -20.0 ± 0.1 Hz for SAM and ΔF = -26.3 ± 0.1 Hz for SLB) is consistent with previously published data [108] and can be attributed to the mobility of the SLB layer, where individual lipid molecules can reorganize and bind SAv more efficiently resulting in higher total bound mass. Similar results were observed for TAv monolayer formation (ΔF = -22.8 ± 0.2 Hz, ΔD = 0.4 ± 0.1 ppm, QCM-D data shown in Fig. 2.12A).

2.2.1.2 Controlling the mobility of surface-anchored molecules on SLBs by GTA cross-linking of SAv/TAv

One critical distinction of SAMs compared to SLBs is that thiol molecules in a SAM are essentially immobile whereas lipids in fluid SLBs can move in the bilayer plane. The lack of mobility is particularly advantageous for our application in studying the cell adhesion in a microfluidic system, since it allows the layer to withstand the drag force exerted on it when cells or cell mimetics interact with the surface upon landing. On the other hand, the lateral mobility of the SLB offers specific benefits, particularly by facilitating the subsequent attachment of molecules through lipids' reorganization. An important consideration for this project thus was if the SAv/TAv-on-SLB platform could be adapted to tune the mobility of anchored molecules.

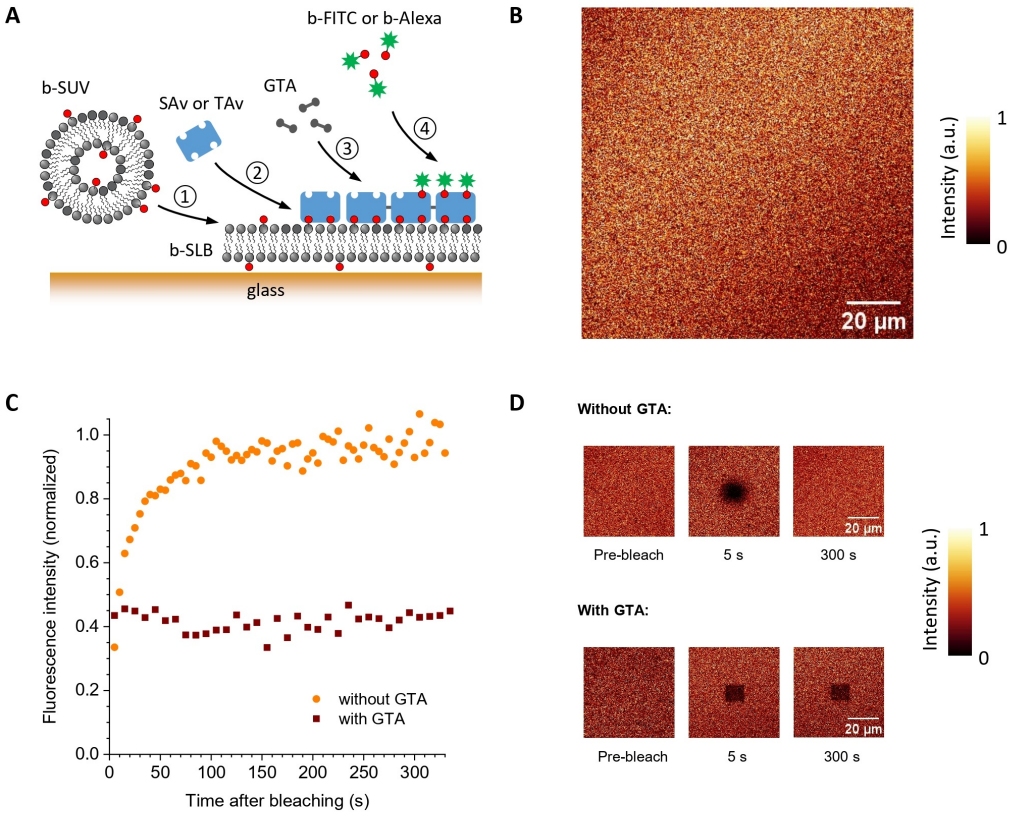

Figure 2.11: Fluorescence recovery after photobleaching for GTA cross-linked layer and non-cross-linked layers. A. Schematic drawing of the surface functionalization: ① SLB formation, ② SAv or TAv monolayer formation, ③ GTA cross-linking, ④ b-FITC or b-Alexa adsorption **B.** Representative micrograph with fluorescently labelled SAv, demonstrating that SAv coverage is essentially uniform. A few small defects are noticeable as darker patches with a typical size of 1 µm or less, but these occupied only a small fraction of the total surface area and negligibly impacted the data analysis. **C.** Fluorescence intensity for the non-GTA-treated layer (orange circles) and the GTA treated SAv layer (brown squares). The intensities measured inside the bleached area are normalized to the intensities of the outside areas. **D.** Snapshots of the mobile and immobile layers taken before bleaching ("pre-bleach"), and 5 s and 300 s after bleaching. The intensities are normalized against unbleached areas.

A straightforward approach to limit the mobility of SAv or TAv on SLBs is by cross-linking of the proteins. Previous studies have demonstrated that glutaraldehyde (GTA) is capable of cross-linking neighboring SAv molecules [66], including the SAv monolayer formed on SLB [77].

In the experiments outlined in this and subsequent sections, streptavidin and traptavidin are

introduced as potentially interchangeable proteins. At times, we utilized one or the other to investigate the mobility of the layer and the formation of the HA brush. While they can be regarded as interchangeable to a certain extent, it's important to note that they also exhibit distinct differences, which will be comprehensively discussed in Section 2.2.2.

We employed confocal microscopy to visualize the SAv or TAv monolayers. The glass coverslip was functionalized following the procedures outlined in the "Methods" section, and the SAv or TAv layer was labeled with biotinylated fluorophores: biotinylated fluorescein isothiocyanate (b-FITC) or biotinylated Alexa 647 (b-Alexa) (Fig. 2.11A). Typically, the SAv surfaces were mostly homogeneous (no structures larger than 1 μm were detected), as shown in Fig. 2.11B. TAv monolayers, however, occasionally exhibited crystalline structures and lacked homogeneity, as will be discussed in Section 2.2.2.2.

We used fluorescence recovery after photobleaching (FRAP) to quantify the impact of GTA cross-linking on the mobility of the SLB-based protein layers. A square region with a width of 10 μm at the center of the image was bleached, and the subsequent fluorescent recovery originating from lateral movement of SLB-based SAv or TAv was observed. Figure 2.11C shows the normalized intensities of fluorescence for both the GTA treated and non-treated SAv layers, while representative snapshots are presented in Fig. 2.11D. Notably, the layer that did not undergo GTA treatment showed recovery over time almost to initial level (>90%), whereas the treated layer remained immobile even after an extended observation period (several hours). In an additional experiment (not shown here), we observed that the cross-linked layer did not recover even after 4 days post-bleaching. The diffusion constant of the untreated layer, calculated using Eq. 1.13, was $\approx 1 \mu m^2/s$, which is comparable to the diffusion constant of SAv-anchored lipids [107]. On the other hand, the diffusion constant of GTA-treated layer was $< 10^{-6}$ $\mu m^2/s$. Similar results were observed on SLB-based TAv monolayers. This compellingly demonstrates the success of the GTA-cross-linking strategy for the SAv and TAv, providing an effective means to control the motility of the SLB layer.

2.2.1.3 GTA cross-linking of SAv/TAv does not impact the anchorage of biotinylated molecules

We further tested if GTA cross-linking had any adverse effects on the biotin binding capacity of SAv or TAv on SLBs. We initially monitored the traptavidin cross-linking using QCM-D (Fig. 2.12A). During GTA incubation (30-40 min), a frequency and dissipation shift were observed, likely attributed to the differences in viscosity and density of GTA solution compared to HEPES buffer. Upon rinsing in buffer the frequency shift returned to its initial value ($\Delta F \leq 1$ Hz). Notably, the final dissipation shift decreased significantly ($\Delta D = 0.3 \pm 0.1$ ppm), providing evidence that GTA rigidifies the surface coating, consistent with SAv or TAv cross-linking.

We also employed QCM-D to evaluate the binding of biotinylated molecules to both mobile and immobile layers. Although the frequency shift alone does not directly indicate the quantity of bound substrate, we can still use the final shifts at the binding equilibrium to qualitatively assess the efficiency of binding. For this purpose, we selected the b-ZZ adapter molecule (time-resolved data for b-ZZ binding will be shown further in Fig. 2.22A), which is sufficiently small so that it can occupy all available biotin-binding sites on a dense SAv or TAv layer [44]. Figure 2.12B shows the comparison between the final shifts observed for b-ZZ incubated until saturation on GTA-cross-linked TAv layer and mobile SAv platform. Both TAv and SAv monolayers were incubated under the same conditions (concentration, incubation time) until saturation characterized by a plateau in the QCM-D response. The results indicate that the binding efficiency to the cross-linked layer is comparable to that of the mobile platform. Some disparities in final frequency shifts (about 12%) are likely due to fluctuations in the surface coverages of SAv and TAv (TAv final shifts: $\Delta F = -21.8 \pm 0.3$ Hz and $\Delta D = 0.6 \pm 0.2$ ppm; SAv final shifts: $\Delta F = -25.6 \pm 0.3$ Hz and $\Delta D = 0.6 \pm 0.1$ ppm). Variations in the incubation conditions for SAv or TAv can lead to slightly different surface coverages, impacting the maximum achievable b-ZZ density on such a monolayer. Further

elaboration on this topic will be provided in Chapter 3.

Finally, we conducted tests to assess HA brush formation on both the mobile and immobile platforms. The thickness of the obtained brushes was measured using colloidal probe RICM (details provided in the "Methods" section). The results demonstrated that GTA cross-linking of the platform, either before or after HA brush formation, had no significant impact on the final thickness of the film (Fig. 2.12C). This indicates that both strategies are equally effective in forming a thick brush on an immobilized platform.

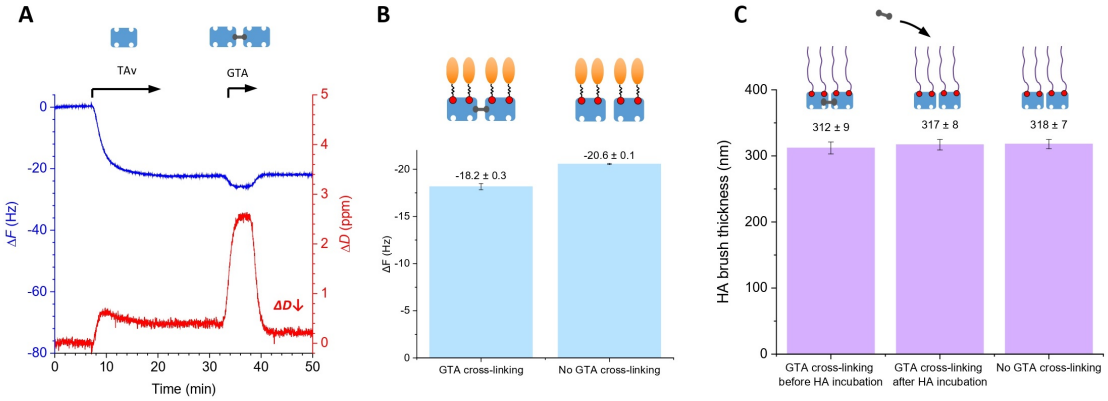

Figure 2.12: Effect of GTA cross-linking on subsequent layer formation. A. *In situ* observation of TAv cross-linking with GTA. QCM-D frequency shifts (ΔF – blue line) and dissipation shifts (ΔD – red line) for the 5th overtone measured over time. Flow rate at all steps – 10 µL/min. The start and the duration of incubation with each sample are indicated with black arrows at the top of the graphs. Before and after each incubation step there were rinsing steps with HEPES buffer. Final shifts for TAv incubation: ΔF = -22.8 ± 0.2 Hz and ΔD = 0.4 ± 0.1 ppm, for GTA cross-linking: $\Delta F \leq$ 1 Hz and ΔD = 0.3 ± 0.1 ppm. **B. b-ZZ binding to GTA cross-linked and non-cross-linked layer.** Final frequency shifts (ΔF) for b-ZZ incubated until saturation on (i) TAv layer cross-linked with GTA and (ii) SAv layer without GTA treatment. TAv final shifts: ΔF = -21.8 ± 0.3 Hz and ΔD = 0.6 ± 0.2 ppm; SAv final shifts: ΔF = -25.6 ± 0.3 Hz and ΔD = 0.6 ± 0.1 ppm. **C. Effect of GTA cross-linking on HA brush grafting on TAv monolayer.** HA-280 brushes were grafted onto TAv layers under three different conditions: (i) TAv layer cross-linked with GTA before HA incubation; (ii) TAv layer cross-linked with GTA after the completion of HA incubation; (iii) mobile TAv platform (no GTA treatment). The measured HA brush thicknesses were similar in all three tests (variations falling within the range of experimental errors). All the conditions for SLB formation, TAv and HA-280 incubation were kept the same for all three experiments: SLB formation: C(DOPC:DOPE-cap-b = 95:5) = 50 µg/mL, incubation time: 30 min; SAv or TAv monolayer formation: C = 20 µg/mL, incubation time: 30 min; HA-280 brush growth: C = 20 µg/mL, incubation time: 15 hours.

2.2.1.4 HA brushes form equally well on SLB vs. SAM platforms

As a next step, we aimed to compare the quality of the HA film (e.g., final thickness, stability over time) formed on both SLB and SAM platforms to determine which one would be more suitable for our application.

To assess the stability and efficiency of HA binding to the anchorage platform, we utilized two primary techniques: QCM-D for monitoring the *in situ* binding and stability of the HA film upon rinsing in working buffer, and RICM for measuring the final thickness of the formed brush and assessing its long-term stability. The long-term stability assessment is particularly crucial for our application, as functionalized surfaces must remain stable for extended periods, given the potentially lengthy duration of our experiments. Schematic representations of the surface functionalization procedures are shown in Fig. 2.13(A-B). SAM and SLB were created as described

above, followed by a SAv or TAv monolayer formation.

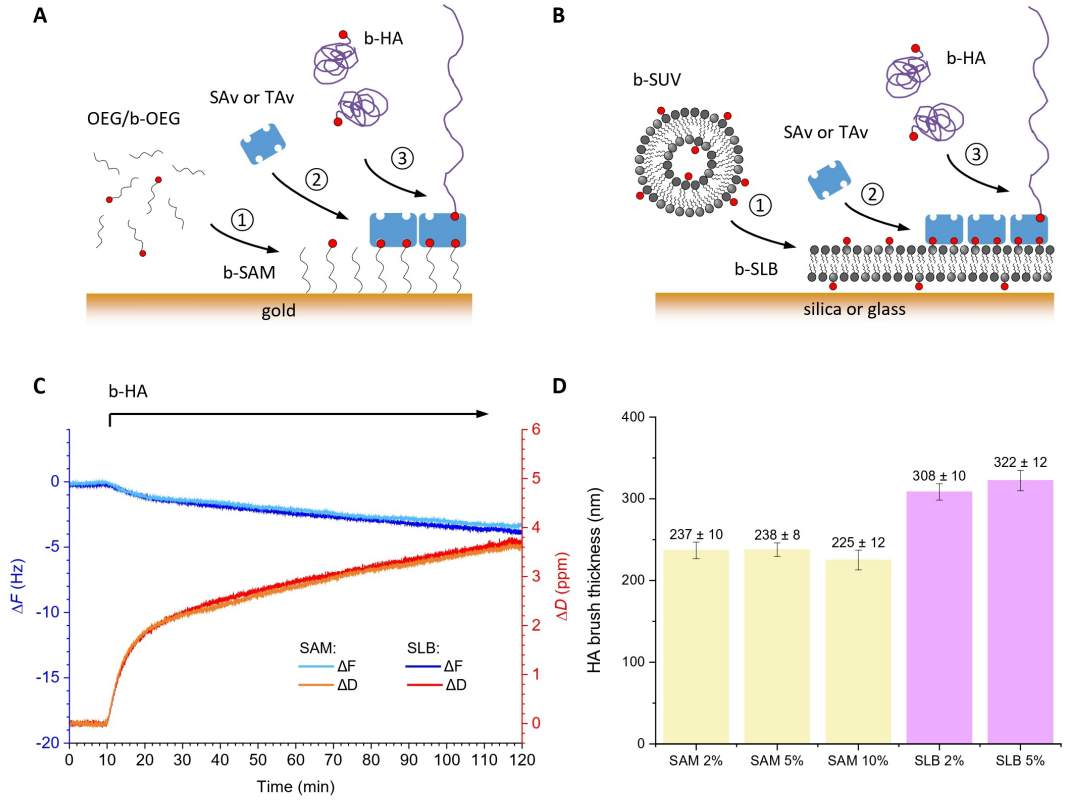

Figure 2.13: HA brush formation on SAM and SLB platforms. A. Schematic drawing of brush formation on SAM: ① SAM formation (*ex situ)*, ② streptavidin or traptavidin monolayer formation, ③ b-HA adsorption. **B. Schematic drawing of brush formation on SLB:** ① SLB formation, ② streptavidin or traptavidin monolayer formation, ③ b-HA adsorption. **C. b-HA adsorption on SAM and SLB monitored with QCM-D.** QCM-D frequency shifts (ΔF – blue and light blue lines) and dissipation shifts (ΔD – red and orange lines) for the 5th overtone measured over time. Flow rate – 20 µL/min. The start and the duration of HA incubation is indicated with a black arrow. Before and after HA incubation there were rinsing steps with HEPES buffer. In both tests b-HA-840 was incubated for 120 min at the concentration of 23.8 nM (20 µg/mL). Final shifts for HA incubation on SAM platform: ΔF = -3.8 ± 0.1 Hz and ΔD = 3.7 ± 0.1 ppm, on SLB: ΔF = -3.1 ± 0.3 Hz and ΔD = 3.4 ± 0.1 ppm. **D. HA brush growth on SAM and SLB with different fractions of biotinylated molecules.** HA-280 brushes were formed on two different platforms – SAM or SLB – covered with a monolayer of traptavidin. The fraction of biotinylated OEGs varied from 2% to 10%, and the fraction of biotinylated SUVs varied from 2% to 5%. The thickness of HA brushes formed on SAMs showed slight variations depending on the fraction of biotinylated OEGs, but remained significantly lower than the brushes formed on the SLB platforms. All conditions for TAv monolayer (C = 20 µg/mL, incubation time: 30 min) and HA-280 brush anchorage (C = 20 µg/mL, incubation time: 15 hours) were kept constant in all 5 experiments.

Figure 2.13C shows the dynamics of binding of b-HA-840 to a traptavidin monolayer formed on a SAM (light blue and orange lines) and SLB (blue and red lines). The binding curves were found to be essentially identical, indicating that the binding efficiency was equally effective for both platforms. This outcome was expected, considering that slight differences in TAv coverages and the number of biotin binding sites would have minimal impact on HA binding. As we will demonstrate further, even at very dense packing, the average distance between hyaluronan anchor points (over 70 nm for HA-840) remains several times larger than the average distance between biotin-binding sites on a densely packed TAv monolayer (about 4.5 nm). On both platforms, the binding of HA did not reach the saturation (plateau) phase during the observed incubation period.

This behavior was anticipated for long HA-840 molecules, as the binding rate of extended HA chains gradually decelerates with increasing surface coverage, as previously demonstrated [42].

However, the formation of HA brushes on the glass coverslip revealed notable differences between the two platforms (Fig. 2.13D). The thickness of HA-280 brushes formed on SAMs consistently appeared to be lower than those formed on SLBs, regardless of the fraction of biotinylated molecules (b-OEG-thiol or DOPE-cap-b) incorporated into the SAM or SLB, respectively. This observation was inconsistent with the QCM-D results, especially considering that both QCM-D sensors and gold-coated glass coverslips were functionalized simultaneously and in the same manner. To explain this discrepancy, we hypothesized that the quality of SAM formation on the glass support was significantly inferior compared to that on the QCM-D sensor. Indirect confirmation of this hypothesis came from RICM micrographs of the glass with Au deposition, which revealed an overall heterogeneous surface with visible patches distributed across the field of view. One potential explanation for this heterogeneity could be the uneven distribution of gold deposition.

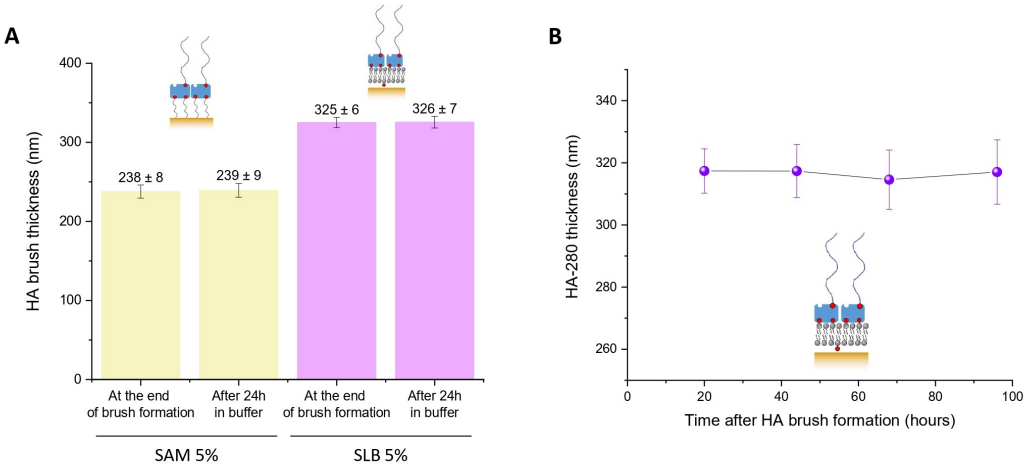

Figure 2.14: Stability of HA brushes formed on different platforms. A. Stability of HA-280 brushes formed on SAM and SLB with 5% fraction of biotinylated molecules. The thickness of HA-280 grafted on SAM or SLB was first measured after the end of brush formation, then – after 24 hours. Conditions: TAv monolayer formation: C = 20 µg/mL, incubation time: 30 min; HA-280 brush growth: C = 20 µg/mL, incubation time: 15 hours. **B. Long-term stability of HA-280 brush formed on SLB (5% biotinylated SUVs).** The thickness of HA brush formed on TAv monolayer was subsequently measured from 20h to 96h after brush formation. Conditions: TAv monolayer formation: C = 20 µg/mL, incubation time: 30 min; HA-280 brush growth: C = 20 µg/mL, incubation time: 15 hours.

Additionally, we investigated the stability of HA brushes grafted onto the two different platforms. The motivation for this study arose from previous research indicating that the monovalent binding of SAv to SAMs is not stable [44]. Given the random presentation of essentially immobile biotin on a SAM, it may pose a challenge for each SAv or TAv molecule to locate at least two binding sites, leading to the hypothesis that some SAv/TAv molecules may not be stably bound and could potentially detach from the layer along with the bound HA molecule. As previously discussed, our specific application demands that the thickness of the HA brush remains stable for at least 24 hours, given the possibility of experiments spanning more than one working day. Therefore, we aimed to assess the long-term stability of formed HA brushes by measuring their thickness 24 hours after the HA formation process.

The HA-280 brush height was measured right after the end of HA incubation and rinsing in HEPES buffer and then again after it was left in buffer for 24 hours at room temperature. Remarkably, our results demonstrated that hyaluronan brushes exhibited excellent stability over a day on both the SAM and supported lipid bilayer (SLB) anchorage platforms (Fig. 2.14A). To

further investigate, we monitored the thickness of HA-280 brushes formed on a supported lipid bilayer for 96 hours after the HA incubation ended. The thickness of hyaluronan film remained stable throughout the 4-day observation period (Fig. 2.14B).

These results indicate that the formed HA brushes exhibited exceptional stability over time, regardless of the underlying platform. The inconsistencies with previously observed effects are likely attributable to differences in surface preparation and SAM formation. Variations in factors such as the gold deposition protocol, surface cleaning procedures and the specific biotin surface density achieved may account for the disparities between our study and previous research.

2.2.1.5 Summary of platform analysis

After careful evaluation of SAM and SLB, we opted for the use of supported lipid bilayers as the anchor platform in our application and for all further investigations described in this thesis. SAMs, while possessing similar characteristics in terms of SAv binding, proved to be more complex and challenging to handle in practice. Its preparation requires additional precautions to achieve a high-quality layer. In contrast, SLB proved more straightforward to work with and consistently provided a homogeneous layer of biotin in most of the experiments. The ability to form SLB *in situ* makes it particularly desirable for surface functionalization in microfluidic channels.

The only potential concern with SLB is its lateral mobility, which may not systematically be desired in flow assays. However, we successfully developed a protocol to adjust and control this mobility reliably.

Nonetheless, it is worth noting that both platforms can be employed for surface functionalization, and SAM could potentially replace SLB in our molecular model of glycocalyx if the need arises. Flexibility remains in the choice of platforms, but for our specific application, SLB has proven to be the more suitable option.

2.2.2 Choice of the biotin-binding support – SAv vs. TAv

As mentioned earlier, the previous glycocalyx model was constructed using traptavidin (TAv), a mutant of streptavidin (SAv) with a higher binding energy to biotin. This decision was primarily driven by the need to enhance the stability of the HA brush over time, especially when subjected to drag forces applied to the film under flow. In line with established protocols, I initially utilized traptavidin to create a platform of biotin-binding sites for accommodating biotinylated species. However, during the course of my project, I observed some significant differences between TAv and SAv, prompting me to delve deeper into this aspect and investigate the impact of the protein choice on our molecular model.

In the following section I will provide a comparison between the TAv- and SAv-based molecular layers and explain the rationale behind selecting one over the other for our specific application.

2.2.2.1 HA brushes form equally well on SAv and TAv platforms

As discussed in Section 2.1.2, traptavidin and streptavidin share similar chemical characteristics, enabling them to form monolayers with comparable biotin-binding capacities, and, therefore, can be interchangeably used in our glycocalyx model. To ensure this, we conducted additional tests by growing the HA brush on both SAv and TAv, and then compared their thickness and stability over time (Fig. 2.15). The results revealed that the formed brushes had similar thickness and exhibited comparable stability even 24 hours after the end of the incubation period.

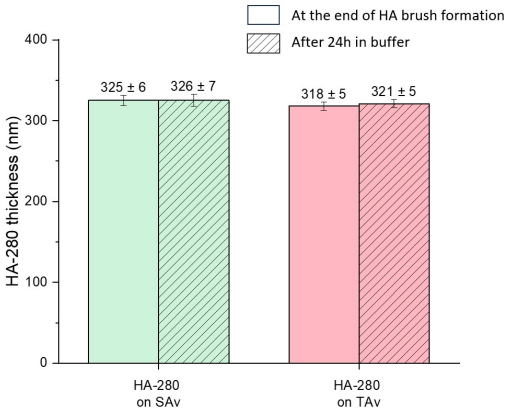

Figure 2.15: Thickness and stability of HA brushes formed on SAv and TAv. Conditions: SLB formation: C = 100 µg/mL, incubation time: 30 min; SAv or TAv monolayer formation: C = 20 µg/mL, incubation time: 30 min; HA-280 brush growth: C = 20 µg/mL, incubation time: 15 hours.

2.2.2.2 2D crystallization impairs the lateral homogeneity of TAv monolayers, and much less so of SAv monolayers

One drawback of using traptavidin became evident during its visualization with the help of confocal microscopy, where it showed a tendency to form 2D-crystalline structures when grafted on a supported lipid bilayer (Fig. 2.16, left panels). The intensity of fluorescence within the crystalline fraction was larger than the one of the background, indicating a higher protein concentration in these regions. While such heterogeneities at this scale might have minimal impact on HA brush formation, they could significantly influence the mobility of the layer and the anchoring of b-ZZ molecules to the substrate. Consequently, we conducted a detailed investigation of the 2D crystallization of traptavidin.

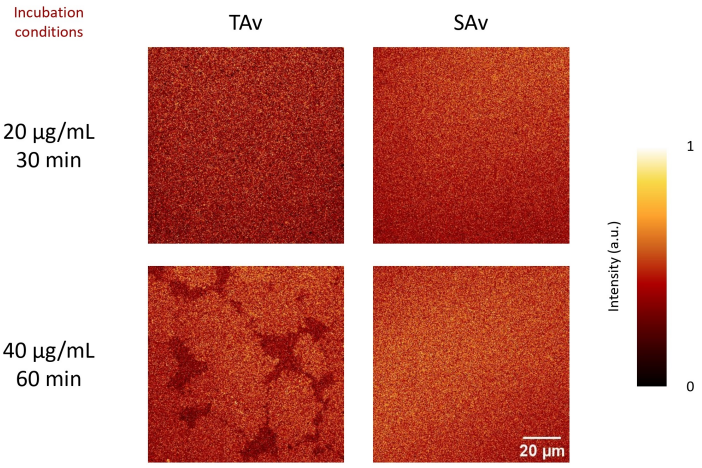

Figure 2.16: TAv and SAv monolayers visualized with fluorescent microscopy. Snapshots of TAv and SAv monolayers formed on SLBs (DOPC:DOPE-cap-b = 95:5) under conditions (incubation time, concentration) indicated at the left side of the panel, and subsequently labelled with biotinylated FITC. To avoid undesirable quenching effect during the fluorescence measurement b-FITC was mixed with biotin in [1:9] molar ratio (refer to Appendix A for details).

Although the 3D-crystallization ability of traptavidin has been reported previously [29], the 2D crystals had not been observed in previous glycocalyx models. The primary explanation for

this discrepancy is the choice of the platform for TAv monolayer formation. In contrast to previous tests conducted on self-assembled monolayers, we utilized SLB in our model. The fluidity of the SLB may promote the reorganization of TAv molecules, potentially leading to enhanced crystal formation. In contrast, streptavidin, when subjected to the same incubation conditions, was not prone to crystallization (Fig. 2.16, right panels), yet when increasing incubation time and/or protein concentration further, SAv crystals started appearing in the field of view (data not shown here). The size of TAv crystals showed variation, ranging from a few nanometers to approximately 60-70 nm, depending on the specific incubation conditions. Notably, the size of the crystals was found to increase with longer incubation periods and higher TAv concentrations.

Next, we investigated the mobility of the crystalline and non-crystalline fractions of TAv-coated surface. For this, we selected a region where both types of fractions were present and conducted a photobleaching experiment. Using a high-intensity laser, we bleached a thin line that traversed both fractions, as indicated by the black arrows in Fig. 2.17. Subsequently, the surface was allowed to recover, and we imaged it again after a 3-minute interval.

The non-crystal fractions, marked with white dashed ovals in Fig. 2.17, successfully recovered to their initial intensity levels, indicating their mobility and ability to reorganize. On the other hand, the TAv crystals remained unaffected and showed no signs of recovery, indicating their full immobility.

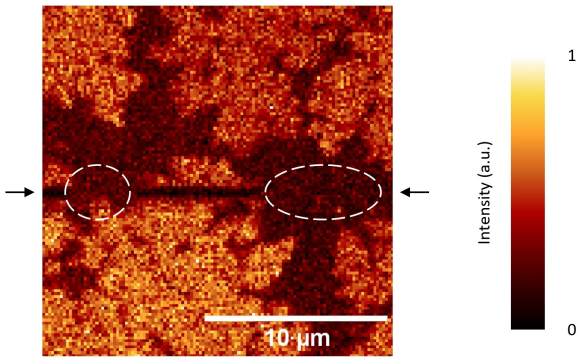

Figure 2.17: Micrograph of the TAv monolayer with a bleached line across the image. The black arrows show the straight line photobleached across the field of view. Conditions: SLB (DOPC:DOPE-cap-b = 95:5) formation : C = 100 µg/mL, incubation time: 30 min; TAv monolayer formation: C = 20 µg/mL, incubation time: 30 min; b-FITC was pre-mixed with free biotin in molar concentration [7:3], total concentration: 10 µg/mL.

During our investigation of TAv crystallization, we uncovered several practical aspects that should be taken into consideration when forming the TAv monolayer:

- *Incubation conditions*: Crystallization proved to be sensitive to the precise concentration of protein at the surface. Therefore, the incubation concentration and incubation time must be carefully selected.
- *Thorough rinsing procedure*: To prevent unwanted crystallization, it is crucial to remove all excess protein from the solution after incubation. We found that an effective rinsing procedure involves reducing the protein concentration in solution to 50 pM and below. This can be accomplished by introducing a buffer volume into the well (dilution factor: 5), performing multiple pipette mixings, and then aspirating the same volume of liquid. For an initial protein concentration of 40 µg/mL, this process should be repeated 7 times.
- *GTA cross-linking:* The process of GTA cross-linking can "freeze" the monolayer at its current state by blocking the lateral mobility of TAv anchored to SLB. This prevents TAv

reorganization and, therefore, crystal formation.

After investigating the phenomenon of TAv crystallization, it became evident that despite its increased biotin-binding energy, TAv appeared to be less reliable in terms of formation of homogeneous layer. Given the fact that we didn't observe any significant differences for HA brush density and stability for these two platforms, we decided to work with the more predictable protein, SAv.

2.2.3 Tuning HA brush properties

2.2.3.1 Formation of HA brush with physiological mechanical characteristics

To confirm the successful formation of the brush of physiological mechanical properties on SLB-based anchorage platform, I used the protocol described previously for HA-840 brushes formed on SAM [33].

HA-840 was incubated on the SLB-based SAv monolayer using established incubation conditions, including concentration, incubation time, and solution composition. The thickness of the resulting brush was measured using 25-µm microbeads, similar to the method used before. The obtained brush height was slightly larger but comparable to that reported previously (Fig. 2.18). This contrasted with the significant variations in brush height observed for HA-280 brushes grafted on both SLB and SAM platforms, as detailed in Section 2.2.1.4. However, it is important to note that the grafting densities of these brushes significantly differ, with approximately 70 nm for the HA-840 brush and around 22 nm for HA-280. Consequently, the HA-840 brush would be less susceptible to potential heterogeneities in the SAM, and its height would be more comparable to that of the brush formed on SLB.

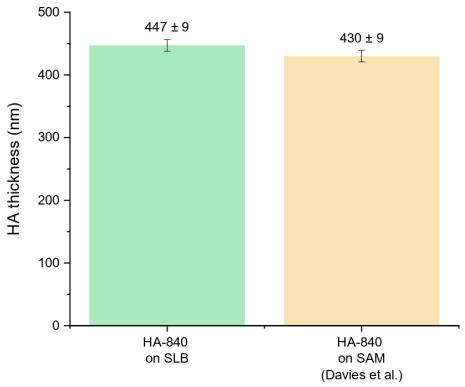

Figure 2.18: HA-840 brushes formed on SLB and SAM. Thickness of HA-840 brushes formed on streptavidin-coated SLB and traptavidin-coated SAM. Conditions: c(b-HA-840) = 23.8 nM (20 µg/mL), incubation time: 2 hours; incubation in working HEPES buffer. Brush height was measured using 25-µm polystyrene beads. This experiment was performed by Clément Lassagne, and the data was analyzed by Delphine Débarre. HA brush formed on SAM is taken from Davies et al. [33]

The Young's modulus of the brush formed on the SLB was theoretically determined using Equations 2.1 and 2.2 and found to be 48 ± 4 Pa, consistent with the physiological elasticity of the hyaluronan brush in the glycocalyx (10-1000 Pa [98]). This makes this HA-840 brush well-suited for use in our *in vitro* model for the investigation of cell-glycocalyx interactions in scenarios where the mechanical properties of the HA brush closely resemble those of the endothelial glycocalyx.

2.2.3.2 Grafting a very dense and stiff HA brush

To provide a negative control scenario for P-selectin/PSGL-1 interaction, our objective was to create a brush with well-defined mechanical properties, as described in Section 2.1.4.2. We aimed to create a brush that is sufficiently thick (over 300 nm) and at the same time also rather stiff (Young's modulus of the order of 1 kPa), thus allowing to screen the P-selectin/PSGL-1 interaction when the functionalized bead indents the HA film. Achieving this required the HA brush to exhibit a high density (with approximately 25 nm between grafting points), necessitating the development of a novel brush formation protocol.

Maximizing HA brush density by tuning the ionic strength and pH of the incubation solution

As described before, we explored two strategies to enhance brush formation: increasing the salt concentration in solution and, thus, reducing the repulsion between hyaluronan chains and decreasing the pH of solution to achieve more compact HA conformation. Both strategies were expected to lead to a more dense HA packing at the surface compared with the usual working HEPES buffer and, therefore, to enhanced binding rate for the same incubation time and hyaluronan concentration.

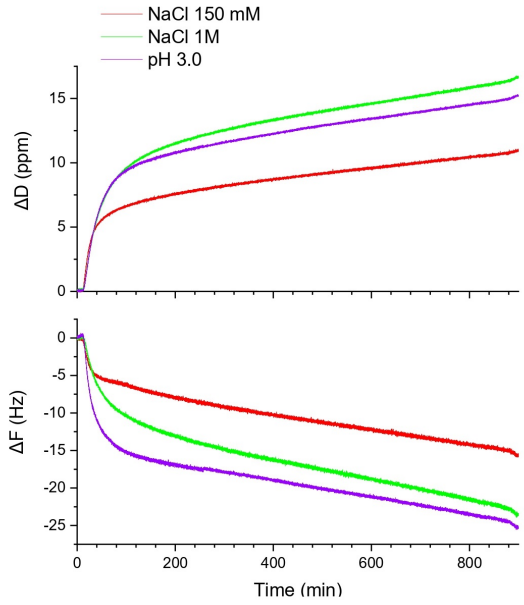

Figure 2.19: HA-280 brush formation *in situ* in different buffers. QCM-D dissipation shifts ΔD (top) and frequency shifts ΔF (bottom; for overtone i = 5) obtained for HA-280 incubation on TAv monolayer. HA was diluted in 3 different buffers: HEPES buffer (10 mM HEPES, 150 mM NaCl, pH 7.4), HEPES buffer with increased salt concentration (10 mM HEPES, 1 M NaCl, pH 7.4) and low pH phosphate buffer (150 mM KH_2PO_4 and K_2HPO_4, pH 3.0). Conditions: b-HA-280 concentration: 35.7 nM (10 µg/mL), flow rate: 0.5 µL/min, incubation time: 15 hours.

To observe the effects of these strategies on the amount of bound HA over time, we used QCM-D. Figure 2.19 demonstrates the attachment of HA chains to SLB-based TAv monolayer for an extended period of time (15 hours) in 3 different conditions: working HEPES buffer (salt concentration: 150 mM), high-salt HEPES buffer (salt concentration: 1 M) and low-pH phosphate buffer (pH 3.0).

In all three experiments, a similar initial rapid binding phase was observed during the first 80 minutes, followed by a slower linear increase in dissipation and a decrease in frequency, indicating crowding of HA molecules at the surface. Notably, the binding did not reach saturation within the observed time frame, suggesting the potential for even longer grafting periods to further enhance

brush density. For practical reasons, we decided to use a 15-hour incubation period for this and subsequent tests.

It is worth noting that both selected strategies demonstrated enhanced binding of HA-280 compared to HA incubation in the standard HEPES buffer. This enhancement is evidenced by a more pronounced decrease in frequency shift, indicating a greater mass of HA bound (with the highest mass increase was shown for the brush incubated in low-pH buffer). Additionally, a more pronounced increase in dissipation signifies the formation of a thicker film.

Following the incubation period, each of the three layers underwent a rinsing process, initially with the buffer utilized for brush formation, and subsequently with the working HEPES buffer. The resulting shifts in frequency and dissipation, measured within the working HEPES buffer, were then compared as depicted in Figure 2.20.

Remarkably, the final frequency shifts for HA-280 were higher for both brushes incubated in the high-salt buffer and the low-pH buffer, indicative of a greater amount of bound mass compared to the brush incubated in working buffer. Similarly, the final dissipation shifts indicated the formation of thicker films in both cases. The low-pH buffer yielded superior results in terms of the final shifts compared to the high-salt buffer, therefore, it was selected as the preferred condition for the protocol of dense HA brush formation.

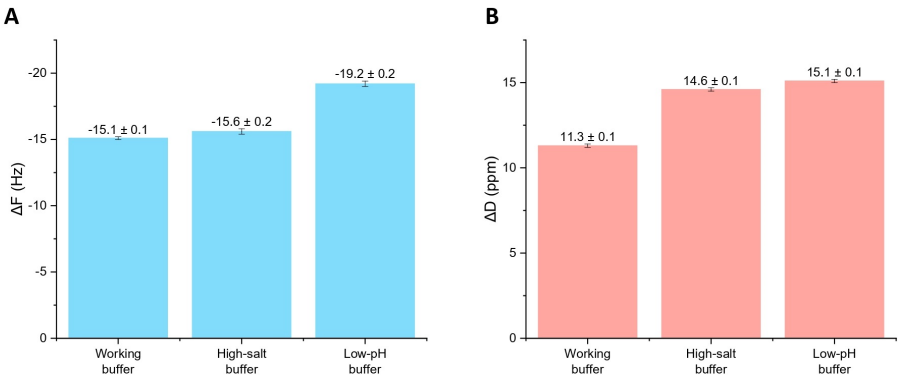

Figure 2.20: Final shifts after the HA-280 brush formation in different buffers. Buffer compositions: working buffer: 10 mM HEPES, 150 mM NaCl, pH 7.4; high-salt buffer: 10 mM HEPES, 1 M NaCl, pH 7.4; low-pH buffer: 150 mM KH_2PO_4 and K_2HPO_4, pH 3.0. **A.** Final frequency shifts (ΔF) after the end of the brush formation. **B.** Final dissipation shifts (ΔD) after the end of the brush formation.

Testing the stability of the HA brushes

Upon the successful formation of thick HA brushes, we proceeded with additional tests for all three brushes to assess the stability of the grafted chains. To do so, we utilized a HEPES buffer without NaCl salt. Prior research has indicated that reducing the salt concentration in the solution down to 0 significantly enhances the repulsive forces between neighboring HA chains. This, in turn, results in brush swelling and internal pressure within the brush, ultimately promoting the release of a fraction of the anchored HA chains [150]. Consequently, by subjecting our formed brushes to these conditions, we aimed to evaluate the stability of their attachment to the platform.

Figure 2.21 illustrates the stability assessment of the brush formed in the high salt concentration buffer. Initially, the brush underwent rinsing in the working buffer (35-45 min) and subsequently in a no-salt buffer (60-80 min). Notably, the changes in frequency and dissipation observed during these rinsing steps were entirely reversible, signifying the absence of HA detachment. These changes are most likely attributed to the changes in density and/or viscosity of the solution. Similar tests were conducted on the other two HA brushes (not presented here), and all exhibited exceptional stability. This stability is in line with prior research, which indicated that

less dense HA brushes also maintained their stability when subjected to rinsing in both high and low salt concentrations [150].

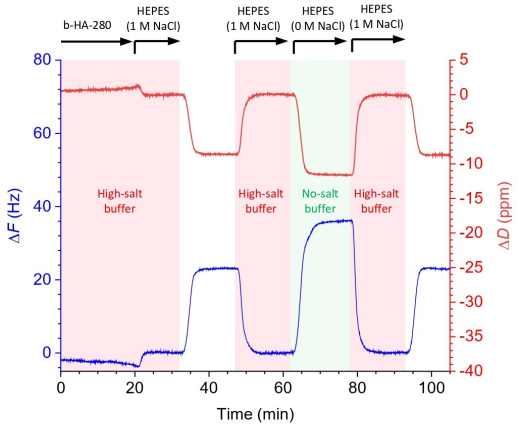

Figure 2.21: Testing the stability of HA-280 brushes formed in different buffers. QCM-D frequency shifts (ΔF – blue line) and dissipation shifts (ΔD – red line) for the 5th overtone measured over time. Flow rates: HA incubation – 0.5 µL/min, all other steps – 10 µL/min. The start and the duration of incubation with each sample are indicated with black arrows at the top of the graphs, the color stripes indicate different buffers. The steps between the black arrows are rinses with working HEPES buffer. A little change in frequency observed when switching from HA incubation to the corresponding buffer is likely due to the differences in flow rates. The HA brush was formed in high-salt buffer and then rinsed first with working HEPES buffer (30-50 min), then in no-salt buffer (60-75 min).

Estimating the mechanical properties of dense HA brushes

Having successfully established the protocol for the formation of thick and dense HA brushes with the assistance of QCM-D, our next step was to evaluate the mechanical properties of these brushes. To achieve this, the HA-280 films were formed within Teflon wells and their thickness were measured using colloidal probe RICM. The results of these measurements have been presented in earlier sections (Fig. 2.12C, Fig. 2.13D, Fig. 2.14A and B, Fig. 2.15).

The average thickness of the HA-280 film was estimated to be approximately 320 nm. Consequently, the distance between individual polymer chains, as calculated using Equation 2.1, amounts to about 22.5 nm, while the brush elastic modulus stands at approximately 1.3 kPa. These values meet the requirements for the mechanical properties of the brush necessary to effectively screen the interaction between P-selectin and PSGL-1. Therefore, our objective of developing a stiff and thick HA brush has been successfully achieved.

2.2.4 P-selectin grafting

2.2.4.1 P-selectin anchorage with the help of b-ZZ adapter protein

To anchor P-selectin receptors to the surface, an additional step of surface functionalization was necessary. This involved first attaching the b-ZZ adapter protein to the surface, creating binding sites for the Fc-tag of P-selectin (Fig. 2.22A). The attachment of b-ZZ could be achieved through two methods: incubating b-ZZ alone, which would saturate all available biotin-binding sites due to its relatively small size, or co-adsorbing it with free biotin to decrease the surface density of b-ZZ and, consequently, P-selectin. More details and theoretical background on the mechanisms of this co-adsorption method will be provided in Chapter 3. In the graphs presented throughout this section, we used either pure b-ZZ or pre-mixed it with free biotin in specific molar ratios as indicated in order to reduce the surface coverage of subsequently bound P-selectin.

To assess the feasibility of grafting P-selectin using the b-ZZ adapter protein, we initially examined their interaction using QCM-D (Fig. 2.22B). The relatively small size of b-ZZ facilitated rapid binding to the surface (5-10 min in Fig. 2.22B), reaching saturation within just 5 minutes, as indicated by the plateau phase of the binding curve. In contrast, the binding of P-selectin-Fc was prolonged (25-95 min in Fig. 2.22B) and did not reach saturation even after 1 hour of incubation. Both b-ZZ and P-selectin-Fc remained stable upon rinsing in HEPES buffer, demonstrating good stability at the surface.

As a negative control, we assessed the binding of P-selectin-Fc to a surface saturated with biotin (Fig. 2.22C). Due to the very small molecular weight of free biotin (244 g/mol), its binding response (20-30 min in Fig. 2.22C) was below the sensitivity range of QCM-D and was not noticeable. The incubation of P-selectin-Fc (60-70 min in Fig. 2.22C) resulted in a minimal frequency and dissipation change, suggesting only a small non-specific binding. The amplitude of this response was approximately 100 times smaller than the frequency change observed for P-selectin-Fc binding to b-ZZ, confirming the specificity of the interaction with b-ZZ.

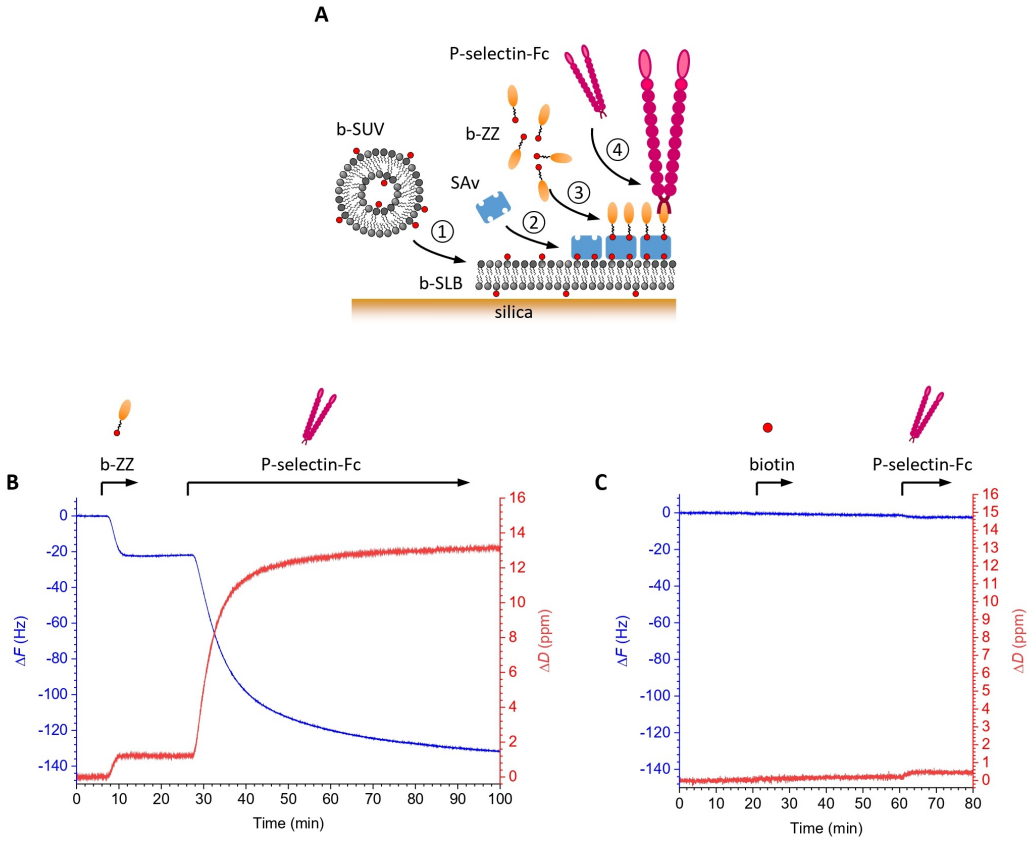

Figure 2.22: P-selectin anchorage. A. Schematic drawing of the surface functionalization: ① SLB formation, ② streptavidin monolayer formation, ③ b-ZZ adsorption,④ P-selectin-Fc anchorage. **B-C.** QCM-D frequency shifts (ΔF – blue line) and dissipation shifts (ΔD – red line) for the 5th overtone measured over time. Flow rate at all steps is 10 µL/min. The start and the duration of incubation with each sample are indicated with black arrows at the top of the graphs. Before and after each incubation step there were rinsing steps with HEPES buffer. b-ZZ or biotin were adsorbed on SAv monolayer formed on SLB (Fig. 2.10 (B) Final shifts for b-ZZ adsorption: ΔF = -22.3 ± 0.1 Hz and ΔD = 1.2 ± 0.1 ppm, for P-selectin-Fc binding: ΔF = -109.3 ± 0.1 Hz and ΔD = 11.9 ± 0.1 ppm. (C) Final shifts for biotin adsorption: ΔF = -0.6 ± 0.2 Hz and ΔD = 0.1 ± 0.2 ppm, for P-selectin-Fc binding: ΔF = -1.7 ± 0.2 Hz and ΔD = 0.3 ± 0.2 ppm.

2.2.4.2 Surface-anchored P-selection binds its ligand PSGL-1 in a Ca^{2+}-dependent manner

Having confirmed the specificity and stability of P-selectin anchorage at the surface, our next objective was to investigate whether the receptor retained its activity in binding to its ligand PSGL-1. To assess this, we employed QCM-D (Fig. 2.23). Previous studies have shown that the specific interaction between P-selectin and PSGL-1 is facilitated by the presence of Ca^{2+} ions as co-factors and thus is inhibited by the presence of ethylenediaminetetraacetic acid (EDTA), which chelates divalent metal ions [105]. We thus prepared two different buffer solutions, one containing Ca^{2+} ions (2 mM) and the other with EDTA (2 mM), for this experimental evaluation.

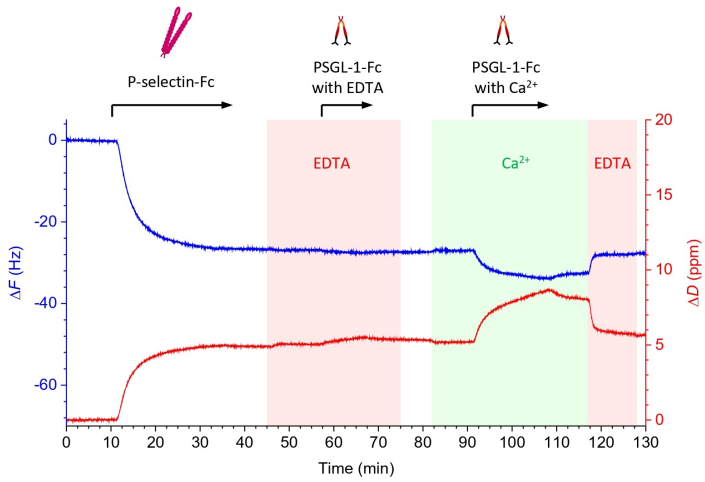

Figure 2.23: Specific interaction between P-selectin and PSGL-1. QCM-D frequency shifts (ΔF – blue line) and dissipation shifts (ΔD – red line) for the 5th overtone measured over time. Flow rate at all steps is 20 µL/min. The start and the duration of incubation with each sample are indicated with black arrows at the top of the graphs, the color stripes indicate different buffers. The steps not marked with arrows are rinsing with HEPES buffer. P-selectin was incubated until saturation on the layer consisting of SLB, SAv monolayer and b-ZZ at 2% of the maximal surface density; final shifts: ΔF = -26.6 ± 0.1 Hz, ΔD = 4.9 ± 0.1 ppm. The surface was rinsed with HEPES buffer containing EDTA (2mM), then PSGL-1-Fc (concentration of the dimer: 40 nM, equivalent to 10 µg/mL) diluted in HEPES with EDTA was incubated for 10 min. Then, the surface was rinsed with HEPES buffer with Ca^{2+} (2 mM), and PSGL-1-Fc (40 nM or 10 µg/mL) diluted in HEPES with Ca^{2+} was incubated; final shifts: ΔF = -6.8 ± 0.1 Hz, ΔD = 3.5 ± 0.1 ppm.

Initially, we anchored P-selectin at the surface, incorporating b-ZZ at a concentration of 2% of its maximum surface coverage. At such a low surface concentration, P-selectin-Fc could reach saturation in binding, meaning that all available Fc-binding sites were occupied. As a negative control, PSGL-1 was introduced into the system in the presence of EDTA in solution (55-65 min). This incubation resulted in minimal changes in frequency and dissipation, indicating virtually no binding.

Next, PSGL-1 was injected into the system in the presence of Ca^{2+} (90-110 min). This time, the incubation led to significant changes in frequency and dissipation, suggesting specific binding to P-selectin. Subsequently, upon rinsing in a buffer containing Ca^{2+} ions, a small fraction of the bound PSGL-1 molecules (less than 10% of the final frequency shift for bound PSGL-1) detached from the surface. On the other hand, when rinsed in a buffer containing EDTA (115-125 min), most of the bound PSGL-1 molecules rapidly detached from the surface. These observations confirm the specificity of the binding between P-selectin and PSGL-1.

Our findings demonstrate that P-selectin not only remained stably anchored at the surface but also retained its functionality in binding specifically to its ligand, PSGL-1.

2.2.5 Creating a glycocalyx model presenting P-selectin receptors embedded in an HA brush

Finally, we integrated the two main components of our molecular model, the hyaluronan (HA) brush, and the surface receptors, to confirm their co-presentation at the surface (Fig. 2.24A). Initially, the HA-840 brush was grafted onto the surface (0-120 min), and then b-ZZ was co-adsorbed along with free biotin (125-135 min). Subsequently, P-selectin-Fc was anchored at the available Fc-binding sites (140-180 min). As previously demonstrated, even with a very thick HA brush, not all the biotin-binding sites on the surface were saturated, leaving room for b-ZZ to adsorb. Consequently, both b-HA and P-selectin can be added subsequently to the layer, enabling them to be co-presented while remaining stably bound.

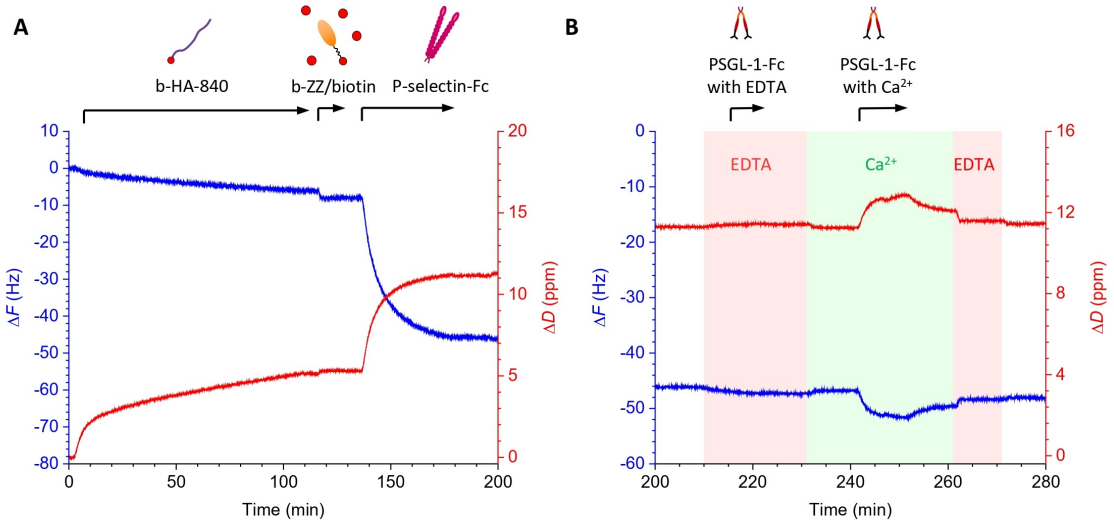

Figure 2.24: *In situ* formation of the glycocalyx model presenting an HA brush with embedded P-selectin receptors (A) and functionality test for PSGL-1 ligand binding (B). QCM-D frequency shifts (ΔF – blue line) and dissipation shifts (ΔD – red line) for the 5th overtone measured over time. Flow rate at all steps is 20 µL/min. The start and the duration of incubation with each sample are indicated with black arrows at the top of the graphs. The steps not marked with arrows are rinsing with HEPES buffer. The layer was created on the molecular platform consisting of SLB (5% biotinylated SUVs) and SAv monolayer (final shifts for SLB formation: ΔF = -24.1 ± 0.1 Hz, ΔD = 0.09 ± 0.02 ppm; for SAv incubation: ΔF = -25.5 ± 0.1 Hz, ΔD = 0.5 ± 0.1 ppm). Final shifts: HA-840: ΔF = -6.1 ± 0.1 Hz, ΔD = 5.2 ± 0.1 ppm; b-ZZ/biotin: ΔF = -1.9 ± 0.1 Hz, ΔD = 0.14 ± 0.07 ppm; P-selectin-Fc: ΔF = -37.9 ± 0.1 Hz, ΔD = 5.6 ± 0.1 ppm; PSGL-1-Fc (with Ca^{2+}): ΔF = -5.7 ± 0.1 Hz, ΔD = 1.7 ± 0.1 ppm.

To verify the functionality of the bound P-selectin, we conducted the same test as described previously, adding PSGL-1 into the system. Similar to the case of P-selectin grafted alone, it remained active in its specific interaction with PSGL-1 when co-adsorbed together with the HA brush (Fig. 2.24B), although the release of the bound PSGL-1 upon rinsing in buffer with Ca^{2+} (250-260 min) was larger than the one observed for P-selectin grafted alone (Fig. 2.23). This effect was also evaluated on a thick HA-280 brush incubated for over 15 hours, where PSGL-1 seemed to remain stable upon rinsing in both HEPES with Ca^{2+} and working HEPES buffer (Fig. B.2). As of now, a conclusive explanation for the variation in PSGL-1 stability remains elusive, with potential attributions to experimental variability.

These results indicate that both components, the HA brush and P-selectin, can be successfully co-presented at the surface, and their functionality is generally preserved even in this combined state.

2.3 Discussion

The molecular model of glycocalyx presented in this chapter serves as a well-controlled and versatile system for studying cell-glycocalyx interactions. By carefully selecting parameters, we have developed a model that can not only mimic the biophysical and chemical properties of the glycocalyx but also can present certain features in enhanced (beyond physiological) manner, facilitating investigations into the mechanisms of cell-glycocalyx interactions.

In brief, the protocol for constructing a molecular model of the glycocalyx involves the following steps:

1. ***Selection of anchorage platform.*** In this chapter, we have opted for a streptavidin monolayer formed on SLB as our primary anchorage platform. However, it's worth noting that alternative options, such as SAM-based platforms or SAv substituted with TAv, can be considered based on specific research objectives.

2. ***Generation of HA brush with desired mechanical properties.*** As demonstrated earlier, the mechanical properties of the hyaluronic acid (HA) brush can vary significantly depending on factors such as HA molecular weight and incubation conditions.

3. ***Attachment of receptor(s) of interest.*** Surface receptors can be introduced after the formation of the HA brush. Depending on the preferred anchoring mechanism, they can be directly grafted (e.g., through biotin-streptavidin interactions) or with the assistance of adapter proteins, as illustrated by our use of b-ZZ. Chapter 3 will elaborate on achieving the desired surface receptor density.

The thorough study undertaken to choose the molecular platform and design the monolayer with biotin-binding sites has resulted in a reliable and reproducible molecular system. Furthermore, our observation regarding the ability to tune the fluidity of the supported lipid bilayer opens up numerous opportunities for creating tailored molecular models suited for diverse applications, including investigations under flow conditions. Employing the methodologies outlined in this chapter for establishing the immobile supported SLB-based anchoring platform, it becomes feasible to construct other model systems for flow assays. For instance, this approach can be applied to investigate the adhesion of various types of living cells and microorganisms in well-controlled *in vitro* conditions under flow.

The capability to generate hyaluronan brushes with diverse mechanical qualities holds potential for studying glycocalyx mimetics under both physiological and pathological conditions. Our successful creation of a thick HA brush, potentially capable of screening interactions with surface adhesion molecules located beneath it due to its thickness and high density, makes this system particularly valuable as a negative control when investigating specific interactions with these receptors.

Our findings show that P-selectin receptors, when anchored alongside the HA brush in our molecular model, retain their functionality in specific interactions with their ligand PSGL-1. This characteristic enables the investigation of specific interactions between P-selectin and cells or cell mimetics that carry PSGL-1.

However, there are certain limitations to our current system. To anchor surface receptors to our platform, they must possess a biotin-tag to attach to the streptavidin monolayer. Alternatively, the use of other adapter proteins, as demonstrated with b-ZZ anchoring P-selectin containing Fc-tag, can provide flexibility in this regard.

Moving forward, our model offers the flexibility to co-present not only P-selectin but also other surface adhesion molecules together with the HA brush. Replacing P-selectin with different receptors or even anchoring multiple receptors simultaneously, alongside the HA brush, can be

achieved straightforwardly. This opens up exciting possibilities for investigating complex cell-glycocalyx interactions involving various receptor combinations and exploring their implications in different biological processes.

As an illustrative example, our current model can be enhanced by incorporating E-selectin, a surface adhesion molecule known to contribute to cell rolling under flow, in addition to P-selectin. E-selectin is typically expressed at a later stage of the immune response, with P-selectin being expressed within minutes and E-selectin within hours after the immune response initiation [76]. Consequently, E-selectin becomes a subsequent player in the cell-glycocalyx interaction process. Investigating the role of E-selectin and P-selectin co-presented alongside a dense hyaluronan brush in cell adhesion under flow represents an intriguing research inquiry that can be effectively addressed using a platform constructed according to the protocols outlined in this chapter.

In the broader global context of research, our molecular model holds the potential to significantly enhance the understanding of cell-glycocalyx interactions. While previous efforts to investigate these interactions have been made, employing computer simulations [32, 145] or conducting *in vitro* experiments involving endothelial cell layers [41], it is noteworthy that, to our knowledge, there exists a gap in the scientific literature regarding the development of a comprehensive molecular model specifically dedicated to studying the contribution of the individual receptors. By bridging this gap, our study not only contributes to the study of the mechanical aspects of cell-glycocalyx interactions but also establishes a solid foundation for future advancements in the fields of biophysics and surface chemistry.

2.4 Conclusion

In conclusion, our carefully designed molecular model offers a valuable and versatile tool for investigating cell-glycocalyx interactions in a controlled environment. With its ability to mimic biologically relevant properties and adapt to various experimental conditions, this model holds significant promise for future advancements in glycocalyx-related research and biomedical applications.

3

Control of the surface densities of the receptors

Short summary

This chapter presents a novel method to controllably tune the number of receptors of interest at the surface. In the frame of my project, the need for controlling the surface density of the receptors arose from the need to mimic the biomolecular layer with the proteins located at a sufficient (and biologically relevant) distance from each other. Something that started as a tool for developing the glycocalyx model, ended up being a whole fundamental research with a large number of applications and great significance in the field of surface chemistry.

Acknowledgements

The theoretical considerations presented in this chapter were developed with a great help of my thesis supervisors: Ralf P. Richter, Delphine Débarre and Lionel Bureau. Most of the experiments presented here were designed, performed and analyzed by myself, except for the combined QCM-D/SE assay, for which I would like to acknowledge Ralf P. Richter. The SE experiments were performed in the Richter Lab, at the University of Leeds, and the QCM-D experiments were conducted in the Département de Chimie Moléculaire (DCM) at UGA. The theory for the competitive co-adsorption of biotinylated species and some of the experiments illustrating it presented in this chapter were summarized in [82].

Contents

3.1 Introduction

While developing the biolayer mimicking the vascular wall glycocalyx, we encountered the need to locate the surface receptors (P-selectin) at a sufficient and biologically relevant distance from each other. The density of P-selectin receptors on endothelial cells is estimated to be around 350 per μm^2, which results in an average distance of approximately 50 nm between receptors [15]. In contrast, the densely packed streptavidin monolayer used in our molecular model has a density of approximately 40,000 biotin-binding sites per μm^2, reflecting a significant disparity. This highlights the importance of quantitative tuning to align the model system more closely with the biological conditions.

The aim of the study presented in this chapter was to develop a method allowing to reliably and controllably reduce P-selectin's surface concentration within our model system (microfluidic channel) while operating under flow conditions. Additionally, we aimed to establish a protocol to assess the density of post-functionalized P-selectin within the microfluidic channel. The previous attempts of controlling the density of grafted molecules described in the literature were mostly relying on the binding kinetics of the compounds. The desired ligand coverage was achieved by adjusting the ligand concentration and/or incubation time [17, 33, 118]. However, there are some limitations to this method. First, the incubation time and ligand bulk concentration must be carefully controlled since they have a direct impact on the final density of ligands. Second, the binding rate is also highly sensitive to the incubation conditions, so the binding can be limited by diffusive and/or convective transport of ligands to the surface. For example, when samples are in stagnant solutions, they need to be mixed initially to distribute the ligands evenly and then mixed again at the end of incubation to remove any excess ligands. Binding that occurs during these transient phases can significantly contribute to the overall binding process [60], thereby introducing errors in determining the ligand surface density. Other factors such as temperature, solution viscosity, flow geometry and rate can also contribute to the mass-transport conditions of binding species. Altogether, such methods are difficult to establish and reproduce in different experimental settings (e.g., different flow geometry) and require thorough calibration.

Another type of reported methods relies on ligand depletion in solution [43]. If the incubation is long enough to ensure that all the molecules from the solution can bind to the surface, then the surface density of receptors can be controlled by the exact number of molecules in solution. However, the accuracy of such method is highly dependent on the precise number of receptor molecules present in the solution and the exact number of available anchorage sites. Furthermore, in many applications there is a need to functionalize the surface with a limited number of receptors, and at such small concentrations their tendency to non-specifically adsorb onto the surfaces other than the intended one becomes significant.

Finally, some of the published works demonstrated approaches to control the surface density of receptors by mixing the molecules of interest with inert molecules of similar size and chemical properties [4, 39, 71]. However, the assumption that the ratio of molecules in the solution will correspond to the ratio of bound species at the surface holds true only for molecules of similar size and binding properties, which may require specific synthesis to achieve. Consequently, the application and ease of use of this method are limited.

In order to establish a reliable and reproducible surface functionalization protocol in different model systems (such as QCM-D sensor, round well with glass bottom, microfluidic channel), we rejected the idea of controlling the number of molecules on the surface by interrupting the incubation of the protein before its full saturation. This decision was based on the inherent low reproducibility of such an approach across different systems. Instead, we have developed a method allowing to control the surface density of anchored molecules through competitive mass-transport limited adsorption. Not only it allowed us to predict with high accuracy the surface density of P-selectin and create highly reproducible biomimetic layers, it also broadened the scope of existing surface functionalization techniques and contributed to the advancement of biomimetic surfaces.

3.2 Theoretical considerations for co-adsorption of two biotinylated species

The theory focuses on the specific interaction shown in Figure 3.1, where functional molecules with anchor tags (index 1) co-adsorb with free anchors (index 2) on the surface. The main assumptions underlying this theory are as follows:

1. The binding of all species is mass-transport limited: the uptake rate of a solute by the surface is high and the fluid at the surface is almost completely depleted (the concentration of binding species is close to 0 at the surface) [60].
2. The binding between the anchor and the surface is strong and irreversible.
3. Steric hindrance does not impede the binding of the molecules, so all the available binding sites are occupied at the equilibrium.
4. The solution is semi-infinite – there is an unlimited reservoir of binding molecules in solution.

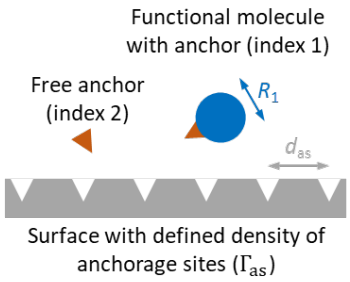

Figure 3.1: Schematic of the interaction scenario considered in the theory. Functional molecule with anchor (index 1) is co-adsorbing at the surface together with the free anchor (index 2).

For most of our experiments, we utilized a streptavidin-coated surface as the substrate for species binding, so the theory presented in this study primarily revolves around adjusting the surface density of biotinylated receptors that are bound to the streptavidin-coated support. However, this theory can be readily expanded to accommodate other types of interactions. It is worth noting that biotin-streptavidin bonds exhibit strong affinity ($K_d \approx 10^{-14}$ M , [166]), which satisfies the aforementioned assumption 2, and its association rate constant is very high ($k_{on} \approx 7.0 \times 10^7 M^{-1} s^{-1}$ [57]), satisfying assumption 1.

During the development of the glycocalyx model, we employed various methods to assess different properties of the biosurfaces. These methods included *in situ* techniques such as QCM-D and SE, as well as post-functionalization methods like confocal microscopy and RICM. Some of these experiments involved the co-adsorption of species under static conditions, while others were conducted under constant flow (Table 3.1). Thus, we needed to develop theoretical predictions for both of these scenarios.

Table 3.1: Functionalization techniques and their respective flow conditions

Functionalization in stagnant conditions	Functionalization under flow
SE wafer	QCM-D sensor
Round well with glass bottom (suitable for confocal microscopy and RICM measurements)	Microfluidic channel

3.2.1 Binding in stagnant solution

Our first attempts to tune the density of receptors of interest were done in a still solution (the model system of a round well with glass bottom). The process of mass-transport limited binding of molecules from a semi-infinite stagnant solution to a flat surface has been previously described in literature (for example, by Hermens et al [60]). It can be expressed as:

$$\Gamma(t) = 2c(Dt/\pi)^{1/2} \tag{3.1}$$

where $\Gamma(t)$ – molar surface density (mol/cm^2);
c – molar concentration of the substrate in the bulk solution (M);
D – diffusion constant of the substrate (cm^2/s).

The diffusion coefficient can be defined using the Stockes-Einstein relation assuming a liquid with low Reynold number (laminar flow):

$$D = \frac{k_B T}{6\pi\eta R} \tag{3.2}$$

where $k_B T$ - thermal energy;
η - solvent viscosity;
R - hydrodynamic radius of the binding molecules.

If two species in the bulk solution are simultaneously adsorbing at the surface, the ratio of their molar surface densities can be described as:

$$\frac{\Gamma_1(t)}{\Gamma_2(t)} = \frac{2c_1\,(D_1 t/\pi)^{1/2}}{2c_2\,(D_2 t/\pi)^{1/2}} = \left(\frac{D_1}{D_2}\right)^{1/2}\frac{c_1}{c_2} = \left(\frac{R_2}{R_1}\right)^{1/2}\frac{c_1}{c_2} \tag{3.3}$$

It can be noted that this ratio depends only on the concentrations of the molecule of interest (c_1) and the inert molecule (c_2), and their respective hydrodynamic radii (R_1 and R_2) and is independent of the incubation time (t).

Considering our assumption that all available binding sites on the surface are occupied once the binding process is complete (i.e., surface saturation is reached), the total molar density of anchorage sites on the surface Γ_{as} is fixed for a given surface and is equal to the sum of the molar surface densities of the functional molecule $\Gamma_{1,sat}$ and inert molecule $\Gamma_{2,sat}$.

Then,

$$\frac{\Gamma_{as}}{\Gamma_{1,sat}} = \frac{\Gamma_1+\Gamma_2}{\Gamma_1} = 1+\frac{\Gamma_2}{\Gamma_1} = 1+\left(\frac{D_2}{D_1}\right)^{1/2}\frac{c_2}{c_1} = 1+\left(\frac{R_2}{R_1}\right)^{1/2}\frac{c_2}{c_1} \tag{3.4}$$

and the ratio of the molar concentration of two species in bulk solution can be determined as:

$$\frac{c_2}{c_1} = \left(\frac{D_1}{D_2}\right)^{1/2}\left(\frac{\Gamma_{as}}{\Gamma_{1,sat}}-1\right) = \left(\frac{R_2}{R_1}\right)^{1/2}\left(\frac{\Gamma_{as}}{\Gamma_{1,sat}}-1\right) \tag{3.5}$$

Equation 3.5 is the main working formula that I used to control the surface density of receptors. By selecting the appropriate ratio of $\Gamma_{as}/\Gamma_{1,sat}$, we can to determine the ratio of molar concentrations for the two species in solution, knowing the hydrodynamic radii of binding molecules. This allows for simple and straightforward experimental planning.

For convenience, we will display in graphs the fractional occupancy of the target molecule: $\Gamma_{1,sat}/\Gamma_{as}$ where Γ_{as} can be expressed as 100% and $\Gamma_{1,sat}$ as the desired percentage of the surface occupied by the molecule of interest.

3.2.2 Binding under flow

In frame of my project, I needed to be able to tune the surface density of P-selectin molecules in the microfluidic channel where the surface functionalization is happening under flow. We thus aimed to extend our theoretical considerations to the case of binding with convective fluid transport. Another practical application of this approach was the functionalization of the QCM-D sensor where the proteins are brought to the surface under continuous flow.

Regardless of the model system, the steady-state rate of mass-transport limited binding can be described as:

$$\frac{\mathrm{d}\Gamma(xy,t)}{\mathrm{d}t} = \Omega D^{2/3} c \tag{3.6}$$

where Ω accounts for the influence of convective fluid transport. It only depends on the location on the surface, but is independent of the incubation time.

If the flow is sufficiently fast, the steady-state condition is reached quickly and the binding rate can be considered constant:

$$\Gamma(xy,t) = \Omega D^{2/3} c t \tag{3.7}$$

Then, the ratio of the two species in the solution can be defined as:

$$\frac{c_2}{c_1} = \left(\frac{D_1}{D_2}\right)^{2/3} \left(\frac{\Gamma_{\mathrm{as}}}{\Gamma_{1,\,\mathrm{sat}}} - 1\right) = \left(\frac{R_2}{R_1}\right)^{2/3} \left(\frac{\Gamma_{\mathrm{as}}}{\Gamma_{1,\mathrm{sat}}} - 1\right) \tag{3.8}$$

that again depends only on the physical properties of the co-adsorbing molecules (their hydrodynamic radii). Thus, the protocol for designing the surface with the desired $\Gamma_{\mathrm{as}}/\Gamma_{1,\mathrm{sat}}$ can be easily established.

Comparing Equations 3.5 and 3.8 reveals that the sensitivity to the ratio D_1/D_2 (or R_2/R_1) is slightly amplified, yet it still retains a relatively weak dependence (power of 2/3) under conditions of convective transport. These equations converge and become identical when the two binders possess comparable sizes ($\mathrm{R_2/R_1 = D_1/D_2 \approx 1}$).

3.2.3 Guidelines for experimental design

Although the method outlined above is simple and straightforward, it relies on several simplifying assumptions. Fortunately, these assumptions can easily be met for a wide range of binder sizes (and hence diffusion coefficients) and intrinsic binding rates, provided that binding is irreversible.

Firstly, to meet the condition of mass-transport limited binding where the surface behaves as an 'perfect sink', the influx of binders to the surface must be significantly lower than the binding rate. This condition is fulfilled when:

1) for binding from stagnant solution:

$$\varepsilon_{\mathrm{still}} = \frac{Dc}{k_{\mathrm{on}}\Gamma_{\mathrm{as}}^2} \ll 1 \tag{3.9}$$

2) for binding from under flow:

$$\varepsilon_{\mathrm{flow}} = \frac{D}{\Gamma_{\mathrm{as}}\delta k_{\mathrm{on}}} \ll 1 \tag{3.10}$$

where k_{on} – the intrinsic binding rate constant, δ – the thickness of the depletion layer across which molecules from the bulk solution need to diffuse to reach the surface.

The derivations of equations 3.9 and 3.10 are described in detail in the Supplementary Methods.

These relations are useful for experimental design. It's evident that $\varepsilon_{\text{still}}$ can be kept small by restricting binder concentration, while $\varepsilon_{\text{flow}}$ can be controlled by reducing flow rate $Q \propto \delta^{-3}$. Importantly, the liquid layer above the functionalized surface must be thicker than the depletion layers of all binding molecules. Otherwise, the bulk solution becomes depleted, rendering our approach invalid.

Secondly, with larger functional molecules ($R_1 > d_{\text{as}}$, as shown in Fig. 3.1), steric hindrance limits grafting beyond a maximum surface density, which can be much lower than anchor site density. Yet, control over surface density using Eqs. 3.5 and 3.8 can be achieved if two conditions are met: (i) surface diffusion remains unaffected and (ii) grafting densities are kept below the maximum threshold. In practice, $N_{\text{A}}/\Gamma_{1,\text{sat}} > R_1^2$ should provide a reasonable condition for Eqs. 3.5 and 3.8 to remain valid.

The experiments presented in the subsequent sections generally satisfy the criteria for theory validity, unless stated otherwise. Additional information on assessing experimental conditions is available in the Supplementary Methods section.

3.3 Results

3.3.1 Experimental validation of the theoretical predictions on a simple model

To validate our theoretical predictions, we initially focused on a simple case of co-adsorption of two molecules with relatively similar molecular weight. Since classical quantitative methods for assessing the adsorbed mass (such as SE) would not be sufficiently sensitive to detect the binding of molecules the size of biotin, we opted to use confocal microscopy instead. By observing the level of changes in the fluorescent signal emitted from the molecules bound to the surface after rinsing, we could estimate the surface density of the adsorbed fluorophores. The co-adsorption of the molecules took place in stagnant conditions (in round Telfon well with glass bottom).

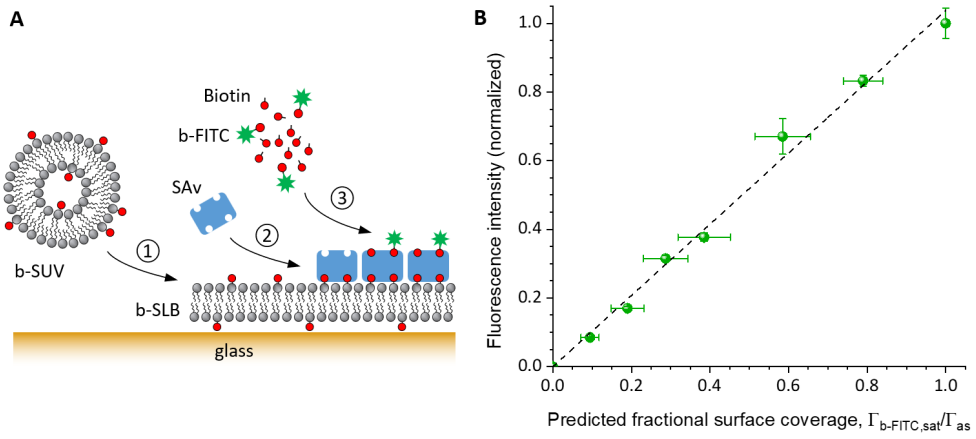

Figure 3.2: Tuning of the surface densities of two biotinylated species of similar size. A. Schematic drawing of the surface functionalisation: ① SLB formation, ② streptavidin (SAv) monolayer formation, ③ co-adsorption of b-FITC and biotin. **B.** Normalised fluorescence intensity measured with confocal microscopy for surfaces functionalised with different mixing ratios of b-FITC and biotin. The horizontal axis shows the fractional surface coverage, $\Gamma_{\text{b-FITC,sat}}/\Gamma_{\text{as}}$, of the b-FITC fluorophore (co-adsorbed with free biotin) predicted according to Eq. 3.5. The black dashed line through the origin confirms the expected linear trend. Conditions: $c_{\text{b-FITC}} + c_{\text{biotin}}$ = 14 µM was maintained constant, with $c_{\text{b-FITC}}$ and c_{biotin} determined according to Eq. 3.5 ($\varepsilon < 0.25$).

Similar to the experiments described in Chapter 2, we chose to use biotinylated FITC fluorophore (b-FITC; $R_{\text{b-FITC}} = 0.63$ nm; Table B.1), which is comparable in size to the free anchor biotin ($R_{\text{biotin}} = 0.37$ nm). After several experimental refinements, we implemented a pre-bleaching step for the b-FITC solution prior to functionalization. This ensured that the intensity of fluorescence was directly proportional to the surface density of the fluorophore (more detail on the development of this experimental protocol can be found in "Quantification of receptor surface density through fluorescence analysis " section in Appendix A. First, the uniform and mobile SAv monolayer (Fig. 2.11) was created in Teflon wells as described before. Then, the surface was incubated with a mix of pre-bleached b-FITC and free biotin in the desired molar ratios ranging from 0% b-FITC (no fluorophore added) to 100% b-FITC (no biotin added) (Fig. 3.2A). Fianlly, the fluorescence intensity at the surface was measured using confocal microscopy.

Fig. 3.2B shows the measured intensity of fluorescence as a function of the fractional surface coverage of b-FITC fluorophore $\Gamma_{\text{b-FITC,sat}}/\Gamma_{\text{as}}$, predicted with the use of the equation 3.5. The background signal (fluorescence intensity of pure biotin) was subtracted and the intensity of fluorescence for all data points was normalized to the maximum fluorescent signal (100% b-FITC). The observed dependence exhibited a clear linear trend (Fig. 3.2B), thereby validating the theoretical prediction in Eq. 3.5.

3.3.2 Control of the surface density of b-ZZ adapter protein

After successfully validating our theoretical considerations with a simple molecular model, we proceeded to adjust the density of b-ZZ protein on the surface by co-adsorbing it with free biotin. The b-ZZ adapter protein is much larger than biotin ($R_{\text{b-ZZ}} = 2.0$ nm; Table B.1), but its size still allows it to occupy all the available biotin-binding sites on a densely packed streptavidin monolayer ($R_{\text{b-ZZ}} < d_{\text{as}}$, where $d_{\text{as}} = 4.5$ nm) [108]. Therefore, the binding of the b-ZZ protein to the surface is not hindered by steric effects, satisfying assumption 3.

3.3.2.1 Quantitative *in situ* density control in stagnant conditions

We started with the quantitative assessment of the bound protein mass by monitoring its interaction with the surface using the spectroscopic ellipsometry (SE) method in stagnant conditions.

First, the SAv-coated surface was prepared following the establised procedure (Fig. B.3). Then, the mix of b-ZZ and biotin at a predetermined molar concentration (defined by Eq. 3.5 in order to obtain the desired surface coverage of b-ZZ) was added to the SE cuvette (Fig. 3.3A). Figure 3.3B shows the dynamic of binding of b-ZZ to the surface and it can be noted that after 10 min the surface was fully saturated with the protein.

Figure 3.3C shows the measured surface density of b-ZZ calculated from the SE data as a function of nominal b-ZZ surface density. The latter was calculated with the use of the equation 3.5 considering the surface density of anchor sites $\Gamma_{\text{as}} = 2\Gamma_{\text{SAv}}$. The data demonstrates a clear linear dependence, which indicates that our theoretical considerations were correct also for the case of a significant difference in the size of co-adsorbing species.

The slope of the linear fit to the data presented in Fig. 3.3C is 0.93 ± 0.02. This indicates that the number of biotin-binding sites per each streptavidin molecule is 1.86 ± 0.04, rather than 2. This finding aligns with earlier published data (1.74 ± 0.22) on dense streptavidin monolayers on SLBs [44] indicating that streptavidin molecules can bind to the SLB using 2, 3, of 4 of their biotin-binding pockets. Consequently, the average "residual valency" can range between 1 and 2.

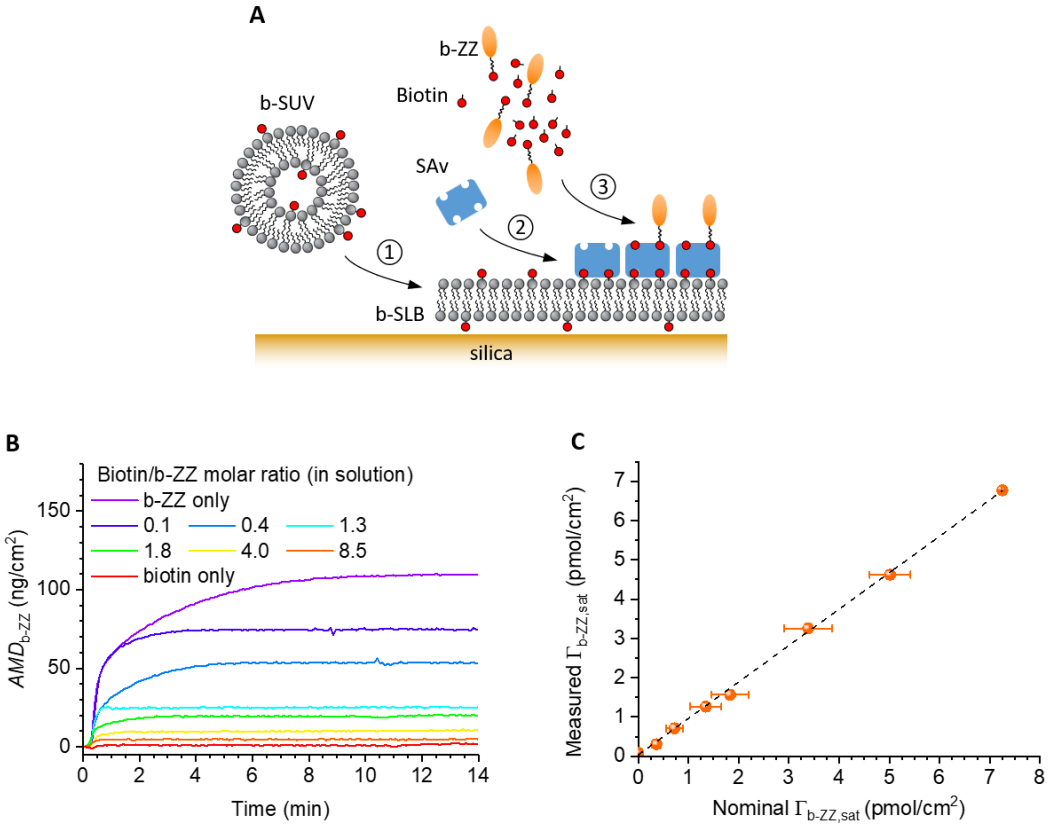

Figure 3.3: Quantitative tuning of the surface density of two biotinylated proteins of different size (in stagnant solution). A. Schematic drawing of the surface functionalisation: ① SLB formation, ② SAv monolayer formation, ③ co-adsorption of b-ZZ and biotin. **B.** Areal mass density of b-ZZ, AMDb-ZZ, over time, determined by spectroscopic ellipsometry for a range of $c_{\text{biotin}}/c_{\text{b-ZZ}}$ molar ratios (as indicated). Conditions: $c_{\text{b-ZZ}} + c_{\text{biotin}} = 0.625\mu\text{M}$ was maintained constant, with $c_{\text{b-ZZ}}$ and c_{biotin} determined according to Eq. 3.5 ($\varepsilon < 0.01$); biotin/b-ZZ incubation – 10 min, starting from 0.3 min; see Figure S4 for details of steps ① and ②. **C.** b-ZZ surface density at saturation, $\Gamma_{\text{b-ZZ,sat}}$, measured by SE as a function of the nominal b-ZZ surface density predicted from the $c_{\text{biotin}}/c_{\text{b-ZZ}}$ molar ratios and $\Gamma_{\text{as}} = 2\Gamma_{\text{SAv}}$ according to Eq. 3.5. Error bars along the horizontal axis represent the uncertainty in the concentrations of biotin and b-ZZ when computing $\Gamma_{\text{as}} = 2\Gamma_{\text{SAv}}$, and the resolution in Γ_{SAv}. Error bars along the vertical axis (about the size of the symbols) represent temporal noise and confidence intervals when fitting the SE data. The black dashed line is a linear fit through the data, with a slope of 0.93 ± 0.02.

3.3.2.2 Control of the density while binding under flow

So far we only illustrated the validity of our method for the co-adsorption of the molecules in stagnant conditions. Since our final goal was to create a microfluidic system mimicking the vascular wall glycocalyx, we needed to verify that the abovementioned assumptions would be valid for the functionalization in constant flow conditions. For this purpose, we used quartz crystal microbalance with dissipation monitoring (QCM-D) to observe the binding of b-ZZ protein to the SAv-coated platform.

First, the streptavidin monolayer was formed on SLB as described earlier (Fig. B.3). Then, b-ZZ adapter protein or the mix of b-ZZ and biotin was added to the system and incubated until the full saturation, which typically occurred after 1-2 min (Fig. 3.4A).

Frequency shifts Δf resulting from the binding of b-ZZ were plotted against the predicted fractional b-ZZ surface coverage ($\Gamma_{\text{b-ZZ,sat}}/\Gamma_{\text{as}}$) revealing a slightly nonlinear trend (Fig. 3.4B). However, it is important to note that as previously reported [13,21,134], the frequency shift cannot be directly translated into the quantity of protein at the surface, since it accounts for not only the mass of the bound compound but also the mass of the solvent hydrodynamically coupled to

the protein. For a monolayer of globular proteins, the contribution of the solvent mass tends to decrease with an increase in the surface coverage of the compound. Therefore, a calibration curve was necessary to establish a relationship between the frequency shift ($\Delta F_{b-ZZ,sat}$) for b-ZZ and the corresponding surface coverage ($\Gamma_{b-ZZ,sat}$). For this, a combined QCM-D and SE experiment was performed as described elsewhere [21]. Fig. 3.4C displays the resulting standard curve, illustrating the correlation between the frequency shift and the surface density of b-ZZ. Using this curve, the measured surface density of b-ZZ was plotted as a function of the predicted ratio $\Gamma_{b-ZZ,sat}/\Gamma_{as}$ (Orange spheres in Fig. 3.4D). The data exhibits a clear linear trend, indicating that the protein's surface density was adjusted in accordance with the theoretical predictions (Eq. 3.8). The maximal b-ZZ surface coverage $\Gamma_{b-ZZ,max} = \Gamma_{as}$ (6.1 ± 0.2 pmol/cm^2) was slightly smaller than the one measured in stagnant conditions (6.8 ± 0.1 pmol/cm^2; Figure 3.3C). This discrepancy can be attributed to variations in the incubation conditions of streptavidin (difference in incubation time and binding dynamics), leading to differences in SAv density and subsequent variations in the number of available biotin-binding sites.

It is important to emphasize that the dimensions of the QCM-D chamber impose significant limitations on the experimental design to fulfil condition 4. In the described set of experiments we used the flow rate 200 µL/min for b-ZZ incubation in order to keep the binding in mass-transport limited conditions. This choice deviates from the typical practices in QCM-D experiments (where flow rates typically range up to 50 µL/min) and can be challenging to implement practically. However, reducing the flow rates would lead to deviations from the theoretical predictions as the binding would occur outside the specified conditions (assumption 1). Grey spheres in Fig. 3.4D show the surface density of b-ZZ adapter protein as a function of the calculated b-ZZ surface coverage. The shape of the curve deviates from the straight line at a target coverage of 10%. Analysis of the mass transport conditions revealed that the thickness of the depletion layer for the fast-diffusing free biotin approaches the fluid thickness above the QCM-D sensing area in the lower flow rate regime (see section B.1.1 in Supplementary Methods). This example demonstrates the importance of an appropriate design of incubation conditions to achieve the desired surface densities.

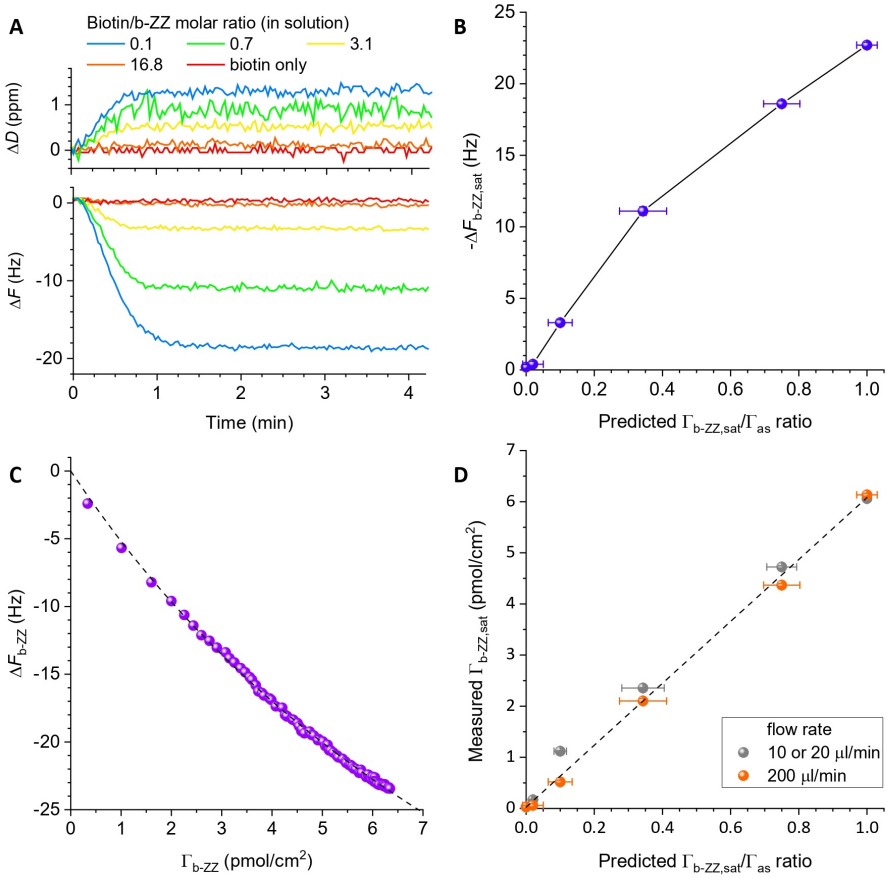

Figure 3.4: Quantitative tuning of the surface density of two biotinylated proteins of different size (under flow). **A**. QCM-D dissipation shifts ΔD (top) and frequency shifts ΔF (bottom; for overtone i= 5) obtained for b-ZZ mixed with free biotin at distinct molar ratios (as indicated). Conditions: $c_{b-ZZ} + c_{biotin}$ = 0.625 µM was maintained constant, with c_{b-ZZ} and c_{biotin} determined according to 3.8 ($(\varepsilon < 0.007)$; b-ZZ/biotin incubation – 3 min, starting from 0 min; during remaining times, plain working buffer was flown over the sensor surface, flow rate – 200 µL/min. b-ZZ only was incubated at a different flow rate (20 µL/min) and therefore is not displayed in the graph; see Figure S6A for details of the SAv-on-SLB sensor functionalisation and b-ZZ grafting. **B.** Frequency shifts at saturation ($\Delta F_{b-ZZ,sat}$) vs. the predicted fractional b-ZZ surface coverage ($\Gamma_{b-ZZ,sat}/\Gamma_{as}$). **C.** Standard curve relating frequency shifts to b-ZZ molar surface density, obtained through a combined QCM-D/SE experiment (see B.2 for details). This data was acquired and analyzed by R. P. Richter. The dashed line is an empirical fit to the data, with $\Gamma_{b-ZZ} = (\alpha - 1)/\left[M_{b-ZZ}\left(\beta + C^{-1}\Delta F^{-1}\right)\right]$ and $\alpha = 0.8389 \pm 0.0012$, $\beta = 7.83 \pm 0.14 \times 10^{-4}$ cm^2/ng, the mass sensitivity constant $C = 18.0$ ng/(cm^2 Hz), and the molecular mass M_{b-Zz} =16.2 kDa. **D.** Plot of the measured b-ZZ surface density as a function of $\Gamma_{b-ZZ,sat}/\Gamma_{as}$ for two distinct flow rate regimes (200 µL/min - orange spheres; 10 or 20 µL/min – grey spheres). The black dashed line is a linear fit through the purple data (200 μL/min), with a slope of 6.1 ± 0.2 pmol/cm^2. b-ZZ surface densities were determined using the empirical fit from panel C.

3.3.3 Control of the surface density of P-selectin

3.3.3.1 Quantitative *in situ* density control in stagnant conditions

Having established reliable protocols for tuning the surface density of the b-ZZ adapter protein, we proceeded to our main objective and verified the possibility of reducing the surface density of P-selectin grafted onto the b-ZZ-functionalized layer. We employed the same b-ZZ layers shown in 3.3C to graft P-selectin-Fc. The incubation conditions (incubation time, P-selectin concentration) were kept the same for all experiments.

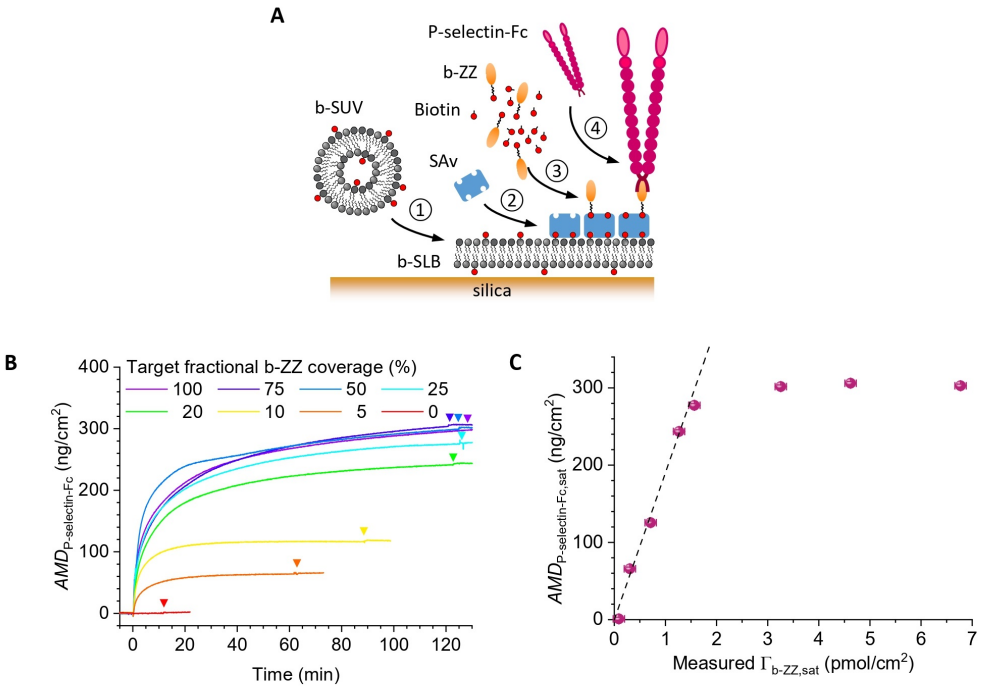

Figure 3.5: Tuning the surface density of P-selectin receptors through the surface density of b-ZZ adapter protein. A. Schematic drawing of the surface functionalisation: ① SLB formation, ② streptavidin monolayer formation, ③ co-adsorption of b-ZZ and biotin, ④ P-selectin-Fc anchorage. **B.** Areal mass density, AMD, of P-selectin over time, determined by SE for a range of fractional b-ZZ surface coverages (as indicated). Conditions: P-selectin-Fc (67 nM) was incubated at 0 min; the start of rinses with working buffer is indicated by arrowheads in matching colours. C. Areal mass density of P-selectin at saturation or after 2 hours of incubation (derived from B) as a function of the measured b-ZZ surface density (taken from Figure 3.3C). Error bars along both axes are about the size of the symbols and represent temporal noise and the effects of confidence intervals and parameter correlations when fitting the SE data for b-ZZ and P-selectin-Fc binding, respectively. The black dashed line is a linear fit through the data for $\Gamma_{b-ZZ,sat} \leq 1.5$ pmol/cm^2

The kinetics of binding of P-selectin is demonstrated in Figure 3.5A. For the small surface coverages of b-ZZ adapter protein (below 20% of maximal coverage), the surface was saturated with P-selectin within 1 hour of incubation. However, for higher surface densities, the binding dynamics of P-selectin notably slowed down after an initial rapid binding phase, and complete saturation was not achieved even after two hours of incubation. This observation is consistent with expectations since P-selectin is a relatively large protein with a molecular mass of 300 kDa. As a result, once a certain amount of protein is present on the surface, steric hindrance impedes the binding of additional molecules. No binding of P-selectin was observed on surfaces with 0% b-ZZ coverage (i.e., surfaces functionalized with pure biotin). For all other surface coverages, the

mass of bound protein remained unchanged after rinsing with HEPES buffer, indicating stable and specific binding (Fig. 3.5B).

Figure 3.5C illustrates the relationship between the maximal areal mass density of P-selectin bound to the surface and the measured surface density of b-ZZ. The first four experimental points (ranging from 0% to 20% b-ZZ coverage) exhibit a linear dependence, demonstrating the controllable tuning of P-selectin surface density for smaller surface coverages. However, for higher b-ZZ densities (>25%), the maximal bound mass of P-selectin reaches a saturation point at approximately 300 ng/cm^2. Considering a molecular mass of 300 kDa for the P-selectin-Fc construct, this corresponds to a maximal surface density of 1.0 pmol/cm^2 for the P-selectin-Fc homodimer, or approximately $\Gamma_{\mathrm{P-\ selectin,max}} \approx 2.0\mathrm{pmol/cm^2}$ for the P-selectin protomer. The transition to the plateau phase occurs at around 25% b-ZZ coverage (equivalent to 1.6 pmol/cm^2), which corresponds to an average surface area of 110 nm^2 per b-ZZ. This value aligns with the expected effective cross-section of P-selectin, taking into account that P-selectin-Fc molecules are homodimers and that P-selectin ectodomains have an elongated structure, typically measuring 40 nm in length and a few nanometers in diameter [160].

3.3.3.2 *In situ* density control under flow

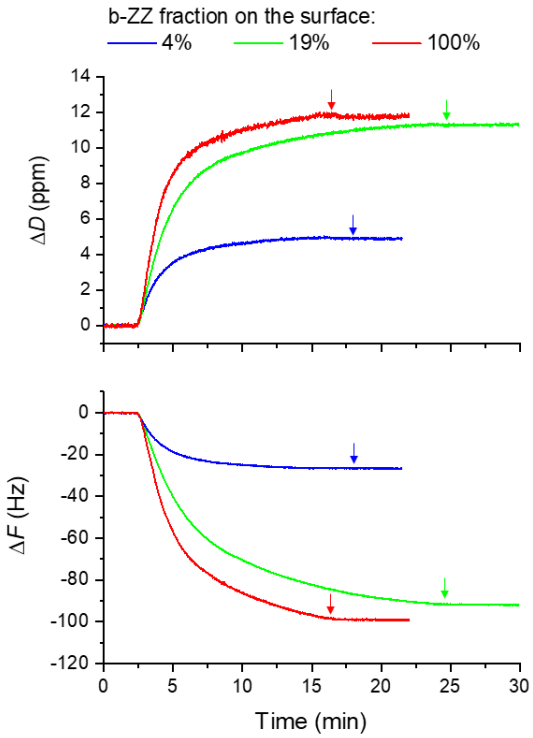

Figure 3.6: Dynamics of binding of P-selectin to the surfaces functionalized with various surface coverages of b-ZZ. The upper graph shows the dissipation changes and the bottom one – the frequency changes (i = 5) for three different surface densities of b-ZZ. The surface coverages of b-ZZ are expressed as the fraction of the maximal density, where at 100% all the biotin-binding sites are occupied with b-ZZ ($\Gamma_{\mathrm{as}} = 6.8 \pm 0.1\mathrm{pmol/cm^2}$). The incubation with P-selectin starts at 2.5 min, the arrows show the end of the incubation process. Conditions: P-selectin concentration: $33.3\mu\mathrm{M}(10\mu\mathrm{g/mL})$ in HEPES buffer, flow rate: 20 μL/min.

To confirm our ability to effectively adjust the density of P-selectin within the microfluidic channel, we conducted an additional series of experiments. We employed the QCM-D method to validate the modulation of P-selectin surface coverage under flow conditions. Although this was an expected outcome based on the b-ZZ data demonstrated previously, we wanted to confirm

that reducing the density of b-ZZ adapter protein at the surface would indeed result in a smaller QCM-D response for P-selectin. Since we have already extensively studied the controlled surface density of b-ZZ in both stagnant and flow conditions, our focus was not on quantifying the bound mass of P-selectin, but rather on obtaining qualitative evidence that our concept was functioning as intended. Due to the complexity and resource requirements of the combined QCM-D/SE technique, we chose to rely on conventional QCM-D measurements and assess the change in P-selectin binding qualitatively.

Figure 3.6 illustrates the binding dynamics of P-selectin to the surface functionalized with the b-ZZ adapter protein at various fractions of maximal surface coverage (ranging from 4% to 100%). Similar to the case in stagnant solution, even at a relatively low surface coverage (19%), the surface was already saturated with P-selectin. Another notable observation from the graph is that the binding of P-selectin is highly dependent on the incubation time, indicating kinetic limitations rather than limitations imposed by the number of available binding sites on the surface. These QCM-D experiments confirmed the successful modulation of P-selectin density under flow conditions.

3.3.3.3 Method for quantifying the density of receptor at the functionalized surface

In the previous discussion, we explored experimental approaches to effectively control the density of P-selectin using *in situ* observation methods like SE and QCM-D. However, when creating biomolecular layers in the microfluidic channel, it is practical to employ post-characterization techniques to determine the number of bound receptors. To this end, we developed a procedure to fluorescently label P-selectin bound to the surface. Similarly to the example with b-FITC (Fig. 3.2), we employed fluorescence microscopy to quantify the relative surface coverage of P-selectin.

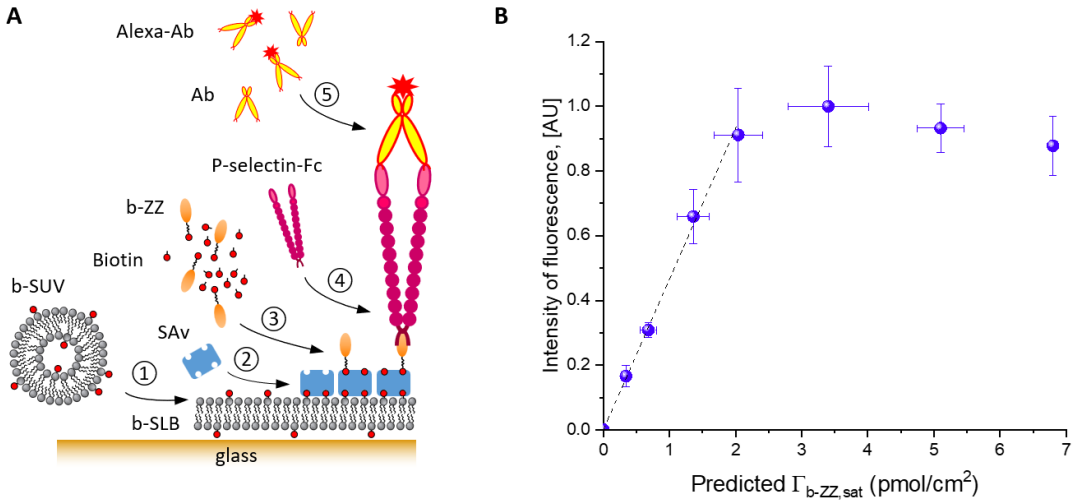

Figure 3.7: P-selectin density control quantified with the help of confocal microscopy. A. Schematic drawing of the surface functionalization: ① SLB formation,② streptavidin monolayer formation, ③ co-adsorption of b-ZZ and biotin, ④ P-selectin-Fc anchorage, ⑤ P-selectin staining with the mix of fluorescent (Alexa) and non-fluorescent antibodies. **B.** Normalized fluorescence intensity measured with confocal microscopy for surfaces functionalized with different surface densities of b-ZZ (and, subsequently, P-selectin). The horizontal axis shows the predicted $\Gamma_{b-ZZ,sat}$ calculated with the use of the Eq. 3.5 The black dashed line is a linear fit for the low surface densities of P-selectin (3.1 pmol/cm^2).

For convenience, we conducted the experiments in a well-controlled system suitable for observation under a confocal microscope. The system consisted of round 50 µL wells with Teflon walls and glass bottoms. Prior to confocal measurements, multiple wells were functionalized simultaneously, aiming for different b-ZZ surface coverage obtained with the use of the Eq. 3.5.

At the end of the functionalization, P-selectin layers with varying surface densities were stained using P-selectin specific antibodies (Fig. 3.7A). Here, Alexa-647-labelled antibodies were mixed with non-labelled antibodies of the same clone to enable accurate quantitative detection of the fluorescent signal. Further information on the methodologies for quantifying fluorescence intensity can be found in the section Appendix A.

Figure 3.7B presents the fluorescent signal obtained from eight surfaces with b-ZZ coverages ranging from 0% to 100% of the maximal density. The fluorescence intensity exhibited a linear increase for low surface densities (up to 30%, or 2.0 pmol/cm^2), similar to what was observed in the SE experiment (Fig. 3.7C). However, at higher densities, a plateau phase became evident, indicating surface saturation with P-selectin.

Subsequently, a calibration curve shown in Fig. 3.7B was used for assessing the surface density of P-selectin in microfluidic channels.

3.3.4 Reduced surface density of P-selectin grafted together with the HA brush

Finally, we created a complex layer presenting both HA brush and P-selectin (as described in Section 2.2.5) and measured the intensity of fluorescence of grafted P-selectin. The aim of this study was to check if our strategy for reducing the density of surface-grafted receptors remains valid for more complex cases when the available biotin-binding sites are partially occupied by b-HA chains. A layer similar to the one described in section 3.3.3.3 was created with the only difference that HA brush was formed before the start of the co-adsorption of b-ZZ and biotin (Fig. 3.8A). The surface density of the anchor sites was considered $\Gamma_{as} = 6.8 \pm 0.1 \text{pmol/cm}^2$, same as described above.

We chose 4 different combinations of HA brushes and P-selectin surface coverages:

- b-HA-280 + P-selectin at its maximal surface coverage;
- b-HA-58 + P-selectin of 10% of its maximal surface coverage;
- b-HA-280 + P-selectin of 10% of its maximal surface coverage;
- b-HA-840 + P-selectin of 10% of its maximal surface coverage.

The choice of the fractional density of P-selectin was driven by prior findings, which established that P-selectin, when grafted independently, could achieve binding equilibrium within one hour on layers presenting b-ZZ at 10% of its maximum surface coverage. Therefore, when P-selectin is co-grafted alongside an HA brush, we anticipated that it would also bind to available b-ZZ sites within a comparable timeframe. We employed HA brushes with varying mechanical properties to compare P-selectin binding efficiency under different conditions.

Figure 3.8B presents the intensity of fluorescence measured from P-selectin grafted on the surfaces presenting HA-58 (purple sphere), HA-280 (violet spheres) and HA-840 (green sphere) compared to the intensity of fluorescence of P-selectin grafted alone (blue spheres, same data as in Fig. 3.7B).

Notably, the fluorescence intensity measured from P-selectin co-presented with the HA-840 brush aligns with the established calibration curve for P-selectin only. This conclusion is substantiated by our previous findings shown in Section 2.2.3.1, where the average spacing between HA-840 chains was approximately 70 nm, while the distance between biotin-binding sites on the dense SAv layer was about 4.5 nm. Consequently, the presence of the HA-840 brush does not obstruct b-ZZ binding to the layer, and the difference in the ultimate number of available b-ZZ sites between layers with and without HA-840 is negligible.

In contrast, the fluorescence intensity of P-selectin diminishes by approximately 2-fold when co-presented with the thicker HA-280 brush (as shown in Fig. 3.8C). One obvious explanation would be the difference in the maximal number of accessible biotin-binding sites. As demonstrated

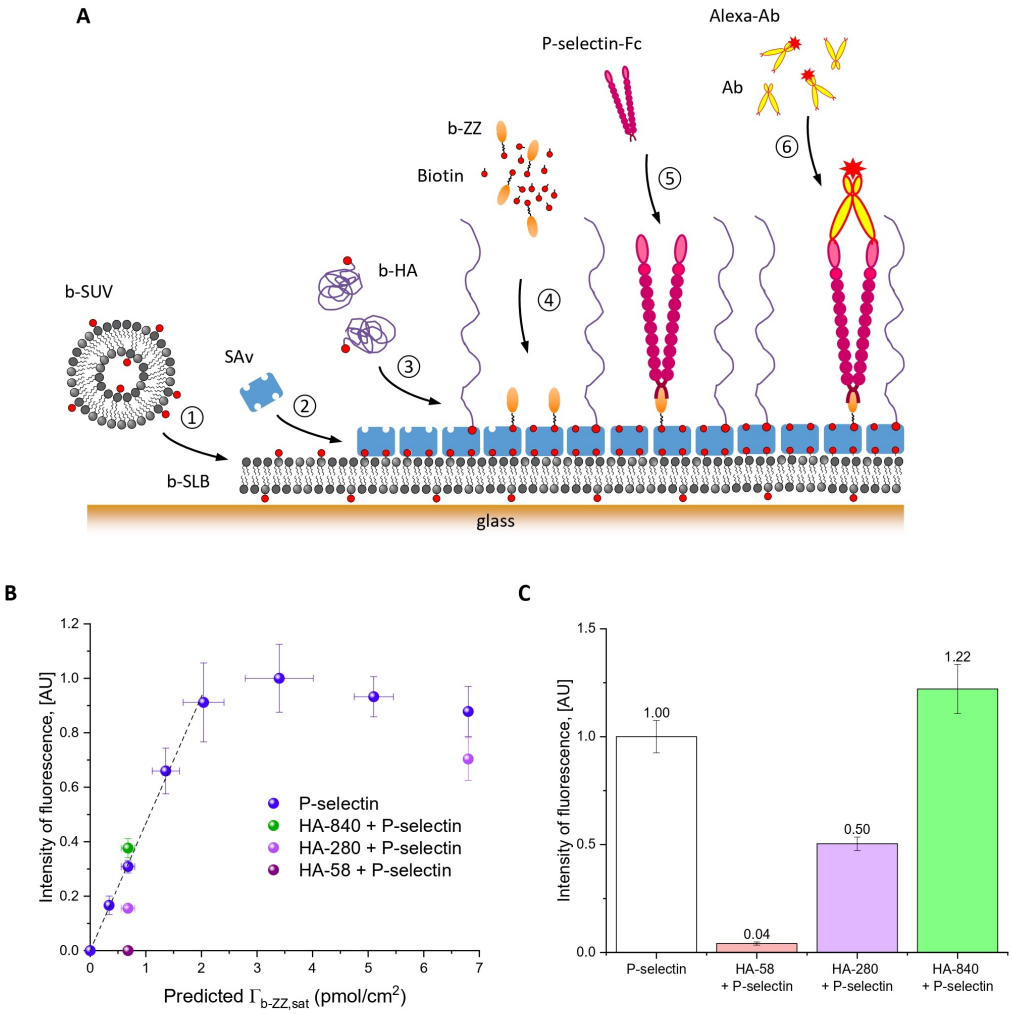

Figure 3.8: Complex molecular layers presenting both HA brush and P-selectin with reduced surface density. A. Schematic drawing of the surface functionalization: ① SLB formation, ② streptavidin monolayer formation, ③ HA brush formation, ④ co-adsorption of b-ZZ and biotin, ⑤ P-selectin-Fc anchorage, ⑥ P-selectin staining with the mix of fluorescent (Alexa) and non-fluorescent antibodies. **B.** Normalized fluorescence intensity measured with confocal microscopy for surfaces functionalized with either P-selectin alone, or P-selectin and HA brushes. Blue spheres represent intensities of fluorescence measured from the surfaces functionalized with P-selectin (repeating the data presented in Fig. 3.7B). Green, violet and purple spheres demonstrate the fluorescent signal measured from the surfaces co-presenting HA brushes of different types and P-selectin (either at the maximal or reduced surface density). **C.** Comparison between the fluorescent signal measured for the surfaces with reduced surface density of P-selectin (10% of the max coverage) either alone or co-presented with different types of HA brushes. Conditions: c(b-HA-840) = 23.8 nM (20 µg/mL), incubation time: 15h; c(b-HA-280) = 71.4 nM (20 µg/mL), incubation time: 15h; c(b-HA-58) = 86 nM (5 µg/mL), incubation time: 15h. All 3 HA brushes were incubated in low-pH buffer. C(P-selectin) = 66.7 nM(20 µg/mL, incubation time: 1h, c(P-selectin Ab) = 5 µg/mL, incubation time: 1h.

in Section 2.2.3.1, dense HA-280 brush has an average intermolecular distance of 22 nm, meaning that about 10% of all the biotin-binding sites would be inaccessible for b-ZZ binding. Although such difference would affect the final surface coverage of P-selectin, but it would not account for a 50% decrease in fluorescence intensity. Consequently, additional factors must contribute to the reduced efficiency of P-selectin binding, such as differing binding kinetics due to the rigidity of the HA brush. As a result, the actual surface density of P-selectin, as deduced from the calibration curve in Figure 3.7B, corresponds to roughly 5% of the maximum b-ZZ surface coverage.

A similar situation was observed for P-selectin co-presented with a stiff and dense HA-58 brush. Here, the fluorescence signal intensity from the grafted P-selectin layer was over 25 times smaller than that of independently anchored P-selectin grafted alone under identical conditions. As per the calibration curve, the actual surface density of anchored P-selectin corresponds to less than 1% of the maximal surface density of b-ZZ.

This dataset demonstrates that the control of receptors in presence of HA brush is much more complex than that for P-selectin anchored alone, influenced not only by the number of the available binding sites, but also on the kinetics of binding of the protein to the surface. In order to create the biomolecular layer with the predicted density of the receptors, a separate calibration curves for each type of brushes is required. Our assumption is that our theoretical predictions still hold for the b-ZZ/biotin co-adsorbtion (yet the number of available binding sites Γ_{as} needs to be recalculated according to the type of the HA brush), but the dynamics of binding of P-selectin and P-selectin antibodies is likely affected by presence of thick HA layer at the surface.

3.4 Discussion

This chapter presented a novel approach to quantitatively tune the surface density of biotinylated receptors on SAv-coated support. In the framework of my project, this study was essential to mimic the biologically relevant distance between P-selectin receptors. However, the described theoretical considerations can become a versatile tool for a range of applications.

In short, the guideline to control the surface density of anchored receptors includes the following steps:

1. Define the total number of the available binding sites at the surface.

2. Check that the chosen co-adsorbing species and the experimental conditions meet requirements 1-4 for the validity of the theory.

3. Using equations 3.5 for stagnant conditions or 3.8 for flow conditions define the concentrations of the binding species to get the desired density of receptors at the surface.

Importantly, the presented method for controlling the surface density under flow or in still conditions can be extended to anchors other than biotin, as long as their binding rates are sufficiently high to ensure the mass-transport limited binding. As an example, the binding rates in the range of $10^5 M^{-1}\ s^{-1}$ have been reported for nickel chelation of polyhistidine tags [86], as well as for IgG binding to protein A or protein G [132]. In the case of DNA hybridization, the intrinsic binding rate can also reach values as high as $10^5 \ldots 10^6 M^{-1}\ s^{-1}$. Thus, while ensuring that ε values are kept sufficiently small, these anchors can be used in our model of competitive binding. This significantly increases the number of possible applications for our novel method.

An additional potential application of this study is the quantification of contamination in a solution of anchor-tagged molecules due to the presence of free anchor reactants. In our recent work [82] we provided a comprehensive description of the quantification process for biotinylated

glycosaminoglycans (GAGs), including the assessment of contamination caused by free biotin reactants in the eluate fractions. As demonstrated in section 3.3.4, our method has limitations when designing the surfaces that are already presenting a thick layer of glycosaminoglycans. Going forward, a more thorough study is required to assess how the presence of HA brush influence binding of the co-adsorbing species.

3.5 Conclusion

In conclusion, our newly designed approach allows to create the molecular layers with well-defined density of receptors of interest. Due to its simplicity, this tool can be used in variety of applications to tune the surface concentrations of the receptors of interest.

4

Microbeads presenting the ligands for glycocalyx and for cell surface receptors

Short summary

Aiming to mimic circulating white blood cells for studying their interaction with glycocalyx models *in vitro,* I have established a protocol for the functionalization of polystyrene microbeads with two specific receptors: CD44, which binds to the HA brush representing the glycocalyx model, and PSGL-1, serving as a ligand for the cell surface receptor P-selectin. A new method demonstrates precise control over the density of these receptors on the bead surface. Furthermore, a new protocol allows the simultaneous grafting of two distinct receptors of interest onto the bead surfaces at desired surface fractions.

Acknowledgements

All the experiments presented in this chapter were designed, performed and analyzed by myself. However, I would like to acknowledge Clément Lassagne, an M1 student under my supervision, for conducting numerous preliminary tests that were instrumental in the development of the effective protocols for bead functionalization.

Contents

4.1 Introduction

While developing a well-controlled system to investigate cell-glycocalyx interactions, one of our goals was to mimic the circulating cells bearing specific surface receptors tailored for interactions with receptors located in glycocalyx. This involved designing cell-sized microbeads as cell mimetics with two receptor types: CD44 for interacting with HA chains in the dense HA brush, and PSGL-1 as a ligand for the concealed P-selectin receptor beneath the HA brush. Our aim was to ensure stable presentation of these receptors on the microbeads and the ability to control their density.

4.1.1 Microbeads as cell mimetics

Microbeads and nanobeads find diverse applications in the field of biomedicine. Typically varying in diameter from 50 nm to 2 mm [58], they can be composed of different materials such as glass [85], polymers [47], ceramics [16], or porous biocompatible materials [65]. Due to their versatility, microspheres are widely used in targeted drug delivery [81], diagnosis of cancer [173] and other diseases, blood purification [46], and more.

Table 4.1: Benefits and limitations of employing microbeads as mimetics for circulating cells in *in vitro* flow assays

Benefits	Limitations
1. *Focused study of one or several receptors of interest.* Functionalized microbeads enable an isolated investigation of specific receptor pairs, allowing a detailed understanding of their role in cell adhesion.	1. *Mismatching mechanical properties.* Some mechanical properties (density, rigidity, shape) of microbeads may not precisely match those of living cells, potentially leading to variations in behavior, especially in confined environments. However, this characteristic can also be viewed as advantageous, when the goal is to differentiate between the impacts of surface density and bead mechanics on adhesions, comparing the behavior of rigid and soft spheres can be beneficial.
2. *Control over surface receptor density.* Similarly to cell surface models created on planar surfaces, the surface density of the receptor can be adjusted on beads (within the physiologically relevant range and beyond), facilitating the study of density effects.	
3. *Enhanced experimental robustness.* Functionalized microbeads exhibit robustness to fluctuations in temperature, medium composition, light, and mechanical disturbances, reducing experimental sensitivities.	
4. *Facilitated bead height measurement*. The perfectly round shape of microbeads simplifies height measurements in flow assays, particularly when employing reflection interference contrast microscopy (see RICM section for details).	

Microbeads can also function as biomimetic models in *in vitro* studies. For instance, functionalized synthetic microbeads have been employed as simplified bacterial models in adhesion studies under flow conditions [106]. In another study, functionalized streptavidin-coated microspheres served as mimetics for leukocytes in flow assays aimed at investigating leukocyte interac-

tions with selectins [168]. The wide range of microbead sizes, including those comparable to cell sizes, and their extensive potential for functionalization render them an excellent model system for investigating biological interactions *in vitro*. This includes their utility as mimics for circulating blood cells [2]. In one of the published works the microspheres functionalized with the selectin ligand sialyl Lewis X, were used as leukocyte mimics to study the leukocyte arrest at the endothelium [121].

Table 4.1 provides a comparison of the benefits and limitations of microspheres as a model system in cell adhesion assays, as opposed to employing living blood cells for the same purpose.

4.1.2 Microbeads as molecular model of white blood cells

Numerous methods are available for the functionalization of synthetic microbeads, including chemical coupling of functional chloride groups [170], thiol-end functionalization [54] and covalent coupling of proteins and nucleic acids [96]. Additionally, there are many commercially available types of microspheres coupled with biotin, avidin, streptavidin, protein A and other anchoring compounds. The presence of these universally used proteins on the microsphere surface allows for simple and straightforward functionalization with a diverse range of receptors of interest.

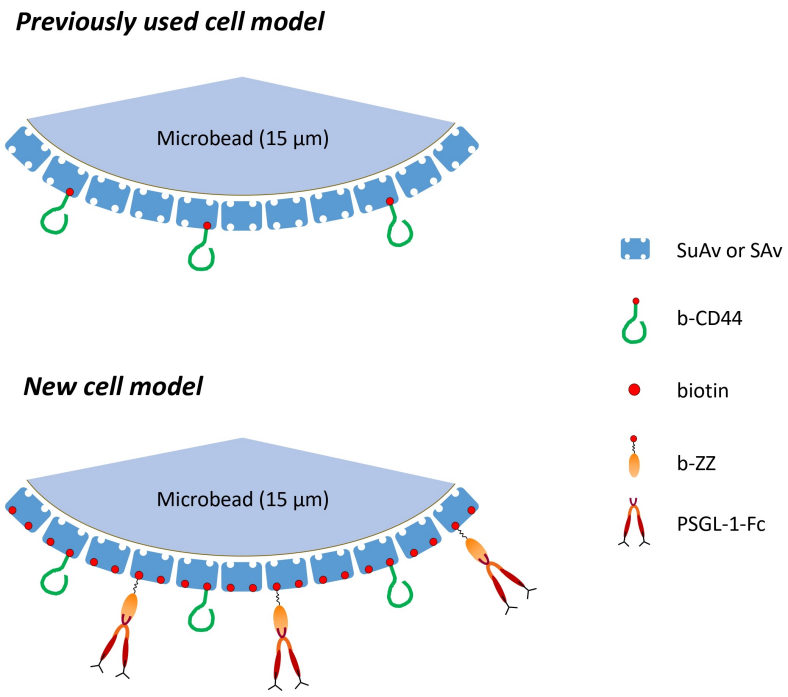

Figure 4.1: Schematic drawing of previously used [33] and new molecular models of white blood cells. SuAv/SAv molecules are covalently linked to the bead surface and drawn in ordered arrangement for simplicity, while in reality their orientation remains unknown. All molecules are drawn approximately to scale.

In the study preceding my project [33], microspheres with a diameter of 15 µm, purchased from Bangs Lab and coated with SuperAvidin (SuAv) were employed. The size of these beads matched the average size of white blood cells (10-20 µm [144]. SuperAvidin is a proprietary molecule from Bangs Lab supposed to provide a superior binding affinity to biotin compared to streptavidin, while also exhibiting lower levels of non-specific binding. In the initial stages of my experiments, I employed SuAv-coated beads. However, due to an unexpected binding behavior

exhibited by these beads during subsequent tests, I transitioned to SAv-coated microspheres of equivalent diameter (further details regarding bead selection will be discussed in Section 4.3.1). Additionally, modifications were made to the functionalization strategy.

Figure 4.1 schematically shows a previously employed blood cell mimetic and the complexified model I have developed. In the previous model, microbeads presented only one receptor, CD44, on their surface. This design allowed to investigate the role of CD44-HA interactions in cell capture under flow conditions. In our current study, we aim to broaden our understanding of the adhesion process by introducing another surface receptor, PSGL-1, which can interact with P-selectin located beneath the thick HA brush within the molecular glycocalyx model.

Another significant distinction between the old and new models lies in the method of controlling the surface concentration of receptors of interest. In the previous model, the density of CD44 receptors was regulated by the total number of molecules in solution during the incubation step. This depletion-based approach proved highly sensitive to variations in the number of microbeads in solution and the CD44 concentration. As a consequence of variations in the number of beads in the solution, which, in turn, is influenced by the precise manipulation procedure, the detected fluorescence intensity from beads functionalized using the same protocol could vary by as much as tenfold between experiments. In our new model, we adopt a different approach to control the surface receptor concentration. Biotinylated receptors are co-adsorbed with free biotin in a defined molar ratio, employing similar strategies as detailed in Chapter 3. This method is independent of the precise number of beads in solution and provides a more robust approach to bead functionalization. The ultimate surface density of the proteins is solely determined by the concentration ratio of the three species (two biotinylated receptors and free biotin) in the solution. Further details on the co-adsorption of three biotinylated species will be provided in Section 4.3.3.

In both the old and new models, biotinylated CD44 receptors are directly coupled to SuperAvidin or streptavidin-coated microbeads. However, as there is no commercially available and reliable biotinylated PSGL-1 receptor, attaching the PSGL-1-Fc receptor necessitates the use of a b-ZZ adapter protein, following a similar approach as described for surface functionalization with P-selectin-Fc in Chapter 2. This introduces an additional incubation step in the bead functionalization process.

4.1.3 Assessment of microbead functionalization quality

To evaluate the quality of microbead functionalization, we established a robust experimental procedure. Flow cytometry, a widely adopted technique for quantifying the fluorescent intensity of cells, and by extension functionalized microbeads [51, 161], was employed. This method offers the benefit of rapidly assessing a large number of beads, readily generating statistics based on several thousand beads.

To quantitate the surface density of receptors on the functionalized beads using flow cytometry, a series of steps is necessary. First, the beads must be stained with fluorescently labeled antibodies, and calibration curves (covering a range of surface densities) must be established for each receptor of interest. Subsequently, to determine the surface density quantitatively, the fluorescent signal measured from the bead sample with the receptor of interest is compared to the corresponding calibration curve. To ensure reliable fluorescent measurements, it is essential to take specific precautions. This includes maintaining laser stability consistently throughout various experiments and eliminating the fluorescence quenching effect (which leads to a reduction in the intensity of fluorescence in individual fluorophores due to their proximity to each other). More detailed information on this can be found in "Quantification of receptor surface density through fluorescence analysis" section in Appendix A.

In cases where a bead is functionalized with two types of receptors (here, CD44 and PSGL-1), two distinct antibodies labelled with fluorophores must be used (this will be described in detail in Section 4.3.3). The fluorescence intensity of each type of antibody should be measured separately

and then compared to the pre-established calibration curves corresponding to each receptor.

Furthermore, flow cytometry also enables the evaluation of the size and shape distributions of the microbeads within the sample. Figure B.6 illustrates an instance of measuring bead forward scatter (FSC), offering insights into the relative distribution of object size, and side scatter (SSC), which provides information about granularity in the context of living cells or surface roughness in the case of polystyrene microbeads. Consequently, flow cytometry not only allows for the quantitative evaluation of receptor surface densities but also provides a qualitative assessment of bead size distribution and surface quality.

4.1.4 Principles of bead functionalization

While bead functionalization is a common practice across various applications, it is not a straightforward procedure and demands specific practical precautions that diverge from planar surface functionalization protocols. A primary objective when functionalizing beads is to achieve a uniform surface coverage of receptors on a batch of beads, ensuring even distribution across the entire bead surface, as well as across the pool of beads. One significant challenge in bead functionalization involves determining the appropriate incubation concentration, which must account for the number of beads in the sample and, consequently, the number of accessible binding sites. Another challenge pertains to the washing procedure, which beads must undergo both before functionalization and after each of the incubation steps. Throughout the course of my project, I have developed a new protocol for bead functionalization with one or more receptors of interest. This protocol is presented in detail in Supplementary information. Briefly, the bead functionalization procedure includes the following steps:

1. Determine the necessary quantity of beads for functionalization and compute the appropriate reagent concentration to occupy all available binding sites on the bead surface.
2. Perform a preliminary bead wash using HEPES buffer.
3. Introduce the requisite reagent to achieve the desired functionalization concentration.
4. Incubate the beads on an Eppendorf shaker.
5. Conduct a bead wash in HEPES buffer to remove any excess reagent.

4.2 Theoretical considerations for co-adsorption of biotinylated species on microbeads

As previously discussed, the method for regulating the density of biotinylated receptors by co-adsorbing them with free biotin was developed to provide more dependable means of controlling the number of receptors on the surface compared to the depletion-controlled approach. Chapter 3 extensively covered the theory behind the co-adsorption of two or more biotinylated species on planar surfaces. In this section, I will focus on applying these theoretical concepts to spherical objects (microbeads) and extend the discussion to include the co-adsorption of three distinct species. In my specific case, the approach will be tested with the b-CD44 receptor, the b-ZZ adapter protein required for PSGL-1-Fc binding, and free biotin.

4.2.1 Control of the surface density of one type of biotinylated receptor

We can extend the principles of co-adsorption for multiple biotinylated species, previously discussed in the context of planar surfaces, to spherical surfaces. This extension remains valid as long as the streptavidin or SuperAvidin coating on the beads forms a homogeneous coverage, same as on the planar surfaces. The average distance between biotin-binding sites on the microbeads was determined to be approximately 5 nm (please refer to microbeads functionalization protocol for the calculations), which is comparable to the average spacing between binding sites on a densely packed SLB-based SAv monolayer – 4.5 nm [108]. Therefore, both systems are expected to yield similar results concerning the binding capacity for biotinylated species. At the scale of the distance between biotin-binding sites (a few nanometers), the spherical shape of the beads (bead curvature – several micrometers) can be considered locally flat.

However, several additional assumptions are necessary:

1. The incubation of the beads on the Eppendorf shaker is considered to occur under "flow conditions", drawing from the analysis of the similarities between stirring and flow conditions presented by Hermens et al [60].

2. It is assumed that SuperAvidin behaves similarly to streptavidin in terms of adsorbing biotinylated species, having the same affinity for both free biotin and biotinylated proteins.

3. Given that the bead functionalization process cannot rely on an unlimited supply of binding molecules due to high reagent consumption, we make the assumption that having 4-5 times more molecules than available binding sites represents an adequate compromise between reagent consumption and the validity of our theoretical framework.

Based on these considerations, we hypothesize that the Equation 3.8 for competitive binding under flow conditions can be applied to describe the co-adsorption of biotinylated species on the bead surface:

$$\frac{c_2}{c_1} = \left(\frac{R_2}{R_1}\right)^{2/3} \left(\frac{\Gamma_{as}}{\Gamma_{1,sat}} - 1\right) \tag{4.1}$$

where c_1, c_2 – concentrations of the molecule of interest (c_1) and the inert molecule (c_2), R_1 and R_2 – their respective hydrodynamic radii, Γ_{as} – total molar density of anchorage sites on the surface, $\Gamma_{1,sat}$ – surface density of the functional molecule.

4.2.2 Dual functionalization of beads: control of the surface density of two biotinylated receptors

The co-adsorption method initially designed for two binders can be readily extended to three species, specifically two biotinylated molecules and free biotin. Given the assumptions mentioned earlier, we anticipate that this theoretical framework can be effectively applied to microbead functionalization. To establish the concentrations of these binding species, we can derive the following ratio from Eq 4.1:

$$\frac{\Gamma_i}{\Gamma_j} = \left(\frac{R_j}{R_i}\right)^{\frac{2}{3}} \frac{c_i}{c_j} \tag{4.2}$$

Hence, by selecting an arbitrary concentration for one of the binding species, we can calculate the concentrations of the other two. However, it is important to note that the total concentration $\left(c_{tot} = c_i + c_j + c_k\right)$ must be sufficiently high to ensure that the assumption 4 is satisfied.

We selected a fixed concentration of 200 nM for b-CD44 due to its limited availability, as it was produced by our collaborators [8] and is not commercially accessible. Then, the concentrations of

biotin and b-ZZ were calculated as follows:

$$c_{b-ZZ} = c_{b-CD44} \left(\frac{R_{b-ZZ}}{R_{b-CD44}} \right)^{\frac{2}{3}} \frac{\Gamma_{b-ZZ}}{\Gamma_{b-CD44}} \tag{4.3}$$

$$c_{biotin} = c_{b-CD44} \left(\frac{R_{biotin}}{R_{b-CD44}} \right)^{\frac{2}{3}} \frac{\Gamma_{biotin}}{\Gamma_{b-CD44}} \tag{4.4}$$

4.3 Results

4.3.1 Validating the theory of co-adsorption of biotinylated species on microbeads

To validate the applicability of the theory of co-adsorption of two binding species in the context of microbead functionalization, we functionalize the microbeads with a biotinylated fluorophore, b-FITC, using the same procedure as outlined in Section 3.3.1 for planar surfaces. Our objective was to confirm that the fluorescence intensity observed from these beads, functionalized with biotinylated fluorophores at various surface densities, exhibited a linear relationship with the predicted surface coverage of the fluorophore. To ensure that the intensity of fluorescence was proportional to the fraction of the fluorophore at the surface and to mitigate the influence of quenching effects, the fluorophore solution was pre-bleached pre-bleached sufficiently to avoid quenching (see Appendix A for details).

This section presents a comparative analysis of b-FITC functionalization of SuAv-coated polystyrene beads from Bangs Laboratories and SAv-coated polystyrene beads from Spherotech. We will see that SuAv-coated beads show an unusual behavior, which was a major reason to consider SAv-coated beads for future work.

The experimental procedure for bead functionalization consisted of an initial washing step in HEPES buffer, followed by incubation with a mixture of b-FITC and free biotin (Fig. 4.2A) at molar ratios defined by Eq. 4.1. Since the exact density of biotin-binding sites on both types of beads remained unknown and could only be estimated empirically, we expressed the desired surface densities of b-FITC as a percentage of the maximum surface coverage. Both types of beads were functionalized to achieve surface coverages of 0% (biotin only), 20%, 40%, 60%, 80%, and 100% (b-FITC only) of fluorophore, and the resulting fluorescence intensity per bead was quantified using flow cytometry (Fig. 4.2B-C). Both types of beads exhibited consistent functionalization homogeneity, with all measured samples displaying an approximately Gaussian distribution of approximately constant width of fluorescent signal. This indicated that the majority of beads in each sample adsorbed a similar amount of b-FITC onto their surfaces.

However, the total fluorescence signal obtained from Bangs Lab and Spherotech beads, both functionalized to achieve the same fractional surface density of b-FITC, exhibited significant differences (Fig. 4.2D). Specifically, Bangs Lab beads demonstrated a 2.2-fold lower efficiency in binding at the maximum b-FITC coverage compared to Spherotech beads. Bangs Lab beads also displayed a higher level of background noise (as observed in the 0% b-FITC sample) in contrast to Spherotech beads.

More importantly, Bangs Lab beads exhibited an intriguing pattern: in intermediate mixtures, there was a lower amount of b-FITC than anticipated when compared to the maximal coverage. This unexpected behavior resulted in a pronounced superlinear trend in the relationship between the fluorescent signal and the quantity of bound b-FITC (Fig. 4.2E). In contrast, Spherotech beads exhibited a closer-to-linear dependence (violet dashed line in Fig. 4.2E). This observation, coupled with the generally more consistent bead size and fluorescent signal distribution within individual

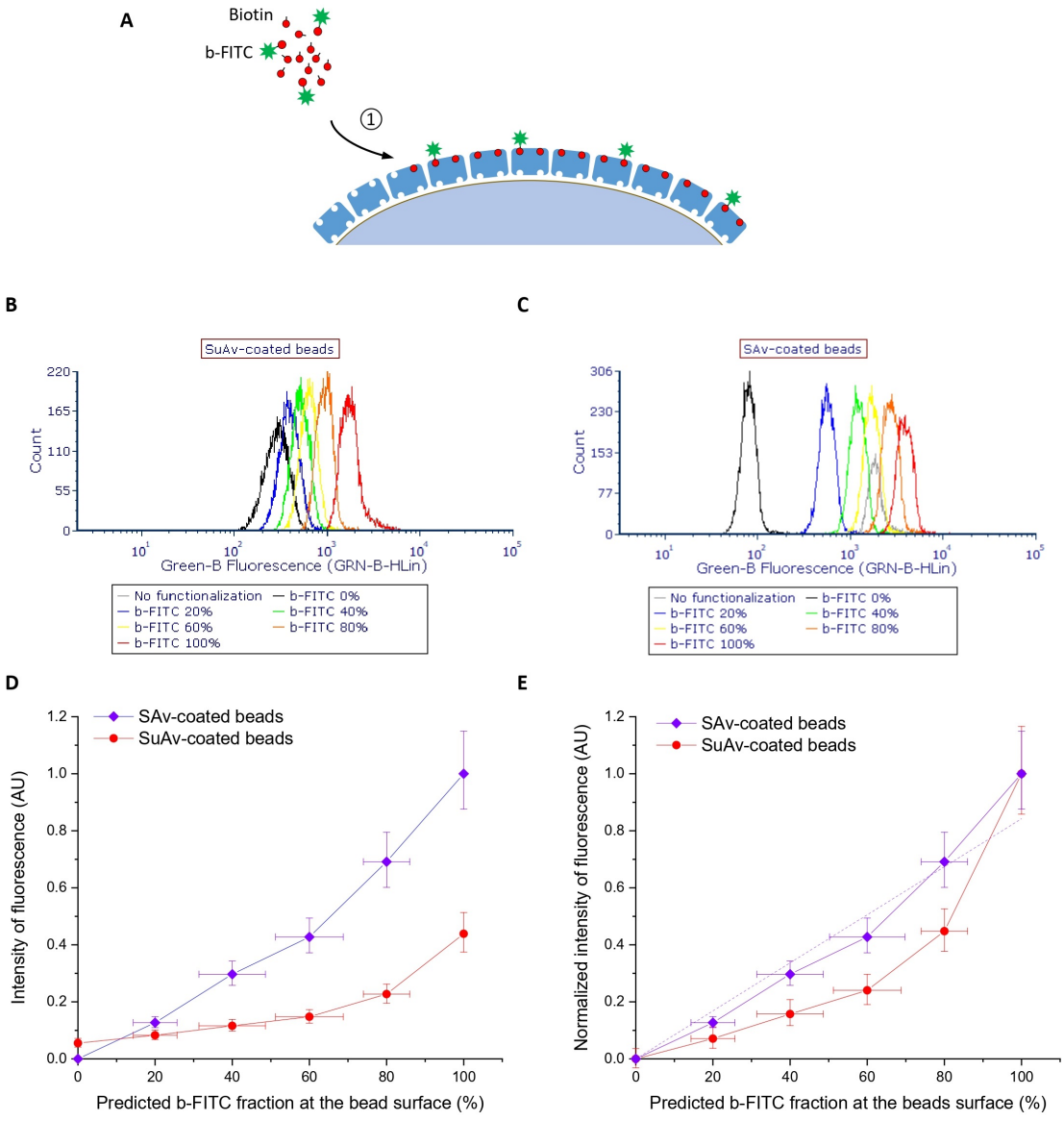

Figure 4.2: Microbeads functionalized with b-FITC. A. Schematic drawing of bead functionalization with b-FITC: ① co-adsorption of b-FITC with biotin. **B-C.** Fluorescence histograms obtained by flow cytometry for microbeads with different target surface fractions of b-FITC (SuAv-coated beads – **B**, SAv-coated beads – **C**). **D-E.** Fluorescence intensity for non-functionalized beads and beads presenting different target surface fractions of b-FITC (**D** – comparison of fluorescence intensity between two types of beads, **E** – fluorescent signal with subtracted background and normalized by the values at 100% for curve shape comparison). Dashed violet line in **E** is a linear fit for SAv-coated beads curve (slope: 0.0084 ± 0.0008), show to demonstrate close-to linear trend for SAv-coated beads. Conditions: bead concentration: 0.5% *w/v*, $c_{\mathrm{b-FITC}} + c_{\mathrm{biotin}}$ = 14 M was maintained constant, functionalization time: 1 hour. Statistics for the flow cytometry data was taken on at least 10000 events. The horizontal axis shows the fractional surface coverage of fluorophore predicted according to Eq. 4.1. Data points represent the median of detected events, with error bars along the vertical axis indicating the interquartile range (75th and 25th percentiles), and error bars along the horizontal axis representing uncertainty in b-FITC and biotin concentrations.

samples for Spherotech beads (see Fig. B.6 in the Supplementary Information), led us to select Spherotech beads for continued use in our functionalization experiments.

The reason for the non-linearity observed in the relationship between fluorescence signal and the surface density of adsorbed b-FITC, particularly evident in Bangs Lab beads, remains a subject of uncertainty. Clearly, the above-proposed theory does not fully describe the competitive binding process. What could be the reason for the discrepancy? Our hypothesis centers on the possibility that the random orientation of SuAv/SAv molecules at the bead surface may be responsible.

Bangs Laboratories and Spherotech beads feature the covalent linkage of SuperAvidin and streptavidin, respectively, to their surfaces. The precise orientation of these proteins remains undisclosed, and it is possible that molecules are presented in a range of orientations, leaving us uncertain about the number of biotin-binding sites exposed to the solution. This unpredictable orientation has the potential to obstruct the binding of large biotinylated molecules due to steric hindrance, rendering free biotin a more favorable option for binding to the bead surface than biotinylated FITC. This effect is notably pronounced when dealing with SuAv-coated beads. One potential explanation for this is the potential glycosylation of SuAv (which is derived from avidin, as opposed to SAv produced by the bacterium Streptomyces avidinii), which might contribute to the steric hindrance in the binding of larger molecules.

4.3.2 Beads functionalization with one type of receptor

4.3.2.1 Beads functionalization with CD44

After selecting SAv-coated beads as our main model for mimicking living cells, we proceeded to functionalizing them with CD44 receptor. We first verified using QCM-D that the batch of CD44 that we were planning to use for the bead functionalization was binding HA in a stable and irreversible manner (Fig. B.7).

To achieve variable CD44 receptor density on the beads, we then applied the co-adsorption approach, combining b-CD44 molecules with inert free biotin (Fig. 4.3A). Subsequently, anchored CD44 molecules were labeled with CD44 IM7 antibodies, employing a mixture of Alexa-labeled antibodies and non-fluorophore antibodies at a ratio of [1:3]. This strategy was implemented to mitigate the quenching effect that can occur between neighboring antibody molecules (for details, see Appendix A).

The analysis using flow cytometry resulted in a single-peak fluorescent signal distribution for each bead sample, with the peak width comparable across different conditions (Fig. 4.3B). Notably, the signal distribution exhibited an asymmetry with an elongated tail towards higher intensities, a feature absent in beads functionalized with b-FITC. The precise cause behind the emergence of this tail remains undetermined. Some degree of non-specific binding of CD44 antibodies was observed in the biotin-only functionalized beads (black histogram in Fig. 4.3B) compared to non-functionalized beads (grey histogram), although it was relatively minor when contrasted with the specific binding of antibodies to beads functionalized with CD44 (for a quantitative assessment of non-specific binding, please refer to Fig. B.11A). The additional test revealed no non-specific binding of CD44 antibody to the bead surface (Fig. B.11A).

The calibration curve for beads functionalized with varying surface fractions of CD44 is presented in Figure 4.3C. As expected, it demonstrates an increase within the range of lower surface coverages, reaching up to 40% of the maximum CD44 surface coverage, followed by a gradual transition from a linear regime to the plateau at higher surface densities. However, some deviations from linearity observed in the initial phase of the curve require further investigation.

One plausible explanation for these deviations is that the CD44 Alexa 532-labeled antibodies utilized in this test are reported to have an average of 5-7 fluorophores linked to each antibody molecule. Consequently, such antibody types may be more susceptible to quenching effects at high surface coverages compared to, for instance, P-selectin antibodies, which are reported to have

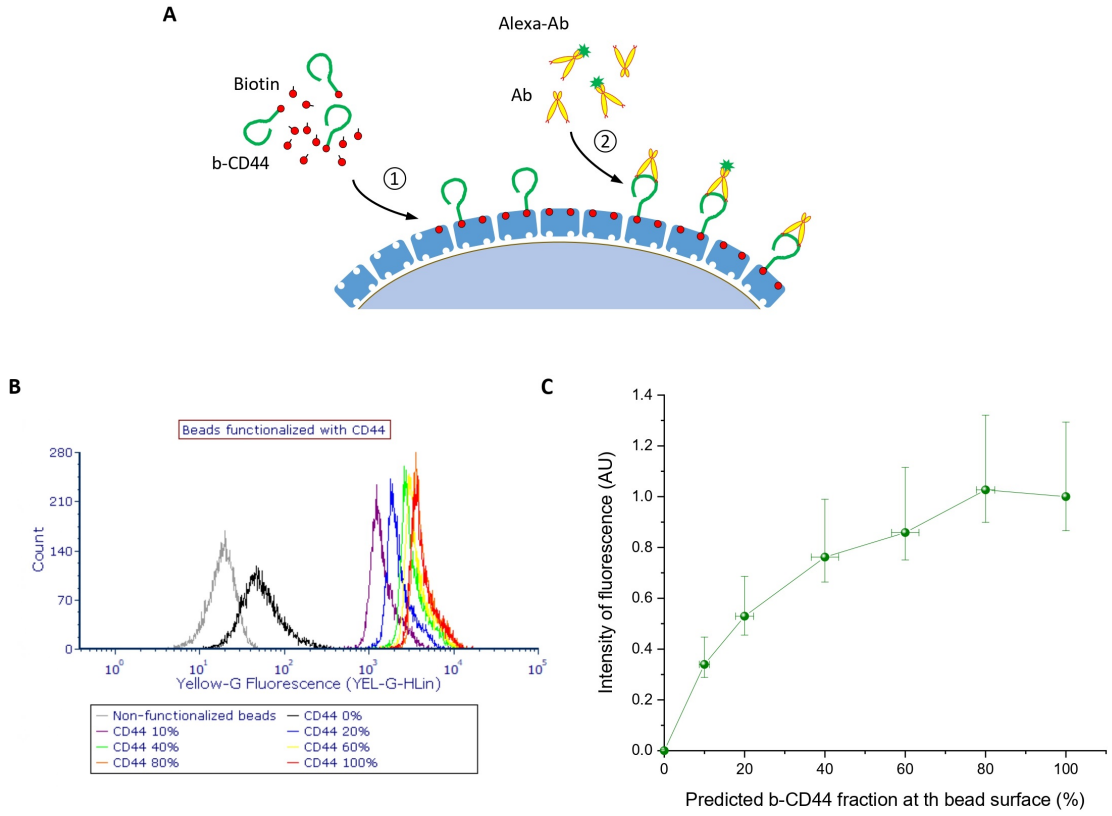

Figure 4.3: Bead functionalization with CD44 alone. A. Schematic drawing of bead functionalization with CD44: 1 co-adsorption of b-CD44 with biotin, 2 CD44 staining with the mix of fluorescent (Alexa 532) and non-fluorescent antibodies. **B.** Histograms of fluorescence intensity as measured by flow cytometry of microbeads functionalized with different CD44 target surface fractions and non-functionalized beads. Statistics for the flow cytometry data was taken on at least 10000 events. **C.** Intensity of fluorescence measured from the beads presenting different fraction of b-CD44 at their surface (with background subtracted). Data points represent the median of detected events, with error bars along the vertical axis indicating the interquartile range (75th and 25th percentiles), and error bars along the horizontal axis representing uncertainty in b-FITC and biotin concentrations. Functionalization conditions: bead concentration: 0.25% *w/v*, $c_{\mathrm{b-CD44}} + c_{\mathrm{biotin}}$ = 700 nM was maintained constant, incubation time: 2 hours. Antibody staining conditions: Alexa 532-labelled and non-labelled antibodies were mixed in a molar ratio of 1:3, total concentration: 10 µg/mL, incubation time: 2 hours.

only 1 fluorophore per antibody molecule. To confirm this hypothesis, conducting an additional test employing a different type of CD44 antibody would be advantageous.

Irrespective of the non-linear features, the calibration curve presented in Fig. 4.3C, can serve as a reference for functionalizing beads with a desired CD44 surface fraction, including its applicability to double functionalization of the beads.

4.3.2.2 Bead functionalization with PSGL-1

Using a similar approach, we established a calibration curve for beads functionalized with varying surface coverages of PSGL-1. This involved an additional incubation step (see Fig. 4.4A): first, b-ZZ was co-adsorbed with free biotin onto the bead surface at a defined ratio of molar concentrations to achieve the desired surface coverage. Subsequently, beads were functionalized with PSGL-1-Fc molecules until saturation for lower surface coverages or until reaching a close-to-equilibrium state for higher surface densities. Finally, the anchored PSGL-1 molecules were labeled using a mixture of fluorescently labeled and non-labeled antibodies at a ratio of 1:3.

In the case of PSGL-1, the selection of fluorescently-labeled antibodies was not straightforward. Initial tests (not shown) with some of the commercially available antibodies produced very low signals with the flow cytometer settings used for our measurements, while others exhibited high non-specific binding to non-functionalized beads. After several experimental trials, we opted to use phycoerythrin (PE)-labeled antibodies due to their broad signal detection range and low level of non-specific binding.

The flow cytometry analysis confirmed the uniform functionalization of all bead samples with a slight asymmetry towards higher intensities, as depicted in Figure 4.4B. The resulting calibration curve for PSGL-1-functionalized beads displayed a linear phase within the range of low surface coverages, extending up to approximately 20% of the maximum surface coverage (see Fig. 4.4C). This observed pattern in the curve aligns with expectations, indicating that PSGL-1, being a relatively large protein, starts saturating the bead surface after reaching about 20% of the maximum surface coverage. Further attachment of PSGL-1 molecules is impeded by the steric hindrance effect, leading to the signal saturation phase. This effect closely resembles what has been observed for P-selectin at planar surfaces, as detailed in Section 3.3.3.1.

4.3.3 Bead co-functionalization with two types of receptors: CD44 and PSGL-1

Finally, the abovementioned approaches were applied to bead functionalization with the two receptors of interest: CD44 and PSGL-1. The functionalization proceeded in three stages (Fig. 4.5A). First, b-CD44 was co-adsorbed with b-ZZ and free biotin. Second, the beads were incubated with PSGL-1-Fc so it saturated the available b-ZZ binding sites. Finally, two identical samples of double-functionalized beads were labeled, one with CD44 antibodies and the other with PSGL-1 antibodies.

In order to assess any potential antibody cross-reactivity, wherein CD44 antibodies might bind to PSGL-1, or vice versa, an additional negative control experiment was conducted (see Fig. B.11 in Supplementary Materials). The results demonstrated the absence of any antibody cross-reactivity.

For the bead functionalization process, surface densities of 10% of the maximum surface coverage were selected for both CD44 and PSGL-1 receptors. These densities were selected to achieve relatively high surface coverages whilst staying in the linear binding range. To validate that the double functionalization strategy worked quantitatively, the fluorescent signal from the double-functionalized beads was compared with the previously established calibration curves (Fig. 4.3C for CD44 and Fig. 4.4C for PSGL-1).

In Figure 4.5B and Figure 4.5D, a comparison is presented between the detected fluorescent signals from the double-functionalized beads stained with CD44 antibodies and beads carrying

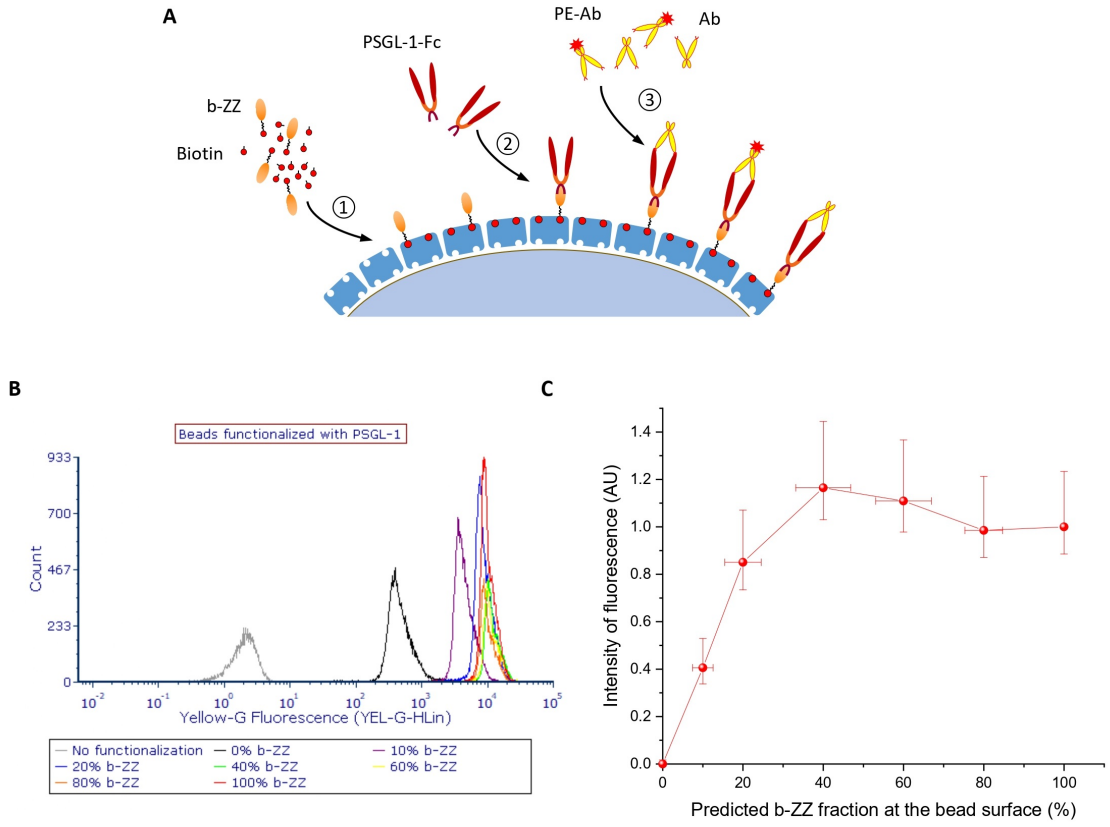

Figure 4.4: Beads functionalization with PSGL-1. A. Schematic drawing of beads functionalization with PSGL-1 : ① co-adsorption of b-ZZ with biotin, ② PSGL-1-Fc incubation, ③ PSGL-1 staining with the mix of fluorescent (PE) and non-fluorescent antibodies. **B.** Histograms of fluorescence intensity as measured by flow cytometry of microbeads functionalized with different PSGL-1 target surface fractions and non-functionalized beads for comparison. Statistics for the flow cytometry data was taken on at least 10000 events. **C.** Intensity of fluorescence measured from the beads presenting different fraction of b-ZZ at their surface. Data points represent the median of detected events, with error bars along the vertical axis indicating the interquartile range (75th and 25th percentiles), and error bars along the horizontal axis representing uncertainty in b-FITC and biotin concentrations. Functionalization conditions: bead concentration: 0.25% w/v, $c_{\mathrm{b-ZZ}} + c_{\mathrm{biotin}}$ = 700 nM was maintained constant, incubation time: 30 min. PSGL-1 incubation: $c_{\mathrm{PSGL-1}}$ = 800 nM, incubation time: 2 hours. Antibody staining conditions: PE-labelled and non-labelled antibodies were mixed in molar ratio of 1:3, total concentration: 10 µg/mL, incubation time: 2 hours.

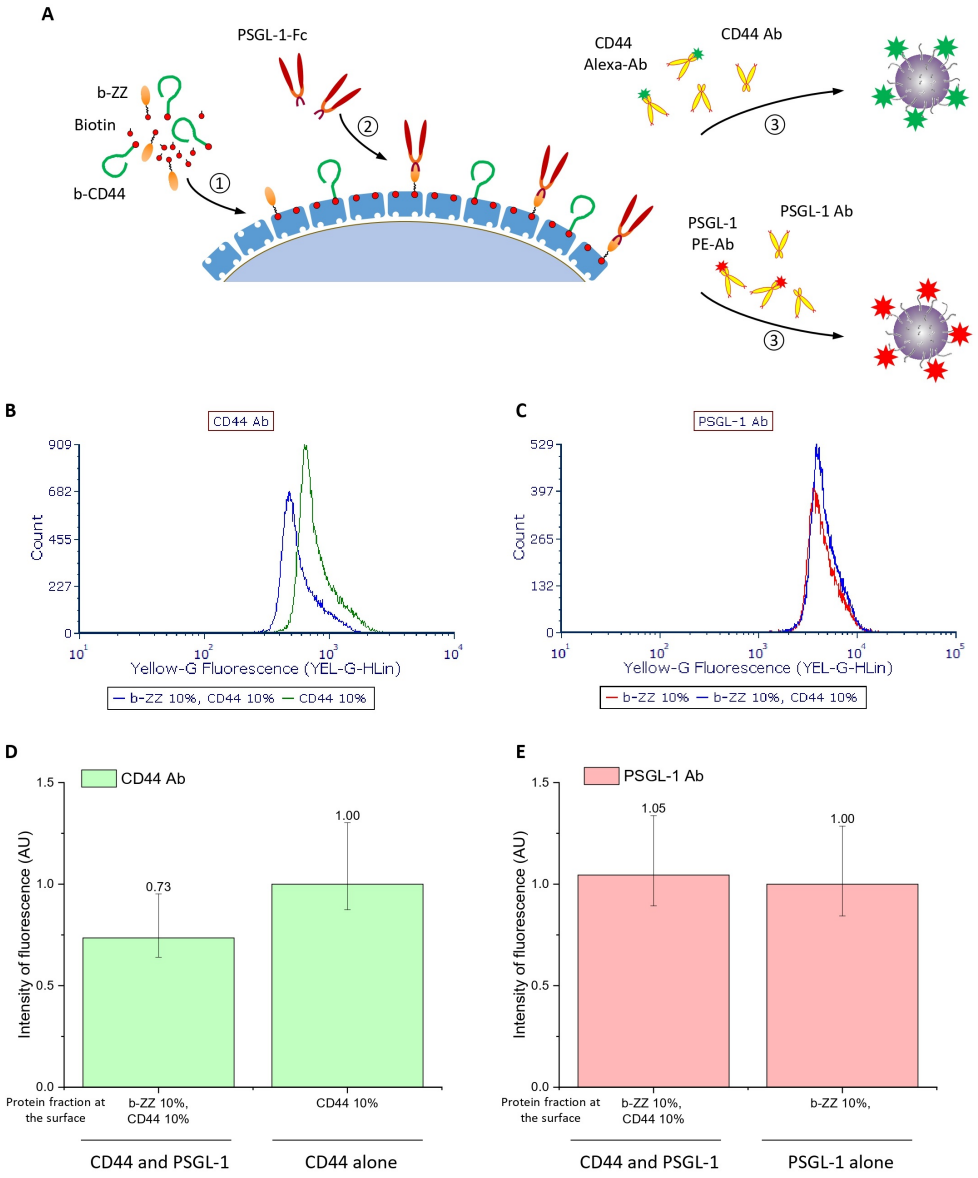

Figure 4.5: Beads functionalization with CD44 and PSGL-1. A. Schematic drawing of beads functionalization with CD44 and PSGL-1 : ① co-adsorption of b-CD44, b-ZZ and biotin,② PSGL-1-Fc incubation, ③ Two samples of double-functionalized beads are stained separately: CD44 staining with the mix of fluorescent (Alexa) and non-fluorescent antibodies; PSGL-1 staining with the mix of fluorescent (PE) and non-fluorescent antibodies. **B.** Histograms of fluorescence intensity as measured by flow cytometry of microbeads functionalized with CD44 only and CD44 together with PSGL-1 and stained with CD44 Alexa 532 antibodies. The flow cytometry data was taken on at least 10000 events. **C.** Histograms of fluorescence intensity as measured by flow cytometry of microbeads functionalized with PSGL-1 only and PSGL-1 together with CD44 and stained with PSGL-1 PE antibodies. The flow cytometry data was taken on at least 10000 events. **D.** Comparison between intensity of fluorescence from CD44 Alexa antibodies on beads functionalized with two types of receptors (CD44 and PSGL-1) and beads functionalized with CD44 only. **E.** Comparison between intensity of fluorescence from PSGL-1 PE antibodies on beads functionalized with two types of receptors (CD44 and PSGL-1) and beads functionalized with PSGL-1 only. Conditions: bead concentration: 0.25% w/v, $c_{\mathrm{b-CD44}} + c_{\mathrm{b-ZZ}} + c_{\mathrm{biotin}}$ = 700 nM; incubation time: 2 hours. PSGL-1 incubation: $c_{\mathrm{PSGL-1}}$ = 800 nM, incubation time: 2 hours. Antibody staining conditions: Alexa 532-labelled and non-labelled CD44 antibodies were mixed in molar ratio of 1:3, total concentration: 10 µg/mL, incubation time: 2 hours; PE-labelled and non-labelled PSGL-1 antibodies were mixed in molar ratio of 1:3, total concentration: 10 µg/mL, incubation time: 2 hours. Columns represent the median of at least 10 0000 detected events, with error bars indicating the interquartile range (75th and 25th percentiles).

CD44 only, which were also stained with CD44 antibodies. The response from the double-functionalized beads appeared slightly lower, though it remained within the interquartile range, as defined by the 75th and 25th percentiles. Similarly, Figure 4.5C and Figure 4.5E show a comparison between the double-functionalized beads stained with PSGL-1 antibodies and beads functionalized with PSGL-1 only, both of which were stained with the same antibodies. Notably, the detected fluorescent responses from both of these samples were identical. These results confirm that the applied strategy for double-functionalization of the beads works as expected, and the desired surface coverages of the receptors of interest can be reliably achieved using the newly established protocol.

4.4 Discussion

This chapter has provided an extensive analysis of strategies for bead functionalization and the practical considerations that must be taken into account during the microbead functionalization process. Moreover, it has established a new approach for regulating the surface density of receptors by co-adsorbing biotinylated receptors with inert biotin, which can be applied to modulate the receptor density on microbeads.

A significant novelty is the development of a method for double functionalization of microbeads with two distinct receptors. While previous attempts in this direction have been made [121], they often lacked quantitative precision. Our novel approach introduces guidelines for the functionalization of microbeads with specific surface fractions of two or more receptors of interest.

However, several crucial aspects need to be considered when applying the co-adsorption approach to microbeads. As illustrated in Section 4.3.1, even in the case of SAv-coated beads, the relationship between the intensity of fluorescence and the fraction of biotinylated fluorophore at the bead surface was not strictly linear. This contrasts with the behavior observed in a similar experiment conducted on a planar surface (refer to Fig. 3.2B). To date, we have not definitively determined the cause of this deviation from linearity. One possible explanation could be that our assumption that the shaking mode can be likened to flow conditions might not be accurate. We explored different theoretical scenarios for the obtained experimental data, including cases where there were no flow conditions ($i = 1/2$) or where the ratio of the concentration of bound molecules at the surface equaled that in solution ($i = 0$). However, the recalculated curves deviated even further from a straight line (see Fig. B.12 in the Supplementary Materials), resulting in more pronounced superlinear trends. Another potential explanation could be that streptavidin adsorbed on the bead surface in unpredictable orientation behaves differently from streptavidin forming a monolayer on the supported lipid bilayer (SLB), potentially exhibiting greater on rate for free biotin than for biotinylated species. Hence, the mechanism of species adsorption on the spherical surface of microbeads remains incompletely understood and has a potential for further investigation.

Another noteworthy aspect is that in the microbeads model system, unlike in SLB-based layers, quantification of surface-bound receptors remains a practical challenge. Currently, quantification relies on empirical methods, necessitating information from the bead provider regarding biotin binding capacity. Moreover, binding capacity may be influenced by the size and shape of the biotinylated probe. While our newly developed method still requires further refinement in the future, it represents a substantial advancement compared to previously published methods for modulating receptor density on microbead surfaces [33, 121].

Moving forward, our novel protocol for functionalizing beads with two types of receptors can be applied to create leukocyte mimetics for adhesion assays with the glycocalyx model. In our project, we chose to employ surface fractions of 10% for CD44 and PSGL-1 receptors. While these

surface densities may not precisely replicate physiological levels on living cells, they do allow us to investigate the influence of these receptors on the mechanisms of cell adhesion effectively.

Furthermore, the techniques described have broader applications in microbead functionalization for diverse research purposes. Microbeads can potentially be coated with various other types of cell surface ligands, enabling the exploration of the impact of different ligand-receptor pairs on cell adhesion under flow conditions. These methods can also be extended beyond cell mimicking, facilitating the investigation of a wide range of research questions involving functionalized microbeads.

4.5 Conclusion

A protocol for functionalizing microbeads to mimic white blood cells has been successfully established and the new method to control the surface density of one or more anchored proteins on microbeads has been developed. The study illustrates that the two receptors of interest, CD44 and PSGL-1, can be co-presented on the bead surface at desired surface fractions.

5 Conclusions and perspectives

Contents

5.1 Main achievements of this thesis work

In the "Discussion" sections within Chapters 2-4, the novelty of the *in vitro* platform developed during my PhD project was delineated, highlighting its distinctions from previously described systems for studying cell adhesion. To provide a concise summary, the key attributes of my platform are as follows:

5.1.1 A new molecularly defined *in vitro* model of the endothelial cell surface

I have successfully developed a novel *in vitro* model of the endothelial cell surface, which integrates a glycocalyx-like layer with tunable thickness and elasticity, alongside cell adhesion receptors. Through an extensive investigation to select the appropriate molecular platform and to engineer the monolayer with biotin-binding sites, I have established a highly dependable and consistent molecular system. Notably, our research has demonstrated the capacity to adjust the fluidity of the supported lipid bilayer, paving the way for the creation of customized molecular models suitable for a wide range of applications, particularly in the study of dynamic processes under various flow conditions.

5.1.2 A new method to quantitatively tune the density of surface-anchored molecules

A new approach to precisely adjust the surface density of biotinylated receptors on SAv-coated supports, both in stagnant and dynamic flow conditions, has been developed. Within the scope of my project, this investigation was crucial in replicating the biologically significant spacing between P-selectin receptors. Notably, the theoretical principles outlined here hold promise as a versatile tool applicable to a diverse array of research endeavors and can be extended to anchor types beyond biotin, with examples such as IgG binding to protein A or protein G. Owing to its straightforward implementation, this technique can find widespread utility in various applications, allowing for the precise modulation of surface concentrations for a wide range of target receptors.

5.1.3 A method to co-present more than one receptor on microbeads at defined surface densities

I introduced a new approach for the functionalization of microbeads with specific surface fractions of two or more receptors of interest. These techniques, as outlined, hold broader implications for microbead functionalization in a wide range of research contexts, for example, their utilization as bacterial mimetics for the study of bacterial migration. In addition to the receptors mentioned, microbeads can be coated with various other types of cell surface ligands, thus opening avenues for investigating the influence of different ligand-receptor pairs on cell adhesion under dynamic flow conditions.

5.2 Perspectives

When combined with the controlled conditions within the microfluidic channel, including its geometry and the applied shear rate, this system presents a wide array of potential applications, which will be discussed in the upcoming sections of this chapter.

5.2.1 Integration of the new models of the glycocalyx and circulating cells into laminar flow assays

Initial progress has been made towards incorporating the newly developed molecular glycocalyx model into the laminar flow assays, as outlined in sections 5.2.1.1-5.2.1.3. Following further validation (detailed in section 5.2.2), the new models will enable the study of physical mechanisms of cell-glycocalyx interactions.

5.2.1.1 Microfluidic device for studying cell-glycocalyx interaction *in vitro*

The development of our microfluidic device for *in vitro* analysis of cell-glycocalyx interactions built upon the prior expertise within our research group. Several modifications were introduced to the previously described microfluidic device [33]. The development of the new microfluidic system was done with a great help of Elena Murillo Vilella, an M1 student under my co-supervision, and Yeraldinne Carrasco Salas, a postdoctoral researcher at LIPhy.

The microfluidic device consists of a polydimethylsiloxane (PDMS) part with microfluidic channel sealed to a pre-cleaned glass coverslip (Fig. 5.1A), as described in Methods section. The tubings connected to the inlet and the outlet of the channel are each composed of two parts: a short PDMS section for attachment to the PDMS channel and a longer Teflon section. The choice of Teflon for the latter segment is based on its rigidity and inert properties, ensuring minimal loss of material on the tubing walls.

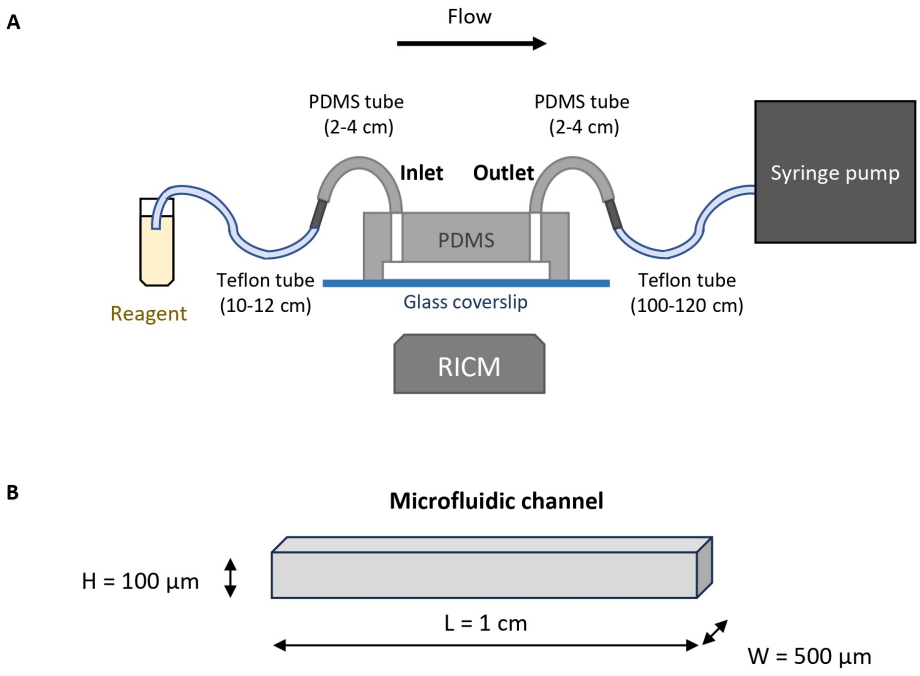

Figure 5.1: Microfluidic device for studying cell-glycocalyx interactions. A. Schematic drawing of the key elements of the microfluidic device (not drawn to scale). The PDMS part with microfluidic channel is sealed onto a cleaned glass coverslip and the tubing consists of a short PDMS section and a longer Teflon segment, connected to the channel's inlet and outlet. The volumetric flow rate (which along with the channel geometry defines the shear rate) is regulated using a syringe pump in withdraw mode. **B.** Dimensions of the microfluidic channel (not to scale). The channel has a rectangular cross section with a length of 1 cm, width of 500 µm and height of 100 µm.

Functionalization of the channel was performed *in situ*. The necessary reagents for the step-

by-step assembly of the glycocalyx molecular model were sequentially introduced into the system through the inlet tube. A channel with rectangular cross section with dimensions of 1 cm in length, 500 µm in width and 100 µm in height (as shown in Fig. 5.1B). These dimensions were chosen to facilitate cell adhesion assays in laminar flow across the relevant range of shear stresses (0-1 dyn/cm^2 [45]).

The functionalization process closely resembled that of QCM-D. Consequently, the incubation conditions, including flow rate, incubation time, and reagent concentrations, were maintained identical to those used in QCM-D experiments. However, we aimed to assess whether the resulting layer exhibited similar properties (homogeneity, surface density of bound proteins) to those observed in the QCM-D chamber.

5.2.1.2 Glycocalyx molecular model presenting a homogeneous layer of P-selectin formed in the microfluidic device

As a first test, I used the microfluidic device to observe the interaction between a surface solely presenting P-selectin (without HA brush) and microbeads bearing the PSGL-1 receptor. Given the prior demonstration of experiments examining HA brush/CD44receptor interactions [33], my aim was to illustrate effective P-selectin/PSGL-1 interactions within carefully controlled conditions. For this, the glass bottom of the microfluidic channel was functionalized with P-selectin at 10% of the anticipated fractional surface density, corresponding to a surface density of 0.7 pmol/cm^2. A separate experiment was carried out to evaluate the uniformity and surface density of the resultant P-selectin layer. This involved staining the layer with fluorescently labeled P-selectin antibodies, following a procedure similar to that described in Section 3.3.3.3. Confocal microscopy was then used to visualize the fluorescently labeled layer.

Figure 5.2A presents a composite of images taken along the channel, demonstrating a predominantly uniform fluorescent signal on the functionalized surface. Due to a slight sample tilt, the micrographs exhibit the highest fluorescence intensity from the bottom-left to the top-right, while the top-left and bottom-right corners appear darker, indicating their position outside the focal plane. A small area near the inlet, as indicated by the white arrowhead exhibited lower fluorescence, likely due to a minor air bubble partially damaging the surface in that region. The individual image shown in Fig. 5.2B is representative of the entire channel, and demonstrates a largely uniform functionalization. Some brighter spots are visible in the field of view (a few examples are indicated by the white arrowheads), presumably indicating the presence of clusters of P-selectin or of P-selectin antibodies on the surface. However, these spots typically occupied less than 1% of the imaged area and can be considered negligible.

This experimental analysis effectively demonstrated the successful formation of a homogeneous P-selectin layer within the microfluidic channel. The P-selectin surface density (Fig. 5.2C) was estimated by determining the average fluorescence intensity across all individual images and comparing the obtained value with the calibration curve previously shown in Fig. 3.7B. The surface density was found to be approximately 17% of all the available Fc-binding sites at the surface (around 1.2 pmol/cm^2), slightly higher than the predicted value from Eq. 3.8 (0.7 pmol/cm^2). This inconsistency could potentially be attributed to variations in the surface coverage of streptavidin (SAv) due to different incubation conditions, an aspect that will be addressed in subsequent experiments.

This experimental analysis effectively demonstrated the successful formation of a homogeneous P-selectin layer within the microfluidic channel.

5.2.1.3 PSGL-1-coated microbeads rolling on the surface presenting P-selectin

After successfully forming a P-selectin layer within the microchannel, we investigated the interaction of PSGL-1 coated microbeads with the P-selectin coated channel surface. The microbeads were modified with three distinct surface fractions of PSGL-1 (0%, 10%, and 100%), following

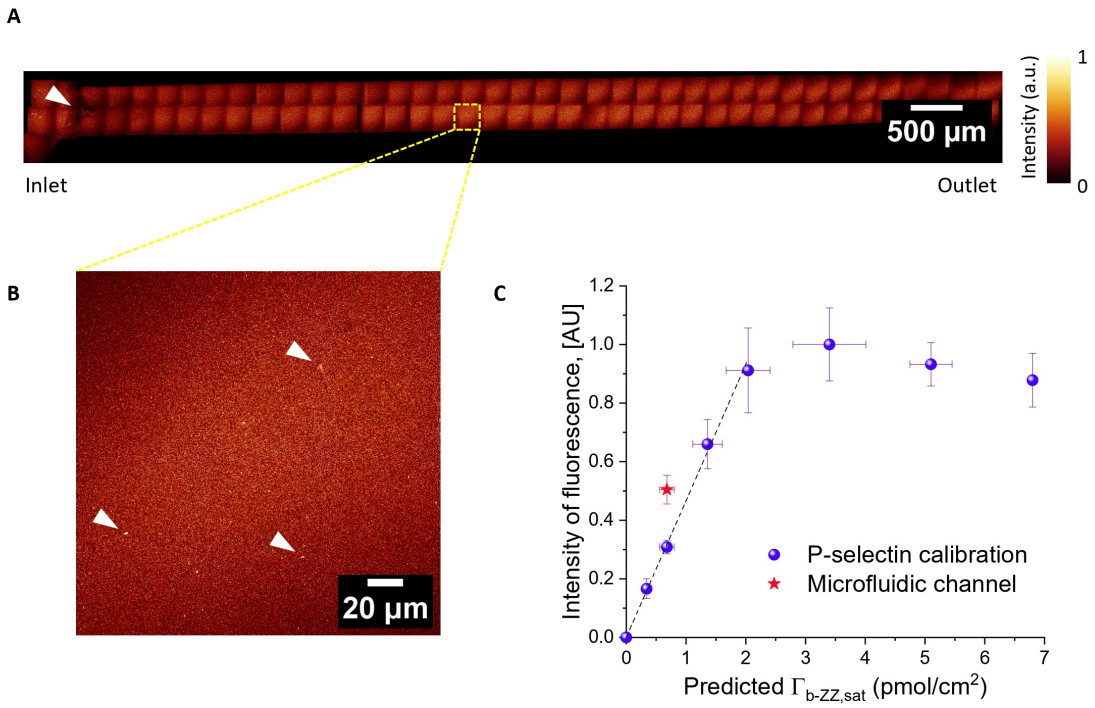

Figure 5.2: Microfluidic channels can be homogeneously functionalized with P-selectin, as visualized with confocal microscopy. A. Tilescan of micrographs captured along the entire length of the channel, demonstrating uniform functionalization across the channel surface. Each square (the dashed yellow square surrounds an example) within the composite tilescan image represents a distinct micrograph. Owing to a slight sample tilt, the highest fluorescence intensity is observed to run from the bottom-left to the top-right in each micrograph, whereas the top-left and bottom-right corners appear darker as they are outside the focal plane. A white arrowhead indicates the area with lower fluorescent signal, likely due to a minor air bubble partially damaging the surface in this region. **B.** A representative micrograph of the channel surface. The surface appears predominantly uniform, with a few noticeable bright spots (some of which are indicated by white arrowheads) covering less than 1% of the surface, likely indicating the presence of clusters of P-selectin or P-selectin antibodies. **C.** Averaged intensity of fluorescence detected within the microfluidic channel (red star) as described in Methods section compared to the previously established calibration curve for P-selectin surface densities (blue spheres, taken from Fig. 3.7B). Channel functionalization conditions (flow rate at all steps: 20 µL/min, corresponding to a shear rate of 4 dyn/cm^2): SLB formation: c(DOPC/DOPE-cap-b) = 50 µg/mL, incubation time: 15 min; SAv monolayer: c(SAv) = 10 µg/mL, incubation time: 15 min; $c_{bZZ} + c_{biotin}$ = 0.625 µM was maintained constant, with c_{bZZ} and c_{biotin} determined according to Eq. 3.8, incubation time: 10 min; c(P-selectin) = 33.3 nM, incubation time: 40 min; c(P-selectin Ab) = 10 µg/mL, incubation time: 30 min.

the protocols detailed in Chapter 4. The selected fractions represent the extremes of protein coverage, as well as a reduced surface density, facilitating the assessment of the impact of PSGL-1 concentration at the bead surface on the strength of P-selectin/PSGL-1 interaction. The movements of the functionalized microbeads in the channel were monitored by bright-field microscopy. The flow rate Q was controlled with the help of a syringe pump, and the corresponding shear stress was calculated as [34]:

$$\tau = \frac{6Q\eta}{h^2 w} \tag{5.1}$$

where η is the solution viscosity ($\eta \approx 1$ mPa·s for water at room temperature [33]), and w and h are the width and height of the channel, respectively.

To perform a quantitative analysis of this experiment, it is essential to analyze a significant number of beads, with a minimum of 20-30 beads for each experimental condition. The application of automated image analysis allows individual bead tracking, with bead positions determined for each frame, enabling the calculation of mean velocities for each bead.

In view of time constraints, this section offers a qualitative comparison of beads with varying PSGL-1 coverage. I selected a single representative bead from each sample, chosen based on the average velocity of the bead population, and manually tracked its movement.

Figure 5.3A illustrates the bead movement within the channel at a constant flow rate of 2 µL/min (equivalent to 0.4 dyn/cm^2), which is in a range of physiological shear stress of post-capillary venules (0-1 dyn/cm^2 [45]). Yellow lines depict the bead trajectories, while white squares represent the positions of the bead's center at each time frame. The bead without PSGL-1 on its surface exhibited a consistent and constant speed while traversing the channel. The bead functionalized with a 10% fractional coverage of PSGL-1 also maintained a constant speed, albeit slower than the non-functionalized bead. The bead with the highest PSGL-1 surface coverage displayed the slowest velocity among the three beads. Notably, its movement was characterized by intermittent periods of increased speed (as indicated by black arrowheads in Fig. 5.3A), suggesting potential ruptures of specific PSGL-1/P-selectin bonds.

This comparative analysis of bead movement highlights the differences in velocity among the selected beads. Figure 5.3B depicts the displacement of each bead over time. From this graph, we can estimate the average bead velocity: for the non-functionalized bead, it was 57.4 ± 0.2 µm/s, for the bead with 10% fractional coverage of PSGL-1 – 31.5 ± 0.3 µm/s, and for the bead with maximal PSGL-1 surface coverage – 7.4 ± 0.4 µm/s. Consequently, the velocity of PSGL-1-functionalized beads moving along the P-selectin layer was significantly (more than 7-fold) lower than that of non-functionalized beads. This provides clear evidence that the specific interaction between P-selectin and its ligand, PSGL-1, is strong enough to affect the bead movement under flow. To enhance this effect, the surface density of P-selectin can potentially be increased further. These findings will prove instrumental in future investigations involving the microfluidic channel co-presenting P-selectin with the HA brush, as they demonstrate that comparable concentrations can be employed to assess the impact of the mechanical properties of the HA brush on facilitating this interaction.

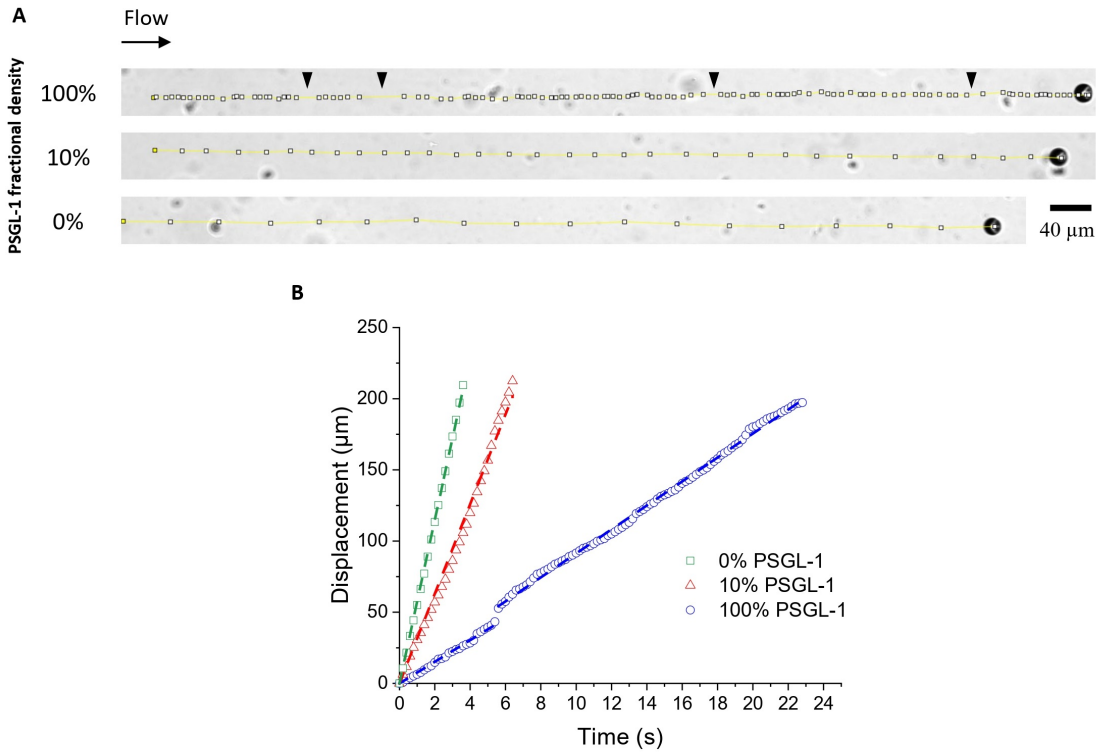

Figure 5.3: Tracking PSGL-1 coated microbeads moving along a P-selectin functionalized microchannel. A. Movement trajectories of three microbeads with varying PSGL-1 surface densities moving within a microfluidic channel presenting P-selectin (see Figure 5.2) at a constant flow rate of 2 µL/min (0.4 dyn/cm^2). The pictures show the final positions of each of the beads, the direction of the flow is indicated by the black arrow at the top of the figure. Yellow lines depict the trajectories of microbead motion, and white squares indicate the bead center at 200 ms intervals. The dark spots in the background of the images are optical artefacts. **B.** Time-dependent displacement in the direction of the channel axis of microbeads within the channel. Green squares represent beads functionalized with 100% biotin (lacking PSGL-1), with a linear fit (slope: 57.4 ± 0.2, dashed line). Red triangles correspond to microbeads functionalized with 10% PSGL-1, with a linear fit (slope: 31.5 ± 0.3, dashed line). Blue circles depict microbeads with 100% PSGL-1, with linear fits (slopes: 7.6 ± 0.1 and 7.1 ± 0.7, dashed lines).

5.2.2 Going forward

The *in* vitro model described in my work allows to investigate both the mechanical and biochemical aspects of cell-glycocalyx interactions by addressing a number of research questions:

1. *Investigation of the HA brush mechanical properties on the P-selectin/PSGL-1 interaction.* This study will involve the use of microfluidic channels where beads functionalized with two receptor types, CD44 and PSGL-1, will traverse along the channel while encountering P-selectin receptors concealed beneath the hyaluronan (HA) brush. Two specific scenarios will be explored:

   - a soft HA-840 brush facilitating bead indentation, thereby enabling the P-selectin/PSGL-1 interaction;
   - a stiff HA-280 brush screening the P-selectin/PSGL-1 interactions.

   This research endeavors to test the hypothesis that the mechanical characteristics of the glycocalyx are pivotal in mediating cell adhesion by either facilitating or impeding interactions between cells and cell adhesion molecules located on the surface of endothelial cells.

2. *Examination of the impact of HA brush mechanical properties on leukocyte adhesion.* Similar to the previous approach, this study will use the aforementioned glycocalyx platform, with the exception that living white blood cells will replace the cell mimetics. My preliminary test has demonstrated that both CD44-positive and CD44-negative AKR1 T-lymphocytes that have previously been used by our research group bear PSGL-1 receptors on their surface, making them suitable for this study. The transition to living cells interacting with our novel platform will validate the findings about the significance of the mechanical properties of vascular glycocalyx observed with cell mimetics.

3. *Assessment of the influence of receptor mobility on blood cell adhesion under flow.* By implementing newly established protocols for controlling the lateral mobility of surface-anchored receptors, we aim to discern the differences in cell adhesion to mobile and immobile platforms. This investigation will aim to validate the hypothesis that receptor recruitment is pivotal during blood cell adhesion. Both cell mimetics and living cells can be used in this study.

There are, however, other potential improvements to our *in vitro* platform to accommodate the study of additional facets of cell-glycocalyx interactions or elevate its complexity to emulate *in vivo* scenarios more closely. The glycocalyx mimetic can be refined by introducing additional components that contribute to its structural and mechanical properties, such as heparan sulphate and chondroitin sulfate, which together with hyaluronan contribute to about 90% of the entire glycocalyx structure in living systems [87]. Attaching these biotinylated glycosaminoglycans to our streptavidin-based platform is a straightforward procedure, and the principles of species co-adsorption discussed in Chapter 3 can be readily employed to achieve the desired fractional surface coverage of each of these species. The integration of more intricate models may offer the opportunity to explore a broader spectrum of mechanical properties (thickness, rigidity) of the glycocalyx model, potentially including certain pathological conditions, as it was demonstrated that glycocalyx can become significantly thinner due to sepsis [11] or chronic kidney disease [90].

Furthermore, to increase the complexity of our platform, we can consider the addition of other types of surface-anchored cell adhesion molecules. For instance, introducing E-selectin would facilitate the study of the mechanisms behind the initial cell capture and rolling on endothelial surfaces. Similarly, the inclusion of ICAM-1 and/or VCAM-1 receptors would enable the examination of leukocyte stabilized adhesion.

As for the bead mimetics, their complexity can be enhanced by incorporating additional receptors that contribute to cell capture under flow conditions, such as L-selectin, β1-integrin VLA-4, and/or β2-integrin LFA-1. Achieving this can be accomplished by anchoring these receptors onto the bead surface through biotin-streptavidin bonds, similar to as described in Chapter 4. This strategy will enable the assessment of the individual significance of each receptor type in blood cell adhesion, as well as the examination of various physiological and non-physiological conditions and their impact on blood cell adhesion.

Additionally, one potential approach to enhancing the resemblance of cell mimetics to living cells can involve introducing lateral mobility to receptors on the bead surface. To achieve this, one viable approach is the formation of a supported lipid bilayer on non-functionalized polystyrene microspheres. This SLB can serve as a platform for creating a streptavidin monolayer, enabling the subsequent attachment of receptors. This approach allows for the investigation of receptor recruitment effects on the leukocyte surface during cell adhesion. While it may introduce some complexity to bead functionalization, there are existing protocols in the literature [9, 18] that describe the formation of SLBs on microbead surfaces and that can be adapted for our specific application. This approach will enable the validation of the hypothesis concerning the significance of receptor reorganization on the cell surface in cell adhesion under flow conditions.

5.2.3 Beyond the leukocyte-glycocalyx interaction

The main aim of developing the platform discussed in this research was to investigate the interaction between immune cells and the glycocalyx under controlled conditions. However, the methodologies introduced here have the potential to address a variety of other research inquiries, extending beyond blood cell migration within the bloodstream. Our novel system enables the manipulation of the soft layer's mechanical and chemical properties and the shear rate, facilitating its application in both fundamental and practical studies. Below are some additional examples of the platform's potential applications:

1. Investigating the functions of the intestinal epithelial glycocalyx. The epithelial glycocalyx in the intestine is composed of mucins and acts as a barrier against microbial and bacterial adherence. Our platform can be utilized in studies focusing on how the mechanical properties of the soft layer affect bacterial adhesion. By adjusting the soft film's elasticity, our system facilitates the examination of bacterial adhesion under diverse mechanical conditions. This is particularly pertinent as certain types of bacteria have been reported to adhere to the glycoproteins and glycolipids on the epithelial cell glycocalyx through specific glycan recognition mechanisms [14].

2. Investigating cell adhesion in cancer metastasis. By replicating the mechanical conditions of the extracellular matrix, our platform can contribute to understanding how variations in the glycocalyx influence the adhesion and spread of cancer cells, potentially offering crucial insights into metastatic processes.

3. Blood coagulation studies. A microfluidic system that emulates the mechanical properties of blood vessels can be employed to study the dynamics of blood coagulation, which can be crucial for understanding thrombosis and designing anticoagulant therapies.

4. Investigating protein unfolding kinetics under mechanical stress. With its application of a streptavidin monolayer as an anchorage platform, our system ensures a defined orientation of surface-bound proteins. This feature is advantageous for fundamental research centered on understanding how proteins respond to mechanical stress, for example, when exposed to substantial shear rates.

5. Cell sorting. The surface of the platform can be modified to introduce specific molecules or ligands that are known to interact with the target cells. These could include antibodies, aptamers, or other ligands that bind to unique cell surface markers present on the cells of interest. As the cells flow through the system, the platform's surface chemistry and mechanical conditions will selectively allow the target cells to adhere while others will not. This can be achieved based on the specific binding interactions between the target cells and the modified surface. While some efforts have already been made in this direction [40], our system can offer an alternative with a greater number of adjustable parameters.

In summary, the implications of this research extend beyond the initial investigation of immune cell-glycocalyx interactions. The developed platform's adaptability and diverse applications make it valuable in the fields of biophysics, cell biology, and biomaterials science.

Materials and Methods

Materials

Buffers

Working buffer (often referred to as "HEPES buffer") used in the majority of the experiments consisted of 10 mM HEPES (Acros Organic, Belgium), pH 7.4, 150 mM NaCl (Sigma Aldrich, France) to match with physiological salt levels and pH. It was prepared in ultrapure water (uH_2O; resistivity 18.2 $M\Omega cm^{-1}$).

High-salt buffer used for the thick HA brush formation was prepared with 10 mM HEPES at pH 7.4 and 1 M NaCl in ultrapure water.

Low-pH buffer used for HA-280 brush formation was prepared with 150 mM K_2HPO_4 and 150 mM KH_2PO_4 at pH 3.0 in ultrapure water.

To test the stability of HA brush the working buffer without salt was used (referred to as "no-salt buffer): 10 mM HEPES at pH 7.4 in ultrapure water.

To assess the specificity of the binding between PSGL-1 and P-selectin, the following working buffers were employed: one containing Ca^{2+}ions (2 mM Ca^{2+} in HEPES buffer) and another containing EDTA (2 mM EDTA in HEPES buffer).

All buffers were filtered with the use of a syringe filter (pore size: 0.2 microns) and stored in the fridge at 4°C. Prior to experiments buffers were brought to the room temperature and degassed for 30-60 minutes using the ultrasonic bath sonicator (Nickel-Electro Ltd, UK).

Lipids

Lyophilised 1,2-dioleoyl-sn-glycero-3-phosphocholine (DOPC) and 1,2-dioleoyl-sn-glycero3-phosphoethanolamine-N-(Cap Biotinyl) (DOPE-cap-B) were purchased from Avanti Polar Lipids (Alabaster, USA).

Small unilamellar vesicles (SUVs) displaying biotin were prepared following a previously established procedure [135]. In brief, lipids were combined in chloroform at a ratio of 95 mol.% DOPC and 5 mol.% DOPE-cap-B, totaling 5 μmol. The mixture was evaporated using a stream of nitrogen gas, followed by vacuum drying for 2 hours. The resulting lipid mixture was re-suspended in the working buffer at a concentration of 2 mg/mL and homogenized through five cycles of freezing, thawing, and vortexing.

To produce small unilamellar vesicles, the lipid suspension underwent tip sonication using a pulse mode (1 second on/1 second off) for a period of 30 minutes, with refrigeration. The resulting SUV suspension was then subjected to centrifugation at 12,100×g for 10 minutes to eliminate titanium debris originating from the sonicator tip.

The lipid solution was stored at 4 °C under a nitrogen gas environment.

OEGs

Oligo-ethylene glycol (OEG) thiol and biotinylated OEG (bOEG) thiol were purchased from Polypure, Oslo, Norway. They were stored at 4 °C.

SAv and TAv

Lyophilized SAv was purchased from Sigma Aldrich, and lyophilized TAv was provided by Mark Howarth (University of Oxford). Both proteins were reconstituted in uH_2O at 1 mg/mL and stored at -20 °C until use.

GTA

GTA solution (8% in H_2O) was purchased from Sigma Aldrich and stored at 4 °C in darkness.

b-ZZ

b-ZZ adapter protein was previously expressed from the pCA1 plasmid as described earlier [44]. It was diluted in uH_2O at 500 µg/mL and stored at -20 °C.

biotin

Biotin was purchased as a powder from Sigma Aldrich, reconstituted in uH_2O at 1 mg/mL and stored at -20 °C.

b-FITC

Biotinylated FITC fluorophore was purchased from ThermoFischer Scientific, USA as a lyophilized powder. It was reconstituted at 500 μg/mL in uH_2O and stored at -20 °C.

In some of the experiments the fluorophore solution in working buffer was partially photobleached to reduce the concentration of fluorescent b-FITC and prevent self-quenching on the surface. A halogen lamp (KL 1500 LCD; Schott, Germany) was used to cover the entire visible spectrum, effectively exciting and bleaching the FITC fluorophore. The fluorophore solution (20 μg/mL in working buffer) was placed in a transparent glass vial, positioned 1.5 cm away from the light source, and illuminated. During the illumination process, the solution was briefly vortexed once per minute to ensure uniformity.

Fluorescence emission spectra were measured using a spectrofluorometer (FluoroMax-4; Horiba, Japan) in plastic cuvettes (UV-Cuvette micro 70 μL; BRAND GmbH, Germany) before illumination and after 30 minutes of illumination. The resulting b-FITC solution contained a defined total concentration of fluorescent and non-fluorescent molecules.

b-Alexa 647

Biotinylated Alexa 647 was purchased from ThermoFischer Scientific, USA at the concentration of 100 nM. It was stored at -20 °C until use.

Hyaluronan

b-HA-840, b-HA-280 and b-HA-58 were purchased from Hyalose, USA. They were reconstituted at 1 mg/mL, 0.25 mg/mL and 0.1 mg/mL respectively and were left in the fridge for 2 hours allowing HA chains to swell. Then, the hyaluronan samples were aliquoted and stored at -20 °C until use.

P-selectin-Fc and PSGL-1-Fc

Both proteins were purchased in lyophilized form from R&D Systems, USA. They were reconstituted at the concentration of 0.1 mg/mL and snap-frozen in liquid Nitrogen. Both proteins were stored at -80 °C, a fresh aliquot was taken for every experiment.

b-CD44

Biotinylated CD44 was produced by M.Howarth (University of Oxford, UK) as described elsewhere [8]. The aliquots at 50 μg/mL in uH_2O were stored at -20 °C, a fresh aliquot was taken for every experiment.

BSA

Bovine serum albumin (BSA) was purchased as a powder from Sigma Aldrich, France. The solution of desired concentration (typically, 10 mg/mL for the passivation) was prepared prior to use.

Antibodies

- P-selectin Alexa 647 antibodies, clone AK4, were purchased from BioLegend, USA, at a stock concentration of 100 µg/mL. They were stored in darkness at 4 °C.
- P-selectin non-labelled antibodies, clone AK4, were purchased from BioLegend, USA, at a stock concentration of 500 µg/mL. They were stored in darkness at 4 °C.
- CD44 Alexa 532 antibodies, clone IM7, were purchased from ThermoFischer Scientific, USA, at a stock concentration of 200 µg/mL. They were stored in darkness at 4 °C.
- CD44 non-labelled antibodies, clone IM7, were purchased from ThermoFischer Scientific, USA, at a stock concentration of 500 µg/mL. They were stored at 4 °C.
- PSGL-1 PE antibodies, clone KPL-1, were purchased from BioLegend, USA, at a stock concentration of 100 µg/mL. They were stored in darkness at 4 °C.
- PSGL-1 non-labelled antibodies, clone 688101, were purchased from R&D Systems, USA. They were stored at 4 °C.

Microbeads

- SuAv-coated microbeads, diameter: 15.3 µm, were purchased from Bangs Laboratories, USA, at a stock concentraion of 1% *w/v*. They were stored at 4 °C.
- SAv-coated microbeads, diameter: 15.0 µm, were purchased from Spherotech, USA, at a stock concentraion of 0.5% *w/v*. They were stored at 4 °C.
- Non-coated beads, diameter: 25.0 µm, were purchased from Polysciences, USA, at a stock concentraion of 2.6% *w/v*. They were stored at 4 °C.
- Non-coated beads, diameter: 45.0 µm, were purchased from Polysciences, USA, at a stock concentraion of 2.56% *w/v*. They were stored at 4 °C.

Methods

Quartz crystal microbalance with dissipation monitoring (QCM-D)

QCM-D measurements were performed with a Q-Sense E4 system equipped with Flow Modules (Biolin Scientific, Västra Frölunda, Sweden) on silica-coated sensors (QSX303; Biolin Scientific). The flow rate was controlled with a syringe pump (Legato; World Precision Instruments, Stevenage, UK) at 20 µl/min unless otherwise stated. The working temperature was 23°C. Before each use, sensors were cleaned in a 2% (w/v) aqueous solution of sodium dodecyl sulfate (SDS) detergent for 30 min, rinsed with ultrapure water, blow dried with N_2 gas, and treated with UV/ozone for another 30 min. QCM-D data were collected at six overtones (i = 3, 5, 7, 9, 11 and 13, corresponding to resonance frequencies of approximately 15, 25, 35, 45, 55, and 65 MHz). Changes in normalized resonance frequency ($\Delta F = \Delta f_i/i$) and dissipation (ΔD) of the fifth overtone (i = 5) are presented. All other overtones provided comparable information.

The incubation conditions of all the reagents used in QCM-D assays are indicated in the respective figure legends.

Spectroscopic ellipsometry (SE)

SE measurements were performed *in situ* in a custom-built open cuvette (Ĩ00 µL volume) with glass windows, on silicon wafers, at room temperature with a spectroscopic rotating compensator ellipsometer with a horizontal plane of incidence (M-2000 V; J. A. Woollam, Lincoln, NE). Ellipsometric angles Δ and Ψ were acquired over a wavelength range from λ = 370 to 1000 nm, at an angle of incidence of 70° and with a time resolution of 5 to 10 s. All samples (in working buffer) were directly pipetted into the cuvette, and homogenised by a magnetic stirrer, located at the bottom of the cuvette. SUVs were incubated under continuous stirring. All other samples were stirred for approximately 5 s after sample injection, and for the remainder of the sample incubation time, the stirrer was turned off and adsorption was left to proceed from still solution. Excess sample was rinsed away by flowing working buffer through the cuvette; this was assisted by a flow-through tubing system and a peristaltic pump (IPC; Ismatec, Germany) operated at a flow rate of 5 ml/min; during the rinsing phases, the stirrer was turned on to ensure homogenisation and maximise exchange of the cuvette content.

Areal mass densities (AMD) and molar surface densities of adsorbed biomolecules were determined by numerical fitting of the SE data using the software CompleteEASE (J. A. Woollam). A model with a stack of multiple isotropic layers relates the measured ellipsometric angles Δ and Ψ as a function of λ to the optical properties of the substrate, the adsorbed films and the surrounding buffer solution. The semi-infinite bulk solution was treated as a transparent Cauchy medium (refractive index: $n_{sol}(\lambda) = A_{sol} + B_{sol}/\lambda^2$, where A_{sol} = 1.325 and B_{sol} = 0.00322 μ m^2 [21]). The native oxide film on the Si wafers was modelled as a single and transparent Cauchy layer. Its optical properties were determined from the measurements acquired in the presence of bulk solution but in the absence of the biomolecular film, which were then fitted over the range of λ using the tabulated values for the underlying Si substrate (implemented in CompleteEASE) [44]. The adsorbed biomolecular film was fitted with the help of two separate layers. The combination of SLB, the monolayer of streptavidin and b-ZZ adapter protein (or the mix of b-ZZ with biotin) was treated as a single layer (index 1), which was treated as a transparent Cauchy medium with thickness (d_1) and a wavelength-dependent refractive index $n_1(\lambda) = A_1 + B_1/\lambda^2$. As this layer was thin (d_1 < 10 nm), the optical parameter A_1 and B_1 were kept fixed, and d_1 was the only adjustable parameter. A_1 = 1.4 was set as a typical value for a solvated biomolecular film, and the dispersity was set equal to the bulk solution ($B_1 = B_{sol}$). The thicker layer of P-selectin, adsorbed on b-ZZ, was treated as a separate transparent Cauchy layer (index 2) with thickness d_2 and $n_2(\lambda) = A_2 + B_2/\lambda^2$. Here, d_2 and A_2 were adjustable fitting parameters, and the change in B_2 with the protein concentration was neglected so that $B_2 = B_{sol}$. Layer 1 was assumed to re-

main unchanged during P-selectin binding. The root mean square error remained typically below 2 throughout the time-resolved data fitting, which indicated a good fit. The areal mass densities were determined through a variant of de Fejter's equation [139], $AMD = [d\,(A - A_{\mathrm{sol}})]\,/\,(\mathrm{d}n/\mathrm{d}c)$ using the refractive index increments, dn/dc, of 0.18 cm^3/g for all proteins, and 0.169 cm^3/g for lipids. The molar surface density was calculated from the areal mass density for b-ZZ and P-selectin as $\Gamma = AMD/M_{\mathrm{w}}$, where M_{w} is the molecular weight of the protein. Errors in AMD and Γ comprise the temporal noise and the confidence intervals of the data fitting.

A representative SE data for SLB formation on Si wafer followed by SAv monolayer formation in shown in Fig. B.3 in Supplementary Information.

The incubation conditions of all the reagents used in SE experiments are indicated in the respective figure legends.

Combined QCM-D and SE assay

The combined QCM-D and ellipsometry assay was conducted to establish a calibration curve relating the QCM-D frequency shifts with the molar surface density of the protein. This experiment was designed, performed and analyzed by Ralf P. Richter using the procedure established earlier [21]. The QCM-D sensor (QSX303) was cleaned as described before and installed in the open flow cell. The SE measurements were established similarly to as described in the "Spectroscopic ellipsometry" section. First, the SUVs were injected into the system at the concentration of 50 μg/mL and incubated for 7 min with constant stirring until the SLB formation was complete. Then, SAv was incubated at the final concentration of 0.13 μM (8 μg/mL) for 30 minutes. SAv monolayer formation is shown in Fig. B.4 in "Supplementary Information" section. As a next step, a b-ZZ solution was added to the flow cell to the final concentration of 0.31 µM (5 µg/mL) and incubated for 30 minutes. The calibration curve for b-ZZ binding is presented in Fig. B.5 in "Supplementary Information" section.

By fitting the calibration curves for SAv and b-ZZ binding with the empirical fits $\Delta F = -\frac{AMD}{C(1-A+B\times AMD)}$, the constants A and B were obtained for three overtones (Table B.2). Mass sensitivity constant C was taken as 18.0 ng/(cm^2 Hz). In the experiments presented in this chapter, we mostly used the 5^{th} overtone.

Surface functionalization in Teflon wells for confocal microscopy and RICM

Glass coverslips with a diameter of 35 mm (VWR, USA) were used for confocal microscopy and RICM analysis. Prior to use, the coverslips were cleaned with Piranha solution (H_2O_2:H_2SO_4 = 1:3) and exposed to H_2O plasma (Plasma surface cleaning system; Diener Electronic, Germany) for 3 minutes. Each coverslip was mounted on a custom-made Teflon holder using a two-component glue (Twinsil, Picodent, Germany) to create four identical wells with a diameter of 5 mm and a volume of 50 μL.

SAM formation

In the experiments where self-assembled monolayers (SAMs) were used, the piranha-cleaned glass coverslips underwent a gold deposition process prior to their attachment to the Teflon holder. This deposition was performed using a homemade sputtering machine at LIPhy. The deposition occurred in two steps within an Argon gas plasma environment at an extremely low pressure ($P < 10^{-6}$ mbar). Initially, a thin layer of Ti (approximately 3 nm) was applied to the glass, facilitating the adhesion of gold to the glass surface. Subsequently, a 10 nm gold layer was deposited onto the titanium-coated surface. To functionalize the gold-coated surface with SAM, the coverslips were first exposed to UV/O_3 for 30 minutes. Then, they were immersed into the thiol mixture of oligo ethylene glycol (OEG) thiol and biotinylated oligo ethylene glycol (bOEG) thiol in ultrapure water

(typically in (95:5) molar ratio if not stated otherwise) for 16-18 hours at 4°C. Then, the surfaces were thoroughly rinsed with uH_2O and attached to the Teflon holders.

SLB formation in Teflon wells

To form supported lipid bilayers (SLBs), surfaces were incubated with 50 μg/ml small unilamellar vesicles (SUVs) in working buffer for 30 minutes, allowing the SLB to form. Excess SUVs were removed by performing 10 washes with working buffer. Each wash involved injecting 100 μL of HBS into the well, gently mixing the solution with a pipette without touching the well's bottom, and then removing 100 μL of liquid. Next, the SLB-coated surface was incubated with 0.33 μM (20 μg/ml) streptavidin (SAv) in working buffer for 60 minutes to create a dense SAv monolayer with biotin-binding sites. Excess SAv was removed by washing the surface 10 times.

HA brush formation in Teflon wells

To form HA brush on SAv or TAv monolayer, biotinylated HA-840 or HA-280 was added into the teflon wells. Incubation conditions (incubation time, concentation) are indicated for each experiment in respective figure legends. After the end of the incubation the surface was washed 5 times with working buffer as described above. After forming HA-280 brush in low-pH buffer, the surface was first was washed 5 times with low-pH buffer, and then 5 times with working HEPES buffer.

Surface functionalization with b-FITC or b-Alexa

Biotinylated fluorophores (either preliminary bleached as described earlier or not) was mixed with free biotin at the desired ratio. The SAv-coated surfaces were then incubated with biotinylated molecules (total concentration: 14 μM for b-FITC and 100 nM for b-Alexa) in working buffer for 14 hours and washed 10 times with working buffer. The extended incubation time was found to improve the uniformity of the layer when examined using fluorescence microscopy.

Surface functionalization with P-selectin

For the experiments with P-selectin surface coverage calibration curves the surfaces were first functionalized with the mix of b-ZZ and biotin in appropriate ratios (total concentration of 0.625 μM) in HEPES buffer for 30 minutes, then rinsed 10 times with buffer. P-selectin was added to all the wells in the constant final concentration 66.7 nM (20 μg/mL) in HEPES buffer and incubated for 1 hour. Its excess was removed by rinsing 10 times with working buffer. To prepare the mix of partially fluorescent molecules, Alexa 647-labelled Ab were mixed with non-labelled Ab in a molar ratio of 1:9. The antibodies were added to the wells in the final concentration of 5 μg/mL and incubated for 1 hour in darkness, then rinsed 10 times with HEPES buffer.

Confocal microscopy and image analysis

The fluorescence intensity of the functionalised surfaces was measured using a confocal laser scanning microscope (TCS SP8, Leica, Germany) using a 40x/1.30 oil objective and a built-in autofocus. The acquisition settings varied depending on the fluorophore used in the experiment:

1. *FITC fluorophore* (used in tests with b-FITC): fluorescence was excited at 488 nm with a power on the sample in the range 0.5-10 μW, and detected in the wavelength range 491-629 nm with a pixel dwell time of 1.2 μs and a sampling of 0.284 μm/pixel.

2. *Alexa 647 fluorophore* (used for staining P-selectin and in tests with b-Alexa): fluorescence was excited at 633 nm with a power on the sample in the range 0.5-10 μW, and detected in

the wavelength range 638-800 nm with a pixel dwell time of 1.2 µs and a sampling of 0.284 µm/pixel.

The autofocus was set such that the maximum intensity (corresponding to an in-focus surface) was located around the centre of the image, ensuring that the in-focus signal was reliably detected in all images. A mosaic of 40 to 100 images, each 292.62 µm x 292.62 µm in size, was then acquired, so as to sample the entire surface of each well.

Acquired images were analyzed with FiJi using custom routines. A band of 200 pixels in width was drawn across the image such that it cut through the region of maximal intensity, and the profile of the mean grey values across the band was defined. The profile was fitted with a polynomial function and the maximum value of the fit function in the field of view was considered as the in-focus intensity of a given image. Intensity values represent the mean ± standard error of the in-focus intensity across all images in a mosaic.

For the FRAP analysis, a square region within the image underwent bleaching. To accomplish this, the field of view was magnified to 10x10 µm, and an image was captured with a high laser intensity, typically set at 30 times higher than the acquisition intensity. Following this initial step, the zoom level was reverted to its original value, and a series of images were captured at one-second intervals until complete surface recovery was observed. Fluorescence intensity was quantified within and outside the bleached area in each of the acquired images, as described previously.

HA brush height measurement with the use of RICM

To measure the thickness of HA films formed in Teflon wells, an RICM method was used with a setup allowing simultaneous imaging at two wavelengths (532 and 635 nm). Samples were mounted on a microscope and preliminary washed (3 times in HEPES buffer) microbeads with a diameter of 25 µm or 45 µm were added to each well. The interference patterns were observed from the light reflected from the bead surface and the substrate, in each well at least 25-30 images of beads were recorded. These images were processed using the custom-made LabView program as described in [33], and the height of each bead sitting on top of the brush was obtained. As a reference, the thickness of the layer before the HA functionalization was checked (the height of the beads sitting on the SAv/TAv layer was measured). This reference height was then subtracted from the height of the beads on HA brush. Afterwards, the surface was rinsed 5 times with HEPES buffer to eliminate the beads.

Beads functionalization

Detailed protocol for the microbeads functionalization can be found in Appendix B. In all experiments beads were functionalized right before the flow cytometry measurement.

Flow cytometry and data analysis

Flow cytometry tests were performed with Guava easyCyte flow cytometer (Merck Group, Germany). The acquisition settings were chosen among the available options for the device such as the fluorescence is detected the most efficiently. Depending on the type of the fluorophore, the following settings were used:

1. b-FITC: "Green-B" setting (excited in blue wavelength range, detected in green). Exitation: 488 nm, detection: 510-521 nm.

2. Alexa 532 (used for staining CD44): "Yellow-G" setting (excited in green wavelength range, detected in yellow). Exitation: 532 nm, detection: 570-587 nm.

3. PE (used for staining PSGL-1): "Yellow-G" setting. Exitation: 532 nm, detection: 570-587 nm.

Measurement was done on at least 10000 beads per sample. The data was analysed using the FSC Express software, the median of the measured fluorescence intensity, 25th and 75th percentile were defined for each sample.

Microfluidic channel preparation

The microfluidic channels were prepared using a silicon wafer facricated by Yeraldinne Carrasco Salas, following an established protocol. The procedure for microfluidic channel preparation involved several steps: first, a PDMS liquid polymer solution, mixed with a cross-linking agent and degassed, was poured onto the mold to match its pattern. It was then cured at 65°C for 2 hours. After curing, the PDMS channel was carefully detached from the mold, and inlet and outlet holes were punched at both ends of the circuit.

Subsequently, the PDMS circuit was sealed onto a glass coverslip, which had been pre-cleaned as described above. This sealing process involved exposing both surfaces to plasma for 60 seconds, bringing them into contact, and then curing them at 65°C for an additional 2 hours. Following this, PDMS tubes were inserted at the inlet and outlet of the microfluidic channel, with one end connected to a syringe pump to establish controlled flow.

Appendices

A

Quantification of receptor surface density through fluorescence analysis

A.1 Introduction

Fluorescent staining is a commonly employed method for visualizing surface-bound proteins [53, 124]. In my project, I utilized well-established fluorescence-based techniques, such as confocal microscopy and flow cytometry, to measure the fluorescence intensity. These measurements are typically intricate to quantitatively analyze due to several potential biases, including fluorophore photobleaching over time, quenching effects between neighboring fluorophores, autofluorescence bias, biases arising from sample heterogeneity and laser stability. To address these challenges, researchers often employ advanced fluorescence-based techniques to acquire quantitative data. For instance, fluorescence fluctuation spectroscopy [126, 167] a method that tracks fluctuations in fluorescence intensity within a small volume (on the order of 1 femtoliter) within the sample [111], is commonly used. Here, our goal was to develop a straightforward protocol that utilizes the available methods (confocal microscopy and flow cytometry) for evaluating detected fluorescent signals and enabling comparisons among various samples. Specifically, we aimed to determine the conditions under which the detected fluorescent signal correlates proportionally with the number of fluorophores present at the surface.

In my study, the motivation for quantitative fluorescence assessment stemmed from the need to determine the density of receptors (P-selectin as a part of the glycocalyx model and PSGL-1 on cell mimetics) bound to the surface following functionalization. While *in situ* techniques like QCM-D and spectroscopic ellipsometry are valuable for establishing surface functionalization protocols, they cannot be integrated with glass coverslips in microfluidic devices or for microbeads functionalization. Post-functionalization analysis, including fluorescent staining and surface visualization using confocal microscopy, serves as essential quality control measure in these types of experiments. Furthermore, this technique enables the evaluation of surface homogeneity.

When it comes to functionalizing microbeads, there is no simple method for monitoring receptor attachment. Consequently, the only viable approach for assessing the binding of receptors of interest, including their density and binding stability, is through flow cytometry, which relies on post-functionalization fluorescent analysis.

The following considerations are limited to two specific scenarios of fluorescence staining: 2D surfaces that uniformly display fluorescent molecules and microbeads homogeneously presenting fluorophores.

To ensure the reliability of quantifying receptor density using fluorescent analysis, several critical considerations must be taken into account:

1. *Establishing a reference value for the surface density of binding sites*. Fluorescent analysis provides a relative measurement of surface-bound proteins. Therefore, it is essential to establish a reference value, for instance, the maximal density of available binding sites, to relate detected fluorescence to the quantity of bound receptors.

2. *Implementing a standardized protocol for fluorescence detection*. Consistency in how fluorescence is detected across all experiments is essential to enable meaningful comparisons.

3. *Monitoring the stability of the light source (laser) over time*. Maintaining consistent laser performance is crucial to ensure accurate and reproducible measurements.

4. *Verifying the direct proportionality of detected fluorescence to bound receptor density.* If the surface density of bound receptors is high, the fluorophores used for staining may exhibit self-quenching effects, which could affect the detected fluorescent signal.

Throughout the course of my project, I developed protocols for quantitatively detecting receptor surface density using both confocal microscopy and flow cytometry. The following sections will offer guidelines to ensure the accurate measurement of fluorescence.

A.2 Establishing a reference value for the surface density of binding sites

A.2.1 Reference value for the number of the binding sites on plane surfaces

Defining the number of binding sites on SLB-based SAv monolayer formed on a plane surface is easily achieved through spectroscopic ellipsometry, as presented in Section 3.3.2. By employing the same surface functionalization protocol (reagent concentrations, incubation time, flow conditions) on both glass coverslips, observed through confocal microscopy, and silica wafers used in spectroscopic ellipsometry, we can anticipate comparable levels of bound protein on these surfaces.

Consequently, by employing the calibration curve for P-selectin binding to surfaces functionalized with varying surface densities of the b-ZZ adapter protein (see Fig. 3.5C), we can effectively estimate the surface density of P-selectin based on the fluorescence intensity measured using confocal microscopy (see Fig. 3.7B). In this particular case, the reference value for the maximum number of binding sites is determined by the surface coverage of streptavidin and subsequently, the surface density of the b-ZZ adapter protein. The maximum density of b-ZZ binding sites is found to be $\Gamma_{as} = 6.8 \pm 0.1$ pmol/cm^2, as detailed in Section 3.3.2.1.

A.2.2 Reference value for the number of the binding sites on the microbeads

Quantifying the biotin-binding capacity of SAv-coated microbeads experimentally can pose challenges. We rely on information provided by the manufacturer, typically expressed as the mass of biotinylated FITC fluorophore bound per unit mass of the bead. This can be converted to the number of b-FITC molecules bound per bead, approximately 5.8×10^7 biotin-binding sites per bead for Bangs Lab beads (refer to Supplementary Methods for calculations).

If the number of binding sites per bead is unknown, flow cytometry can still be employed for relative quantitative measurements. By creating a calibration curve using different fractions of

bound protein on the microbead surface, one can estimate the surface density of the protein as a percentage of the maximum bead binding capacity.

A.3 Ensuring reproducibility of the fluorescence detection

Maintaining consistent measurement of fluorescent signals across various experiments is of utmost importance. While the flow cytometer used in this project offered limited flexibility in adjusting acquisition parameters, the confocal microscope, being a more intricate system, demanded more meticulous parameter adjustments.

Various acquisition parameters, including the wavelength range selected for detection, detection gain, and pixel dwell time, exerted influence on the detected signal's magnitude. Consequently, these parameters needed to be held constant across all measurements being compared. Moreover, the method of selecting the focal point played a critical role in influencing the detected signal.

To ensure consistent focal point selection across different samples, we exploited the natural variation in fluorescence intensity caused by the slight tilt of the coverslip. This tilt, which could vary depending on the exact amount of glue used to attach the coverslip to the Teflon holder (for details, refer to the Methods section), was noticeable in most experiments. When configuring autofocus for image acquisition, the sample was positioned such that the maximum fluorescence intensity coincided with the image's center. Subsequently, during image analysis, the maximum intensity within this central region was determined and considered the in-focus intensity for that specific image (see the Methods section for more detail on image analysis).

These precautions enabled us to obtain reproducible data regarding fluorescence intensity per field of view and facilitated comparisons between different samples.

A.4 Monitoring the laser stability over time

Since there are some evidences that the laser performance can degrade over time in both confocal microscope [74, 129] and flow cytometer [155], alongside observed short-term intensity fluctuations, it is important to monitor its stability to ensure the comparability of fluorescence intensity measurements across different days. To address this, we have devised protocols for assessing laser performance in both confocal microscopy and flow cytometry, and these measurements were consistently conducted prior to each experiment.

In the case of confocal microscopy, we initiated each experimental day by capturing a reference image. This reference image included the reflected light from the coverslip, detected within a wavelength range of ± 3 nm from the laser's wavelength (for the experiments with P-selectin Alexa 647 antibodies, a 633 nm laser was used, and fluorescence was detected in the range of 630-636 nm). This approach ensured that the detected signal exclusively represented the reflected laser light, excluding any fluorescence from the functionalized coverslip. Notably, we observed laser power fluctuations of less than 1% over a span of more than a year of confocal measurements.

To validate the stability of the laser used in the flow cytometer, we conducted an additional measurement during each experiment using commercially available fluorescent calibration particles. By comparing the detected fluorescence across different experiments, we found that fluctuations in fluorescence intensities typically remained below 5%.

A.5 Avoiding self-quenching effect during the fluorescent analysis

In the context of the fluorescence signal and receptor density, one factor to consider is the self-quenching effect. This phenomenon involves a reduction in the fluorescence intensity of a fluorophore molecule when it is in close proximity to another fluorophore. The self-quenching effect has been observed in various synthetic fluorophores, including FITC [37], Alexa 647 [5] and PE [78] fluorophores.

To mitigate the self-quenching effect, a straightforward approach is to decrease the surface density of anchored fluorophores, thereby increasing the separation between neighboring fluorophore molecules. We employed two distinct strategies for achieving this:

- *Fluorophore pre-bleaching.* In this method, the solution containing fluorophores was exposed to illumination from a halogen lamp, leading to partial photobleaching of the fluorophores. This approach is particularly effective for fluorophores that are highly susceptible to bleaching, such as FITC.

- *Co-adsorption of fluorophore or fluorescently labelled antibody with non-labelled competitor.* The protocols outlined in Chapter 3 can be adapted to reduce the surface density of fluorophores through the co-adsorption of either the fluorophore itself or a fluorescently labeled antibody in the presence of a non-labeled competitor.

To assess the surface densities at which fluorophores become susceptible to self-quenching, we applied these two strategies to a simple scenario involving the binding of biotinylated fluorophores to either a planar surface or the surface of microbeads.

A.5.1 Evaluating the self-quenching limit of b-FITC by its pre-bleaching

Fluorophore pre-bleaching presents a straightforward approach to mitigate self-quenching effects without relying on the mechanisms of co-adsorption of different species. We assume that such method preserves the chemical structure of the anchor tag attached to the fluorophore and binding affinity of pre-bleached and non-bleached fluorophores.

In our investigation, we employed biotinylated FITC fluorophores, known for their susceptibility to bleaching. SAv-coated microbeads were used to assess the quenching impact of bound b-FITC. The motivation for investigating the quenching properties of FITC fluorophores stemmed from our extensive use of this molecule for visualizing SAv and TAv monolayers, as detailed in Section 2.2.2.2.

The biotinylated fluorophore solution was divided into two vials, one of which underwent an extended preliminary bleaching process lasting 2 hours. Subsequently, bleached and non-bleached solutions were mixed in various molar ratios and employed to functionalize the SAv-coated microbeads (see Fig. A.1A). Flow cytometry was utilized to measure the fluorescence intensity from the functionalized beads (see Fig. A.1B). Notably, beads functionalized with bleached b-FITC exhibited only about 2% of the fluorescence intensity compared to those functionalized with non-bleached b-FITC, indicating substantial fluorophore bleaching over the 2-hour period.

The relationship between fluorescence intensity and the fraction of non-bleached b-FITC fluorophore is presented in Fig. A.1C. The curve shows a linear increase in fluorescence intensity for low fractions of fluorescent molecules (below 20%), followed by a saturation phase for higher fractions of non-bleached b-FITC and a slight decrease for the largest percentages. This suggests that when more than approximately 20% of the available binding sites on the bead surface are occupied by fluorescing molecules, self-quenching induces a deviation from linearity in the relationship between the surface concentration of fluorescing molecules and the measured fluorescent signal. Therefore above about 20% occupation of the binding sites by fluorescing molecules, the fluorescent signal cannot be considered as linearly dependent on the surface concentration of

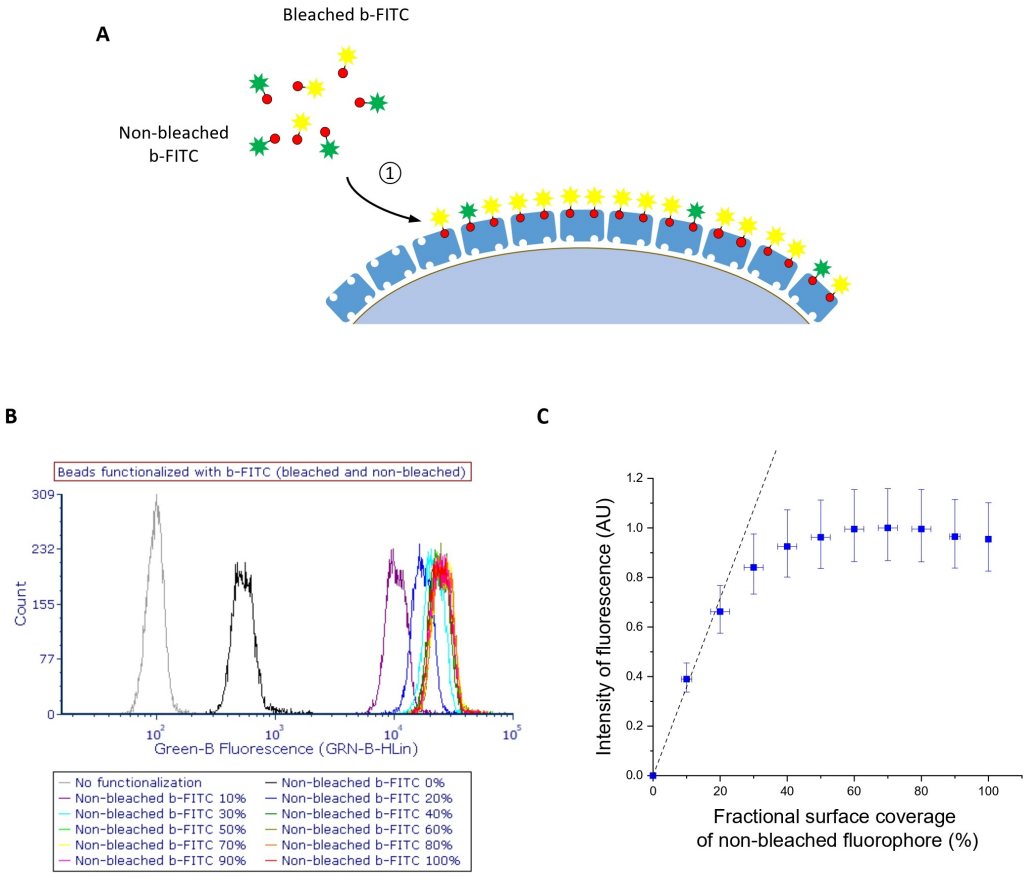

Figure A.1: Quantifying the quenching effect on microbeads. **A.** Schematic drawing of beads functionalization with partially bleached b-FITC: ① adsorption of partially bleached b-FITC. **B.** Fluorescence histograms obtained by flow cytometry of microbeads functionalized with different ratios of bleached/unbleached b-FITC (bleaching time: 2 hours) and non-functionalized beads. Statistics for the flow cytometry data was taken on at least 10000 events. **C.** Intensity of fluorescence for the beads presenting different fractions of non-bleached FITC fluorophore at their surface. Conditions: bead concentration: 0.25% w/v, $c_{\text{bleached b-FITC}} + c_{\text{non-bleached b-FITC}} = 14$ M was maintained constant, functionalization time: 1 hour. Data points represent the median of detected events, with error bars along the vertical axis indicating the interquartile range (75th and 25th percentiles), and error bars along the horizontal axis representing uncertainty in b-FITC and bleached b-FITC concentration. Dashed line – linear fit for the range of surface density < 10% of non-bleached b-FITC.

fluorescent molecules. As the surface density of active fluorophores increases, the quenching effect becomes more pronounced, resulting in decreased total measured fluorescence for the highest fractions (90-100% of active fluorophores).

In summary, our experiment demonstrates that to mitigate self-quenching effects affecting the measured fluorescence signal on microbead surfaces, it is essential to reduce the density of fluorescing b-FITC fluorophores to at least 10% of the maximum capacity. This upper limit should also safely apply to the other fluorophores of relevance to this work, such as Alexa 568 or PE, as they were found to be less susceptible to self-quenching than FITC [97, 172].

A.5.2 Evaluating self-quenching limits of FITC and Alexa 647 fluorophores by co-adsorbing them with non-labelled competitor

In the case of fluorophores with higher resistance to bleaching, such as Alexa fluorophore, we evaluated the self-quenching effect by varying the surface density of biotinylated fluorophores. This was achieved by co-adsorbing them with free biotin, a method detailed in Section 3.2.

In the subsequent experiments, we employed a streptavidin monolayer on a supported lipid bilayer as an anchorage platform and utilized confocal microscopy to visualize the biotinylated fluorophores that were bound to it. We investigated two types of biotinylated fluorophores, b-FITC and b-Alexa 647, to assess the quenching differences arising from their distinct chemical structures. Our primary motivation for studying the quenching properties of the Alexa fluorophore stemmed from the use of Alexa 647-labeled antibodies in our experiments to stain surface-bound P-selectin. Therefore, we aimed to determine the surface density at which the self-quenching effect begins to impact the relationship between the detected signal and the fluorophore's surface density.

The formation of SLB-based streptavidin monolayers followed the protocol outlined in Chapter 2. Biotinylated fluorophores (b-FITC or b-Alexa 647) were mixed with free biotin in molar ratios determined by Equation 3.5 and exposed to the streptavidin monolayer, as illustrated in Figure A.2A-B. The resulting curves, depicting the relationship between fluorescence intensity and the fraction of surface-bound fluorophore, are presented in Figure A.2C-D.

The curve obtained for the b-FITC fluorophore closely resembles the one shown in Figure A.1B, with a minor distinction being the extension of the linear portion of the curve up to about 30% surface coverage by b-FITC. This difference can be attributed to variations in the surface densities of SAv between the microbeads and the SLB platform.

For different surface fractions of b-Alexa, the dependence exhibits a linear increase within the range of surface densities up to 30%, followed by a plateau phase for higher fluorophore coverages. Overall, both fluorophores exhibit fairly similar self-quenching limits.

By leveraging the spectroscopic ellipsometry experiments conducted with the same anchorage platform and employing the identical functionalization protocol for SLB and SAv formation as in the present experiments, we can quantitatively evaluate the quenching limits for b-FITC and b-Alexa 647 fluorophores. The reference value for the maximal density of biotin-binding sites (Γ_{as} = 6.8 ± 0.1 pmol/cm^2) represents 100% fractional coverage of the fluorophores. Consequently, the self-quenching limit for b-FITC, which becomes apparent at approximately 40% of the maximum surface coverage, corresponds to approximately 2.7 pmol/cm^2. For b-Alexa, the density at which the quenching effect initiates is approximately 2.0 pmol/cm^2.

A.5.3 Quantitative measurement of the densities of biotinylated fluorophores

Following our assessment of the self-quenching limits of FITC and Alexa 647 fluorophores, our objective was to determine the conditions under which fluorescence intensity would exhibit a linear relationship with the surface-anchored biotinylated fluorophore density across the entire range of surface densities. This comprehension was crucial for the comparative analysis of biotin-binding

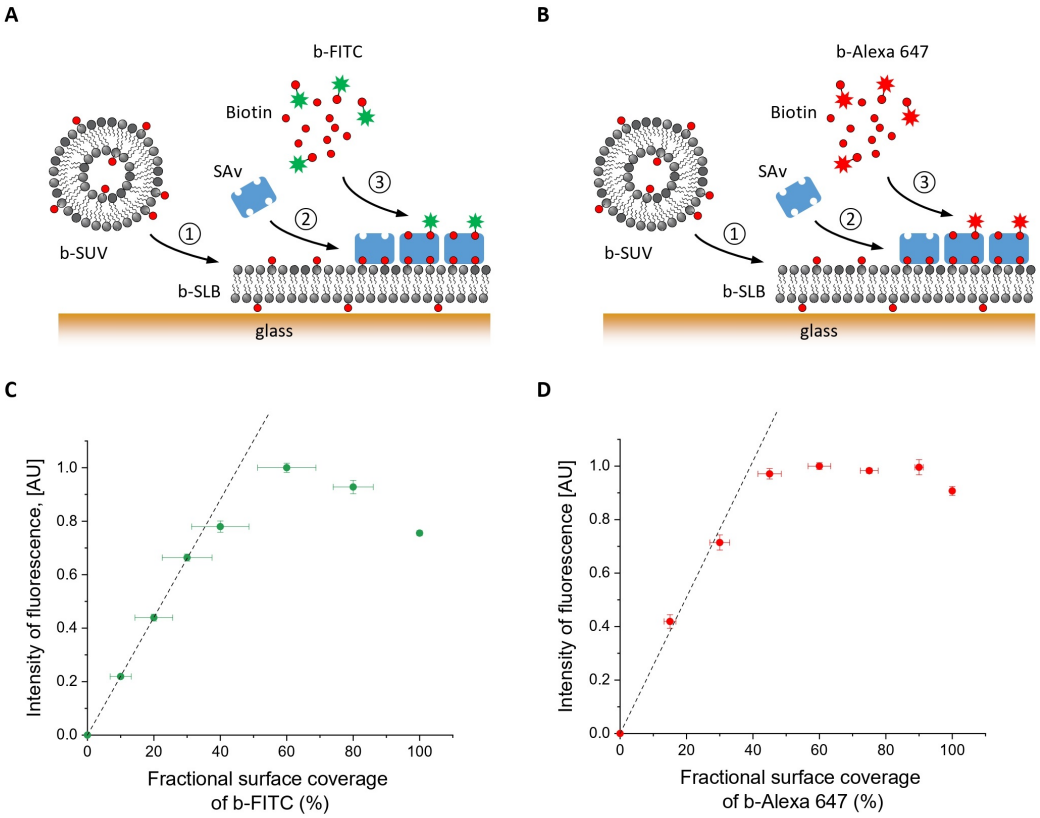

Figure A.2: Quantifying the quenching effect on different fluorophores. A-B. Schematic drawing of the surface functionalization: ① SLB formation, ② SAv monolayer formation, ③ co-adsorption of b-FITC **(A)** or b-Alexa **(B)** and biotin. **C-D.** Normalized fluorescence intensity measured with confocal microscopy for surfaces functionalized with different mixing ratios of b-FITC **(C)** or b-Alexa **(D)** and biotin. The horizontal axis shows the fractional surface coverage of fluorophore predicted according to Eq. 3.5 The black dashed lines through the origin confirms the expected linear trend for low surface concentrations (slope for b-FITC: 0.022 ± 0.004; for b-Alexa: 0.025 ± 0.002). Conditions: $c_{b\text{-FITC}} + c_{biotin}$ = 14 µM and $c_{b\text{-Alexa}} + c_{biotin}$ = 14 µM were maintained constant, with $c_{b\text{-FITC}}$, $c_{b\text{-Alexa}}$, and $c_{b\text{-biotin}}$, determined according to Eq. 3.5 ($\varepsilon <$ 0.25).

site densities across different anchoring platforms (SLB-based streptavidin or traptavidin, SAv-coated microbeads). Building upon the earlier findings, we introduced a partial pre-bleaching step for the fluorophores prior to their co-adsorption with free biotin.

This experiment involved b-FITC fluorophore binding to both the SLB-based SAv monolayer (Fig. A.3A) and SAv-coated microbeads (Fig. A.3B). For plane surfaces (co-adsorption in stagnant conditions), we employed molar ratios defined by Eq. 3.5, while for the microbeads (co-adsorption under shaking conditions), we used the ratios specified by Eq. 3.8.

Figure A.3C illustrates the relationship between the fluorescent signal and the fraction of surface-bound pre-bleached b-FITC, compared with a similar curve using non-bleached b-FITC fluorophore. Notably, partial pre-bleaching resulted in a highly satisfactory linear relationship, confirming the successful elimination of the self-quenching effect.

A similar test conducted with SAv-coated microbeads is depicted in Fig. A.3D. Partially pre-bleached fluorophores also displayed a linear relationship between the detected signal and the surface fraction of b-FITC on the microbead surface. The maximal fluorescence intensity was lower than that observed on the SLB platform, primarily due to variations in the pre-bleaching time for b-FITC: 30 minutes for plane surfaces and 2 hours for microbead functionalization.

In summary, these data demonstrate that fluorophore bleaching effectively eliminates the self-quenching effect, even at high surface densities of bound molecules.

A.5.4 Quantitative measurement of the density of surface-bound protein

Finally, we investigated the self-quenching phenomenon in a more intricate molecular context, specifically involving P-selectin anchored to the surface through the b-ZZ adapter protein, which, in turn, is bound to a streptavidin monolayer on a SLB (Fig. A.4A). We explored various surface coverages of b-ZZ and subsequently P-selectin, employing two staining protocols. Given the resistance of our P-selectin antibodies to bleaching, which are labeled with Alexa 647, we adopted a co-adsorption strategy for fluorescently labeled and non-labeled molecules.

In the first set of experiments, we stained P-selectin molecules exclusively with Alexa 647-labeled P-selectin antibodies (represented by red circles in Fig. A.4B-C). In the second set, we pre-mixed fluorescently labeled P-selectin antibodies with non-labeled antibodies from the same clone in a molar ratio of [1:9] (indicated by green squares in Fig. A.4B-C). Considering that the molecular weight of the AKR4 P-selectin antibody (approximately 91 kDa) is significantly greater than that of the Alexa fluor tag (about 1200 g/mol), we assumed approximate molecular weight equality between labeled and non-labeled molecules and assumed their binding affinities to P-selectin to be similar. The [1:9] ratio was chosen based on our previous experiments (Fig. A.2D) to ensure that the fraction of Alexa-labeled molecules was well below 30% of the maximum surface coverage.

The resulting curves depicting the fluorescent signal as a function of the b-ZZ surface fraction illustrate that the use of a mixture of labeled and non-labeled P-selectin antibodies led to a significant (approximately fivefold) reduction in fluorescence intensity (Fig. A.4B). However, both curves exhibited the same characteristic pattern, with a linear increase up to approximately 40% of b-ZZ surface coverage, followed by a plateau phase at higher surface fractions. When these two curves were normalized to the maximum signal value (Fig. A.4C), it became evident that they essentially overlapped. As previously discussed in Section 3.3.3.3, the plateau phase in both graphs is attributed to steric hindrance, preventing P-selectin from occupying more than 40% of the available Fc-binding sites. It remains an open question whether the self-quenching effect between Alexa-labeled P-selectin antibodies also occurs at this surface coverage or if it is observable at higher surface coverages.

These experiments demonstrate that both mixed and non-mixed fluorescent antibodies can be employed to quantify the surface density of anchored P-selectin. In subsequent tests, we opted to use the mixture of Alexa-labeled and non-labeled antibodies in a [1:9] ratio.

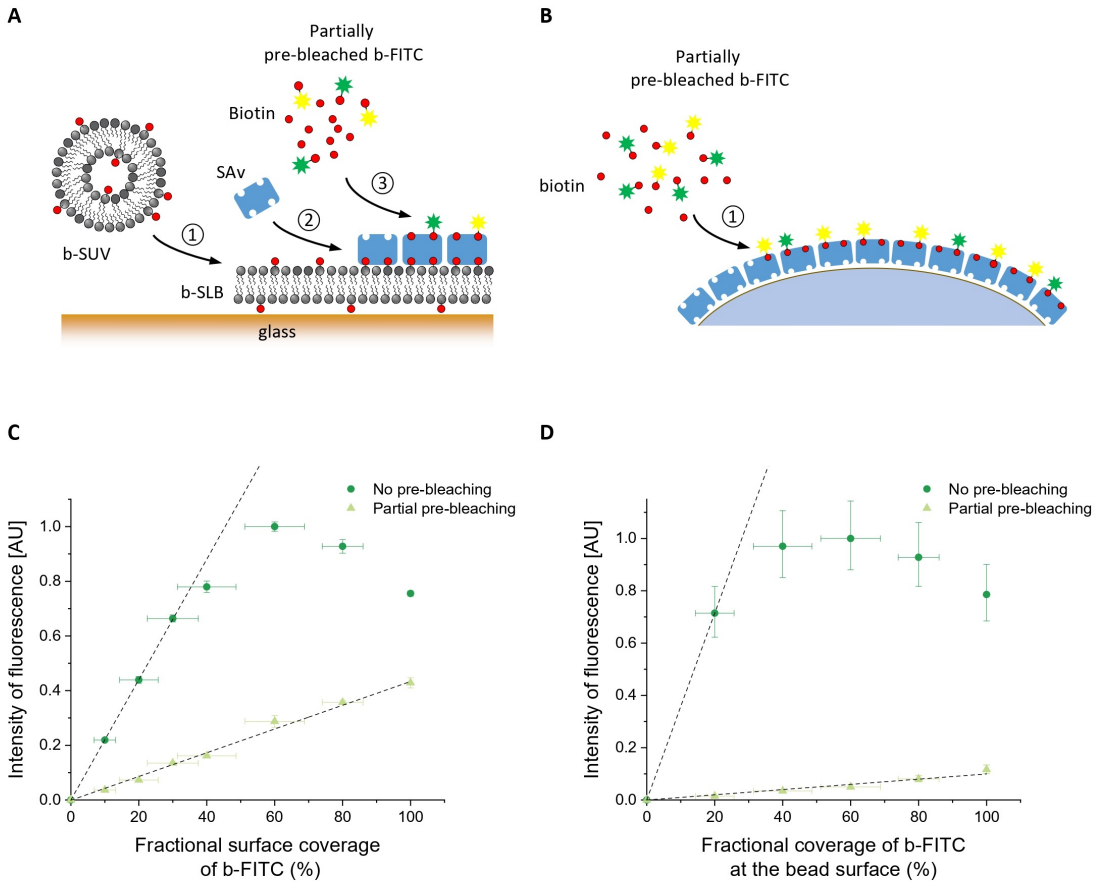

Figure A.3: Quantitative measurement of fluorescence on a plane surface and on microbeads. A. Schematic drawing of the surface functionalization: ① SLB formation, ② SAv monolayer formation, ③ co-adsorption of partially pre-bleached b-FITC and biotin. **B**. Schematic drawing of beads functionalization with b-FITC: ① co-adsorption of partially pre-bleached b-FITC with biotin. **C.** Normalized fluorescence intensity measured with confocal microscopy for surfaces functionalized with different mixing ratios of partially pre-bleached b-FITC (bleaching time: 30 min) and biotin (light green triangles, same data as in Fig. 3.2. Normalized fluorescence intensity for surfaces functionalized with different mixing ratios of non-bleached b-FITC and biotin (dark green circles). The horizontal axis shows the fractional surface coverage of fluorophore predicted according to Eq. 3.5. The black dashed lines through the origin confirm the expected linear trend for partially pre-bleached b-FITC (slope: (slope: 0.0043 ± 0.0002)) and for the range of low surface densities of non-bleached b-FITC (slope: 0.022 ± 0.004). Conditions: $c_{b-\,\mathrm{FITC}} + c_{\mathrm{biotin}} = 14\mu\mathrm{M}$ was maintained constant. **D.** Intensity of fluorescence measured from the beads with different fraction of partially pre-bleached FITC fluorophore (bleaching time: 2h) at their surface (light green triangles, same data as in Fig. 4.2. Intensity of fluorescence measured from the beads with different fraction of non-bleached FITC (dark green circles).The horizontal axis shows the fractional surface coverage of fluorophore predicted according to Eq. 3.8. Conditions: bead concentration: 0.25% w/v, $c_{\mathrm{bleached\ b\text{-}FITC}} + c_{\mathrm{non\text{-}bleached\ b\text{-}FITC}} = 14\mu\mathrm{M}$ was maintained constant, functionalization time: 1 hour. The flow cytometry data was taken on at least 10000 events. Data points represent the median of detected events, with error bars along the vertical axis indicating the interquartile range (75th and 25th percentiles), and error bars along the horizontal axis representing uncertainty in b-FITC and bleached b-FITC concentration. Dashed lines – linear fits for partially pre-bleached b-FITC (slope: (slope: 0.0099 ± 0.0008)) and for the range of surface densities < 20% of non-bleached b-FITC (slope: 0.035 ± 0.005).

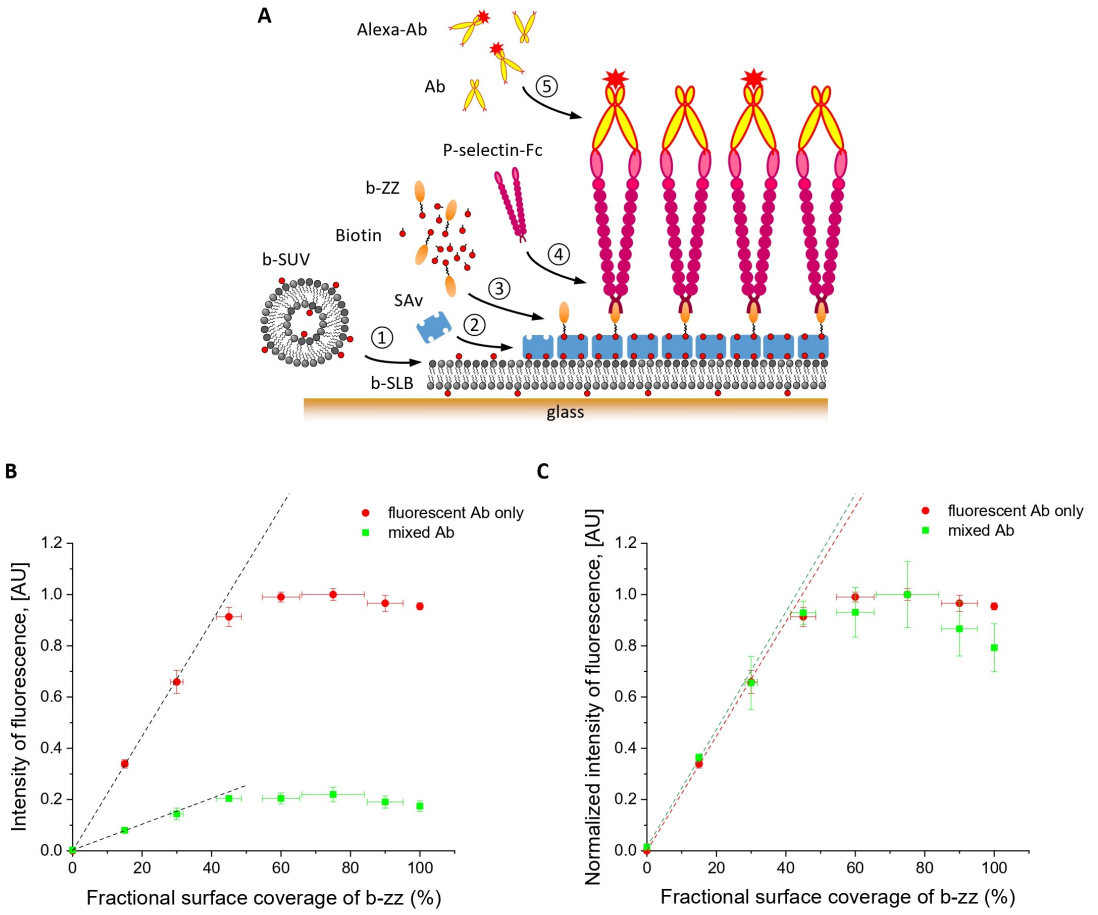

Figure A.4: Quantitative measurement of fluorescence at the surfaces functionalized with P-selectin. **A.** Schematic drawing of the surface functionalization: ① SLB formation, ② streptavidin monolayer formation, ③ co-adsorption of b-ZZ and biotin, ④ P-selectin-Fc anchorage, ⑤ P-selectin staining with the mix of fluorescent (Alexa 647) and non-fluorescent antibodies. **B.** Intensity of fluorescence measured with confocal microscopy for surfaces functionalized with different surface densities of b-ZZ (and, subsequently, P-selectin). The red curve shows demonstrated the intensity of fluorescence detected with the use of pure Alexa-labelled P-selectin antibodies (slope for the low surface coverages of b-ZZ: 0.022 ± 0.001), green curve – with the use of the mix of Alexa-labelled and non-labelled (1:9) P-selectin antibodies (same data as in Fig. 3.8, slope for the low surface coverages of b-ZZ: 0.0050 ± 0.0003). The horizontal axis shows the predicted$\Gamma_{b-ZZ,sat}$ calculated with the use of the Eq. 3.5. **C.** Same data as in (B) with the intensity of fluorescence normalized to the maximum value of each of the curves. Green and red dashed lines show the linearity for low surface densities for fluorescent antibodies only (slope: 0.022 ± 0.001) and for the mix of antibodies (slope: 0.023 ± 0.001).

A.6 Summary

In preceding sections, various aspects related to the quantitative assessment of receptor surface density through fluorescence analysis were discussed. Table A.1 summarizes the key findings and provides practical recommendations for quantifying fluorescence through confocal microscopy and flow cytometry.

Table A.1: Guidelines for quantitative fluorescence measurement via confocal microscopy and flow cytometry.

Aspect	Confocal microscopy	Flow cytometry
Reference value for the maximal surface density of binding sites	Density of biotin binding sites on SAv monolayer defined by spectroscopic ellipsometry	Data on the maximal functionalization capacity of microbeads provided by the manufacturer (if this is unknown, a quantitative relative measurement can be performed).
Standardized fluorescence detection protocol	Optimal in-focus position characterized by maximum detected signal intensity; visible with slight sample surface tilt	Not applicable
Laser stability over time	Reference image: laser reflection detected from the coverslip	Commercially available fluorescent calibration particles
Avoiding quenching effect	Partial pre-bleaching of fluorophores or co-adsorption of fluorescently labelled molecules with non-labelled competitors	

While these protocols were initially developed specifically for our model system to reliably assess the surface receptor density after functionalization, they hold intrinsic interest and can be adapted for various applications in surface chemistry. These considerations, combined with the theoretical insights into co-adsorption mechanisms presented in Chapter 3, offer the potential to establish quantification protocols for other types of surface-bound receptors. Specifically, the protocols for quantifying receptor density on the surface of microbeads provide a novel tool for creating calibration curves for bead functionalization and accurately measuring the surface density of bound receptors.

These approaches, however, have certain limitations, primarily related to the choice of fluorophores for fluorescence measurements. In cases of fluorophore bleaching, it is crucial to confirm that the illumination with light indeed results in a decrease in total fluorescence from the solution. This can be achieved, for instance, through the use of fluorometry.

Furthermore, some commercially available antibodies are labeled with tandem dyes – conjugates of two different covalently attached fluorophores, where one serves as the donor and the other as the acceptor. These tandem dyes behave as a single fluorophore with the excitation properties of the donor and the emission properties of the acceptor [73]. However, they introduce additional complexities to the bleaching procedure due to the possibility of fluorescence resonance energy transfer (FRET) effects. Consequently, the use of such fluorophores should be approached with caution, as they are not ideal for the approaches presented here.

B

Supplementary Information

B.1 Supplementary Methods

B.1.1 Analysis of the validity range of Eqs. 3.5 and 3.8

This section presents a comprehensive analysis of the validity range of the 'perfect sink' approximation underpinning equations 3.5 and 3.8.

Mass-transport limited binding

The assumption of mass-transport limited binding suggests that the surface acts like a perfect sink, with all arriving molecules binding rapidly and maintaining a concentration of zero near the surface during binding. However, this assumption fails as the surface density of anchors approaches saturation. At this point, solute concentration near the surface increases over time and eventually approaches the bulk concentration. Additionally, the assumption of mass transport limited binding can fail even before saturation if the intrinsic binding rate k_{on} is low.

Equations 3.5 and 3.8 hold true for any binder size and intrinsic binding rate when both binders share the same hydrodynamic size ($R_2/R_1 = D_1/D_2 = 1$) and intrinsic binding rate ($k_{\mathrm{on},1}/k_{\mathrm{on},2} = 1$), regardless of whether the perfect sink approximation applies during adsorption. These conditions make mass-transport limited binding and kinetically limited binding produce the same relationship: $c_2/c_1 = \Gamma_{2,\mathrm{sat}}/\Gamma_{1,\mathrm{sat}}$. However, these strict requirements are challenging to meet in experiments, limiting the practical utility of this simple relationship.

To evaluate the validity of the perfect sink approximation when binders differ in size, we compare the binding timescale

$$\tau_{\mathrm{binding}} = \frac{1}{k_{\mathrm{on}}\, c} \tag{B.1}$$

with the time needed for sufficient molecules to reach the surface and saturate anchorage sites. This time differs for stationary solutions and convective fluid transport. In stationary solutions, the transport time, simplified as

$$\tau_{\mathrm{transport,still}} = \frac{\pi}{4}\frac{\Gamma_{\mathrm{as}}^2}{Dc^2} \sim \frac{\Gamma_{\mathrm{as}}^2}{Dc^2} \tag{B.2}$$

while in convective fluid transport, a binder-depleted layer forms near the surface. At quasi-steady state, binder concentration and depletion layer thickness δ remain constant (but might vary across the surface). Binders must diffuse through this layer to reach the surface, leading to the transport time

$$\tau_{\text{transport,flow}} = \frac{\Gamma_{\text{as}}\delta(xy)}{Dc} \tag{B.3}$$

These relationships lead to the ratios

$$\varepsilon_{\text{still}} = \frac{\tau_{\text{binding}}}{\tau_{\text{transport,still}}} = \frac{4}{\pi}\frac{Dc}{k_{\text{on}}\,\Gamma_{\text{as}}^2} \sim \frac{Dc}{k_{\text{on}}\,\Gamma_{\text{as}}^2} \tag{B.4}$$

and

$$\varepsilon_{\text{flow}} = \frac{\tau_{\text{binding}}}{\tau_{\text{transport,flow}}} = \frac{D}{\Gamma_{\text{as}}\,\delta k_{on}} \tag{B.5}$$

which are introduced in Eqs. 3.9 and 3.10. The perfect sink approximation holds when ε tends to zero.

Our recent work [82] describes in detail the numerical simulations employed to assess the how well Equations 3.5 and 3.8 reflect real experimental scenarios.

Conditions for mass-transport limited binding are readily met for high affinity interactions, such as the interaction of biotin with streptavidin, as shall be illustrated through two worked examples.

Worked example for binding from stagnant solution.

We consider interactions between biotin and streptavidin, for which $k_{\text{on}} = 10^7\text{M}^{-1}\ \text{s}^{-1}$ [67]. Considering that any biotinylated molecule will diffuse at a rate that is smaller than plain biotin ($D \leq 580\mu\text{m}^2/\text{s}$), and taking $\Gamma_{\text{as}} = 6.8\text{pmol/cm}^2$ (Figure 3.3C), we estimate $\varepsilon_{\text{still}} < 0.02c/\mu\text{M}$. This analysis shows that mass-transport limited competitive binding is readily achieved with sub-μM concentrations of biotinylated binders.

The thickness of the depletion layer in still solution for each binder i increases with time as $\delta_{i,\text{still}} \sim \sqrt{D_i t}$. We can use the surface saturation time $\tau_{\text{still,max}}$ to estimate the maximal extension $\delta_{i,\text{ still,max}}$ of this layer.

At this time, the surface density of binder i is given (Eq. 3.1) by

$$\Gamma_i = 2c_i\sqrt{\frac{D_i\tau_{\text{still,max}}}{\pi}} \tag{B.6}$$

with

$$\sum_{i=1}^{N}\Gamma_i = \Gamma_{\text{as}} \tag{B.7}$$

.

Combining these equations gives

$$\sqrt{\tau_{\text{still,max}}} = \frac{\Gamma_{\text{as}}}{\sum_{i=1}^{N} 2c_i\sqrt{\frac{D_i}{\pi}}} \tag{B.8}$$

and, eventually,

$$\delta_{i,\text{ still,max}} \sim \frac{\sqrt{\pi}}{2}\frac{\Gamma_{\text{as}}\sqrt{D_i}}{\sum_{j=1}^{N} c_j\sqrt{D_j}} \tag{B.9}$$

To match the assumption of an infinite reservoir of molecules in solution, one should ensure that $\delta_{i,\text{ still,max}} < H$, with H the thickness of the liquid reservoir in the direction perpendicular to the surface being functionalized. A simpler (albeit less stringent) expression is obtained when considering the upper bound of the numerator and the lower bound of the dominator in Eq. B.9, as

$$\delta_{\text{still,max}} \lesssim \frac{\sqrt{\pi}}{2}\frac{\Gamma_{\text{as}}}{c_{\text{tot}}}\sqrt{\frac{D_{\text{max}}}{D_{\text{min}}}} = \frac{\sqrt{\pi}}{2}\frac{\Gamma_{\text{as}}}{c_{\text{tot}}}\sqrt{\frac{R_{\text{max}}}{R_{\text{min}}}} \tag{B.10}$$

where D_{max} and D_{min} are the diffusion constants of the smallest (R_{min}) and largest (R_{max}) binder in the process, and c_{tot} is the total concentration of binders. Taking as an example the experimental scenario in Figure 3.3C ($\Gamma_{\text{as}} = 6.8\text{pmol/cm}^2$, $R_{\text{b-Zz}}/R_{\text{biotin}} = 5$, and $c_{\text{tot}} = 0.625\mu\text{M}$), we estimate $\delta_{\text{still,max}} < 100\mu\text{m}$ which is much smaller than the thickness of the well ($H > 1mm$), as required.

B.1.2 Worked example for binding with convective fluid transport

To model the conditions of QCM-D experiments, we consider a surface with anchor site density Γ_{as} forming one of the walls of a slit of width $2w$, height $2h$, and length l. A solution with surface binders flows along the slit with volumetric flow rate Q. The inlet of the slit is located at $x = 0$, and the outlet at $x = l$. The binders are homogeneously distributed throughout the solution at the inlet with concentration c. In quasi-steady state, the binder surface density is described by [60]:

$$\Gamma(x,t) \approx D^{2/3}\left(\frac{3Q}{4h^2wx}\right)^{1/3} ct = \frac{D}{\delta_{\text{flow}}} ct \tag{B.11}$$

which gives a depletion layer thickness

$$\delta_{\text{flow}} = \left(\frac{4Dh^2wx}{3Q}\right)^{1/3} \tag{B.12}$$

Typical conditions for QCM-D experiments are $2w = 11mm$, $2h = 0.2mm$, and the sensing area is centred around $x = 5.5mm$. The table below provides δ and $\varepsilon_{\text{flow}}$ (Eq. B.5) for the two flow rates used in this study, considering $k_{\text{on}} = 10^7\text{M}^{-1}\ \text{s}^{-1}$, $\Gamma_{\text{as}} = 6.1\text{pmol/cm}^2$ (Figure 3.4D), and $D \leq 580\mu\text{m}^2/\text{s}$. It can be seen that the QCM-D flow conditions are within the mass-transport limited regime ($\varepsilon_{\text{flow}} \lesssim 0.01$), and that the depletion layer thickness is nominally inferior to the chamber height ($\delta_{\text{flow}} < 2h$). That we observed deviations from the expected linear dependence in Figure 3.4 for $Q = 10$ to $20\mu\text{l/min}$ is most likely due to the assumed regular slit not representing the QCM-D chamber geometry very well, leading to a slight underestimation of δ_{flow}.

Q	δ_{flow}	$\varepsilon_{\text{flow}}$
10 μl/min	< 112 μm	< 0.0051
20 μl/min	< 89 μm	< 0.0064
200 μl/min	< 42 μm	< 0.014

A similar calculated was done for the microfluidic channel described in Chapter 5 with $2w = 0.5mm$, $2h = 0.1mm$, l = 1 cm. The flow rate Q used for the surface functionalization in the microfluidic channel was 20 µl/min. The flow conditions appeared to be within mass-transport limited regime ($\varepsilon_{\text{flow}} \lesssim 0.01$) with the depletion layer < 20 µm, much smaller than a channel height.

B.1.3 Protocol for microbead functionalization

B.1.3.1 Bead washing protocol

Microbeads, as provided by the supplier, are stored in a water solution containing EDTA, boric acid, sodium tetraborate, BSA, and other agents. Therefore, they require thorough washing in a

working buffer before use. Similarly, washing steps are essential between incubation steps involving different reagents to ensure the removal of excess reagents.

The newly established washing procedure is as follows:

1. Dilute 50 µL of microbead solution in HEPES buffer at a 1:29 ratio within a 1.5 mL Eppendorf tube.
2. Centrifuge the tube in a microcentrifuge at 13,400 rpm for 5 minutes. After centrifugation, the bead pellet should be visible at the bottom of the tube.
3. Remove the supernatant without disturbing the pellet, leaving approximately 50 µL of liquid at the tube's bottom.

All experiments included three rounds of washing before the beginning of the functionalization and between incubation steps. This procedure was chosen based on a previously established protocol [33].

Each washing step results in the loss of a fraction of the beads. The extent of bead loss during the washing process is sensitive to experimental handling, particularly the need for extra care during the removal of supernatant to prevent disturbance of the bead pellet. Depending on the specific experimental procedures, the loss of beads can range from 5 to 30% per washing step.

Furthermore, it has been observed that in some Eppendorf tubes, the formation of the bead pellet was worse compared to others, despite identical centrifugation conditions. Therefore, visual inspection of the bead pellet after each centrifugation step is crucial. A proper bead pellet should exhibit uniformity, settling at the bottom of the tube without any streaks of beads visible along the tube walls. In my project, I used Protein LoBind tubes from Eppendorf, Germany, as they consistently demonstrated good bead pelleting.

B.1.3.2 Selecting the reagent concentration for bead functionalization

It is essential to have a number of molecules in the incubation solution that exceeds the total number of available binding sites, ensuring saturation within the given incubation time. This section provides an example of estimating the number of available biotin-binding sites on the bead surface and selecting an appropriate reagent concentration based on this assessment. This approach was used in all experiments presented in this work.

Incorrect selection of the incubation concentration may lead to flow cytometry data displaying a broadened histogram peak (see Fig. B.9). This broadening suggests that not all beads were uniformly functionalized with the protein, and a fraction of the biotin-binding sites remained unoccupied.

Based on previously established protocols, the concentration of beads for functionalization was chosen as 0.25 % *w/v* (0.25 g of beads in 100 mL solution) within the reaction volume of 50 µL. This concentration ensured a sufficient quantity of beads for microscopy measurements in the flow assays. Consequently, the total mass of beads within this volume equals 0.125 mg.

The total number of beads in this volume can be calculated as:

$$N_{\text{beads}} = \frac{3m}{4\pi R^3 \rho} \tag{B.13}$$

where m – total mass of beads in reaction volume; R – bead radius, ρ – density of polystyrene beads.

Taking R = 7.5 µm, and ρ = 1.05 g/mL for polystyrene, the number of microbeads in the reaction volume of 50 µL was estimated to be 67200.

Bangs Laboratories provided a binding capacity of 0.036 µg biotin-FITC per milligram for the SuAv-coated microbeads. The binding capacity of Spherotech beads is unknown and was determined experimentally by comparing the fluorescent signal between Bangs Lab and Spherotech beads functionalized with pre-bleached b-FITC (please refer to Fig. 4.2D for details).

A binding capacity of 0.036 µg b-FITC per mg corresponds to 3×10^{13} b-FITC molecules per mg (taking $Mw_{\text{b-FITC}}$ = 732.8 g/mol), which gives 5.8×10^{7} biotin-binding sites per bead (corresponding to approximately 5 nm between the biotin-binding sites) and a concentration of 130 nM in the reaction volume of 50 µL. The minimal concentration of molecules required to occupy all the available biotin-binding sites on all the beads thus is 130 nM. However, this calculation does not account for potential bead loss during the washing process.

B.1.3.3 Estimating fractional bead loss during washing

To quantify the bead loss during the washing steps, several experimental measurements were conducted (Fig. B.8). Samples with a fixed number of beads were rinsed a defined number of times and then the total number of beads was estimated using flow cytometry. The fraction of beads lost per rinse was calculated using the following formula:

$$\alpha = 1 - \left(\frac{N_i}{N_0}\right)^{\frac{1}{i}} \tag{B.14}$$

where N_0 – initial number of beads, calculated based on the concentration provided by the supplier, N_i – final number of beads after i washing steps, determined through flow cytometry, i – number of washing steps.

Experimental results showed that the fraction of bead loss (α) typically ranged between 5% and 10% per washing step.

The number of beads after a certain number of washing steps can then be estimated as:

$$N_i = N_0(1-\alpha)^i \tag{B.15}$$

For the first functionalization step, i is set to 3 (indicating 3 washing steps before use). Assuming a bead loss fraction (α) of 10%, the minimum concentration of biotinylated species required for saturating all available binding sites is approximately **95 nM**.

For the second functionalization step (after a total of 6 rinsings) this required concentration decreases to **69 nM**. Therefore, each subsequent functionalization step in the protocol requires a lower minimum reagent concentration, leading to reduced reagent consumption.

The calculations outlined above are applicable to Bangs Lab beads with a binding capacity of 0.036 µg b-FITC per mg. In the case of Spherotech beads, their binding capacity was estimated to be approximately 2.2 times greater. Therefore, the minimum required incubation concentrations for Spherotech beads should be increased by a factor of 2.2 compared to Bangs Lab beads. It is advantageous to use concentrations 2-4 times higher than the minimum requirement, accounting for potential variations in bead number due to slight differences in experimental manipulations. In all the experiments described in this work, a concentration of **700 nM** or higher was utilized at all incubation steps, which led to homogeneous signal distribution observed by the flow cytometry. Therefore, it is essential to accurately assess the number of available binding sites and the number of molecules within the reaction volume to ensure uniform functionalization of all beads in the sample.

B.1.3.4 Bead incubation

To achieve uniform distribution of the receptors on the bead surface, it is crucial to maintain consistent mixing of the sample during incubation to prevent bead sedimentation. To accomplish this, I employed an vortex Eppendorf mixer set at a speed of 1000 rpm. This ensured that the beads remained suspended within the reaction volume and do not settle at the bottom of the tube.

The incubation time was adjusted to saturate all available binding sites. Given the complexity of assessing binding kinetics with flow cytometry, I utilized the QCM-D method to examine the binding dynamics of proteins of the comparable concentrations to the surface and the time

required to reach a plateau. In the case of b-CD44, saturation of the streptavidin monolayer was achieved within 30-40 minutes of incubation (Fig. B.7), while b-ZZ achieved binding in less than 10 minutes (Fig. 2.22). For PSGL-1-Fc, which, like P-selectin-Fc, is a large molecule, the steric hindrance at the surface prevented the full saturation on a dense b-ZZ layer, but the binding process significantly decelerated after 25 minutes of incubation (Fig. B.10).

However, QCM-D measurements on SLB-based streptavidin monolayers cannot be directly extrapolated to the microbead system. While the density of biotin-binding sites on the microbeads is comparable to that at the planar surface , the orientation of the SAv/SuAv attached to the surface of microbeads may differ from that of SLB-based streptavidin. The unpredictable orientation of SAv/SuAv at the bead surface can impede the binding of biotinylated species due to steric hindrance, consequently, this discrepancy may impact the total incubation time.

In light of these uncertainties, when incubating the beads with the protein of interest, we extended the incubation times by at least twofold compared to what the QCM-D experiments indicated to be required for saturation: 30 minutes for b-ZZ and 2 hours for larger proteins (b-CD44, PSGL-1, and antibodies).

B.2 Supplementary Figures

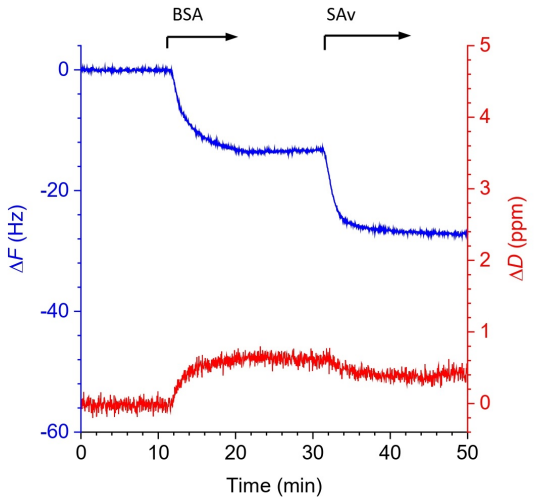

Figure B.1: SAM quality test and SAv monolayer formation affected by inadequate cleaning of QCM-D sensor and/or vial used for functionalization. The gold-coated QCM-D sensor and the glass vials were cleaned with a relatively limited volume of water and ethanol (less than 5 mL in total), while in the experiment shown in Fig. 2.10A the cleaning routine included using at least 20 mL of ultrapure water and ethanol. QCM-D frequency shifts (ΔF – blue line) and dissipation shifts (ΔD – red line) for the 5th overtone measured over time. Flow rate at all steps is 20 µL/min. The start and the duration of incubation with each sample are indicated with black arrows at the top of the graphs. Before and after each incubation step there were rinsing steps with HEPES buffer. BSA test for the non-specific binding to the SAM resulted in substantial response (ΔF = -13.5 ± 0.1 Hz and ΔD = 0.6 ± 0.1 ppm) indicating an SAM of a poor quality. Streptavidin monolayer formation resulted in the final shifts: ΔF = -13.7 ± 0.1 Hz and ΔD = -0.2 ± 0.1 ppm, which was much lower than expected (for example, in Fig. 2.10A ΔF for SAv binding is -26.3 ± 0.2 Hz). Conditions: BSA – 1.5 µM (100 µg/mL), SAv – 0.33 µM.

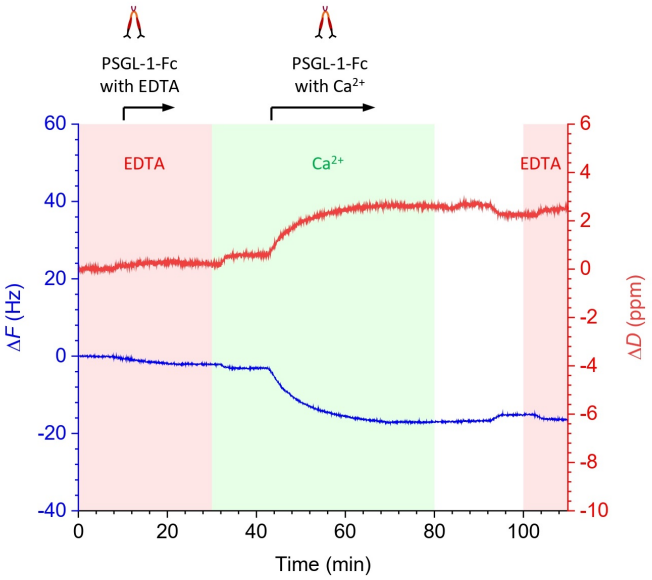

Figure B.2: Functionality test for PSGL-1 ligand binding on the layer presenting thick HA-280 brush. QCM-D frequency shifts (ΔF – blue line) and dissipation shifts (ΔD – red line) for the 5th overtone measured over time. Flow rate at all steps is 20 µL/min. The start and the duration of incubation with each sample are indicated with black arrows at the top of the graphs. The step not marked with arrows is rinsing with HEPES buffer. The layer was created on the molecular platform consisting of SLB (5% biotinylated SUVs) and SAv monolayer (final shifts for SLB formation: ΔF = -24.7 ± 0.1 Hz, ΔD = 0.13 ± 0.04 ppm; for SAv incubation: ΔF = -24.2 ± 0.1 Hz, ΔD = 0.4 ± 0.1 ppm). Final shifts: HA-280: ΔF = -27.9 ± 0.1 Hz, ΔD = 17.4 ± 0.1 ppm; b-ZZ: ΔF = -14.0 ± 0.1 Hz, ΔD = 0.56 ± 0.05 ppm; P-selectin-Fc: ΔF = -53.0 ± 0.1 Hz, ΔD = 6.0 ± 0.1 ppm; PSGL-1-Fc (with Ca^{2+}): ΔF = -15.8 ± 0.1 Hz, ΔD = 2.0 ± 0.1 ppm.

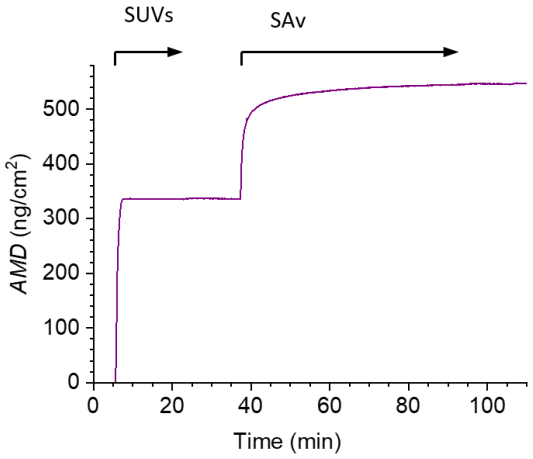

Figure B.3: Representative SE binding assay for the formation of SLBs and SAv monolayers. Shown is the areal mass density, AMD, determined from time-resolved SE analysis (with refractive index increments $dn/dc = 0.169$ cm^3/g, and 0.180 cm^3/g for SAv). The start and duration of the incubation with different samples are indicated by solid arrows atop the graph. There are rinsing steps with working buffer before and after each sample incubation step. The areal mass density of SAv at the end of the incubation process was 211 ± 9 ng/cm^2 (mean ± standard deviation) across all surface preparations (n = 8), illustrating good reproducibility of the surface preparation. This areal mass density corresponds to a molar surface density of 3.52 ± 0.15 pmol/cm^2. Conditions: SUVs – 50 μg/ml, containing 5 mol-% DOPE-CAP-biotin in a DOPC background; SAv – 0.33 μM.

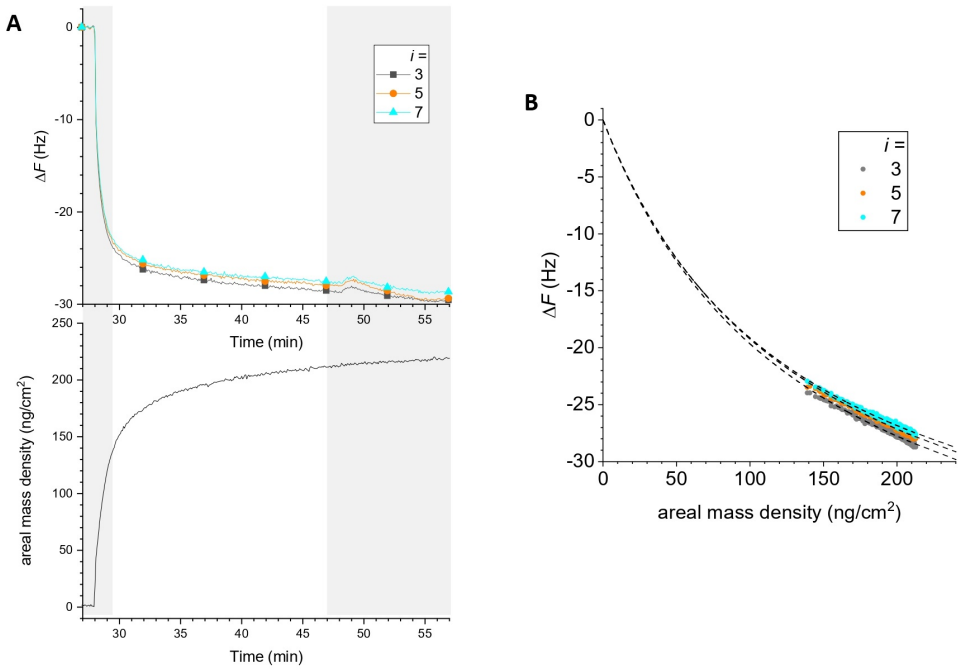

Figure B.4: Combined QCM-D/SE observation of SAv binding. This data was acquired and analyzed by R. P. Richter. **A.** Frequency changes for 3rd, 5th and 7th overtones (at the top) and areal mass density change (at the bottom) detected during the SAv binding. Times in grey mark data excluded from analysis (QCM-D data likely perturbed by temperature variations). **B.** Calibration curve relating frequency changes (for 3rd, 5th and 7th overtones) with the areal mass density. The black dashed lines show fits with $\Delta F = -\frac{AMD}{C(1-A+B\times AMD)}$; $C = 18.06\text{ng}/\left(\text{cm}^2\cdot\text{Hz}\right)$.

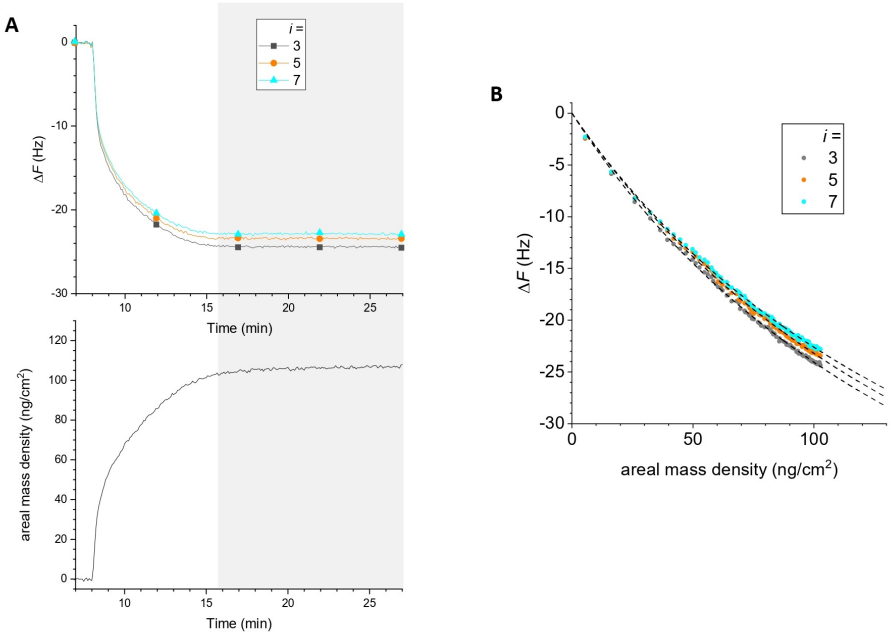

Figure B.5: Combined QCM-D/SE observation of b-ZZ binding. This data was acquired and analyzed by R.P. Richter. **A.** Frequency changes for 3rd, 5th and 7th overtones (at the top) and areal mass density change (at the bottom) detected during the b-ZZ binding. Times in grey mark data excluded from analysis (QCM-D data likely perturbed by temperature variations). **B.** Calibration curve relating frequency changes (for 3rd, 5th and 7th overtones) with the areal mass density. The black dashed lines show fits with $\Delta F = -\frac{AMD}{C(1-A+B\times AMD)}$; $C = 18.06\text{ng}/\left(\text{cm}^2\cdot\text{Hz}\right)$.

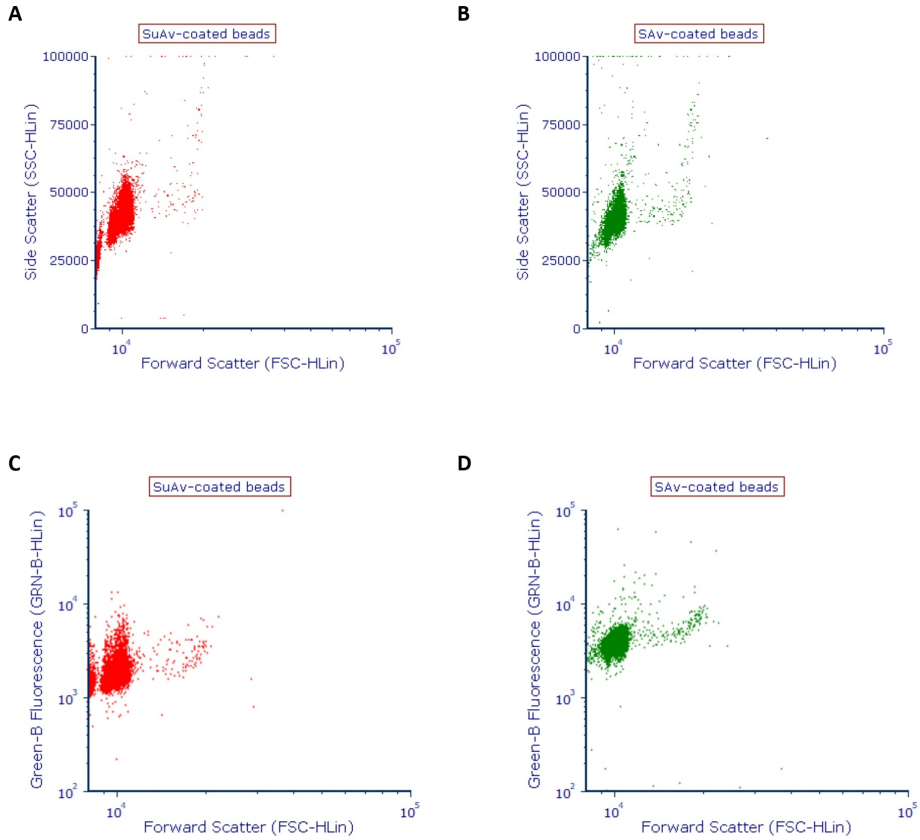

Figure B.6: Flow cytometry of SuAv-coated (A, C) and SAv-coated (B, D) beads demonstrating the homogeneity in bead size and bead functionalization with b-FITC. A-B. Forward scatter (FSC-H) and side scatter (SSC-H) of non-functionalized beads analyzed by flow cytometry. Each dot in the graph represents an event/bead. SuAv-coated beads exhibit some variability in size (two distinct point clouds are observed), whereas SAv-coated beads display more consistent and homogeneous size distribution. **C-D.** Forward scatter (FSC-H) and intensity of fluorescence excited in blue wavelength (488 nm) and detected in green wavelength range (510-521 nm) of beads functionalized with maximal surface density of b-FITC. SAv-coated beads demonstrate more homogeneous signal distribution than SuAv-coated beads. Conditions: bead concentration: 0.5% w/v, $c_{\mathrm{b-\ FITC}}$ = 14 M was maintained constant, functionalization time: 1 hour. The flow cytometry data was taken on 10000 events.

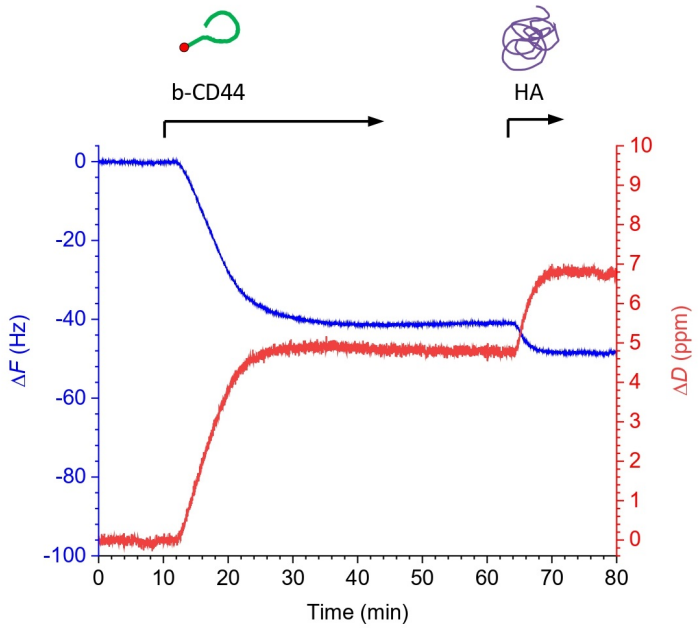

Figure B.7: Specific interaction between HA (250 kDa) and CD44. QCM-D frequency shifts (ΔF – blue line) and dissipation shifts (ΔD – red line) for the 5th overtone measured over time. Flow rate at all steps – 10 µL/min. The start and the duration of incubation with each sample are indicated with black arrows at the top of the graphs. Before and after each incubation step there were washing steps with HEPES buffer. b-CD44 was anchored on SAv monolayer created on SLB as described above. Final shifts for CD44 incubation: ΔF = -41.3 ± 0.2 Hz and ΔD = 4.8 ± 0.1 ppm, for HA binding: ΔF = -7.1 ± 0.2 Hz and ΔD = 2.0 ± 0.1 ppm. Conditions: c(CD44) = 59 nM, c(HA-250) = 20 nM.

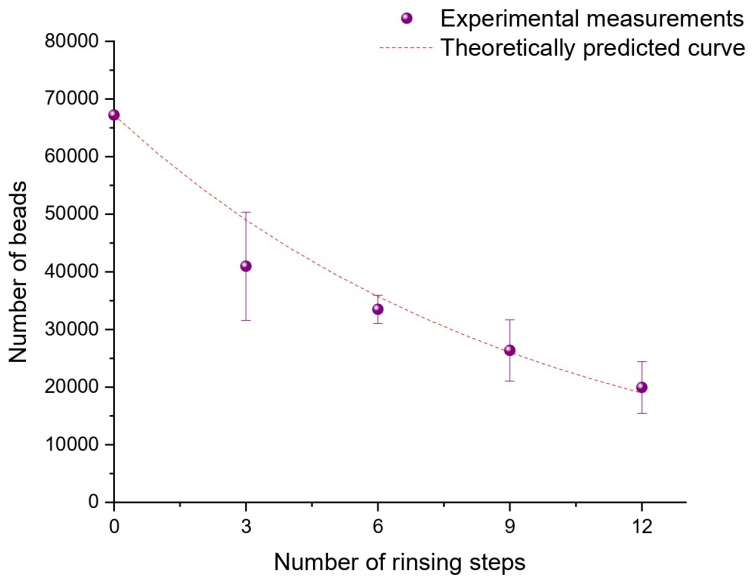

Figure B.8: Quantifying bead loss during washing steps. The violet spheres represent experimental data for the bead counts measured using flow cytometry. The error bars represent the standard deviation between different measurements. The red dashed line represents the curve described by the equation $N_{\text{final}} = N_{\text{init}}\,(1-\alpha)^N$, with initial bead count at 67,200 and a bead loss fraction (α) of 10%. Number of beads was determined as a number of events detected by the flow cytometer, the measurement was performed until less than 1 event/min was detected.

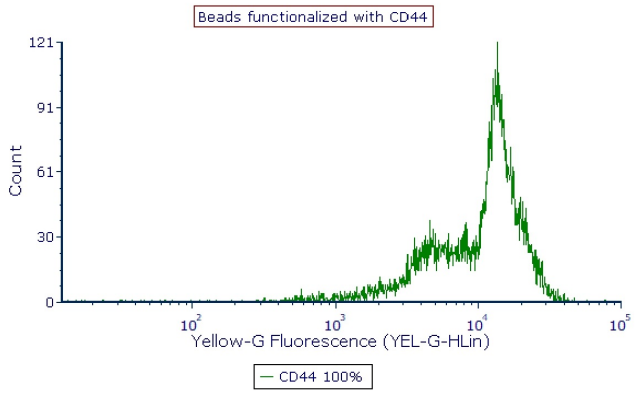

Figure B.9: Insufficient protein concentration leads to heterogeneous bead coating. The fluorescence histogram was obtained by flow cytometry for CD44 coated beads labelled with CD44 Alexa 532 antibodies and displays a widened peak, indicating incomplete functionalization of a fraction of the beads. Conditions: $c_{\text{b-CD44}}$ = 94 nM, incubation time: 1 hour. Antibody staining conditions ensured an excess of the antibody molecules in solution: Alexa 532-labelled and non-labelled antibodies were mixed in a molar ratio of 1:3, total concentration: 10 µg/mL, incubation time: 2 hours. When using sufficiently high concentrations of CD44 (e.g., 700 nM), the signal distribution was characterized by a single narrow peak (as shown in Fig. 4.3B.

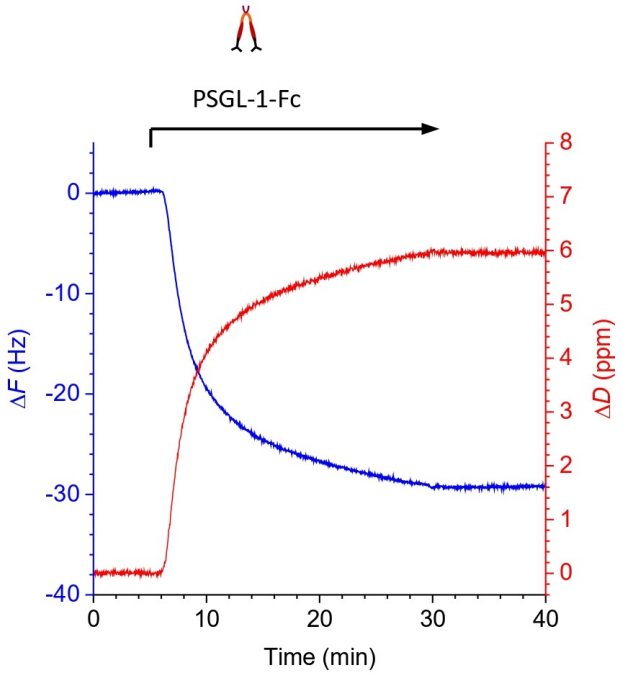

Figure B.10: PSGL-1 is stably binding to b-ZZ layer. QCM-D frequency shifts (ΔF – blue line) and dissipation shifts (ΔD – red line) for the 5th overtone measured over time. Flow rate at all steps – 10 µL/min. The start and the duration of incubation with PSGL-1 is indicated with a black arrow at the top of the graph. Before and after the incubation step there were washing steps with HEPES buffer. PSGL-1 was here incubated on a surface covered with b-ZZ anchored on a SAv monolayer on an SLB as demonstrated in Figure 2.22. Final shifts for PSGL-1 incubation: ΔF = -29.1 ± 0.1 Hz and ΔD = 5.9 ± 0.1 ppm. Conditions: c(PSGL-1) = 40 nM.

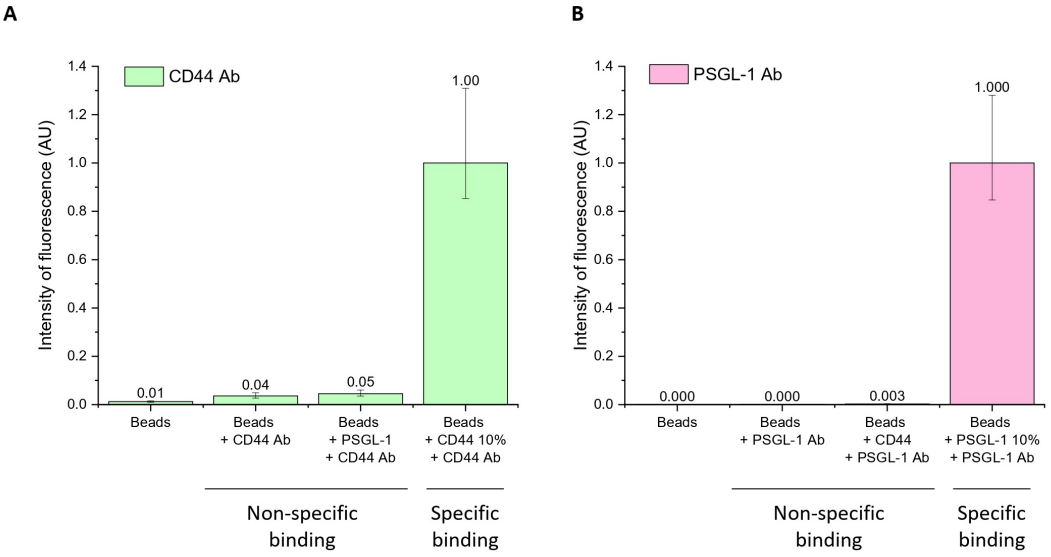

Figure B.11: CD44 and PSGL-1 antibodies show no ross-reactivity. A. Comparison between intensity of fluorescence from CD44 Alexa 532 antibodies on non-functionalized beads ("Beads + CD44 Ab"), beads presenting PSLG-1 ("Beads + PSGL-1 + CD44 Ab") and beads functionalized with 10% fractional surface coverage of CD44 ("Beads + CD44 10% + CD44 Ab") compared with the intensity measured from beads not stained with any antibody ("Beads"). **B.** Comparison between intensity of fluorescence from PSGL-1 PE antibodies on non-functionalized beads ("Beads + PSGL-1 Ab"), beads presenting CD44 ("Beads + CD44 + PSGL-1 Ab") and beads functionalized with 10% fractional surface coverage of PSGL-1 ("Beads + PSGL-1 10% + PSGL-1 Ab") compared with intensity of fluorescence from beads not stained with antibodies ("Beads). Conditions: bead concentration: 0.25% w/v, $c_{\text{b-CD44}} + c_{\text{biotin}} = 700$ nM; $c_{\text{b-ZZ}} + c_{\text{biotin}} = 700$ nM, incubation time: 2 hours. PSGL-1 incubation: $c_{\text{PSGL-1}} = 800$ nM, incubation time: 2 hours. Antibody staining conditions: Alexa-labelled and non-labelled CD44 antibodies were mixed in molar ratio (1:3), total concentration: 10 µg/mL, incubation time: 2 hours; PE-labelled and non-labelled PSGL-1 antibodies were mixed in molar ratio (1:3), total concentration: 10 µg/mL, incubation time: 2 hours. Columns represent the median of at least 10 0000 detected events, with error bars indicating the interquartile range (75th and 25th percentiles). The data in both graphs was normalized by the intensity of fluorescence for the case of specific binding.

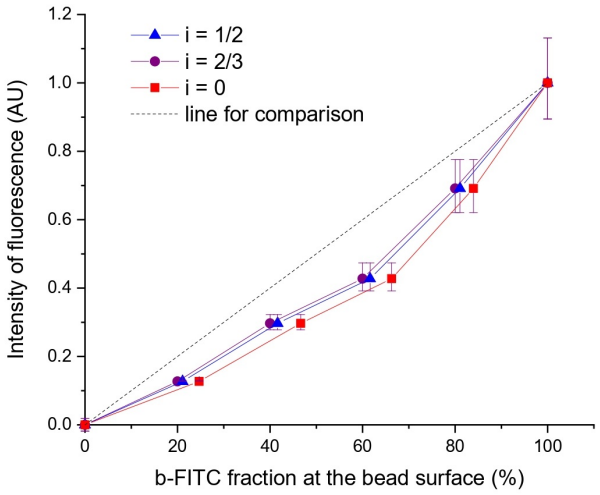

Figure B.12: Different scenarios of co-adsorption of b-FITC. Intensity of fluorescence measured from SAv-coated beads presenting different fractions of b-FITC at their surface, where predicted b-FITC fractions at the bead surface were recalculated for different binding scenarios $\frac{c_2}{c_1} = \left(\frac{R_2}{R_1}\right)^i \left(\frac{\Gamma_{as}}{\Gamma_{1,sat}} - 1\right)$: shaking conditions (i = 2/3) – violet circles; stagnant conditions (i = 1/2) - blue triangles; when diffusion coefficients are equal for both adsorbing species (i = 0) – red rectangles. The dotted straight line is given here for comparison. The recalculated curves deviated even further from a straight line than the original conditions (i = 2/3).

B.3 Supplementary Tables

Table B.1: Masses, hydrodynamic radii and diffusion coefficients of molecules with biotin anchor used in this study.

Molecule	M_w	Hydrodynamic radius	Diffusion coefficient
biotin	244.3 Da	R_{biotin} = 0.37 nm from van der Waals volume ($V_{\text{vdW}} = 0.213\ \text{nm}^3$) assuming a sphere, as previously validated by others [115]	$D_{\text{biotin}} = 580\mu\text{m}^2/\text{s}$ From the hydrodynamic radius [a)]
b-FITC	732.8 Da	$R_{\text{b-FITC}}$ = 0.63 nm from the frequency shift [b)]	$D_{\text{b-FITC}} = 340\mu\text{m}^2/\text{s}$ As previously determined by others [75]
b-ZZ	16.2 kDa	$R_{\text{b-ZZ}}$ = 2 nm from the frequency shift [b)]	$D_{\text{b-ZZ}} = 107\mu\text{m}^2/\text{s}$ Computed following [115] using a radius of gyration $R_g = 1.05 \times \left(\frac{3}{5}\right)^{1/2} \left(\frac{3}{4\pi}\frac{M_W}{\rho N_A}\right)^{1/3} = 1.4$ nm with density $\rho = 1.4\ \text{g/cm}^3$ (typical for proteins); the factor 1.05 accounts for biotin tag likely pointing out of the protein

[a)] Hydrodynamic radii and diffusion coefficients were interconverted using the Stokes-Einstein relation $D = k_B T/(6\pi\eta R)$, with solvent viscosity $\eta = 1.0\text{mPa}\cdot\text{s}$ and thermal energy $k_B T$ at T= 20 °C.

[b)] Hydrodynamic radii was defined using the Sauerbrey equation, as $h = -C\Delta F/\rho$, with the mass-sensitivity constant $C = 18.0\ \text{ng}/\left(\text{cm}^2\ \text{Hz}\right)$. The film density was assumed to be $1.1\ \text{g/cm}^3$, reflecting the solvated nature of the film to a good approximation. We verified that $\Delta D/-\Delta F \ll 0.4\times10^{-6}/\text{Hz}$, to ascertain films are sufficiently rigid for the Sauerbrey equation to provide reliable film thickness estimates [134].

Table B.2: Constants detected from the fits to the calibration curves for SAv and b-ZZ binding.

SAv			b-ZZ		
i	A	B $\left(\mathrm{cm}^2/\mathrm{ng}\right)$	i	A	B $\left(\mathrm{cm}^2/\mathrm{ng}\right)$
3	0.8357 ± 0.0016	0.00117 ± 0.000008	3	0.84842 ± 0.00925	0.000786 ± 0.000011
5	0.8323 ± 0.0015	0.00120 ± 0.000008	5	0.83944 ± 0.00114	0.000780 ± 0.000014
7	0.8344 ± 0.0013	0.00124 ± 0.000007	7	0.83703 ± 0.00121	0.000820 ± 0.000015

C

Résumé détaillé de chaque chapitre

Chapitre 1. Introduction

Ce manuscrit présente un travail expérimental qui vise à créer une plateforme *in vitro* pour étudier les interactions cellule-glycocalyx dans des conditions contrôlées avec précision. Le chapitre d'introduction explore les aspects biologiques et physiques des interactions cellule - glycocalyx sous flux et délimite le champ de cette étude, en mettant l'accent sur les lacunes de la recherche.

Adhésion des cellules sanguines sous flux

Le recrutement des globules blancs est un processus hautement régulé impliquant une cascade d'interactions adhésives entre les molécules d'adhésion sur la couche de cellules endothéliales qui tapissent les vaisseaux sanguins et les ligands correspondants à la surface des leucocytes. Ces interactions passent par des étapes séquentielles, notamment la capture initiale des cellules, le roulement, l'arrêt, l'adhésion renforcée, l'étalement, la reptation intravasculaire et la transmigration.

Les premières étapes sont initiés par les sélectines, une famille de molécules qui facilitent le roulement des leucocytes le long des cellules endothéliales. Les trois principaux sous-types de sélectines sont la L-sélectine, la E-sélectine et la P-sélectine. Ces interactions visent à amener les leucocytes à proximité d'autres molécules de signalisation sur l'endothélium. La P-sélectine, en particulier, joue un rôle crucial et peut exister sous forme de monomère ou de dimère. La dimérisation de la P-sélectine améliore la stabilité de roulement des cellules sous flux. En outre, la P-sélectine et la L-sélectine présentent toutes deux un phénomène de "catch bond", où leur force d'adhésion augmente avec la contrainte de cisaillement, et où les leucocytes qui roulent se détachent lorsque le flux s'arrête.

L'activation des leucocytes et l'adhésion stabilisée suivent le roulement médié par la sélectine. Les chimiokines déposées sur l'endothélium enflammé induisent l'arrêt des monocytes qui roulent et activent les leucocytes. Cette activation augmente la quantité d'intégrines à la surface des leucocytes, et ces intégrines se lient avec les immunoglobulines à la surface des cellules endothéliales, ce qui renforce l'adhésion.

La migration cellulaire transendothéliale, l'étape finale de ce processus, se produit après l'arrêt complet d'un leucocyte dans des conditions de flux. Le leucocyte traverse la couche de cellules endothéliales et migre vers les tissus interstitiels. Ce processus est initié par des ligands des cel-

lules endothéliales, tels que ICAM-1 et VCAM-1, et repose sur des niveaux élevés de calcium endothélial intracellulaire. Certaines molécules de jonction endothéliales jouent également un rôle dans la transmigration des globules blancs.

Le glycocalyx vasculaire : une barrière mécanique protégeant la paroi vasculaire des cellules sanguines

Alors que les cascades d'adhésion cellulaire ont été largement étudiées, le glycocalyx endothélial, une couche molle riche en glycanes recouvrant les surfaces des cellules endothéliales, n'a reçu qu'une attention limitée dans le contexte de l'adhésion cellulaire sous flux.

La structure du glycocalyx endothélial est complexe, composée de protéoglycanes et de glycoprotéines. Les protéoglycanes sont constitués d'une protéine liées à des chaînes de glycosaminoglycanes (GAG), en particulier le sulfate d'héparane, le sulfate de chondroïtine et l'hyaluronane, jouant un rôle dominant dans la configuration maillée du glycocalyx. L' acide hyaluronique, qui s'ancre directement à la membrane des cellules endothéliales par l'intermédiaire du CD44, se distingue par l'absence de groupes sulfates.

Les propriétés mécaniques du glycocalyx varient selon les structures vasculaires et se caractérisent par leur souplesse. Toutefois, ces propriétés peuvent changer dans des conditions pathologiques, entraînant une diminution de l'épaisseur et de la complaisance.

Le rôle du glycocalyx dans l'adhésion des cellules sanguines est double. Il agit comme un coussin répulsif pour la plupart des cellules circulantes, empêchant la coagulation du sang dans les microvaisseaux. D'autre part, certains globules blancs peuvent interagir avec les GAG du glycocalyx, ralentissant leur mouvement et indentant la brosse, ce qui est crucial pour leur adhésion.

Le déficit de recherche réside dans la compréhension du lien entre les propriétés mécaniques du glycocalyx et ses propriétés fonctionnelles, notamment en termes d'adhésion des leucocytes. Bien que certaines données suggèrent l'existence d'une relation, celle-ci reste non quantifiée en raison de la complexité de l'étude de ce phénomène au sein des systèmes vivants.

Mon étude se concentre sur le développement d'outils permettant d'explorer l'impact des propriétés mécaniques du glycocalyx sur la capacité des cellules circulantes à accéder aux molécules d'adhésion de surface situées sous cet épais maillage.

Principes physiques de l'interaction cellule-glycocalyx sous flux

Cette section explore l'impact des parois souples sur l'adhésion cellulaire du point de vue de la physique de la matière molle. Elle souligne que si la migration des cellules sanguines et la dynamique du flux sanguin ont été largement étudiées, la composante liée au glycocalyx des vaisseaux sanguins n'a reçu qu'une attention limitée dans ce contexte.

L'étude, menée en collaboration entre le LIPhy et le laboratoire Richter, se concentre sur les investigations expérimentales des mécanismes régissant la régulation des cellules circulantes. Pour simplifier, la couche de glycocalyx est représentée par une brosse dense d'acide hyaluronique (HA), et ses propriétés mécaniques, telles que l'épaisseur et la flexibilité (liée à l'espacement des points d'attache de la chaîne), sont soigneusement contrôlées. Des particules sphériques sont utilisées pour imiter les cellules en circulation.

Un dispositif expérimental avec un flux de cisaillement contrôlé est mis au point pour suivre l'interaction de ces particules avec la brosse d'acide hyaluronique. Le débit est contrôlé avec précision et le taux de cisaillement à la paroi de la chambre d'écoulement est déterminé à l'aide de formules spécifiques.

La section décrit les forces agissant sur les particules, y compris les forces de portance inertielle et les forces élastohydrodynamiques (EHD). L'équilibre de ces forces et leurs effets sur le comportement des particules en présence de la brosse HA sont discutés. La souplesse de la couche d'HA repousse les mimétiques cellulaires qui n'interagissent pas spécifiquement avec le glycocalyx.

L'interaction entre les parois souples et les interactions biochimiques spécifiques entre le glycocalyx et les récepteurs exprimés à la surface des cellules immunitaires circulantes est explorée. Cet aspect est difficile à étudier *in vivo*, mais des recherches précédentes dans notre groupe fournissent des indications précieuses. On observe que les microbilles portant des récepteurs CD44 à leur surface présentent des interactions spécifiques avec la couche d'HA, y compris le roulement et l'indentation de la brosse. Ces interactions sont influencées par des facteurs tels que la densité de surface des récepteurs CD44 et le module d'élasticité de la brosse.

L'étude démontre qu'en présence d'interactions spécifiques CD44/HA, les modèles de cellules sanguines ralentissent, roulent et s'enfoncent de manière significative dans la brosse d'acide hyaluronique. Cela ouvre la voie à des recherches plus approfondies sur la mécanique de l'adhésion cellulaire dans des conditions d'écoulement.

Hypothèse de recherche

Dans le but d'approfondir la compréhension des étapes initiales de l'adhésion des cellules sanguines, nous aimerions étudier l'interaction entre les mécanismes physiques et biochimiques qui participent à l'étape suivante de l'interaction cellule-glycocalyx : que se passe-t-il après que la cellule a indenté l'épaisse couche de glycocalyx et comment accède-t-elle aux molécules d'adhésion de surface ? Nous supposons que l'indentation du glycocalyx permet d'accéder aux molécules d'adhésion de surface sous-jacentes et nous nous intéressons à la manière dont les propriétés mécaniques du glycocalyx peuvent affecter la capacité des cellules à atteindre ces récepteurs (Fig. C.1). En outre, nous pensons que la fluidité de la surface mimétique des cellules peut jouer un rôle dans le recrutement des molécules d'adhésion cellulaire pendant leur interaction avec les ligands correspondants à la surface des cellules.

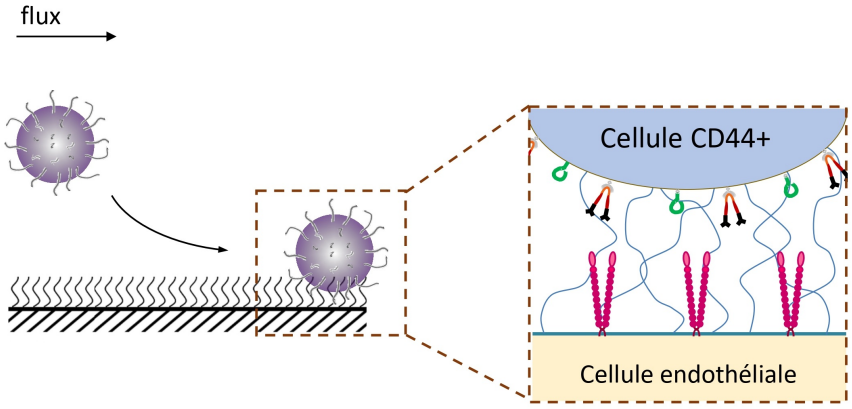

Figure C.1: Représentation graphique de l'hypothèse de recherche. Les cellules sanguines portant le récepteur CD44 interagissent spécifiquement avec le glycocalyx, l'indentent et atteignent les molécules d'adhésion de surface situées en dessous à la surface de la cellule endothéliale.

Plateforme in vitro pour l'étude de l'interaction cellule-glycocalyx

L'étude de l'interaction complexe entre les aspects physiques et biochimiques de l'adhésion cellulaire in vivo pose des défis importants. Cette complexité découle de la difficulté à caractériser précisément les propriétés mécaniques de la couche molle du glycocalyx et à contrôler l'adhésion physique. caractériser précisément les propriétés mécaniques de la couche molle du glycocalyx et de contrôler les paramètres physiques dans les systèmes vivants. dans les systèmes vivants. Par conséquent, la façon la plus prometteuse d'aborder cette question de recherche est d'utiliser

un système *in vitro*. est d'utiliser un système *in vitro* aux caractéristiques précisément définies, permettant une manipulation contrôlée des paramètres physiques. manipulation contrôlée des paramètres physiques.

L'application d'une plate-forme *in vitro* présente plusieurs avantages par rapport aux systèmes in vivo :

1. Le réglage fin des propriétés mécaniques du glycocalyx, telles que son épaisseur et son élasticité, permet une évaluation systématique de leur impact sur l'interaction des cellules avec la paroi molle.

2. La manipulation du type et de la densité de surface des récepteurs endothéliaux permet d'évaluer l'influence distincte de chaque type de récepteur sur l'adhésion cellulaire sous flux.

3. Le remplacement des leucocytes vivants par des mimétiques cellulaires permet une différenciation fiable entre l'impact des récepteurs spécifiques se liant au glycocalyx et ceux se liant aux molécules d'adhésion des cellules endothéliales au cours du processus d'adhésion cellulaire.

4. La régulation de la dynamique du flux dans le système facilite l'examen des interactions cellule-glycocalyx dans différentes conditions de cisaillement.

5. L'utilisation d'un système spécialisé basé sur la microscopie permet une observation et une caractérisation plus robustes de l'interaction entre les mimétiques de cellules sanguines et le modèle de glycocalyx dans des conditions de flux.

La plateforme in vitro précédemment établie par Davies et al [33] avec des propriétés mécaniques réglables du glycocalyx et un taux de cisaillement contrôlé dans le système microfluidique a effectivement facilité l'examen des aspects physiques de l'interaction des cellules avec la paroi molle. Cependant, cette plateforme établie n'a pas pu être utilisée pour répondre à l'hypothèse de recherche de mon projet, ce qui a nécessité le développement de plusieurs nouveaux outils spécifiquement adaptés à cette investigation.

Objectif général et objectifs spécifiques

L'objectif global de ce projet est le suivant :

Comprendre comment les propriétés mécaniques du glycocalyx contrôlent l'accès des cellules sanguines aux récepteurs de surface pendant la phase initiale de l'adhésion cellulaire.

Les objectifs de recherche spécifiques de cette thèse sont les suivants :

1. Développer un nouveau modèle *in vitro* bien défini au niveau biochimique de la surface des cellules endothéliales qui combine une couche de type glycocalyx d'épaisseur et d'élasticité variables recouvrant des récepteurs d'adhésion cellulaire.

2. Développer une méthode pour régler quantitativement la densité des récepteurs de surface ancrés à la surface.

3. Développer des microbilles fonctionnalisées pour imiter les globules blancs qui présentent à leur surface deux récepteurs distincts : l'un se liant au glycocalyx et l'autre à un récepteur d'adhésion des cellules endothéliales.

Méthodologie

Dans cette étude, nous avons choisi de nous concentrer sur un récepteur spécifique de la surface endothéliale, la P-sélectine, et sur son ligand correspondant, PSGL-1, qui est exprimé à la surface des leucocytes. Ce couple récepteur-ligand est connu pour jouer un rôle central dans les phases initiales de l'adhésion des cellules sanguines à l'endothélium. Il représente l'une des premières interactions qui se produisent après que la cellule a indenté la couche dense de glycocalyx. J'ai utilisé une plateforme développée précédemment [33] comme base pour l'affiner et l'améliorer, en la rendant plus adaptée à notre recherche spécifique. La figure C.2 illustre une comparaison schématique entre le modèle original et le modèle amélioré. Le modèle affiné du glycocalyx de la paroi vasculaire consiste en une brosse dense d'HA, sous laquelle se trouvent les récepteurs endothéliaux de la P-sélectine.

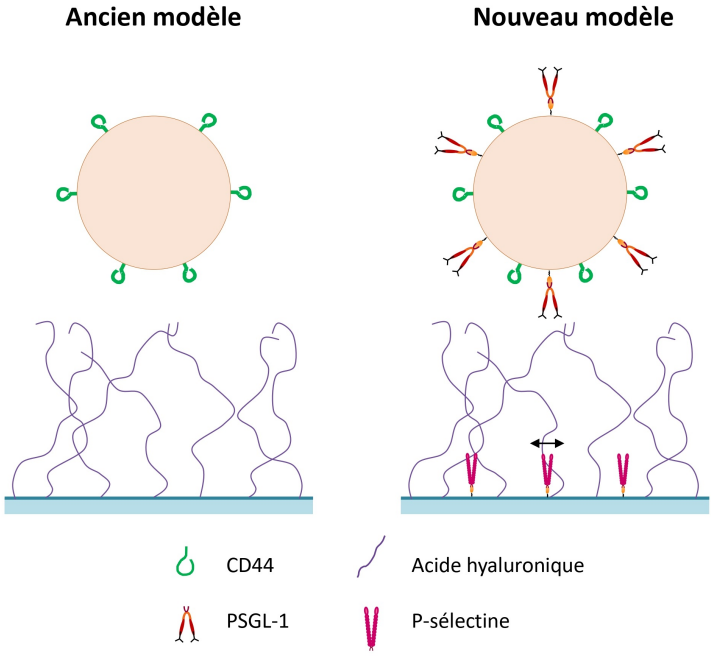

Figure C.2: Biomimétique du glycocalyx et des globules blancs : anciens modèles et modèles améliorés. Dans le nouveau modèle, le récepteur de surface P-sélectine est ajouté au mimétique du glycocalyx et son ligand PSGL-1 est incorporé dans le mimétique cellulaire. Le nouveau modèle intègre l'ancrage fluide des récepteurs dans le mimétique du glycocalyx, ce qui permet d'explorer les effets de recrutement des récepteurs.

Chapitre 2. Modèle de glycocalyx avec des caractéristiques mécaniques et biochimiques définies

Ce chapitre présente un nouveau modèle synthétique de glycocalyx de la paroi vasculaire pour les études *in vitro* des interactions cellule-glycocalyx dans des conditions bien contrôlées. Le modèle est basé sur une bicouche lipidique supportée et incorpore une épaisse brosse d'acide hyaluronique et le récepteur de surface P-sélectine uniformément réparti sur la surface (Fig. C.3). Une méthode a été mise au point permettant d'ajuster la mobilité bidimensionnelle de ce système

via le contrôle de la fluidité de la bicouche supportée.

Ce modèle synthétique du glycocalyx est un système polyvalent pour l'étude des interactions cellule-glycocalyx, car il permet de reproduire les propriétés biophysiques et chimiques de ce dernier. Le protocole d'élaboration de ce modèle implique la sélection d'une plateforme d'ancrage, la création de la brosse HA avec les propriétés mécaniques souhaitées et la fixation des récepteurs de surface d'intérêt.

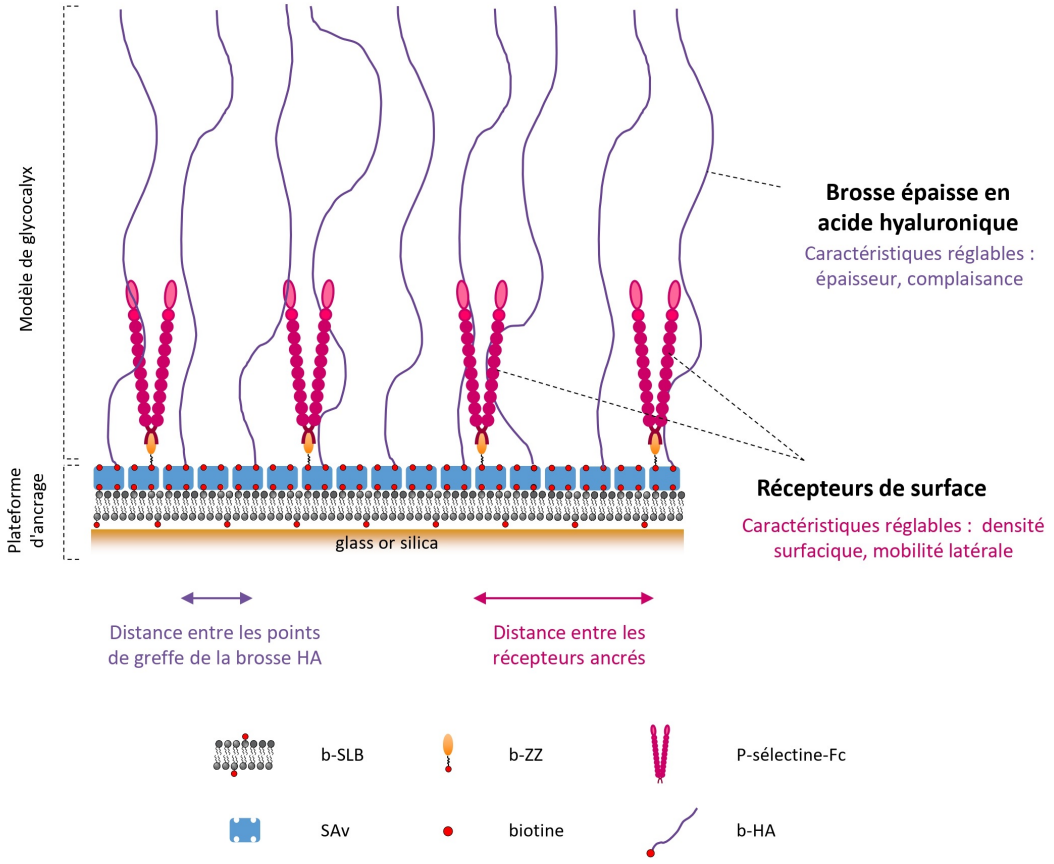

Figure C.3: Schéma du modèle moléculaire du glycocalyx. La plateforme d'ancrage est composée d'une bicouche lipidique supportée biotinylée (b-SLB) formée sur un support en verre ou en silice et d'une monocouche de streptavidine (SAv) facilitant l'ancrage des espèces biotinylées grâce à des liaisons stables entre la biotine et la streptavidine. Le modèle du glycocalyx comprend de longues chaînes d'acide hyaluronique (HA) biotinylées à une extrémité et des molécules de P-sélectine P liées à un motif Fc, reliées à la plateforme par la protéine adaptatrice b-ZZ via des liaisons Fc-ZZ. Le modèle moléculaire présente plusieurs caractéristiques réglables : les propriétés mécaniques de la brosse HA (épaisseur et complaisance), la densité de surface et la mobilité latérale des récepteurs de la P-sélectine.

Ce chapitre met en évidence la fiabilité et la reproductibilité du système moléculaire et la possibilité de régler la fluidité de la bicouche lipidique supportée pour diverses applications, y compris des études sous écoulement. La flexibilité du modèle permet la coprésentation de diverses molécules d'adhésion de surface aux côtés de la brosse HA, ce qui ouvre la voie à l'exploration d'interactions cellules-glycocalyx complexes impliquant différentes combinaisons de récepteurs et leurs implications dans divers processus biologiques.

Dans l'ensemble, ce modèle moléculaire constitue un outil précieux pour l'étude des interactions cellule-glycocalyx, contribuant à la compréhension des aspects mécaniques de ces interactions.

Chapitre 3. Contrôle des densités de surface des récepteurs

Ce chapitre présente une méthode permettant de contrôler la densité de surface des récepteurs d'intérêt dans les couches moléculaires. Le besoin de contrôler la densité des récepteurs est né de la nécessité d'imiter la distance biologiquement pertinente entre les récepteurs de la P-sélectine. Cependant, cette méthode a des applications plus larges dans le domaine de la biofonctionalisation de surface.

La méthode de contrôle des récepteurs de surface utilise des interactions spécifiques, par lesquelles des molécules fonctionnelles s'adsorbent sur la surface via des motifs adhésifs en compétition avec des motifs libres. Les principales hypothèses qui sous-tendent cette théorie sont les suivantes :

1. La fixation de toutes les espèces est limitée par le transport de masse : le taux d'absorption d'un soluté par la surface est élevé et le fluide à la surface est presque complètement déplété (la concentration des espèces qui se fixent est proche de 0 à la surface).

2. L'interaction entre le motif adhésif et la surface est forte et irréversible.

3. L'encombrement stérique n'entrave pas l'adsorption des molécules, de sorte que tous les sites d'adhésion disponibles sont occupés à l'équilibre.

4. La solution est semi-infinie - il existe un réservoir illimité de molécules en solution.

Les concentrations en solution des différentes espèces (molécules d'intérêt et motifs libres) peuvent être définies à l'aide des équations suivantes afin d'obtenir la densité de récepteurs souhaitée:

1) pour des conditions stagnantes :

$$\frac{c_2}{c_1} = \left(\frac{D_1}{D_2}\right)^{1/2} \left(\frac{\Gamma_{\text{as}}}{\Gamma_{1,\text{sat}}} - 1\right) = \left(\frac{R_2}{R_1}\right)^{1/2} \left(\frac{\Gamma_{\text{as}}}{\Gamma_{1,\text{sat}}} - 1\right) \tag{C.1}$$

2) en présence de flux :

$$\frac{c_2}{c_1} = \left(\frac{D_1}{D_2}\right)^{1/2} \left(\frac{\Gamma_{\text{as}}}{\Gamma_{1,\text{sat}}} - 1\right) = \left(\frac{R_2}{R_1}\right)^{1/2} \left(\frac{\Gamma_{\text{as}}}{\Gamma_{1,\text{sat}}} - 1\right) \tag{C.2}$$

Cette approche offre un outil simple et polyvalent pour créer des couches moléculaires avec une densité de récepteurs bien définie.

Chapitre 4. Microbilles présentant des ligands pour le glycocalyx et pour les récepteurs de surface

Dans ce chapitre, l'accent a été mis sur le développement d'un protocole de fonctionnalisation des microbilles de polystyrène imitant les globules blancs circulants dans le cadre d'études *in vitro*. Les microbilles ont été équipées de deux récepteurs spécifiques : CD44, qui interagit avec la brosse HA représentant le modèle de glycocalyx, et PSGL-1, qui sert de ligand pour le récepteur de surface P-sélectine (Fig. C.4). Une nouvelle méthode a été introduite pour contrôler précisément la densité de ces récepteurs à la surface des microbilles. En outre, un protocole a été établi pour permettre le greffage simultané de deux types distincts de récepteurs sur la surface des microbilles à des densités souhaitées.

Le protocole mis au point pour fonctionnaliser les microbilles avec deux types de récepteurs a des applications potentielles dans la création de modèles de leucocytes pour des essais d'adhésion sur le modèle de glycocalyx. Il offre également des applications plus larges dans la fonctionnalisation des microbilles à diverses fins de recherche, permettant l'exploration de différentes interactions ligand-récepteur et leur impact sur l'adhésion cellulaire dans des conditions d'écoulement.

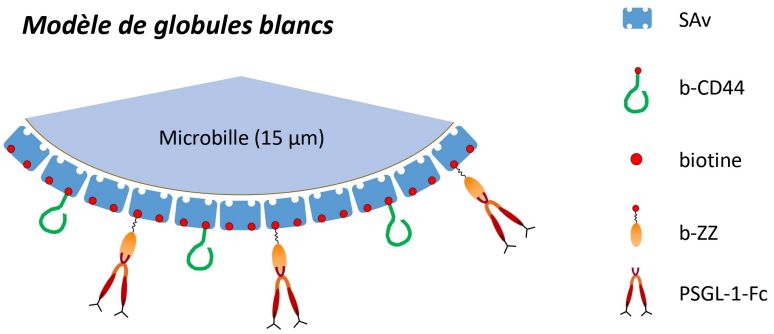

Figure C.4: Schéma des modèles des globules blancs.

Chapitre 5. Conclusions et perspectives

Ce chapitre met en évidence les principaux résultats de cette thèse et les applications potentielles de la plateforme *in vitro* nouvellement développée :

1. *L'étude des propriétés mécaniques des brosses de HA sur l'interaction P-sélectine/PSGL-1.* En utilisant des canaux microfluidiques, des billes avec des récepteurs CD44 et PSGL-1 traverseront et rencontreront des récepteurs P-sélectine dissimulés sous la brosse HA. Cette étude explore la façon dont les propriétés mécaniques du glycocalyx, qu'elles soient souples ou rigides, influencent l'adhésion cellulaire.

2. *Examen de l'impact des propriétés mécaniques des brosses HA sur l'adhésion des leucocytes.* Similaire à l'approche précédente, cette étude utilisera la plateforme glycocalyx mais avec des globules blancs au lieu de modèles. Le passage à des cellules vivantes peut valider les observations faites avec des modèles cellulaires concernant l'importance des propriétés mécaniques du glycocalyx.

3. *Évaluation de l'influence de la mobilité des récepteurs sur l'adhésion des cellules sanguines sous flux.* De nouveaux protocoles de contrôle de la mobilité latérale des récepteurs ancrés en surface peuvent être mis en œuvre pour étudier les différences d'adhésion cellulaire entre les plateformes mobiles et immobiles. Cette étude vise à confirmer l'hypothèse selon laquelle le recrutement des récepteurs joue un rôle crucial dans l'adhésion des cellules sanguines. Des modèles cellulaires et des cellules vivantes peuvent être utilisés dans cette étude.

Ce chapitre présente une première application de la plateforme développée dans des tests d'adhésion sous flux laminaire. En outre, il discute des implications potentielles plus larges de la plateforme au-delà de l'étude des interactions entre les leucocytes et les glycocalyx.

Bibliography

[1] Aysun Adan, Günel Alizada, Yağmur Kiraz, Yusuf Baran, and Ayten Nalbant. Flow cytometry: basic principles and applications. *Critical Reviews in Biotechnology*, 37(2):163–176, March 2017.

[2] Lucas Ahrens, Daniel Vonwil, Neha Arya, Aurelien Forget, and V. Prasad Shastri. Biotin-Avidin-Mediated Capture of Microspheres on Polymer Fibers. *Molecules*, 24(11):2036, May 2019.

[3] Bruce Alberts, Alexander Johnson, Julian Lewis, Martin Raff, Keith Roberts, and Peter Walter. The Lipid Bilayer. In *Molecular Biology of the Cell. 4th edition*. Garland Science, 2002.

[4] Verónica Almeida-Marrero, Fleur Bethlehem, Sara Longo, M. Candelaria Bertolino, Tomás Torres, Jurriaan Huskens, and Andrés de la Escosura. Tailored Multivalent Targeting of Siglecs with Photosensitizing Liposome Nanocarriers. *Angewandte Chemie (International Ed. in English)*, 61(31):e202206900, August 2022.

[5] George P Anderson and Nandan L Nerurkar. Improved fluoroimmunoassays using the dye Alexa Fluor 647 with the RAPTOR, a fiber optic biosensor. *Journal of Immunological Methods*, 271(1):17–24, December 2002.

[6] Jakob Andersson, Pierluigi Bilotto, Laura L. E. Mears, Stefan Fossati, Ulrich Ramach, Ingo Köper, Markus Valtiner, and Wolfgang Knoll. Solid-supported lipid bilayers - A versatile tool for the structural and functional characterization of membrane proteins. *Methods (San Diego, Calif.)*, 180:56–68, August 2020.

[7] Seetharamaiah Attili, Oleg V. Borisov, and Ralf P. Richter. Films of End-Grafted Hyaluronan Are a Prototype of a Brush of a Strongly Charged, Semiflexible Polyelectrolyte with Intrinsic Excluded Volume. *Biomacromolecules*, 13(5):1466–1477, May 2012.

[8] Fouzia Bano, Suneale Banerji, Mark Howarth, David G. Jackson, and Ralf P. Richter. A single molecule assay to probe monovalent and multivalent bonds between hyaluronan and its key leukocyte receptor CD44 under force. *Scientific Reports*, 6(1):34176, September 2016. Number: 1 Publisher: Nature Publishing Group.

[9] T. M. Bayerl and M. Bloom. Physical properties of single phospholipid bilayers adsorbed to micro glass beads. A new vesicular model system studied by 2H-nuclear magnetic resonance. *Biophysical Journal*, 58(2):357–362, August 1990.

[10] J Beaucourt, T Biben, and C Misbah. Optimal lift force on vesicles near a compressible substrate. *Europhysics Letters (EPL)*, 67(4):676–682, August 2004.

[11] Daniëlle MH Beurskens, Martine E Bol, Tammo Delhaas, Marcel CG van de Poll, Chris PM Reutelingsperger, Gerry AF Nicolaes, and Jan-Willem EM Sels. Decreased endothelial glycocalyx thickness is an early predictor of mortality in sepsis. *Anaesthesia and Intensive Care*, 48(3):221–228, May 2020.

[12] M. P. Bevilacqua, R. M. Nelson, G. Mannori, and O. Cecconi. Endothelial-leukocyte adhesion molecules in human disease. *Annual Review of Medicine*, 45:361–378, 1994.

[13] Pit Bingen, Guoliang Wang, Nicole F. Steinmetz, Michael Rodahl, and Ralf P. Richter. Solvation Effects in the Quartz Crystal Microbalance with Dissipation Monitoring Response to Biomolecular Adsorption. A Phenomenological Approach. *Analytical Chemistry*, 80(23):8880–8890, December 2008. Publisher: American Chemical Society.

[14] Timothy D. Blalock, Sandra J. Spurr-Michaud, Ann S. Tisdale, Susan R. Heimer, Michael S. Gilmore, Vijaya Ramesh, and Ilene K. Gipson. Functions of MUC16 in corneal epithelial cells. *Investigative Ophthalmology & Visual Science*, 48(10):4509–4518, October 2007.

[15] Andrew D. Blann, Sunil K. Nadar, and Gregory Y. H. Lip. The adhesion molecule P-selectin and cardiovascular disease. *European Heart Journal*, 24(24):2166–2179, December 2003.

[16] Marc Bohner, Solène Tadier, Noémie van Garderen, Alex de Gasparo, Nicola Döbelin, and Gamal Baroud. Synthesis of spherical calcium phosphate particles for dental and orthopedic applications. *Biomatter*, 3(2):e25103, April 2013. Publisher: Taylor & Francis _eprint: https://doi.org/10.4161/biom.25103.

[17] Diego Bouzas-Ramos, Laura Trapiella-Alfonso, Kelly Pons, Jorge Ruiz Encinar, José M. Costa-Fernández, Vassilis Tsatsaris, and Nathalie Gagey-Eilstein. Controlling Ligand Surface Density on Streptavidin-Magnetic Particles by a Simple, Rapid, and Reliable Chemiluminescent Test. *Bioconjugate Chemistry*, 29(8):2646–2653, August 2018.

[18] Tione Buranda, Jinman Huang, G. V. Ramarao, Linnea K. Ista, Richard S. Larson, Timothy L. Ward, Larry A. Sklar, and Gabriel P. Lopez. Biomimetic Molecular Assemblies on Glass and Mesoporous Silica Microbeads for Biotechnology. *Langmuir*, 19(5):1654–1663, March 2003. Publisher: American Chemical Society.

[19] J. J. Campbell, S. Qin, K. B. Bacon, C. R. Mackay, and E. C. Butcher. Biology of chemokine and classical chemoattractant receptors: differential requirements for adhesion-triggering versus chemotactic responses in lymphoid cells. *The Journal of Cell Biology*, 134(1):255–266, July 1996.

[20] C G Caro, T J Pedley, R C Schroter, and W A Seed. *The mechanics of the circulation; 2nd ed.* Cambridge University Press, Cambridge, 2011.

[21] Ixaskun Carton, Alain R. Brisson, and Ralf P. Richter. Label-free detection of clustering of membrane-bound proteins. *Analytical Chemistry*, 82(22):9275–9281, November 2010.

[22] Alain Carvalho, Matthias Geissler, Heinz Schmid, Bruno Michel, and Emmanuel Delamarche. Self-Assembled Monolayers of Eicosanethiol on Palladium and Their Use in Microcontact Printing. *Langmuir*, 18(6):2406–2412, March 2002. Publisher: American Chemical Society.

[23] Daniel Chappell, Matthias Jacob, Oliver Paul, Markus Rehm, Ulrich Welsch, Mechthild Stoeckelhuber, Peter Conzen, and Bernhard F. Becker. The glycocalyx of the human umbilical vein endothelial cell: an impressive structure ex vivo but not in culture. *Circulation Research*, 104(11):1313–1317, June 2009.

[24] Souvik Chattopadhaya, Lay Pheng Tan, and Shao Q. Yao. Strategies for site-specific protein biotinylation using in vitro, in vivo and cell-free systems: toward functional protein arrays. *Nature Protocols*, 1(5):2386–2398, 2006.

[25] Cheng Chen, Qi-Lai Huang, Shu-Han Jiang, Xiao Pan, and Zi-Chun Hua. Immobilized protein ZZ, an affinity tool for immunoglobulin isolation and immunological experimentation. *Biotechnology and Applied Biochemistry*, 45(Pt 2):87–92, September 2006.

[26] Xinyue Chen and Ralf P. Richter. Effect of calcium ions and pH on the morphology and mechanical properties of hyaluronan brushes. *Interface Focus*, 9(2):20180061, April 2019.

[27] Pradeep Cherukat and John B. Mclaughlin. The inertial lift on a rigid sphere in a linear shear flow field near a flat wall. *Journal of Fluid Mechanics*, 263:1–18, March 1994. Publisher: Cambridge University Press.

[28] Claire E. Chivers, Estelle Crozat, Calvin Chu, Vincent T. Moy, David J. Sherratt, and Mark Howarth. A streptavidin variant with slower biotin dissociation and increased mechanostability. *Nature Methods*, 7(5):391–393, May 2010.

[29] Claire E. Chivers, Apurba L. Koner, Edward D. Lowe, and Mark Howarth. How the biotin–streptavidin interaction was made even stronger: investigation via crystallography and a chimaeric tetramer. *Biochemical Journal*, 435(Pt 1):55–63, April 2011.

[30] Christof Christophis, Isabel Taubert, Georg R Meseck, Mario Schubert, Michael Grunze, Anthony D Ho, and Axel Rosenhahn. Shear stress regulates adhesion and rolling of CD44+ leukemic and hematopoietic progenitor cells on hyaluronan. *Biophysical journal*, 101(3):585–593, August 2011.

[31] Alina A. Constantinescu, Hans Vink, and Jos A. E. Spaan. Endothelial cell glycocalyx modulates immobilization of leukocytes at the endothelial surface. *Arteriosclerosis, Thrombosis, and Vascular Biology*, 23(9):1541–1547, September 2003.

[32] E.R. Damiano. The Effect of the Endothelial-Cell Glycocalyx on the Motion of Red Blood Cells through Capillaries. *Microvascular Research*, 55(1):77–91, January 1998.

[33] Heather S. Davies, Natalia S. Baranova, Nouha El Amri, Liliane Coche-Guérente, Claude Verdier, Lionel Bureau, Ralf P. Richter, and Delphine Débarre. An integrated assay to probe endothelial glycocalyx-blood cell interactions under flow in mechanically and biochemically well-defined environments. *Matrix Biology*, 78-79:47–59, May 2019.

[34] Heather S. Davies, Delphine Débarre, Nouha El Amri, Claude Verdier, Ralf P. Richter, and Lionel Bureau. Elastohydrodynamic Lift at a Soft Wall. *Physical Review Letters*, 120(19):198001, May 2018.

[35] Laura Dean. *Blood Groups and Red Cell Antigens*. National Center for Biotechnology Information (US), 2005.

[36] Heather C. DeGrendele, Pila Estess, and Mark H. Siegelman. Requirement for CD44 in Activated T Cell Extravasation into an Inflammatory Site. *Science*, 278(5338):672–675, October 1997.

[37] C. Deka, B. E. Lehnert, N. M. Lehnert, G. M. Jones, L. A. Sklar, and J. A. Steinkamp. Analysis of fluorescence lifetime and quenching of FITC-conjugated antibodies on cells by phase-sensitive flow cytometry. *Cytometry*, 25(3):271–279, November 1996.

[38] Sridevi Devaraj, Jung-Mi Yun, Grete Adamson, Jose Galvez, and Ishwarlal Jialal. C-reactive protein impairs the endothelial glycocalyx resulting in endothelial dysfunction. *Cardiovascular Research*, 84(3):479–484, December 2009.

[39] Daniele Di Iorio, Mark L. Verheijden, Erhard van der Vries, Pascal Jonkheijm, and Jurriaan Huskens. Weak Multivalent Binding of Influenza Hemagglutinin Nanoparticles at a Sialoglycan-Functionalized Supported Lipid Bilayer. *ACS Nano*, 13(3):3413–3423, March 2019. Publisher: American Chemical Society.

[40] Tohid Fatanat Didar and Maryam Tabrizian. Adhesion based detection, sorting and enrichment of cells in microfluidic Lab-on-Chip devices. *Lab on a Chip*, 10(22):3043–3053, November 2010.

[41] Lawrence N. Diebel and David M. Liberati. Red blood cell storage and adhesion to vascular endothelium under normal or stress conditions: An in vitro microfluidic study. *Journal of Trauma and Acute Care Surgery*, 86(6):943–951, June 2019.

[42] Qin Dong, Xueping Guo, Lian Li, Chen Yu, Lei Nie, Weilu Tian, Hui Zhang, Siling Huang, and Hengchang Zang. Understanding hyaluronic acid induced variation of water structure by near-infrared spectroscopy. *Scientific Reports*, 10:1387, January 2020.

[43] Lonnie Dorgan, Ralph Magnotti, Janming Hou, Terri Engle, Kevin Ruley, and Bruce Shull. Methods to determine biotin-binding capacity of streptavidin-coated magnetic particles. *Journal of Magnetism and Magnetic Materials*, 194(1):69–75, April 1999.

[44] Galina V. Dubacheva, Carolina Araya-Callis, Anne Geert Volbeda, Michael Fairhead, Jeroen Codée, Mark Howarth, and Ralf P. Richter. Controlling Multivalent Binding through Surface Chemistry: Model Study on Streptavidin. *Journal of the American Chemical Society*, 139(11):4157–4167, March 2017.

[45] P Estess, H C DeGrendele, V Pascual, and M H Siegelman. Functional activation of lymphocyte CD44 in peripheral blood is a marker of autoimmune disease activity. *Journal of Clinical Investigation*, 102(6):1173–1182, September 1998.

[46] Marion Ettenauer, Fritz Loth, Katrin Thümmler, Steffen Fischer, Viktoria Weber, and Dieter Falkenhagen. Characterization and functionalization of cellulose microbeads for extracorporeal blood purification. *Cellulose*, 18(5):1257–1263, October 2011.

[47] S. Freiberg and X. X. Zhu. Polymer microspheres for controlled drug release. *International Journal of Pharmaceutics*, 282(1):1–18, September 2004.

[48] Hiroyuki Fujiwara. *Spectroscopic Ellipsometry: Principles and Applications*. John Wiley & Sons, September 2007. Google-Books-ID: tTMn0NKcpjsC.

[49] Jay G. Gandhi, Donald L. Koch, and Matthew J. Paszek. Equilibrium Modeling of the Mechanics and Structure of the Cancer Glycocalyx. *Biophysical Journal*, 116(4):694–708, February 2019.

[50] Sarah Gaudette, Dez Hughes, and Manuel Boller. The endothelial glycocalyx: Structure and function in health and critical illness. *Journal of Veterinary Emergency and Critical Care*, 30(2):117–134, March 2020.

[51] Guillaume Gines, Christine Saint-Pierre, and Didier Gasparutto. A multiplex assay based on encoded microbeads conjugated to DNA NanoBeacons to monitor base excision repair activities by flow cytometry. *Biosensors and Bioelectronics*, 58:81–84, August 2014.

[52] Giulia Giubertoni, Federica Burla, Cristina Martinez-Torres, Biplab Dutta, Galja Pletikapic, Eddie Pelan, Yves L. A. Rezus, Gijsje H. Koenderink, and Huib J. Bakker. Molecular Origin of the Elastic State of Aqueous Hyaluronic Acid. *The Journal of Physical Chemistry B*, 123(14):3043–3049, April 2019.

[53] Alice L. Givan. The Basics of Staining for Cell Surface Proteins. In Rochelle A. Diamond and Susan Demaggio, editors, *In Living Color: Protocols in Flow Cytometry and Cell Sorting*, Springer Lab Manuals, pages 142–164. Springer, Berlin, Heidelberg, 2000.

[54] Anja S. Goldmann, Andreas Walther, Leena Nebhani, Raymond Joso, Dominique Ernst, Katja Loos, Christopher Barner-Kowollik, Leonie Barner, and Axel H. E. Müller. Surface Modification of Poly(divinylbenzene) Microspheres via ThiolEne Chemistry and AlkyneAzide Click Reactions. *Macromolecules*, 42(11):3707–3714, June 2009. Publisher: American Chemical Society.

[55] Martın González, Carlos E Argaraña, and Gerardo D Fidelio. Extremely high thermal stability of streptavidin and avidin upon biotin binding. *Biomolecular Engineering*, 16(1):67–72, December 1999.

[56] Xavier Grandchamp, Gwennou Coupier, Aparna Srivastav, Christophe Minetti, and Thomas Podgorski. Lift and Down-Gradient Shear-Induced Diffusion in Red Blood Cell Suspensions. *Physical Review Letters*, 110(10):108101, March 2013. Publisher: American Physical Society.

[57] NM Green. Avidin. 1. the use of [14c] biotin for kinetic studies and for assay. *Biochemical Journal*, 89(3):585, 1963.

[58] Bib Dolma Gurung and Satinder Kakar. An overview on microspheres. *Int J Health Clin Res*, 3(1):11–24, 2020.

[59] P. H. Erik Hamming and Jurriaan Huskens. Streptavidin Coverage on Biotinylated Surfaces. *ACS Applied Materials & Interfaces*, 13(48):58114–58123, December 2021. Publisher: American Chemical Society.

[60] Wim Th Hermens, Martin Benes, Ralf Richter, and Han Speijer. Effects of flow on solute exchange between fluids and supported biosurfaces. *Biotechnology and Applied Biochemistry*, 39(Pt 3):277–284, June 2004.

[61] Andrés Hidalgo, Anna J. Peired, Martin Wild, Dietmar Vestweber, and Paul S. Frenette. Complete identification of E-selectin ligands on neutrophils reveals distinct functions of PSGL-1, ESL-1, and CD44. *Immunity*, 26(4):477–489, April 2007.

[62] Vera Hintze, Matthias Schnabelrauch, and Sandra Rother. Chemical Modification of Hyaluronan and Their Biomedical Applications. *Frontiers in Chemistry*, 10, 2022.

[63] J. Hope, R. Nayar, L. Mayer, and P. Cullis. -REDUCTION OF LIPOSOME SIZE AND PREPARATION OF UNILAMELLAR VESICLES BY EXTRUSION TECHNIQUES. 2002.

[64] Ferenc Horkay, Peter J. Basser, David J. Londono, Anne-Marie Hecht, and Erik Geissler. Ions in hyaluronic acid solutions. *The Journal of Chemical Physics*, 131(18):184902, November 2009.

[65] Kazi M. Zakir Hossain, Uresha Patel, and Ifty Ahmed. Development of microspheres for biomedical applications: a review. *Progress in Biomaterials*, 4(1):1–19, March 2015.

[66] Cailing Hou, Linxia Zhang, Yue Wang, and Zhimin Wang. Synthesis and application of streptavidin functionalized organosilica microparticles. *Journal of Applied Polymer Science*, 132(9), 2015. _eprint: https://onlinelibrary.wiley.com/doi/pdf/10.1002/app.41560.

[67] Mark Howarth, Daniel J.-F. Chinnapen, Kimberly Gerrow, Pieter C. Dorrestein, Melanie R. Grandy, Neil L. Kelleher, Alaa El-Husseini, and Alice Y. Ting. A monovalent streptavidin with a single femtomolar biotin binding site. *Nature Methods*, 3(4):267–273, April 2006.

[68] A. J. Huang, J. E. Manning, T. M. Bandak, M. C. Ratau, K. R. Hanser, and S. C. Silverstein. Endothelial cell cytosolic free calcium regulates neutrophil migration across monolayers of endothelial cells. *The Journal of Cell Biology*, 120(6):1371–1380, March 1993.

[69] Ning-Ping Huang, Janos Vörös, Susan M. De Paul, Marcus Textor, and Nicholas D. Spencer. Biotin-Derivatized Poly(l-lysine)-g-poly(ethylene glycol): A Novel Polymeric Interface for Bioaffinity Sensing. *Langmuir*, 18(1):220–230, January 2002. Publisher: American Chemical Society.

[70] Yuqing Huo, Andreas Schober, S. Bradley Forlow, David F. Smith, Matthew Craig Hyman, Steffen Jung, Dan R. Littman, Christian Weber, and Klaus Ley. Circulating activated platelets exacerbate atherosclerosis in mice deficient in apolipoprotein E. *Nature Medicine*, 9(1):61–67, January 2003.

[71] Daniele Di Iorio. Designer surfaces for the quantification of multivalent biological interactions. September 2019.

[72] Kathleen M. Job, Ryan O'Callaghan, Vladimir Hlady, Alexandra Barabanova, and Randal O. Dull. Biomechanical Effects of Resuscitation Colloids on the Compromised Lung Endothelial Glycocalyx. *Anesthesia and analgesia*, 123(2):382–393, August 2016.

[73] Ulrika Johansson and Marion Macey. Tandem dyes: Stability in cocktails and compensation considerations. *Cytometry Part B: Clinical Cytometry*, 86(3):164–174, 2014.

[74] James Jonkman, Claire M. Brown, and Richard W. Cole. Quantitative confocal microscopy. In *Methods in Cell Biology*, volume 123, pages 113–134. Elsevier, 2014.

[75] A E Kamholz, E A Schilling, and P Yager. Optical measurement of transverse molecular diffusion in a microchannel. *Biophysical Journal*, 80(4):1967–1972, April 2001.

[76] János Kappelmayer and Béla Nagy. The Interaction of Selectins and PSGL-1 as a Key Component in Thrombus Formation and Cancer Progression. *BioMed Research International*, 2017:e6138145, June 2017. Publisher: Hindawi.

[77] Andreas Karner, Benedikt Nimmervoll, Birgit Plochberger, Enrico Klotzsch, Andreas Horner, Denis G. Knyazev, Roland Kuttner, Klemens Winkler, Lukas Winter, Christine Siligan, Nicole Ollinger, Peter Pohl, and Johannes Preiner. Tuning membrane protein mobility by confinement into nanodomains. *Nature nanotechnology*, 12(3):260–266, March 2017.

[78] A. Kathiravan and R. Renganathan. Fluorescence Quenching of Phycoerythrin by Anthraquinone Dyes. *Zeitschrift für Physikalische Chemie*, 224(9):1337–1346, September 2010. Publisher: De Gruyter (O).

[79] Brian K. Kay, Sang Thai, and Veronica V. Volgina. High-throughput biotinylation of proteins. *Methods in Molecular Biology (Clifton, N.J.)*, 498:185–196, 2009.

[80] Adil I. Khan, Steven M. Kerfoot, Bryan Heit, Lixin Liu, Graciela Andonegui, Brian Ruffell, Pauline Johnson, and Paul Kubes. Role of CD44 and Hyaluronan in Neutrophil Recruitment1. *The Journal of Immunology*, 173(12):7594–7601, December 2004.

[81] Zafar Khan, Mohammed A. S. Abourehab, Neha Parveen, Kanchan Kohli, and Prashant Kesharwani. Recent advances in microbeads-based drug delivery system for achieving controlled drug release. *Journal of Biomaterials Science. Polymer Edition*, 34(4):541–564, March 2023.

[82] Oksana Kirichuk, Sumitra Srimasorn, Xiaoli Zhang, Abigail R. E. Roberts, Liliane Coche-Guerente, Jessica C. F. Kwok, Lionel Bureau, Delphine Débarre, and Ralf P. Richter. Competitive Specific Anchorage of Molecules onto Surfaces: Quantitative Control of Grafting Densities and Contamination by Free Anchors. *Langmuir*, 39(50):18410–18423, December 2023. Publisher: American Chemical Society.

[83] Hana Kolářová, Barbora Ambrůzová, Lenka Švihálková Šindlerová, Anna Klinke, and Lukáš Kubala. Modulation of Endothelial Glycocalyx Structure under Inflammatory Conditions. *Mediators of Inflammation*, 2014:1–17, 2014.

[84] Konstantinos Konstantopoulos, William D. Hanley, and Denis Wirtz. Receptor–ligand binding: 'catch' bonds finally caught. *Current Biology*, 13(15):R611–R613, August 2003.

[85] Nilay J. Lakhkar, Jeong-Hui Park, Nicola J. Mordan, Vehid Salih, Ivan B. Wall, Hae-Won Kim, Scott P. King, John V. Hanna, Richard A. Martin, Owen Addison, J. Fred W. Mosselmans, and Jonathan C. Knowles. Titanium phosphate glass microspheres for bone tissue engineering. *Acta Biomaterialia*, 8(11):4181–4190, November 2012.

[86] Suman Lata, Annett Reichel, Roland Brock, Robert Tampé, and Jacob Piehler. High-Affinity Adaptors for Switchable Recognition of Histidine-Tagged Proteins. *Journal of the American Chemical Society*, 127(29):10205–10215, July 2005. Publisher: American Chemical Society.

[87] E. I. Leonova and O. V. Galzitskaya. Structure and functions of syndecans in vertebrates. *Biochemistry. Biokhimiia*, 78(10):1071–1085, October 2013.

[88] Klaus Ley, Carlo Laudanna, Myron I. Cybulsky, and Sussan Nourshargh. Getting to the site of inflammation: the leukocyte adhesion cascade updated. *Nature Reviews Immunology*, 7(9):678–689, September 2007.

[89] Fugang Li, Harold P. Erickson, Judith A. James, Kevin L. Moore, Richard D. Cummings, and Rodger P. McEver. Visualization of P-selectin Glycoprotein Ligand-1 as a Highly Extended Molecule and Mapping of Protein Epitopes for Monoclonal Antibodies. *Journal of Biological Chemistry*, 271(11):6342–6348, March 1996.

[90] Alexandre Braga Libório, Marcelo Boecker Munoz Braz, Antonio Carlos Seguro, Gdayllon C. Meneses, Fernanda Macedo de Oliveira Neves, Danielle Carvalho Pedrosa, Luciano Pamplona de Góes Cavalcanti, Alice Maria Costa Martins, and Elizabeth de Francesco Daher. Endothelial Glycocalyx Damage is Associated with Leptospirosis Acute Kidney Injury. *The American Journal of Tropical Medicine and Hygiene*, 92(3):611–616, March 2015. Publisher: The American Society of Tropical Medicine and Hygiene Section: The American Journal of Tropical Medicine and Hygiene.

[91] Laurent Limozin and Kheya Sengupta. Quantitative Reflection Interference Contrast Microscopy (RICM) in Soft Matter and Cell Adhesion. *ChemPhysChem*, 10(16):2752–2768, 2009. _eprint: https://onlinelibrary.wiley.com/doi/pdf/10.1002/cphc.200900601.

[92] Chun-Min Lin, Chun-Shian Li, Yu-Jane Sheng, David T. Wu, and Heng-Kwong Tsao. Size-Dependent Properties of Small Unilamellar Vesicles Formed by Model Lipids. *Langmuir*, 28(1):689–700, January 2012. Publisher: American Chemical Society.

[93] Yanchun Liu, Xiao Zheng Shu, and Glenn D. Prestwich. Biocompatibility and stability of disulfide-crosslinked hyaluronan films. *Biomaterials*, 26(23):4737–4746, August 2005.

[94] Niklas Lorén, Joel Hagman, Jenny K. Jonasson, Hendrik Deschout, Diana Bernin, Francesca Cella-Zanacchi, Alberto Diaspro, James G. McNally, Marcel Ameloot, Nick Smisdom, Magnus Nydén, Anne-Marie Hermansson, Mats Rudemo, and Kevin Braeckmans. Fluorescence recovery after photobleaching in material and life sciences: putting theory into practice. *Quarterly Reviews of Biophysics*, 48(3):323–387, August 2015. Publisher: Cambridge University Press.

[95] J. Christopher Love, Lara A. Estroff, Jennah K. Kriebel, Ralph G. Nuzzo, and George M. Whitesides. Self-Assembled Monolayers of Thiolates on Metals as a Form of Nanotechnology. *Chemical Reviews*, 105(4):1103–1170, April 2005. Publisher: American Chemical Society.

[96] V Lund, R Schmid, D Rickwood, and E Hornes. Assessment of methods for covalent binding of nucleic acids to magnetic beads, Dynabeads, and the characteristics of the bound nucleic acids in hybridization reactions. *Nucleic Acids Research*, 16(22):10861–10880, November 1988.

[97] Jafar Mahmoudian, Reza Hadavi, Mahmood Jeddi-Tehrani, Ahmad Mahmoudi, Ali Bayat, Elham Shaban, Mohtaram Vafakhah, Maryam Darzi, Majid Tarahomi, and Roya Ghods. Comparison of the Photobleaching and Photostability Traits of Alexa Fluor 568- and Fluorescein Isothiocyanate- conjugated Antibody. *Cell journal (Yakhteh)*, 13:169–172, September 2011.

[98] Graham Marsh and Richard E. Waugh. Quantifying the Mechanical Properties of the Endothelial Glycocalyx with Atomic Force Microscopy. *Journal of Visualized Experiments*, (72):50163, February 2013.

[99] Bryan T. Marshall, Mian Long, James W. Piper, Tadayuki Yago, Rodger P. McEver, and Cheng Zhu. Direct observation of catch bonds involving cell-adhesion molecules. *Nature*, 423(6936):190–193, May 2003.

[100] A. Martínez-Palomo. The Surface Coats of Animal Cells11Part of the personal work mentioned in this review was performed at the Institut de Recherches Scientifiques sur le Cancer, Villejuif, France. In G. H. Bourne, J. F. Danielli, and K. W. Jeon, editors, *International Review of Cytology*, volume 29, pages 29–75. Academic Press, January 1970.

[101] Braedon McDonald and Paul Kubes. Interactions between CD44 and Hyaluronan in Leukocyte Trafficking. *Frontiers in Immunology*, 6, February 2015.

[102] Rodger P McEver. Selectins: lectins that initiate cell adhesion under flow. *Current Opinion in Cell Biology*, 14(5):581–586, October 2002.

[103] Rodger P. McEver. Selectins: initiators of leucocyte adhesion and signalling at the vascular wall. *Cardiovascular Research*, 107(3):331–339, August 2015.

[104] R. T. A. Megens, S. Reitsma, P. H. M. Schiffers, R. H. P. Hilgers, J. G. R. De Mey, D. W. Slaaf, M. G. A. oude Egbrink, and M. a. M. J. van Zandvoort. Two-photon microscopy of vital murine elastic and muscular arteries. Combined structural and functional imaging with subcellular resolution. *Journal of Vascular Research*, 44(2):87–98, 2007.

[105] Padmaja Mehta, Richard D. Cummings, and Rodger P. McEver. Affinity and Kinetic Analysis of P-selectin Binding to P-selectin Glycoprotein Ligand-1*. *Journal of Biological Chemistry*, 273(49):32506–32513, December 1998.

[106] Muriel Mercier-Bonin, Mathieu Adoue, Sandrine Zanna, Philippe Marcus, Didier Combes, and Philippe Schmitz. Evaluation of adhesion force between functionalized microbeads and protein-coated stainless steel using shear-flow-induced detachment. *Journal of Colloid and Interface Science*, 338(1):73–81, October 2009.

[107] Elisa Migliorini, Dhruv Thakar, Jens Kühnle, Rabia Sadir, Douglas P. Dyer, Yong Li, Changye Sun, Brian F. Volkman, Tracy M. Handel, Liliane Coche-Guerente, David G. Fernig, Hugues Lortat-Jacob, and Ralf P. Richter. Cytokines and growth factors cross-link heparan sulfate. *Open Biology*, 5(8):150046, August 2015.

[108] Elisa Migliorini, Dhruv Thakar, Rabia Sadir, Tino Pleiner, Françoise Baleux, Hugues Lortat-Jacob, Liliane Coche-Guerente, and Ralf P. Richter. Well-defined biomimetic surfaces to characterize glycosaminoglycan-mediated interactions on the molecular, supramolecular and cellular levels. *Biomaterials*, 35(32):8903–8915, October 2014.

[109] Marco Morra and Clara Cassineli. Non-fouling properties of polysaccharide-coated surfaces. *Journal of Biomaterials Science, Polymer Edition*, 10(10):1107–1124, January 1999.

[110] Maxime Moulard and Marie-Laure Ozoux. How validated receptor occupancy flow cytometry assays can impact decisions and support drug development. *Cytometry Part B: Clinical Cytometry*, 90(2):150–158, 2016. _eprint: https://onlinelibrary.wiley.com/doi/pdf/10.1002/cyto.b.21320.

[111] Joachim D. Mueller. Fluorescence Fluctuation Spectroscopy. In Gordon C. K. Roberts, editor, *Encyclopedia of Biophysics*, pages 800–803. Springer, Berlin, Heidelberg, 2013.

[112] William A. Muller. Leukocyte-Endothelial Cell Interactions in the Inflammatory Response. *Laboratory Investigation*, 82(5):521–534, May 2002. Number: 5 Publisher: Nature Publishing Group.

[113] John F. Nagle and Stephanie Tristram-Nagle. Structure of lipid bilayers. *Biochimica et biophysica acta*, 1469(3):159–195, November 2000.

[114] Mary A. Napier and Nortin M. Hadler. Effect of calcium on structure and function of a hyaluronic acid matrix: Carbon-13 nuclear magnetic resonance analysis and the diffusional behavior of small solutes. *Proceedings of the National Academy of Sciences*, 75(5):2261–2265, May 1978. Publisher: Proceedings of the National Academy of Sciences.

[115] Doreen Niether, Mona Sarter, Bernd W. Koenig, Jörg Fitter, Andreas M. Stadler, and Simone Wiegand. Thermophoresis: The Case of Streptavidin and Biotin. *Polymers*, 12(2):376, February 2020.

[116] M. Nieuwdorp, M. C. Meuwese, H. L. Mooij, M. H. P. van Lieshout, A. Hayden, M. Levi, J. C. M. Meijers, C. Ince, J. J. P. Kastelein, H. Vink, and E. S. G. Stroes. Tumor necrosis factor-alpha inhibition protects against endotoxin-induced endothelial glycocalyx perturbation. *Atherosclerosis*, 202(1):296–303, January 2009.

[117] Adaobi Nwaneshiudu, Christiane Kuschal, Fernanda H. Sakamoto, R. Rox Anderson, Kathryn Schwarzenberger, and Roger C. Young. Introduction to confocal microscopy. *Journal of Investigative Dermatology*, 132(12):1–5, December 2012.

[118] Jeffrey A. Nye and Jay T. Groves. Kinetic Control of Histidine-Tagged Protein Surface Density on Supported Lipid Bilayers. *Langmuir*, 24(8):4145–4149, April 2008. Publisher: American Chemical Society.

[119] Ryan O'Callaghan, Kathleen M. Job, Randal O. Dull, and Vladimir Hlady. Stiffness and heterogeneity of the pulmonary endothelial glycocalyx measured by atomic force microscopy. *American Journal of Physiology-Lung Cellular and Molecular Physiology*, 301(3):L353–L360, September 2011. Publisher: American Physiological Society.

[120] D O'Connell, A Koenig, S Jennings, B Hicke, H L Han, T Fitzwater, Y F Chang, N Varki, D Parma, and A Varki. Calcium-dependent oligonucleotide antagonists specific for L-selectin. *Proceedings of the National Academy of Sciences of the United States of America*, 93(12):5883–5887, June 1996.

[121] A. Omolola Eniola and Daniel A. Hammer. In vitro characterization of leukocyte mimetic for targeting therapeutics to the endothelium using two receptors. *Biomaterials*, 26(34):7136–7144, December 2005.

[122] Alina Osypova, Dhruv Thakar, Jérôme Dejeu, Hugues Bonnet, Angéline Van der Heyden, Galina V. Dubacheva, Ralf P. Richter, Eric Defrancq, Nicolas Spinelli, Liliane Coche-Guérente, and Pierre Labbé. Sensor Based on Aptamer Folding to Detect Low-Molecular Weight Analytes. *Analytical Chemistry*, 87(15):7566–7574, August 2015. Publisher: American Chemical Society.

[123] Manolis Y. Pahakis, Jason R. Kosky, Randal O. Dull, and John M. Tarbell. The role of endothelial glycocalyx components in mechanotransduction of fluid shear stress. *Biochemical and Biophysical Research Communications*, 355(1):228–233, March 2007.

[124] Petra Patakova, Michaela Linhova, Pavla Vykydalova, Barbora Branska, Mojmir Rychtera, and Karel Melzoch. Use of fluorescent staining and flow cytometry for monitoring physiological changes in solventogenic clostridia. *Anaerobe*, 29:113–117, October 2014.

[125] Katarzyna Petka-Poniatowska. The principle of the flow cytometry technique and its applicability. pages 199–220. December 2022.

[126] Zdeněk Petrášek and Petra Schwille. Fluctuations as a source of information in fluorescence microscopy. *Journal of the Royal Society Interface*, 6(Suppl 1):S15–S25, February 2009.

[127] Frédéric Pincet, Vladimir Adrien, Rong Yang, Jérôme Delacotte, James E. Rothman, Wladimir Urbach, and David Tareste. FRAP to Characterize Molecular Diffusion and Interaction in Various Membrane Environments. *PLoS ONE*, 11(7):e0158457, July 2016.

[128] Ieva Plikusiene, Vincentas Maciulis, Arunas Ramanavicius, and Almira Ramanaviciene. Spectroscopic Ellipsometry and Quartz Crystal Microbalance with Dissipation for the Assessment of Polymer Layers and for the Application in Biosensing. *Polymers*, 14(5):1056, March 2022.

[129] Marco Polin, Antoine Allard, Kelsey Cremin, Emily Skates, and Orkun S. Soyer. Confocal imaging power settings – protocol and discussion. June 2021.

[130] A. R. Pries, T. W. Secomb, and P. Gaehtgens. The endothelial surface layer. *Pflugers Archiv: European Journal of Physiology*, 440(5):653–666, September 2000.

[131] V. Ramachandran, T. Yago, T. K. Epperson, M. M. Kobzdej, M. U. Nollert, R. D. Cummings, C. Zhu, and R. P. McEver. Dimerization of a selectin and its ligand stabilizes cell rolling and enhances tether strength in shear flow. *Proceedings of the National Academy of Sciences of the United States of America*, 98(18):10166–10171, August 2001.

[132] Peter P. Reader and Andrew M. Shaw. Kinetic Analysis of the Multivalent Ligand Binding Interaction between Protein A/G and IgG: A Standard System Setting. *The Journal of Physical Chemistry. B*, 121(38):8919–8925, September 2017.

[133] Sietze Reitsma, Dick W. Slaaf, Hans Vink, Marc A. M. J. van Zandvoort, and Mirjam G. A. oude Egbrink. The endothelial glycocalyx: composition, functions, and visualization. *Pflugers Archiv*, 454(3):345–359, June 2007.

[134] Ilya Reviakine, Diethelm Johannsmann, and Ralf P. Richter. Hearing What You Cannot See and Visualizing What You Hear: Interpreting Quartz Crystal Microbalance Data from Solvated Interfaces. *Analytical Chemistry*, 83(23):8838–8848, December 2011. Publisher: American Chemical Society.

[135] Ralf Richter, Anneke Mukhopadhyay, and Alain Brisson. Pathways of Lipid Vesicle Deposition on Solid Surfaces: A Combined QCM-D and AFM Study. *Biophysical Journal*, 85(5):3035–3047, November 2003.

[136] Ralf P. Richter. *The Formation of Solid-Supported Lipid Membranes and Two-Dimensional Assembly of Proteins*. PhD Thesis, Bordeaux 1, January 2004.

[137] Ralf P. Richter, Rémi Bérat, and Alain R. Brisson. Formation of Solid-Supported Lipid Bilayers: An Integrated View. *Langmuir*, 22(8):3497–3505, April 2006.

[138] Ralf P. Richter, Kai K. Hock, Jeffrey Burkhartsmeyer, Heike Boehm, Pit Bingen, Guoliang Wang, Nicole F. Steinmetz, David J. Evans, and Joachim P. Spatz. Membrane-Grafted Hyaluronan Films: A Well-Defined Model System of Glycoconjugate Cell Coats. *Journal of the American Chemical Society*, 129(17):5306–5307, May 2007. Publisher: American Chemical Society.

[139] Ralf P. Richter, Keith B. Rodenhausen, Nico B. Eisele, and Mathias Schubert. Coupling Spectroscopic Ellipsometry and Quartz Crystal Microbalance to Study Organic Films at the Solid-Liquid Interface. In Karsten Hinrichs and Klaus-Jochen Eichhorn, editors, *Ellipsometry of Functional Organic Surfaces and Films*, Springer Series in Surface Sciences, pages 223–248. 2014.

[140] Michael Rodahl, Fredrik Höök, Anatol Krozer, Peter Brzezinski, and Bengt Kasemo. Quartz crystal microbalance setup for frequency and Q -factor measurements in gaseous and liquid environments. *Review of Scientific Instruments*, 66(7):3924–3930, July 1995.

[141] Melanie Rodrigues, Nina Kosaric, Clark A. Bonham, and Geoffrey C. Gurtner. Wound Healing: A Cellular Perspective. *Physiological Reviews*, 99(1):665–706, January 2019.

[142] Siham Sabri, Mireille Soler, Colette Foa, Anne Pierres, Anne-Marie Benoliel, and Pierre Bongrand. Glycocalyx modulation is a physiological means of regulating cell adhesion. *Journal of Cell Science*, 113(9):1589–1600, May 2000.

[143] Günter Sauerbrey. Verwendung von Schwingquarzen zur Wägung dünner Schichten und zur Mikrowägung. *Zeitschrift fur Physik*, 155:206–222, April 1959. ADS Bibcode: 1959ZPhy..155..206S.

[144] Geert W. Schmid-Schönbein, Yuan Y. Shih, and Shu Chien. Morphometry of Human Leukocytes. *Blood*, 56(5):866–875, November 1980.

[145] T. W. Secomb, R. Hsu, and A. R. Pries. A model for red blood cell motion in glycocalyx-lined capillaries. *American Journal of Physiology-Heart and Circulatory Physiology*, 274(3):H1016–H1022, March 1998.

[146] Michael Seifert, Matthias T. Rinke, and Hans-Joachim Galla. Characterization of Streptavidin Binding to Biotinylated, Binary Self-Assembled Thiol Monolayers—Influence of Component Ratio and Solvent. *Langmuir*, 26(9):6386–6393, May 2010.

[147] Melanie Simpson, Liliana Schaefer, Vincent Hascall, and Jeffrey D. Esko. Hyaluronan. In Ajit Varki, Richard D. Cummings, Jeffrey D. Esko, Pamela Stanley, Gerald W. Hart, Markus Aebi, Debra Mohnen, Taroh Kinoshita, Nicolle H. Packer, James H. Prestegard, Ronald L. Schnaar, and Peter H. Seeberger, editors, *Essentials of Glycobiology*. Cold Spring Harbor Laboratory Press, Cold Spring Harbor (NY), 4th edition, 2022.

[148] Evgeni V. Sokurenko, Viola Vogel, and Wendy E. Thomas. Catch bond mechanism of force-enhanced adhesion: counter-intuitive, elusive but ... widespread? *Cell host & microbe*, 4(4):314–323, October 2008.

[149] D. M. Soumpasis. Theoretical analysis of fluorescence photobleaching recovery experiments. *Biophysical Journal*, 41(1):95–97, January 1983.

[150] Sumitra Srimasorn, Luke Souter, Dixy E. Green, Lynda Djerbal, Ashleigh Goodenough, James A. Duncan, Abigail R. E. Roberts, Xiaoli Zhang, Delphine Débarre, Paul L. DeAngelis, Jessica C. F. Kwok, and Ralf P. Richter. A quartz crystal microbalance method to quantify the size of hyaluronan and other glycosaminoglycans on surfaces. *Scientific Reports*, 12(1):10980, June 2022. Number: 1 Publisher: Nature Publishing Group.

[151] F Szoka and D Papahadjopoulos. Procedure for preparation of liposomes with large internal aqueous space and high capture by reverse-phase evaporation. *Proceedings of the National Academy of Sciences of the United States of America*, 75(9):4194–4198, September 1978.

[152] L.K. Tamm and H.M. McConnell. Supported phospholipid bilayers. *Biophysical Journal*, 47(1):105–113, January 1985.

[153] Jin-Bao Tang, Xi-Feng Sun, Hong-Ming Yang, Bao-Gang Zhang, Zhi-Jian Li, Zhi-Juan Lin, and Zhi-Qin Gao. Well-oriented ZZ–PS-tag with high Fc-binding onto polystyrene surface for controlled immobilization of capture antibodies. *Analytica Chimica Acta*, 776:74–78, May 2013.

[154] Qianjun Tang, Xiaodi Su, and Kian Ping Loh. Surface plasmon resonance spectroscopy study of interfacial binding of thrombin to antithrombin DNA aptamers. *Journal of Colloid and Interface Science*, 315(1):99–106, November 2007.

[155] William G. Telford. Chapter 15 - Lasers in Flow Cytometry. In Zbigniew Darzynkiewicz, Elena Holden, Alberto Orfao, William Telford, and Donald Wlodkowic, editors, *Methods in Cell Biology*, volume 102 of *Recent Advances in Cytometry, Part A*, pages 373–409. Academic Press, January 2011.

[156] Chiara Tonda-Turo, Irene Carmagnola, and Gianluca Ciardelli. Quartz Crystal Microbalance With Dissipation Monitoring: A Powerful Method to Predict the in vivo Behavior of Bioengineered Surfaces. *Frontiers in Bioengineering and Biotechnology*, 6:158, October 2018.

[157] Igor Tvaroška, Chandrabose Selvaraj, and Jaroslav Koča. Selectins—The Two Dr. Jekyll and Mr. Hyde Faces of Adhesion Molecules—A Review. *Molecules*, 25(12):2835, January 2020. Number: 12 Publisher: Multidisciplinary Digital Publishing Institute.

[158] Abraham Ulman. Formation and Structure of Self-Assembled Monolayers. *Chemical Reviews*, 96(4):1533–1554, January 1996. Publisher: American Chemical Society.

[159] Javier Urzay, Stefan G. Llewellyn Smith, and Beverley J. Glover. The elastohydrodynamic force on a sphere near a soft wall. *Physics of Fluids*, 19(10):103106, October 2007.

[160] S. Ushiyama, T. M. Laue, K. L. Moore, H. P. Erickson, and R. P. McEver. Structural and functional characterization of monomeric soluble P-selectin and comparison with membrane P-selectin. *The Journal of Biological Chemistry*, 268(20):15229–15237, July 1993.

[161] Esther Van Andel, Ian De Bus, Edwin J. Tijhaar, Maarten M. J. Smulders, Huub F. J. Savelkoul, and Han Zuilhof. Highly Specific Binding on Antifouling Zwitterionic Polymer-Coated Microbeads as Measured by Flow Cytometry. *ACS Applied Materials & Interfaces*, 9(44):38211–38221, November 2017.

[162] Bernard M. van den Berg, Max Nieuwdorp, Erik S. G. Stroes, and Hans Vink. Glycocalyx and endothelial (dys) function: from mice to men. *Pharmacological reports: PR*, 58 Suppl:75–80, 2006.

[163] Bernard M. van den Berg, Hans Vink, and Jos A. E. Spaan. The endothelial glycocalyx protects against myocardial edema. *Circulation Research*, 92(6):592–594, April 2003.

[164] P. von Hundelshausen, K. S. Weber, Y. Huo, A. E. Proudfoot, P. J. Nelson, K. Ley, and C. Weber. RANTES deposition by platelets triggers monocyte arrest on inflamed and atherosclerotic endothelium. *Circulation*, 103(13):1772–1777, April 2001.

[165] Mary M. Walczak, Chinkap Chung, Scott M. Stole, Cindra A. Widrig, and Marc D. Porter. Structure and interfacial properties of spontaneously adsorbed n-alkanethiolate monolayers on evaporated silver surfaces, May 2002. Archive Location: world Publisher: American Chemical Society.

[166] Meir Wilchek and Edward A. Bayer. [2] Introduction to avidin-biotin technology. In Meir Wilchek and Edward A. Bayer, editors, *Methods in Enzymology*, volume 184 of *Avidin-Biotin Technology*, pages 5–13. Academic Press, January 1990.

[167] Bin Wu, Jeffrey A. Chao, and Robert H. Singer. Fluorescence Fluctuation Spectroscopy Enables Quantitative Imaging of Single mRNAs in Living Cells. *Biophysical Journal*, 102(12):2936–2944, June 2012.

[168] Tadayuki Yago, Anne Leppänen, Haiying Qiu, Warren D. Marcus, Matthias U. Nollert, Cheng Zhu, Richard D. Cummings, and Rodger P. McEver. Distinct molecular and cellular contributions to stabilizing selectin-mediated rolling under flow. *The Journal of Cell Biology*, 158(4):787–799, August 2002.

[169] Tadayuki Yago, Veronika I. Zarnitsyna, Arkadiusz G. Klopocki, Rodger P. McEver, and Cheng Zhu. Transport governs flow-enhanced cell tethering through L-selectin at threshold shear. *Biophysical Journal*, 92(1):330–342, January 2007.

[170] Chengli Yang, Yueping Guan, Jianmin Xing, and Huizhou Liu. Surface Functionalization and Characterization of Magnetic Polystyrene Microbeads. *Langmuir*, 24(16):9006–9010, August 2008. Publisher: American Chemical Society.

[171] Ajit P. Yoganathan, Edward G. Cape, Hsing-Wen Sung, Frank P. Williams, and Abdul Jimoh. Review of hydrodynamic principles for the cardiologist: Applications to the study of blood flow and jets by imaging techniques. *Journal of the American College of Cardiology*, 12(5):1344–1353, November 1988.

[172] Haozhe Zhang, Chen Tan, Xiaoyue Shi, and Ji Xu. Impacts of autofluorescence on fluorescence based techniques to study microglia. *BMC Neuroscience*, 23(1):21, March 2022.

[173] Hongyan Zhang, Zhen Zhang, Yanhong Wang, Chuanchen Wu, Qingling Li, and Bo Tang. Rapid and Sensitive Detection of Cancer Cells Based on the Photothermal Effect of Graphene Functionalized Magnetic Microbeads. *ACS Applied Materials & Interfaces*, 8(44):29933–29938, November 2016. Publisher: American Chemical Society.